Investigation of Single Functional Molecules on Metal Surfaces by Scanning Tunneling Microscopy

Johannes Mielke

im Fachbereich Physik der Freien Universität Berlin
eingereichte Dissertation

2013

This PhD Thesis was carried out at the Fritz-Haber-Institut of the Max-Planck-Gesellschaft under the supervision of Leonhard Grill.

Erstgutachter:	Leonhard Grill
Zweitgutachter:	José Ignacio Pascual
Datum der Disputation:	03. Juli 2013

Kurzfassung

In der vorliegenden Dissertation wurden zwei Typen funktionaler Moleküle mit dem Rastertunnelmikroskop (RTM) auf Metalloberflächen untersucht.

Das erste Molekül ist *Tetra*-Phenyl-Porphyrin. Auf Au(111) kann es zwei verschiedene Zustände annehmen, die sich in ihrer scheinbaren Höhe auf RTM Bildern unterscheiden. Ihre Tunnelspektren, die Auskunft über die elektronische Struktur in der Nähe der Fermienergie geben, sind sehr ähnlich, aber in ihrer energetischen Position gegeneinander verschoben. Reversibles Schalten zwischen diesen beiden Zuständen ist möglich und der Schaltprozess kann bei Raumtemperatur thermisch oder bei tiefen Temperaturen von ungefähr 5 K durch Spannungspulse, die mit der RTM Spitze angelegt werden, induziert werden.

Durch Analyse des Schaltverhaltens bei Raumtemperatur, Manipulationsexperimente bei tiefen Temperaturen und Vergleich mit Berechnungen der Dichtefunktionaltheorie konnte gezeigt werden, dass in beiden Zuständen der zentrale Porphyrinring in einer sattelförmigen Konformation vorliegt, unter den hell erscheinenden Molekülen allerdings ein zusätzliches Goldadatom vorhanden ist. Dieses Adatom ist für den veränderten Bildkontrast sowie die Verschiebung der Spektren verantwortlich.

Der Schaltprozess wurde bei Raumtemperatur durch wiederholte Abbildung der selben Probenstelle untersucht. Durch die statistische Analyse einer solchen Bildserie können Informationen über korrelierte Prozesse in den Molekülen gewonnen werden, was nur aus Einzelbildern nicht möglich ist. So konnte der Transfer des hellen Zustandes eines Moleküls auf ein Nachbarmolekül beobachtet werden, der durch den Transfer des darunterliegenden Adatoms zustande kommt, sowie zeitlich korrelierte Schaltereignisse, bei denen eine größere Anzahl von Molekülen gleichzeitig schaltet.

Um den Einfluss der Bindung zwischen den Molekülen auf das Schaltverhalten zu untersuchen wurden die Resultate aus dicht gepackten Inseln mit denen von kovalent gebundenen Dimeren verglichen. Beide Seiten eines solchen Dimers können auch weiterhin die zwei Zustände annehmen und der Schaltprozess ist dem der Monomere sehr ähnlich. Es konnte keine „Kommunikation“ zwischen den beiden Seiten eines Dimers nachgewiesen werden, die Schaltprozesse der beiden Seiten sind also unabhängig.

Die zweite Gruppe untersuchter Moleküle sind sogenannte Nano-Autos. Sie enthalten vier Räder, kugelförmige, molekulare Gruppen die, wenn sie auf der Oberfläche rollen, die Bewegung des Nano-Autos auf eine Dimension auf der Oberfläche beschränken und damit die Bewegungsrichtung vorgeben könnten. Außerdem enthalten sie einen molekularen Motor, der im Prinzip dazu in der Lage sein sollte, Licht und Wärmeenergie in Rotation umzuwandeln und damit das Nano-Auto vorwärts zu bewegen.

Die erste Version der Nano-Autos war mit p-Carboran Rädern ausgestattet und konnte erfolgreich auf Gold-, Silber- und Kupferoberflächen adsorbiert werden. Weder durch Anregung mit Licht noch durch mit der RTM Spitze angelegte Spannungspulse konnte der Motor in Rotation versetzt werden. Der Vergleich von RTM Bilder desselben Moleküls vor und nach der Beleuchtung zeigte keine gerichtete Bewegung und keine Änderung im Erscheinungsbild des Motors.

Weil vermutet wurde, dass die p-Carboran Räder zu stark an das Metallsubstrat binden und dadurch die Drehung des Motors verhindert wird, wurden sie in der Hoffnung dadurch die Funktionalität der Moleküle auf der Oberfläche wiederherzustellen, durch Adamantan Gruppen ersetzt. Allerdings konnte auch in dieser zweiten Version der Nano-Autos keine Rotation des Motors durch Beleuchtung oder spitzeninduzierte Spannungspulse angeregt werden.

Abstract

In this thesis, two classes of functional molecules were studied with a scanning tunneling microscope (STM) on metal surfaces.

The first molecule is *tetra*-phenyl-porphyrin (TPP). On Au(111) it adopts two distinct states, which differ in their apparent height in STM images. Their tunneling spectra, which reflect their local electronic structure around the Fermi energy, are similar but shifted in energy with respect to each other. Reversible switching is possible between these two states and the switching process can be activated thermally at room temperature or with voltage pulses from the STM tip at low temperatures of about 5 K.

By analyzing the switching behavior at room temperature, manipulation experiments at low temperature and comparison with density functional theory (DFT) calculations, it could be shown that for both molecular states, the porphyin molecule is in a saddle shape conformation, but that underneath the bright state a gold adatom is present. This adatom causes the changed STM contrast and the spectral shift.

The switching process at room temperature was investigated by imaging the same sample area repeatedly. From the statistical analysis of such an image series, information about correlated processes in the molecular layer can be extracted, which is not possible from single images. A hopping of the bright molecular state could be observed, corresponding to a hopping of the adatom underneath, as well as time correlated switching events, where many molecules switch simultaneously.

To assess the influence of the intermolecular bonding, the results from close-packed islands were compared to covalently bonded dimers of TPP molecules. It was found that either side of the dimers is still capable of adopting the two states and that the switching process is very similar to the one of the monomers. No “communication” between the two sides of the dimer could be found in terms of their switching properties.

The second class of studied molecules are so-called nanocars. They contain four wheels, spherical molecular groups which, when rolling on the surface, could restrict the movement of the car to one dimension on the surface, giving a directionality to the motion of the car. Furthermore, they contain a molecular motor, which is in principle capable of transforming light and thermal energy into a unidirectional rotation and could drive the car forward.

The first version of the car was equipped with p-carborane wheels and was successfully deposited on various coinage metal surfaces. It was not possible to activate the rotation of the motor with light nor with voltage pulses from the STM tip. Comparing STM images of the same molecule before and after the illumination did not show any directed motion or change in the appearance of the motor.

As it was suspected that the p-carborane wheels bind too strongly to the metal surfaces and thereby quench the rotation of the motor, they were replaced by adamantane wheels in the second version of the car, in the hope that different wheels might make it work. However, also in this second version, the molecular motor could not be activated by illumination or voltage pulses applied with the STM tip.

Contents

Introduction

In biological systems, functional molecules play an important role in many areas. Hemoglobin for example transports oxygen from the lungs through the bloodstream to the cells that need the oxygen for performing their specific task in the body [1]. Hemoglobin has four oxygen binding sites, which are coupled together in a cooperative fashion [2]: As soon as one of these binding sites accepts a single oxygen molecule, the other three can bind oxygen much easier than the first one. This communication between the different binding sites is quite remarkable, as they are several *nm* away from each other within the hemoglobin molecule and communication on this length scale is not easily achievable. It has been found that as soon as the first oxygen molecule is bound, the structure of the whole hemoglobin molecule changes to a more open form, in which oxygen molecules can enter the binding sites easier due to geometrically opened pathways [1]. As explained in chapter 4.2, this cooperative effect is crucial for the oxygen transport.

There are several examples of molecular machines which convert externally provided energy into action [3]. One of them is myosin V, which is used to transport cargo inside cells by moving it along an actin filament [4, 5]. It has two groups, which can reversibly bind to the filament. In the presence of adenosine-5'-triphosphate (ATP), which serves as the energy carrier inside the cells, one of these groups detaches from the filament, moves around the other group and binds to the filament again. When this process is repeated, the myosin molecule travels along the filament with a strong directional preference. This motion closely resembles the walking of humans. The complexity of this process is enormous. First of all, there needs to be a communication between the two "legs" such that only one at the time detaches from the filament, which is again a cooperative effect. If this was not the case and both "legs" were detaching simultaneously, the myosin would detach from the filament. Second, the directionality has to be achieved by a sophisticated design of the involved components.

In the two examples given above, cooperativity is important for their functionality. As described in [2], cooperativity is present when a system, containing several subunits, behaves differently as expected for the individual subunits alone. There is positive and negative cooperativity. A system is positively cooperative if the subunits are preferentially found in the same state. This is the case for the hemoglobin, where either zero or four oxygen molecules are bound, but almost no intermediate states can be observed. In the opposite case, when the subunits preferentially are in a different state, the system is negatively cooperative, as in the case of the myosin V, where only one binding group can detach from the filament at the same time.

Due to their importance in biological systems, the study and the understanding of cooperative processes is of great interest. Furthermore, when designing synthetic functional molecules, for example for the use in medicine, nanotechnology [6] or molecular electronics [7], a good understanding and control of cooperativity can be of great help for achieving the desired functionality.

The experimental method which is employed is the STM. It images conducting surfaces in real-space by scanning a very sharp tip across it in a distance of several Å only, which permits electron tunneling between tip and sample (chapter 1). With this microscopy technique, a very high lateral resolution can be achieved, down to resolving individual surface atoms. Molecular adsorbates can, depending on their adsorption geometry, be imaged with intramolecular resolution. Unlike the traditional experimental techniques of surface science based on scattering experiments, the STM does not average over larger

surface areas. This means that within the presented measurements, every single molecule on the surface can be resolved and studied in dependence on its atomic-scale environment, which is particularly important for the study of cooperative interactions.

This thesis consists of two experimental parts, one dealing with cooperativity in a system of molecular switches, the other with molecular machines:

- In chapter 4 derivatives of *tetra*-phenyl-porphyrin molecules are investigated on Au(111). It is known from the literature that similar molecules are capable of adopting different conformations on surfaces [8, 9] and that it is possible to switch them reversibly between these states. If such a switching process can also be observed in close-packed islands on Au(111), it would be interesting to investigate whether there is a cooperative interaction between neighboring molecules and, if present, what the mechanism behind this cooperative process could be. The Au(111) surface is promising in this context because it has been shown [10] that the intermolecular interaction between the porphyrins can be changed from close-packed to covalently bonded and consequently, a potential cooperative effect could also be investigated as a function of the bonding mechanism.

- In chapter 5, a synthetic molecular machine, a so-called nanocar [11] is investigated on various surfaces. It consists of four wheels, which could roll over the surface, restricting the motion of the car to one dimension on the surface and a molecular motor, which needs light and thermal energy to perform a unidirectional rotation and could drive the car forward. If the motor can be activated on the surface (as in [12]) it would be interesting to know whether its rotation leads to directed motion of the car and how the exact excitation mechanism works. If the motor cannot be activated, it would be necessary to understand the reason for the quenching of its functionality and how to overcome it in future versions of the molecule.

Part I.

Physical background and experimental methods

1. Physics of the tunneling effect

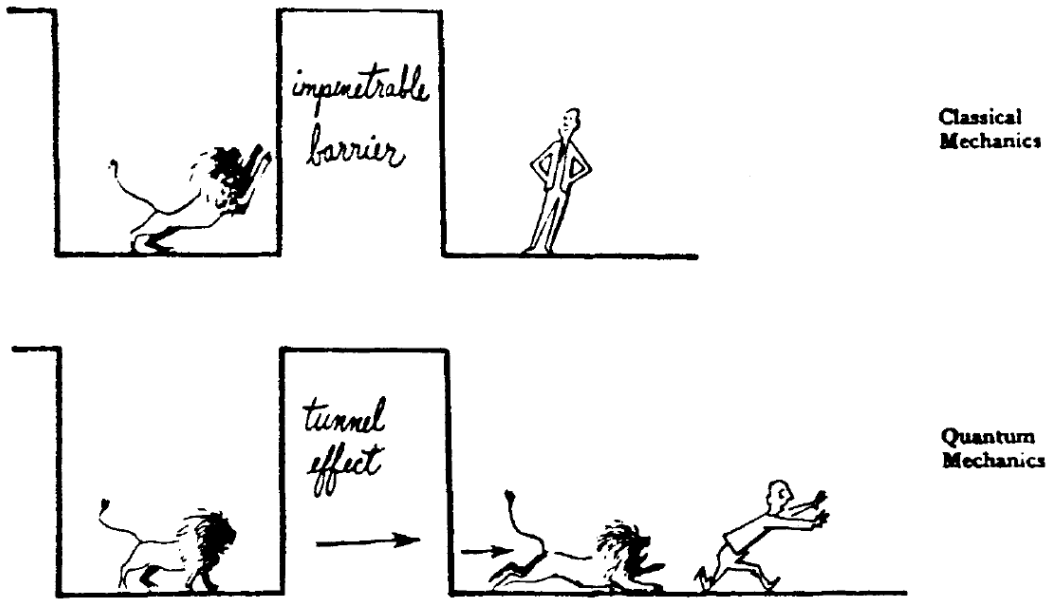

Figure 1.1.: Difference between classical and quantum mechanics. Quantum mechanics permits tunneling through a potential barrier even if the tunneling particle has not enough energy to overcome it. Reprinted with permission from [13]. Copyright 1984, Taylor & Francis.

The main experimental method used in this thesis is scanning tunneling microscopy (STM), which is a technique for imaging conducting surfaces and its adsorbates with atomic resolution. The method was invented 1982 by Gerd Binnig and Heinrich Rohrer at the IBM research labs in Switzerland [14]. It was the first method capable of atomic resolution on flat surfaces in real space and only shortly after, 1986, the two inventors were awarded the Nobel prize in physics together with Ernst Ruska, the inventor of the electron microscope.

STM relies on scanning an atomically sharp metal tip across the surface in a very short distance of typically less than 1 *nm*, which enables tunneling of electrons from the tip to the sample and vice versa. By applying a bias voltage between tip and sample, a net tunneling current is created, which strongly depends on the distance between them. In the most common mode of operation, constant current imaging, this tunneling current is kept constant by adjusting the tip sample distance. Recording the tip height as a function of the lateral tip position yields a map of the surface. It is important to note that the recorded height contains contributions of both, the real height of the surface and the local electronic structure of tip and surface.

In this chapter, the physical background of the tunneling process is described, in chapter 2 follows a detailed description of how the measurements are performed and the experimental realization is presented in chapter 3.

1.1. One-dimensional tunneling

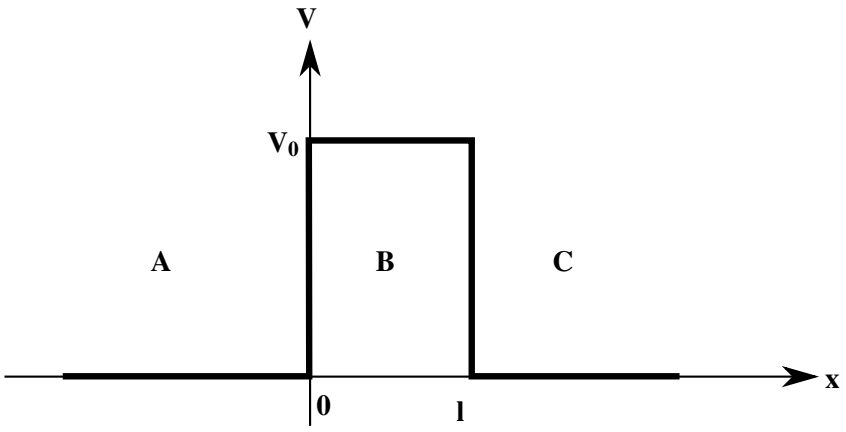

Figure 1.2.: Potential barrier extending from $x = 0$ to $x = l$ where it has the value V_0. For the other regions of x, it has the value zero. Adopted from [15]

In many quantum mechanics text books [15], one of the first examples of the difference between classical and quantum mechanics is the tunneling effect (Fig. 1.1). If a particle approaches a potential barrier (Fig. 1.2) which is higher than its energy, classical mechanics would expect it to be repelled by the barrier, i.e. there is a zero probability for the presence of the particle behind the barrier. However, in quantum mechanics, this is not necessarily the case.

To understand this, it is necessary to look at the one-dimensional time-independent Schrödinger equation for a constant potential V:

$$\frac{d^2}{dx^2}\varphi(x) + \frac{2m}{\hbar^2}(E-V)\varphi(x) = 0 \tag{1.1}$$

which needs to be solved for $\varphi(x)$. The potential barrier is created of several regions with a constant potential V and the particle energy E is larger than V before and after the barrier, but smaller than V in the barrier. In the first step, the Schrödinger equation (1.1) needs to be solved for these two cases separately. For $E > V$, the general solution is:

$$\varphi(x) = Ae^{ikx} + A'e^{-ikx} \quad \text{with} \quad k = \frac{\sqrt{2m(E-V)}}{\hbar} \tag{1.2}$$

and for the opposite case ($E < V$):

$$\varphi(x) = Be^{\rho x} + B'e^{-\rho x} \quad \text{with} \quad \rho = \frac{\sqrt{2m(V-E)}}{\hbar}. \tag{1.3}$$

Both of these solution can be verified by simply inserting them into equation 1.1.

When the particle energy is higher than the potential energy (equation 1.2), its wavefunction has oscillatory behavior with a constant probability density ($|\varphi(x)|^2 = const$). In the opposite case (equation 1.3), the wavefunction shows an exponential decay.

To obtain the full solution for the potential barrier (Fig. 1.2), where $V_0 > E > 0$, it needs to be defined piecewise for the three domains A, B and C:

$$\varphi_A(x) = A_1 e^{ikx} + A_1' e^{-ikx} \tag{1.4}$$
$$\varphi_B(x) = A_2 e^{\rho x} + A_2' e^{-\rho x} \tag{1.5}$$
$$\varphi_C(x) = A_3 e^{ikx} + A_3' e^{-ikx} \tag{1.6}$$

The particle is coming from the left (region A) and can either be reflected by the barrier or tunnel to region C, which would classically be forbidden. As in C after passing the barrier, the particle can only travel to the right, $A_3' = 0$. At the boundaries between the three regions the total wavefunction and its first derivative need to be continuous, yielding four conditions for solving the prefactors. However, this is one too few as in total five prefactors need to be determined. The last prefactor is responsible for the normalization, which is impossible to do for infinitely extended plane waves. Therefore, one of the prefactors stays indetermined and only ratios of the prefactors can be evaluated in the following.

From the ratio between A_1 and A_3, the transmission probability between region A and C can be calculated [15]:

$$T = \left|\frac{A_3}{A_1}\right|^2 = \frac{4E(V_0 - E)}{4E(V_0 - E) + V_0^2 \sinh^2 \frac{\sqrt{2m(V_0 - E)}l}{\hbar}} \tag{1.7}$$

If $\rho l \gg 1$, which can either occur when the barrier is sufficiently long or the barrier is sufficiently high, the transmission probability T can be approximated by

$$T \approx \frac{16E(V_0 - E)}{V_0^2} e^{-2\rho l}. \tag{1.8}$$

From this equation it is apparent that the tunneling probability depends exponentially on the width l of the barrier.

In the STM geometry, a metallic tip is in close vicinity to a conducting sample. These two conducting regions correspond to the regions A and C in Fig. 1.2. In both of them, the conduction electrons at the Fermi level can be regarded as free electrons in a first approximation. In the vacuum region between them, the potential is by the work function Φ higher than the Fermi level in the metals and therefore presents a barrier for the tunneling electrons. Tunneling can happen in both directions, from the tip to the sample and vice versa, but when applying an external voltage between them, the tunneling current is biased to either direction and can be measured experimentally. The exponential dependence of the tunneling current between tip and sample in the setup described above was first observed by Binnig and Rohrer [16] who performed this experiment as a preparation for the construction of the first STM.

For a metal with a work function of $\Phi = V_0 - E = 4\ eV$, the scale parameter is $\rho \approx 1\ \mathring{A}^{-1}$. This small decay length together with the exponential dependence of the tunnel current on the tip sample distance l is responsible or the extremely high lateral resolution of the STM.

1.2. Bardeen's approach

Long before it was experimentally feasible to observe tunneling between tip and sample, tunneling phenomena have been studied between layers of conducting materials, separated by a thin insulating layer [17, 18]. For this setup, Bardeen has developed a theoretical description in 1961 [19].

Because solving the Schrödinger equation for the full system was too complicated, he considered the independent solutions for both electrodes, ψ_μ and ψ_ν (which contain the full time dependence,

in contrast to the φ from chapter 1.1 which only depends on the space coordinates), and derived in a time-dependent perturbation theory approach the tunneling current between them [20]:

$$I = \frac{2\pi e}{\hbar} \sum_{\mu,\nu} \left\{ f(E_\mu)\left[1 - f(E_\nu + eU)\right] - f(E_\nu + eU)\left[1 - f(E_\mu)\right] \right\} \left|M_{\mu\nu}\right|^2 \delta(E_\mu - E_\nu) \tag{1.9}$$

where f is the Fermi distribution, U the bias voltage applied between the electrodes and $M_{\mu\nu}$ are the tunneling matrix elements, which can be calculated from:

$$M_{\mu\nu} = \frac{-\hbar^2}{2m} \int d\mathbf{S} \cdot \left(\psi_\mu^* \nabla \psi_\nu - \psi_\nu \nabla \psi_\mu^*\right) \tag{1.10}$$

The integration has to be performed over a region between the two electrodes. A detailed derivation of these formulas can be found in [21].

1.3. Tunneling in the STM geometry

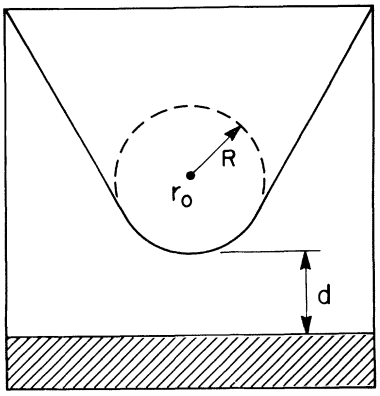

Figure 1.3.: Tunnel junction with a spherical tip apex as in the approximation by Tersoff and Hamann. Reprinted figure with permission from [22]. Copyright 1983 by the American Physical Society. Readers may view, browse, and/or download material for temporary copying purposes only, provided these uses are for noncommercial personal purposes. Except as provided by law, this material may not be further reproduced, distributed, transmitted, modified, adapted, performed, displayed, published, or sold in whole or part, without prior written permission from the American Physical Society.

Bardeen's calculations, which are of a very general nature and do not make any assumptions about the electrodes besides that they are conducting, have been adopted by Tersoff and Hamann to the geometry of the STM junction (Fig. 1.3) [22, 23]. They assumed the wave function within the sample to be a Bloch function (as in periodic crystals):

$$\psi_\nu = \Omega_s^{-\frac{1}{2}} \sum_G a_G \cdot e^{-\sqrt{k^2 + \left|\vec{k}_\parallel + \vec{G}\right|^2} z} \cdot e^{i\left(\vec{k}_\parallel + \vec{G}\right)\cdot\vec{x}} \tag{1.11}$$

with Ω_s the sample volume, $k = \sqrt{2m\Phi}/\hbar$ and Φ is the work function. The tip is assumed to be locally spherical at the apex and is therefore approximated by a spherical s-wave function:

$$\psi_\mu = \Omega_t^{-\frac{1}{2}}\ c_t\ k\ R\ e^{kR}\ \frac{e^{-k|\vec{r} - \vec{r}_0|}}{k\,|\vec{r} - \vec{r}_0|} \tag{1.12}$$

with Ω_t the tip volume, k as in equation 1.11 and R is the tip radius at the apex.

Now the tunneling matrix elements can be calculated using equation 1.10:

$$M_{\mu\nu} = \frac{\hbar^2}{2m}\, 4\,\pi\, k^{-1}\, \Omega_t^{-\frac{1}{2}}\, k\, R\, e^{kR}\, \psi_\nu(\vec{r}_0) \tag{1.13}$$

and by inserting them in equation 1.9, the tunneling current is obtained. In the limit of low temperatures and small bias voltages U, this can be further simplified to:

$$I = 32\pi^3\hbar^{-1}e^2U\Phi^2D_t(E_F)R^2k^{-4}e^{2kR}\sum_\nu |\psi_\nu(\vec{r}_0)|^2\,\delta(E_\nu - E_F) \tag{1.14}$$

where $D_t(E_F)$ is the local density of states of the tip at the Fermi level. The last term in this equation, the sum over all states of the surface at the Fermi level is just the density of states of the sample at the center of the tip. It yields again the exponential dependence of the tunnel current on the tip sample distance as the surface wave functions (equation 1.11) decay exponentially in the vacuum region. Furthermore the tunneling current depends linearly on the applied bias voltage U (in the approximation of small voltages).

Usually STM images are recorded in constant-current mode, where the tunneling current is kept constant by adjusting the tip height and the bias voltage is also constant. As can be seen in equation 1.14, the only term which shows lateral variability is the sum over the surface wave functions. Therefore, in constant-current mode, the STM tip follows the surface of constant local density of states which contains both, a contribution from the electronic surface structure, but also from the geometric surface height.

Although the atomic-scale structure of the STM tip is generally unknown, this Tersoff-Hamann approximation can very successfully be applied for calculating STM images for known surface structures [24], yielding calculated STM images, which are very similar to the measured ones. This shows that the approximation of a spherical tip is a reasonable choice.

Recently it has been demonstrated, that when the tip is functionalized with a CO molecule [25], the STM image is not only a result of the s-wave at the tip, but that also tunneling through molecular p-orbitals has to be taken into consideration.

2. Scanning Tunneling Microscopy

After having understood the tunneling effect from a quantum mechanical point of view (chapter 1), this chapter is dedicated to to the working principle of the scanning tunneling microscope (STM).

The STM can be used for imaging of conducting surfaces and thin adsorbates, but furthermore it can also be used to manipulate the surface with the tip and to gain spectroscopic information with atomic resolution.

2.1. Imaging

The STM is mainly a microscope technique capable of producing images of conducting surfaces with atomic resolution. This is done by scanning an atomically sharp metal tip across the surface. Images can be acquired in two modes (Fig. 2.1), constant-current or constant-height imaging, which will be presented in the following.

- In *constant-current* mode, a fixed bias voltage is applied between tip and sample and while scanning, the tunneling current is detected by an external preamplifier. The STM electronics adjusts the tip height such that the tunneling current stays constant at all times during the scanning process. Recording the tip height as a function of the lateral tip position yields a topographic map of the surface, but as was demonstrated in chapter 1.3, the tip follows the surface of constant density of states, which contains contributions from the geometric surface height but also from its electronic structure.

  All STM images presented in this thesis were recorded in constant-current mode.

- In *constant-height* mode, the tip is scanned in a plane parallel to the surface, applying a fixed bias voltage. The tunneling current is recorded as a function of the lateral tip position and constitutes the resulting image.

  This mode has the advantage over constant current imaging that the tip height does not need to change and therefore images can be acquired with higher speed (in the absence of a feedback loop). Additionally, images can be recorded at greater tip heights compared to constant current, because at greater distances the tunnel current is smaller, sometimes so small that the noise on the current measurement would prohibit a defined regulation of the z-height in constant-current mode.

  But also disadvantages exist: Constant-height measurements are very susceptible to small misalignments between sample and scan piezo, which need to be corrected before starting the measurements. Furthermore, if unexpected high surface structures are encountered during scanning, the tip crashes into them when the scanning height is lower than the height of the structure. Therefore it is usually necessary that before starting a constant-height measurement, the surface is first scanned in constant-current mode for measuring and correcting the sample tilt, checking the roughness of the surface and choosing the tip height accordingly.

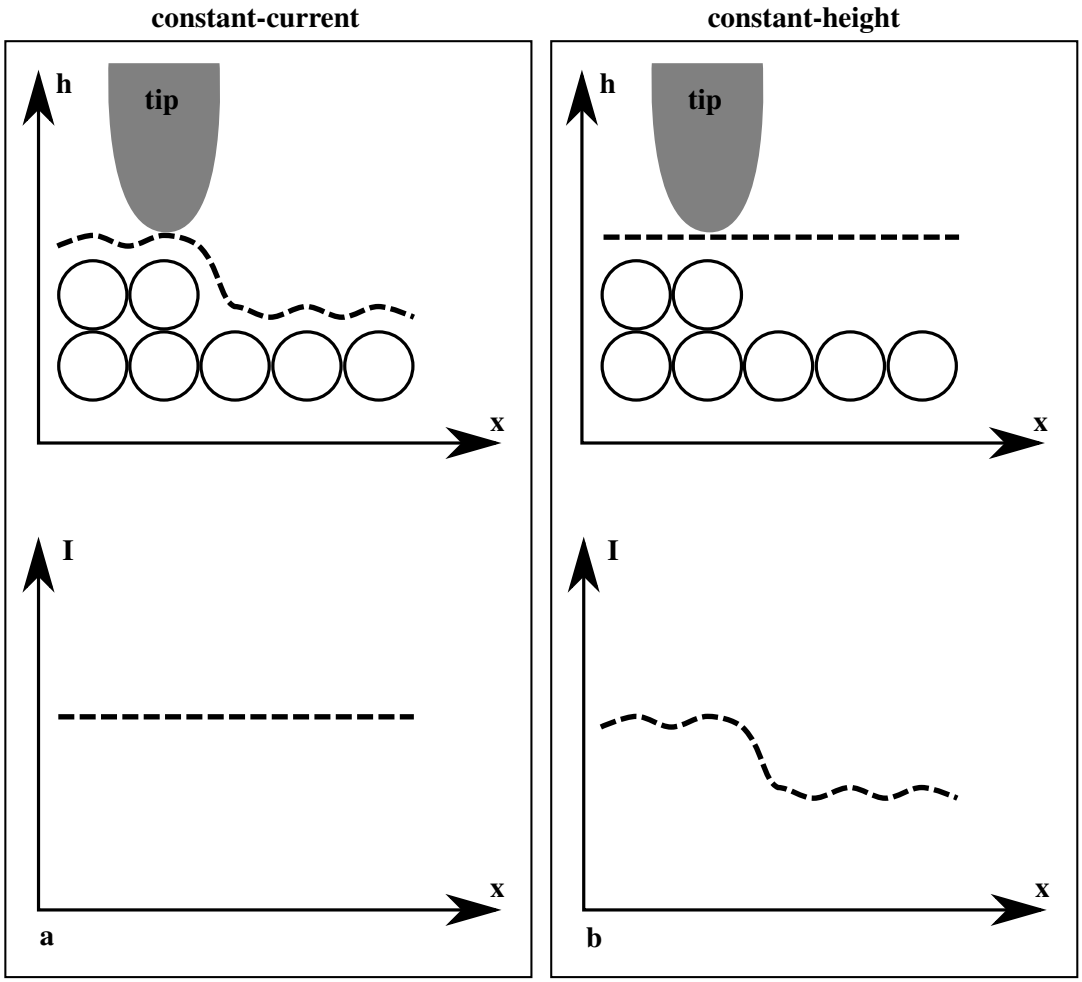

Figure 2.1.: Scanning modes of the STM. In (a) the constant current mode is shown, the tunneling current is kept constant and the tip follows the contour of the surface, (b) shows the constant height mode where the tip height is fixed and the information about the topography is reflected in the current signal.

If the surface is purely metallic and consists of only one material, following a surface of constant density of states is more or less equivalent to following the surface topography. If adsorbates are present, due to their particular electronic structure, the recorded constant-current image does not necessarily agree with the topography. An example can be found in Fig. 2.2. (a) shows a sketch of the adsorption of CO on Cu(111) which clearly shows that the CO molecules are higher than the surface atoms. In the upper panel of (b), CO and O_2 molecules are imaged with a metallic tip and although they are higher than the substrate atoms, they appear as depressions in the STM image.

Additionally, the contrast in STM images depends on the tip condition. In the lower panel of Fig. 2.2 (b), the same surface area is imaged but this time with a CO terminated tip. This termination was achieved by picking up the CO molecule, which is marked in the upper panel with a white arrow and is consequently missing in the lower image. The other CO molecules now appear as protrusions, whereas the one O_2 molecules still appears as a depression (black arrow), making it possible to differentiate between the chemical species on the surface. This demonstrates what implications the imaging of the

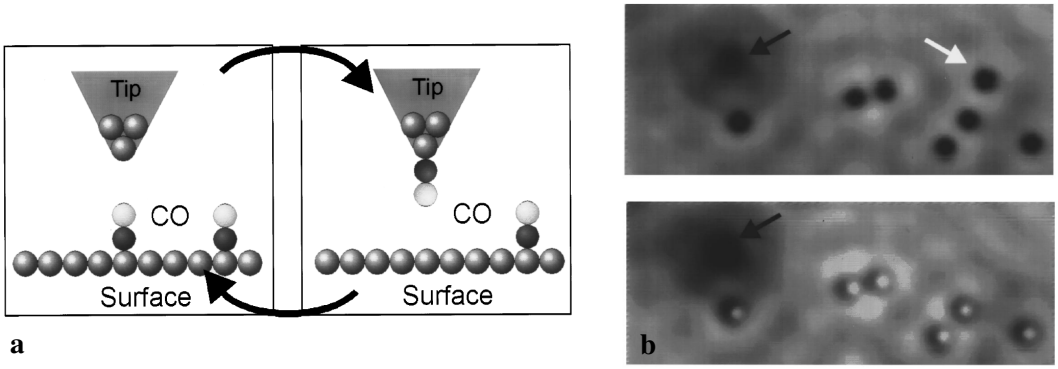

Figure 2.2.: Chemical contrast in STM imaging and dependence on the tip condition. (a) shows a sketch of the adsorption geometry of CO on Cu(111) and its transfer to the STM tip. In (b) CO and O_2 (black arrow) molecules are imaged on Cu(111). In the upper panel, a metallic tip was used, in the lower panel, the CO molecule indicated in a with the white arrow was transferred to the tip apex. Reprinted with permission from [26]. Copyright 1997, American Institute of Physics.

constant density of state has and how crucially the images depend on the tip condition [26].

2.2. Spectroscopy

Another strength of the STM is that it can be used to gain local spectroscopic information. To understand this, one needs to look at the tunneling current as resulting from the Tersoff-Hamann approach (chapter 1.3) but without the approximation of small voltages U [20]:

$$I \propto \int_0^{eU} n_t(\pm eU \mp \varepsilon) \cdot n_s(\varepsilon) \cdot T(\varepsilon, eU) d\varepsilon \tag{2.1}$$

where n_s and n_t are the local densities of states of sample and tip, respectively and $T(\varepsilon, eU)$ is the transmission coefficient given by:

$$T(\varepsilon, eU) = \exp\left\{-2(d+R)\sqrt{\frac{2m}{\hbar^2}\left(\frac{\Phi_t + \Phi_s}{2} + \frac{eU}{2} - \varepsilon\right)}\right\} \tag{2.2}$$

with Φ_t and Φ_s the work functions of tip and sample, respectively and d and R as in Fig. 1.3.

Under the assumption that the tip is purely metallic, a constant density of tip states is expected close to the Fermi level:

$$\frac{dn_t}{dU} \approx 0 \tag{2.3}$$

Calculating the derivative of equation 2.1 with respect to U using assumption 2.3 one obtains:

$$\frac{dI}{dU}(U) \propto e n_t(0) n_s(eU) T(eU, eU) + \int_0^{eU} n_t(\pm eU \mp \varepsilon) n_s(\varepsilon) \cdot \frac{dT(\varepsilon, eU)}{dU} d\varepsilon \tag{2.4}$$

The property dI/dU can be measured directly by using a lock-in amplifier, which modulates the bias voltage with a small sinusoidal oscillation and records the current change as a function of the

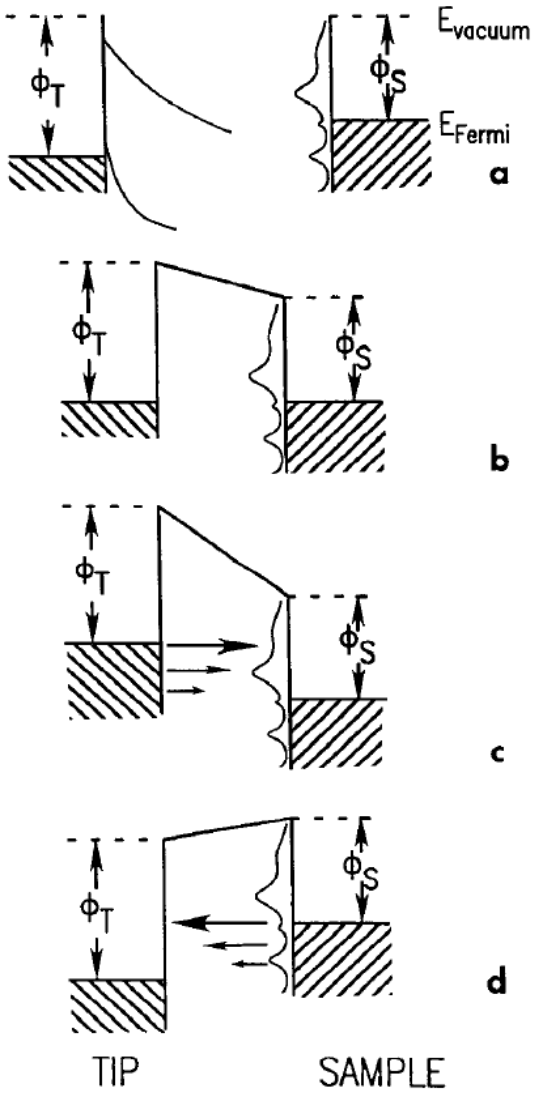

Figure 2.3.: Energy scheme of the tip and sample. In (a) both metals are so far apart that they have no influence on each other, the vacuum levels align. If they are close but not touching (b), electrons can tunnel between the two, aligning the two Fermi levels. When a positive sample bias is applied (c), electrons tunnel from the tip to the sample, and for a negative sample bias (d), the electrons tunnel in the opposite direction. Republished with permission of Annual Reviews, from [27]; permission conveyed through Copyright Clearance Center, Inc.

bias voltage. As T (equation 2.2) is monotonic and smooth [20], the dI/dU signal from equation 2.4 is dominated by n_s of the first term, the second term only results in a smooth background. With this method, the density of states of the sample at the tip position can be investigated. When the applied sample bias voltage is negative, the occupied states of the sample are probed, at positive bias the unoccupied ones (Fig. 2.3).

However, it is important to keep in mind that assumption 2.3 is crucial. If the tip has a density

of states showing distinct features, the dI/dU signal is not roughly proportional to n_s any more, but rather shows a convolution of n_s with n_t. In the experiments, this situation can easily occur when a non metallic atom or a molecule is adsorbed at the tip apex. Special care has therefore to be taken to ensure the metallicity of the tip when performing spectroscopic measurements, for example via the visibility of the characteristic surface state on (111) surfaces of noble metals [28, 29].

2.3. Manipulation

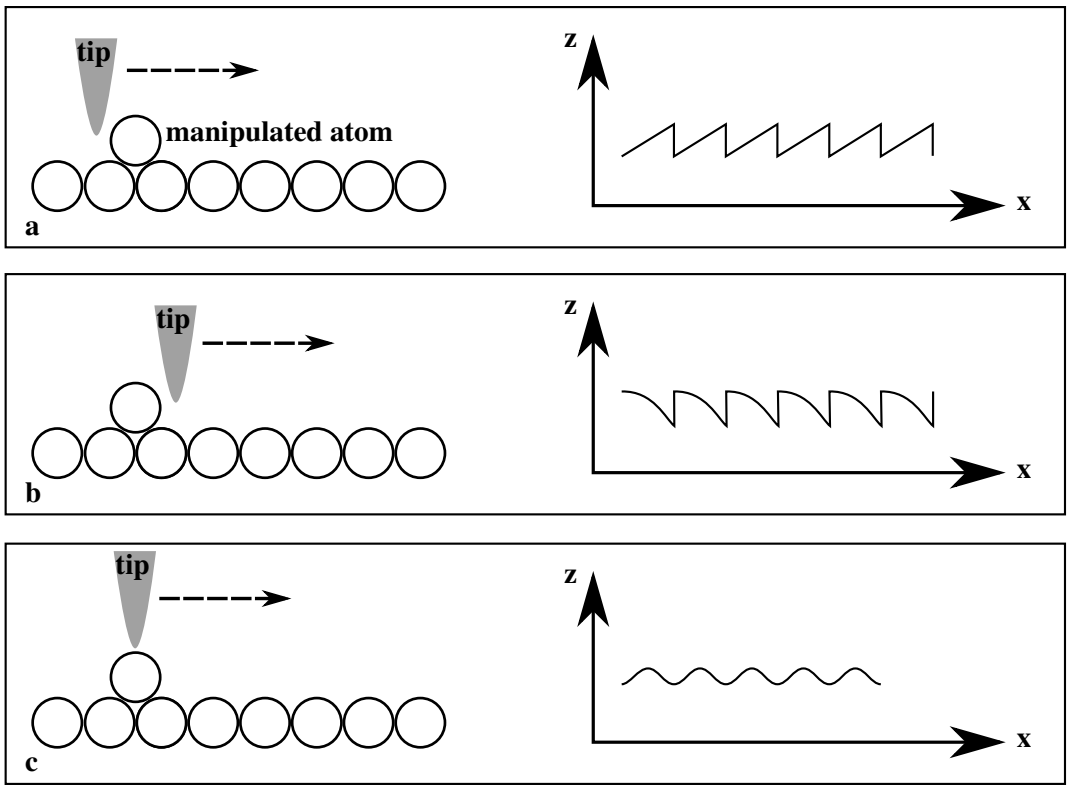

Figure 2.4.: Lateral manipulation in constant current mode, from the z signal during manipulation, the different modes can be distinguished, (a): pushing, (b): pulling, (c): sliding [30].

What makes the STM so fascinating is that it is not only an imaging and spectroscopy technique, but the tip can also be used for manipulating single atoms and molecules with atomic scale position.

When the tip approaches an adsorbate on the surfaces, short range forces start acting between them, which can lead to a lateral displacement of the adsorbate. It was shown in [31], that the threshold for a successful manipulation attempt depends on the tip – adsorbate distance only. In the considered case, an attractive force was observed at distance of (1.3 ± 0.2) $\mathring{A}$, where an overlap between the electronic states of tip and adsorbate probably leads to a chemical attraction. When such a chemical attraction is not possible due to the particular electronic structures, Pauli repulsion will set in at even smaller distances, leading to a repulsive force. These forces can be exploited for lateral tip manipulation.

Surface modifications can already occur during scanning, when the bias voltage was chosen too low or the tunneling current was chosen too high, such that the tip is in close proximity to the sample. The first intentional surface modification was reported in [32], where germanium atoms are re-deposited

from the tip onto a Ge surface. Some years later, Eigler et al. [33] showed that they could move Xe atoms on a Ni surface at 4 K to any position, allowing them to build up nanostructures of their choice. For demonstration purposes, the built up the letters IBM with Xe atoms. Even a rolling motion of molecules could be induced by the tip [34].

But not only the lateral position of adsorbates can be changed with the STM tip, also internal changes can be induced in them. Single Au atoms can be charged and discharged [35], several molecular switches can be switched between two states [36, 37, 38, 39] and O_2 molecules could successfully be dissociated [40]. It was even possible to induce all steps of a chemical reaction on a surface [41].

There are two basic modes of manipulation [42]: *Lateral manipulation* where the moved object never loses the contact to the surface and *vertical manipulation*, where the object is picked up by the tip and released in the desired position.

The mechanism of the lateral manipulation were investigated by Bartels et al. [30], who could identify the modes *pushing*, *pulling* and *sliding* by their characteristic height signals during constant current manipulation (Fig. 2.4). In the pushing mode, there is a repulsive interaction between tip and adsorbate. When the tip approaches the adsorbate, it needs to retract because a higher current is detected close to it. When it comes too close, the atom jumps to the next lattice site, leading to an abrupt jump in the tip height. In the pulling mode, the interaction is attractive and the atom follows the tip. First the tip moves down the slope of the atom, but at some point it will follow, leading to a sudden retraction of the tip. Finally, in the sliding mode, the tip stays above the atom and both move together across the surface, the tip height reflects the surface corrugation. The manipulation signal is in many cases a great help in determining what is happening during the manipulation. For example in [34], the rolling of the molecule could be proven by the manipulation signal which does not show the lattice periodicity, which would be expected to be seen if a hopping motion occurred. It is important to note that lateral manipulation can also be done in constant-height mode, which has the advantage over constant-current manipulation that much higher forces can be applied [43, 44].

Vertical manipulation works as presented in Fig. 2.2 (a), the tip is positioned above one molecule which is then picked up by applying a voltage pulse. The tip is moved to a different position where the molecule can be returned to the surface by applying another voltage pulse [45, 26, 46]. The mechanism works as follows [47, 48]: The molecule is located in its potential minimum at the surface. However, it could also bind to the tip and when the tip is located above it, a second potential minimum is present for the adsorption at the tip. These minima are separated by a barrier, which prevents the molecule from binding to the tip directly. By applying an electric field, the barrier height and the relative depths of the minima can be changed, such that one of the minima is clearly preferred and the molecule will then be found in this minimum with a high probability. Changing the polarity of the electric field will, however, invert the situation and the molecule will then preferentially be found in the other minimum, making the tip - surface transfer of a molecule a reversible process.

3. Experimental details

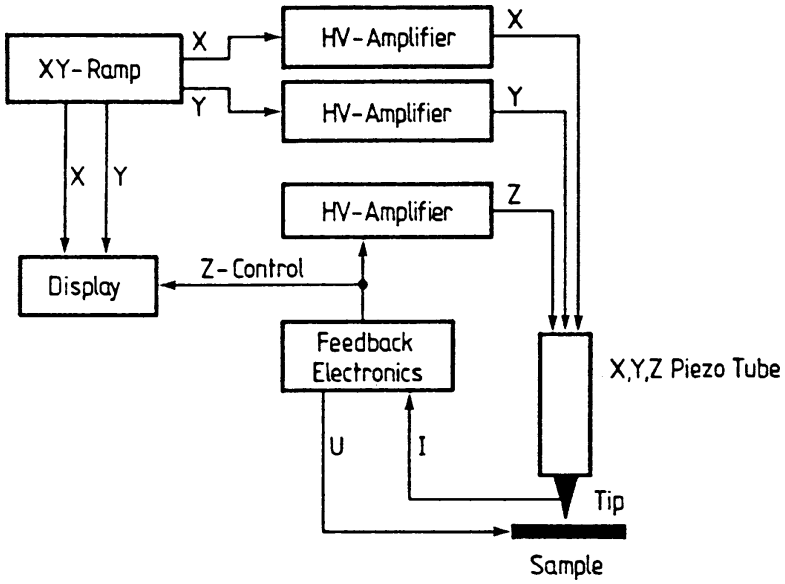

Figure 3.1.: Schematic setup of an STM. The tip is moved across the sample using a piezo element. The tunneling current is amplified, passed to the feedback electronics which adjusts the tip height such that the tunneling current stays constant at all times. The tip height is sent to the measurement computer, where it is displayed as a function of the lateral tip position to form the STM image. Reprinted from [49] (Copyright Springer-Verlag Berlin Heidelberg 2010) with kind permission from Springer Science and Business Media.

In the present chapter the experimental methods employed in this thesis are described. The principle setup of an STM is shown in Fig. 3.1: The measurement computer generates the X and Y voltages, which move the tip across the surface via a piezo element. The resulting tunneling current is measured and the feedback electronic adjusts the tip height such that the current stays constant. The STM image is formed in the measurement computer by displaying the tip height as a function of the lateral tip position.

The following chapters discuss at first the setup of the low temperature STM (chapter 3.1) and the variable temperature STM (chapter 3.2), followed by the preparation of clean metal surfaces (chapter 3.3) and the deposition of the molecules (chapter 3.4). This is followed by a detailed description of the laser systems used for illuminating the samples (chapter 3.5) and the statistical evaluation methods (chapter 3.6).

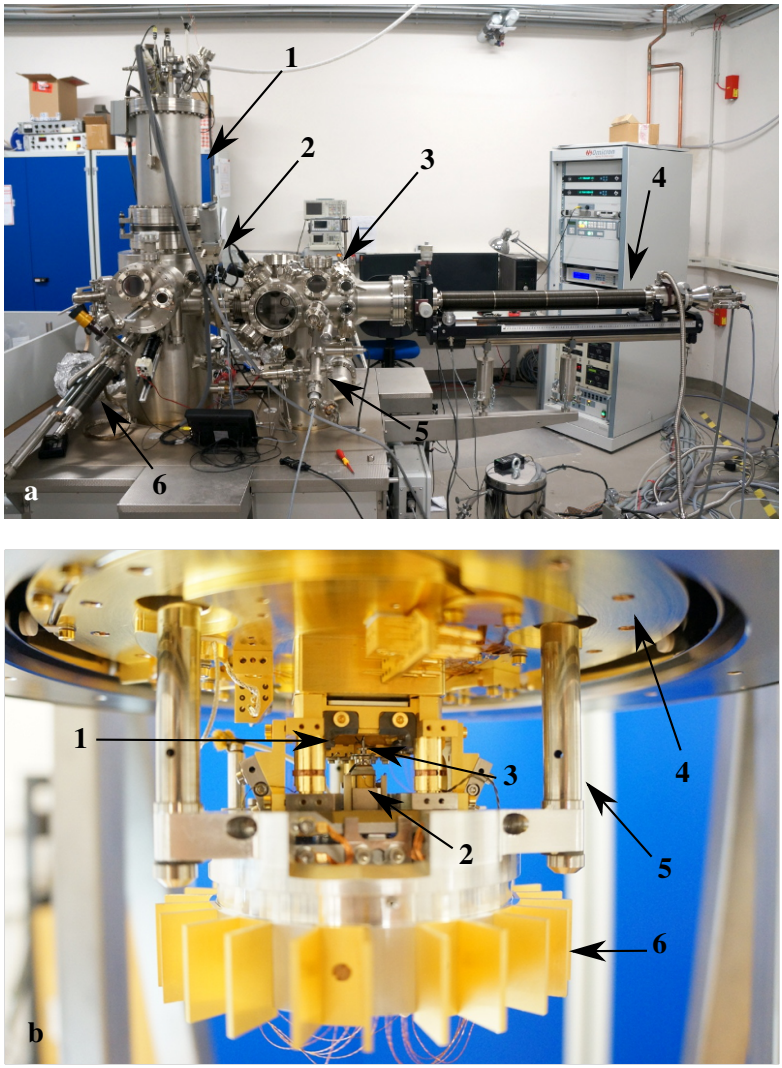

Figure 3.2.: Omicron low temperature STM. (a) overview image of the UHV chamber. 1: Helium cryostat, 2: STM chamber, 3: preparation chamber, 4: helium cooled manipulator, 5: sputter gun, 6: STM evaporator. (b) shows the STM itself without the radiation shields. 1: Sample reception, 2: scan piezo, 3: tip, 4: lower end of the cryostat, 5: suspension springs inside a metal tube, 6: eddy current damping.

3.1. Omicron low temperature STM

All the low temperature (5 K) measurements of this thesis were acquired with the low temperature STM presented in Fig. 3.2. It was purchased at Omicron.

Its ultra-high-vacuum (UHV) chamber has two parts which are separated by a gate valve: the STM chamber where the STM itself is located and the preparation chamber which is used for preparing the sample. This separation in two parts is necessary because, as will be demonstrated in chapter 3.3, relatively high pressures ($\approx 10^{-6}$ $mbar$) are needed for cleaning the metal substrates. These high gas loads would, if in contact with the helium cooled STM, lead to high condensation on the STM and the cryostat. Both chambers are equipped with ion gauges, ion getter as well as with titanium sublimation

pumps. At the preparation chamber all sorts of tools for sample preparation are attached:

- A turbo molecular pump for pumping down the whole system or parts of it and for sputtering.
- A liquid helium cooled manipulator which holds the sample during all steps of the preparation and is used to transfer the sample to the STM chamber. It has a heating station in which the sample can be heated to more than 600°C with a heating element behind the sample. Semiconductors can be annealed by applying a direct current to the sample. Furthermore there is a cooling station in which the sample can be cooled down to $\approx 15\ K$ using liquid helium.
- A sputter gun for cleaning metal substrates (see chapter 3.3).
- A quadrupole mass spectrometer (QMS) for analyzing the rest gas in the chamber, leak testing and thermal desorption spectroscopy (TDS).
- A molecule evaporator (Kentax) which has three independent quartz crucibles and can be cooled using water or liquid nitrogen.
- A quartz micro balance for measuring the evaporation rate of molecules coming from the evaporator (see chapter 3.4).
- A load lock for introducing samples or STM tips into the chamber without breaking the vacuum inside.
- A UHV screwdriver to fix the sample to the cooling station of the manipulator in order to increase the thermal contact.

In the STM chamber there is the STM itself, a wobble stick for transferring the sample in and out of the STM, an additional molecule evaporator which can evaporate molecules directly into the cold STM and a dosing system for liquids with a high vapor pressure.

The STM is hanging below a bath cryostat filled with liquid helium (4.2 K) and is surrounded by a radiation shield which is also at liquid helium temperature. The helium reservoir is surrounded by a reservoir of liquid nitrogen (77 K) for thermal isolation and at the lower end there is another radiation shield at liquid nitrogen temperature surrounding the STM. For cooling down the STM, it can be pressed against the cryostat to establish a good thermal contact between the two. While the STM is not pressed against the cryostat, it is hanging below it held by three springs in order to decouple it mechanically from the cryostat and the rest of the chamber. However, the STM temperature can be raised using a heater element on the STM and an external temperature controller (Fig. 4.6). When the inner cryostat is filled with liquid helium, the temperature can be raised up to $\approx 90\ K$, when it is filled with liquid nitrogen up to $\approx 150\ K$.

The STM temperature is measured using a Si diode through which an electric current of 10 mA is passed. The necessary voltage depends on the temperature of the diode and can be looked up in calibration tables or is directly converted to a temperature by the attached temperature controller.

Vibration damping is achieved on two stages: First the whole UHV system rests on pneumatic feet which decouple the chamber from the vibrations of the floor and second, the STM head is decoupled from the rest of the chamber and the cryostat by suspending it on three springs and damping its movement by an eddy current damping.

It is important to note that in this system the sample is held on the ground potential and the bias voltage is applied to the STM tip. Therefore, all images taken with this STM show U_{tip} in the figure caption which is the tip voltage with respect to the sample.

The STM is controlled by a Nanonis control electronics, which provides the high voltage signals for the piezo elements, reads the tunneling current and contains the feedback loop for regulating the tip height. Its software displays and saves the recorded images, controls the spectroscopy and manipulation experiments and is easily extendable with self-written LabView scripts.

It is possible to illuminate the sample while it is inside the STM using a laser. UHV windows and openings in the radiation shields are present at the right position to allow a laser beam coming from outside to hit the sample at an angle of 65° from the surface normal and the reflected light to leave the UHV system again. It is possible to retract the tip for the time of illumination by several *mm* out of the laser beam and to reapproach it to the surface with a lateral shift of less than 100 *nm* such that the same sample position as before the illumination can be retrieved, allowing a direct before-after comparison of one and the same molecule.

3.2. Århus variable temperature STM (Specs)

The room temperature results of the chapters 4.5 and 4.7.4 were obtained using two Århus variable temperature (VT) STMs, produced by the company Specs (Fig. 3.3). The respective UHV chambers contain more or less the same equipment as the low temperature STM, but the manipulators are only coolable with liquid nitrogen.

The biggest difference is the STM itself. It is designed to work in a temperature range between 120 K and 400 K. To ensure high temperature stability and thereby low thermal gradient across the instrument, the compact scanner assembly is tightly attached to a 3 kg copper block which serves as a heat reservoir. When the STM shall be operated at reduced temperatures, a cold finger can be pressed against this copper block, which is then cooled with liquid nitrogen. When the temperature of the copper block is below the desired temperature the cold finger is removed and an electric heating is used to adjust the temperature to the requirements of the experiment. In the older version of this microscope, there was no continuous cooling possible, therefore the temperature could never be stabilized at a fixed value, it always drifted back to room temperature. In the newer version, continuous cooling is possible even after the removal of the cold finger due to copper braids connecting the cold finger and the copper block. Both versions were used within this thesis, but as the measurements were taken exclusively at room temperature, this difference did not play a role.

During the measurement, the tip, scan piezo and coarse motor are always held at room temperature. This ensures that the same piezo constants can be used, regardless of the sample temperature. Temperatures above room temperature can be achieved by electric heating of the copper block.

In this STM, however, the tip is kept on the ground potential and the bias voltage is applied to the sample. Therefore, all images coming from this STM have a value for U_{sample} in the figure caption.

Due to the compact and very rigid design of the STM, not much vibration damping is needed. When the cold finger is not attached, the STM including the copper block is hanging on springs, which are slightly damped with viton bands parallel to them (Fig. 3.3 (b)). No pneumatic feet nor eddy current damping is needed.

Two different electronics were used to control the STM, the Nanonis electronics, which is comfortable to use, has a very low noise level and "analog to digital" converter (ADC) with a very high resolution. The only drawback is that it is relatively slow, it can record a scan line in about 30 *ms* at fastest. An image with the dimensions of 256×256 pixel can be acquired in 13.2 s at the highest speed (forward and backward scan). With the special electronics for this microscope from the company Specs, much higher frame rates can be achieved (5 *ms* per scan line). With this electronics, images can be recorded much faster than the noise level of the system permits, in practice, the fastest usable frame rates were in the order of 8 s per image.

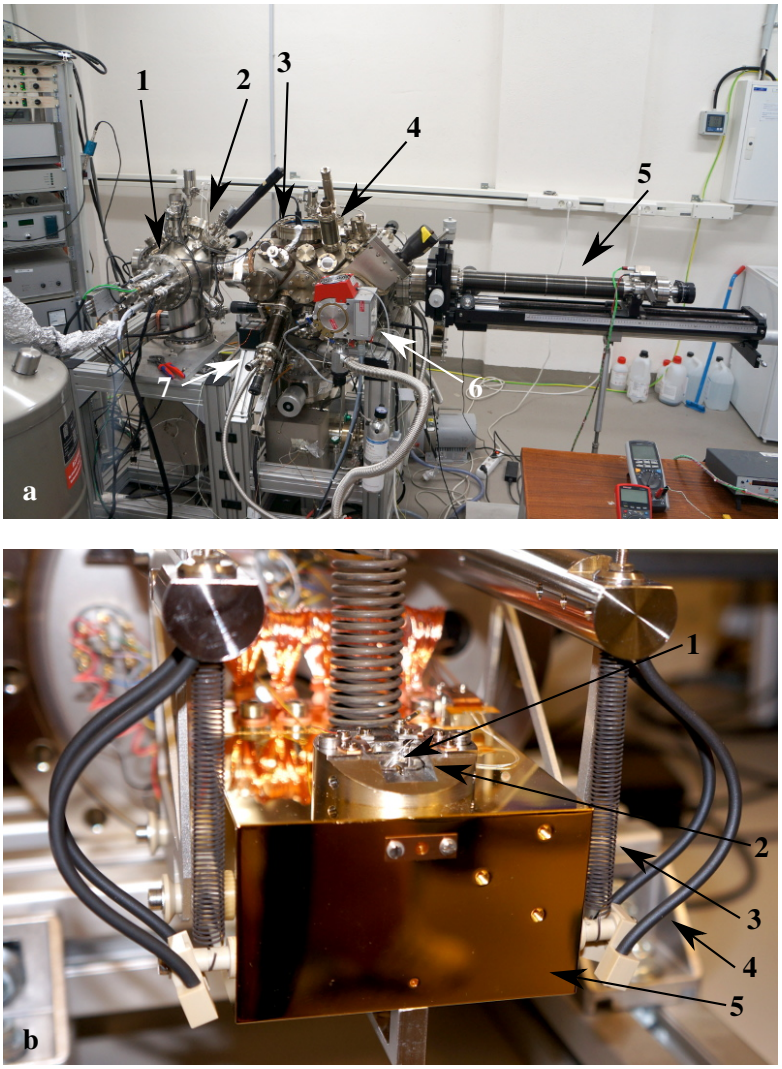

Figure 3.3.: Specs Århus variable temperature STM. (a) overview image of the UHV chamber. 1: STM flange, 2: STM chamber, 3: preparation chamber, 4: quadrupole mass spectrometer, 5: manipulator, 6: turbo molecular pump, 7: molecule evaporator. (b) shows the STM itself. 1: tip, 2: sample reception, 3: spring, 4: viton band, 5: copper block.

3.3. Sample preparation

In this thesis metal surfaces are used as a substrate for the molecules. These can be bought as single crystals, which are cut and polished in the desired crystallographic orientation with a precision of $\leq 0.1°$. The most commonly used surfaces in this thesis are Au(111), Ag(111) and Cu(111), but also Cu(110) was used. These three metals have a face-centered cubic crystal structure, but they differ in their reactivities and catalytic activities [50, 51]. Of these surfaces only Au(111) shows a reconstruction [52]. This so-called herringbone reconstruction emerges because in the surface layer, 23 gold atoms occupy the space of 22 bulk lattice sites. This lattice mismatch leads to parallel reconstruction lines with a periodicity of 63 $\AA$.

Especially when the crystals are newly bought, but also after they have been exposed to air or

between different experiments, these surfaces have to be cleaned inside the UHV system in order to remove all adsorbates. The standard method for cleaning noble metal samples is to sputter them with Ar gas followed by annealing of the sample [49]. This is done by leaking Ar gas in the chamber until a pressure of about $5 \cdot 10^{-6}$ *mbar* is reached. Inside the sputter gun, the Ar is ionized to Ar^+ and accelerated with 1500 V towards the sample. Where the ions hit the sample, some material is removed, leaving a rough surface behind [53]. In this thesis an ion current of about 4 μA was directed at the sample for 45 *min*.

After the sputtering, the surface needs to be annealed in order to make it flat again. For the used metals typically annealing at 400°C to 500°C for 10 *min* was enough to obtain flat surfaces. By the increase in temperature the surface atoms obtain the energy necessary to diffuse to their favorite adsorption site, which is the flat surface because in this geometry the atoms have the highest coordination number.

However, especially in new crystals, impurities present in the bulk of the material also obtain the energy to diffuse to the surface, from where they can only be removed by another round of sputtering. Usually a new crystal needs up to 20 sputtering - annealing cycles until the bulk crystal is sufficiently depleted of impurities such that clean single crystal surfaces can be observed in STM.

3.4. Molecule deposition

The molecules to be investigated usually come as a powder and have to be transferred to the clean sample in the UHV system. The easiest way is to evaporate them from a so-called Knudsen cell, consisting of a glass or metal crucible, in which the molecules are heated in vacuum to their sublimation temperature. At this temperature, the molecules start to sublime out of the crucible in a rather unfocused beam, in which the sample is positioned for deposition. This molecular beam as well as the molecules on the surface are generally invisible to the human eye, due to the low numbers of molecules involved.

To control the coverage on the sample the deposition rate can be measured using a quartz crystal micro balance, working as follows: A quartz crystal is excited to oscillate by an external electrical signal and its eigenfrequency of about 6 MHz is measured by a frequency counter with a very high precision (of 0.01 Hz). When molecules adsorb on the crystal, its mass increases and thereby the eigenfrequency decreases, whereby the rate of the frequency change has a linear relationship with the deposition rate of the molecules on the crystal. By multiplying the deposition rate with the deposition time, the total coverage on the sample can be judged. However, it is important to keep in mind that the observed frequency change depends on several parameters as the molecular weight, the size of the quartz and its distance from the crucible. The coverage on the sample depends on the evaporation rate, the distance between evaporator and surface and the area, a molecule occupies on the surface. Not all of these parameters are known in advance and therefore it is impossible to dose precisely the desired amount of molecules on the surface at the first attempt. The first evaporation is generally used to find the relation between frequency change during the evaporation and coverage on the surface, which is used in all following preparations to precisely attain the desired coverage.

The porphyrin molecules from chapter 4 can be evaporated easily at temperatures between 230°C and 270°C, leading to very clean preparations due to their high stability. If not stated otherwise, the molecules were deposited at samples held at room temperature or slightly above (up to 50°C).

The nanocars from chapter 5, however, are much harder to get intact on the surface. Their evaporation temperature lies between 270°C and 310°C, which is for these large molecules close to their decomposition temperature. Consequently, the preparations are very dirty as many molecular fragments adsorb on the sample as well and often it takes a long time to find intact nanocars at all. Furthermore, the total amount of preparations from one crucible is rather limited, generally only three acceptable

sample preparations could be achieved with one evaporator filling, after which the crucible had to be cleaned and refilled with new molecules.

Also the thin NaCl layers from chapter 5.1.5 were evaporated onto the sample by the same method, at a crucible temperature of about 510°C. When a submonolayer coverage of NaCl is evaporated on a Cu(111) or Au(111) surface, it tends to build NaCl bilayers. Their shape strongly depends on the sample temperature during deposition, when depositing on a sample at 0°C, highly structured, small islands are found as observed in [44]. Depositing the same amount of NaCl at room temperature also leads to bilayer islands, which can be so large that finding their border with STM can be a time-consuming task. Therefore, NaCl was generally deposited in between these two temperature at around 10°C.

3.5. Laser systems

The molecules studied in chapter 5 are excitable with UV light in solution and within this thesis it was tried whether this is also possible on a surface. Therefore, the sample with the molecules was illuminated with UV lasers without taking the sample out of the STM. Viewports in the UHV chamber and openings in the radiation shields of the STM are present, permitting the laser beam to enter the STM, illuminate the sample and the reflected light to leave the UHV system (chapter 3.1).

As the standard UHV windows are not transparent for UV light, the viewports where the light beam enters and leaves the chamber had to be changed to CaF_2 windows, which have a high transmission down to wavelength of $\lambda = 200\ nm$.

The molecules in chapter 5.1 were illuminated using an excimer laser PSX-100, from the company Neweks. It was filled with KrF, which yields an output wavelength of $\lambda = 248\ nm$. This is a pulsed laser with a repetition rate of 10 Hz to 100 Hz, a pulse duration of 5 ns and 5.5 mJ maximum pulse energy. However, as the gas filling degrades over time, the output power drops. As there was no powermeter available in the lab this drop could not be measured, but when a visual drop of the intensity could be detected, the gas filling was renewed. The manufacturer states the typical life-time of the KrF gas is 10^6 pulses. Dielectric mirrors, specially adopted to have a very high reflectivity ($> 99.5\ \%$) at the wavelength of the laser, were used to direct the beam onto the sample.

The lasers used to illuminate the molecules in chapter 5.2, were FTSS355-Q2 and FQSS266-Q2, both from the company CryLas. Both are Nd:YAG solid state lasers with a base wavelength of $\lambda = 1064\ nm$, which are frequency tripled and frequency quadrupled to $\lambda = 355\ nm$ and $\lambda = 266\ nm$, respectively before the output. Both lasers have a pulse duration of 1 ns and the repetition rate can be adjusted to up to 10 kHz. The energy of the individual pulses are 4.6 μJ and 1.1 μJ, respectively. As both lasers were used in the same setup, the dielectric mirrors were replaced by Al coated mirrors, which have a good reflectivity ($\approx 90\ \%$) in the whole UV range.

3.6. Statistical evaluation methods

In chapter 4.5, porphyrin molecules are studied at room temperature with the aim of identifying possible cooperative interactions among neighboring molecules. Therefore, the same surface area was scanned over and over again to study the evolution of the molecules in this specific case. The evaluation methods and especially the statistical test applied to the resulting movies are explained in this section.

The recorded STM images were first opened in the software Gwyddion [54] for performing standard image treatments like plane correction and calibration. The processed images were then loaded into a self-written python program, containing all the procedures for correcting the thermal drift, extracting the

apparent molecular height from the images, classifying the molecules as bright or dark and performing the statistical evaluation. Its source code is provided with this thesis (appendix A).

3.6.1. Drift correction

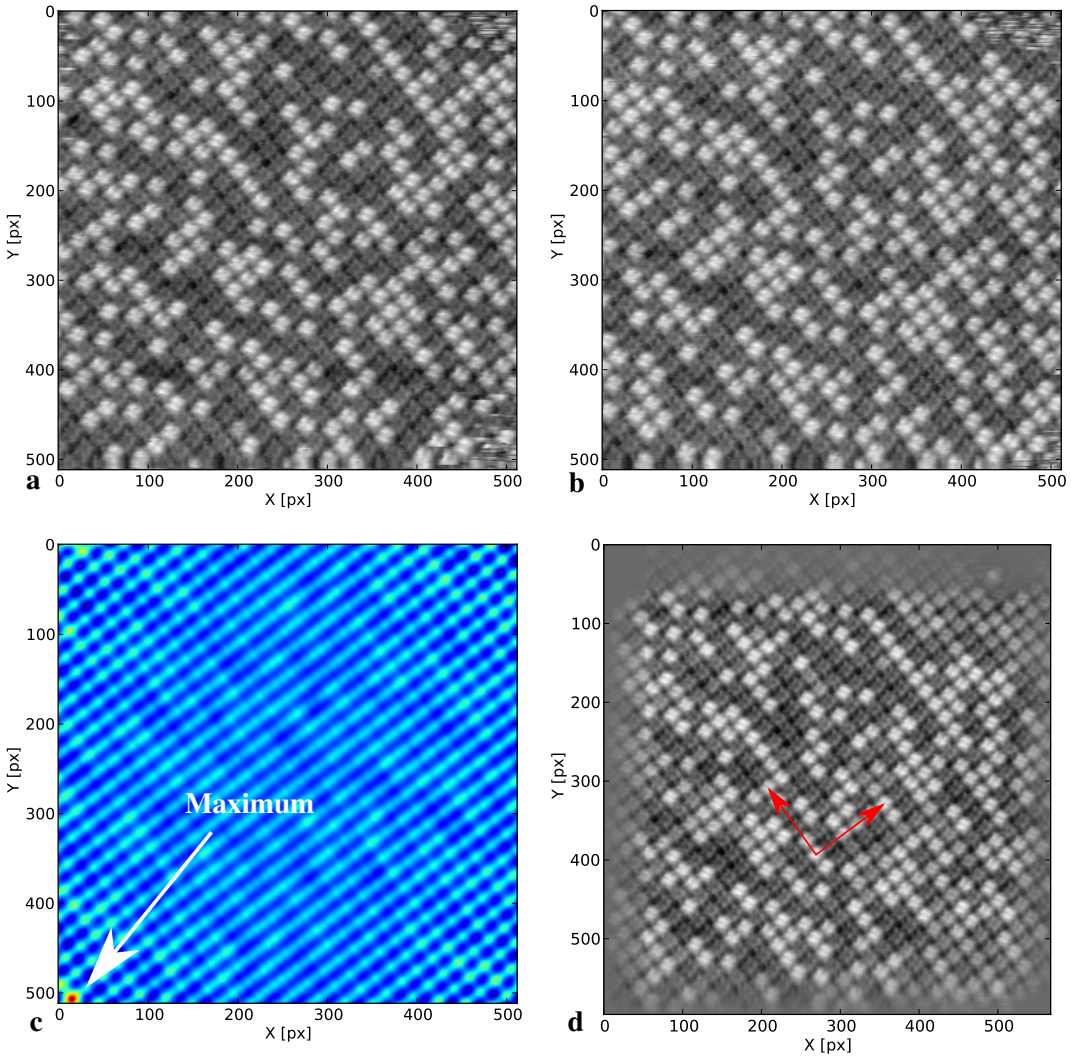

Figure 3.4.: Demonstration of the drift correction. (a) and (b) are two images out of a movie of Br_4TPP on Au(111) with the image parameters: $37.5 \times 37.5\ nm^2$, $U_{sample} = 0.884\ V$, $I = 0.14\ nA$, $T = 300\ K$. (c) Cross correlation of (a) and (b), the maximum is marked by the arrow, determining that the shift in x direction is 15 pixel and in y direction 6 pixel, corresponding to 1.1 *nm* and 0.44 *nm*, respectively. (d) shows the average image of the full movie after drift correction. The basis vectors of the lattice (multiplied by five for better visibility) are shown as red arrows.

Due to small temperature gradients present in the STM setup, the position of the tip slowly drifts over time because the piezo elements responsible for the tip positioning will slightly change their length upon temperature change. This effect is usually very small ($< 1\ nm/hour$) in low temperature

STMs (5 K), where the whole STM is surrounded by radiation shields which limit the heat exchange with the surroundings to a minimum. On the contrary, due to their more open construction, and the desire to readily change temperatures in a variable temperature STM, the expected drift rates are larger and need to be accounted for.

The drift manifests itself as a lateral shift between two subsequent STM images and a slight image distortion. In all the recorded movies of sufficient quality for a detailed analysis, the distortion was so small that it could be neglected, but the shift needs to be corrected for. When the two images $A(x,y)$ and $B(x,y)$, which need to have the same physical and pixel dimensions ($x \in [0, x_{max}[$ and $y \in [0, y_{max}[$), still have a considerable overlap, i.e. the drift between them was much less than the image dimensions, the shift in x and y direction can be obtained by calculating the two dimensional cross correlation of both images:

$$(A * B)(x,y) = \sum_{x'=0,y'=0}^{x_{max}-1,y_{max}-1} A(x',y')B(x+x'-ix_{max}, y+y'-jy_{max}) \tag{3.1}$$

with i and j chosen such that $0 \leq x+x'-ix_{max} < x_{max}$ and $0 \leq y+y'-jy_{max} < y_{max}$. x' and y' are the summation indices. However, calculating the cross correlation in this form is very time consuming. A much faster way is to exploit the speed of the fast Fourier transform algorithm:

$$(A * B)(x,y) = \mathscr{F}^{-1}\left(\mathscr{F}^{*}(A)\mathscr{F}(B)\right) \tag{3.2}$$

where $\mathscr{F}$ is the Fourier transform and * stands for complex conjugation. If the two images are sufficiently similar, the drift is given by the position of the brightest pixel in the cross correlation $A * B$. This method is illustrated in Fig. 3.4. The cross correlation image (c) reflects the overall translation symmetry of the surface, but there is a clear maximum in the lower left corner, which is used to determine the shift between the images, namely 15 pixel in x and 6 pixel in y direction.

When calculating the drift for every frame of a movie, the most precise results are obtained when comparing all frames with its first frame. Although this algorithm is quite stable it might fail because of several reasons: The drift might be so strong that after some frames the images do not overlap with the first image any more, or the surface is not so similar to the first frame any more due to its evolution (molecular switching, diffusion, ...) and also tip changes during the movie might make frames dissimilar to the first. In these cases it is helpful to compare all frames up to a certain number to the first frame and then take the last working frame as a reference for all the following ones. In difficult cases, it can also be necessary to compare every frame to its predecessor.

3.6.2. Determining the molecular state

When the drift of all frames in a movie has been determined as described in section 3.6.1, every image is pasted into a larger array filled with zeros at the position according to its drift values. After this has been done, every molecule has the same pixel position in every frame of the movie and an average image of the full movie can be calculated (Fig. 3.4 (d)), which is usually a good overview of the movie.

It is larger than the original images because of the space needed to compensate the drift. The central region, which is imaged in almost every frame, appears very clear, the regions at the border have less contrast because they are only visible in some of the frames and subsequently contribute less to the average image.

For all the following evaluation it is necessary to know the (pixel) positions of all molecules. As the molecules are arranged in a regular lattice within close-packed islands, it is easy to determine all the

positions by just defining the two basis vectors $\mathbf{a_1}$ and $\mathbf{a_2}$ and extending the lattice to the border of the imaged area

$$\mathbf{r} = m\mathbf{a_1} + n\mathbf{a_2} \tag{3.3}$$

where m and n are two integer numbers.

To determine the state of every molecule in every frame, the pixel values within a certain radius around the central molecular position are median averaged. A molecule is classified as "bright" if its height is above a certain threshold above the average molecular height and as "dark" if it is below. This threshold needs to be adjusted manually for every movie, but is usually between 0.2 and 0.5 standard deviations above the average. Molecules which are not imaged in the current frame obtain the state "out of image" and can be excluded from the statistical analysis as needed.

3.6.3. Random patterns

When observing a pattern of dark and bright molecules as in Fig. 3.4 (a), it is interesting to know if this pattern is random or whether there is some sort of order in it. To answer this question, two statistical tests were applied to the measured data:

- The molecular island of one frame is divided into patches of three by three molecules and the number of bright molecules in every patch is counted. The corresponding random distribution is the binomial distribution [55]:

$$P(r;p,n) = p^r(1-p)^{n-r}\binom{n}{r} = p^r(1-p)^{n-r}\frac{n!}{r!(n-r)!} \tag{3.4}$$

  (where r is the number of bright molecules per patch, n is the total number of molecules in the patch (9 in this case) and p the total concentration of bright molecules in this frame) which can be plotted in the same graph as the distribution of bright molecules in the patches. If the experimentally observed distribution deviates from the binomial distribution, it can be concluded that the bright molecules are not randomly distributed.

  However, as this method only counts the number of bright molecules, all information about directional correlation on the surface is lost, which could potentially lead to a situation where spatial correlation in certain directions is averaged out by the other uncorrelated directions.

- The second approach is similar to the short range order (SRO) parameter α known from studies of metal alloys [56, 57, 58]. In these articles, α was given in a distance dependent formulation only ($\alpha(r) = 1 - p(r)/c$ with r the distance), but here it is used as a function of the lattice position m and n of the molecular island:

$$\alpha(m,n) = 1 - \frac{p(m,n)}{c} \tag{3.5}$$

  where $p(m,n)$ is the probability of finding a molecule of the opposite type at the relative lattice position (m,n) and c is the concentration of this opposite species on the surface. If there is no correlation between these two sites, the SRO parameter α has the value zero, because in this case $p = c$. If the molecules are likely to have the same state, α will be close to one, and in the opposite case α will be negative. Compared to the first approach counting the bright molecules in 3x3 patches, this method has the advantage that correlations in all directions could be resolved.

For both approaches, only one single frame out of the full movie can be taken into account, because only very few molecules change their state in between two frames and many never switch (chapter 4.5.5). Consequently, most of the three by three patches do not change the number of bright molecules between the frames. When the number N of patches with a certain number of bright molecules k is counted in one frame, the corresponding error is $\sqrt{N}$ (Poisson statistics) and consequently the signal to noise ratio (SNR) is $N/\sqrt{N} = \sqrt{N}$. Assuming for a moment that the movie has M frames and that all the frames are identical, the number of patches with k bright molecules in the full movie is $N \cdot M$, the error is $\sqrt{N \cdot M}$ and the SNR is also $\sqrt{N \cdot M}$. This means that compared to counting only one frame, which holds the same information as all the other frames, the SNR was increased by a factor of $\sqrt{M}$. Consequently, counting the same data several times artificially increases the SNR without increasing the data quality.

In the measured movie, some molecules switch between the frames and due to the thermal drift, some patches leave the imaged area and others appear, but compared to the total number of patches, the changes are very small. That is why realistic errors can only be obtained when concentrating on a single frame and no precision gain can be expected when counting all patches in all frames of the movie. This is also true for SRO parameter, where the errors are also estimated using Poisson statistics.

3.6.4. Time dependence

Whenever looking at thermally induced processes that are independent from each other, the main parameter governing the evolution of the system are the temperature and the time constants involved, which is also the case for the switching between the dark and bright state of porphyrin molecules at room temperature.

If only a single time constant governs the switching of a molecule from a to b, the dwell time distribution is given by:

$$P_{a\to b}(t) = \frac{1}{\tau_a} e^{-\frac{t}{\tau_a}} \tag{3.6}$$

and for the other direction by :

$$P_{b\to a}(t) = \frac{1}{\tau_b} e^{-\frac{t}{\tau_b}}. \tag{3.7}$$

In other words: the dwell times are exponentially distributed, and the first factor ensures the normalization so that

$$\int_0^\infty P_{a\to b}(t)dt = 1$$

If the evolution of the system is described by only one time constant, the easiest way of estimating[1] it is to calculate the mean of the dwell times:

$$\langle t \rangle = \int_0^\infty t \cdot P(t)dt = \int_0^\infty \frac{t}{\tau} e^{-\frac{t}{\tau}} dt = \tau \tag{3.8}$$

However, if the measured dwell times are not exponentially distributed, e.g. if several processes with different time constants are governing the change of state at the same time, this method of just averaging them will not yield any sensible information. Therefore it is actually necessary to always inspect their histogram before doing so as it was done in this work unless stated otherwise.

[1] Throughout this thesis the term “estimation” is used in its precise statistical meaning [55]. It signifies that a value is extracted from measured data using a certain procedure and is therefore clearly distinct from the unprecise “guessing”, wich is used equivalently in the spoken language.

If the dwell times cannot be explained by a single exponential function, one can try, if the data quality permits, to fit the histogram with a sum of several exponentials to estimate their respective rate constants. However, this method also has its drawbacks: Fitting procedures need supervision, fitting low quality data can be unstable and one needs to put in assumptions (in this case the number of exponentials). A method overcoming all the described problems is described in [59], where the dwell time distribution is given by:

$$P(t) = \int \rho(k) k e^{-kt} dk \quad \text{with} \quad k = \frac{1}{\tau} \tag{3.9}$$

where $\rho(k)$ is the distribution of the k values. When choosing $\rho(k) = \delta(k - k')$ this expression is equivalent to equation 3.6. From equation 3.9 one can see that $P(t)$ is actually the Laplace transform of $\rho(k)k$. As $P(t)$ is experimentally measured, for obtaining $\rho(k)$ this Laplace transform needs to be inverted in a numerically stable and assumption-free way [59]. It also includes a working implementation of this method which has been applied to the measured dwell times from the room temperature movies.

3.6.5. Random distances

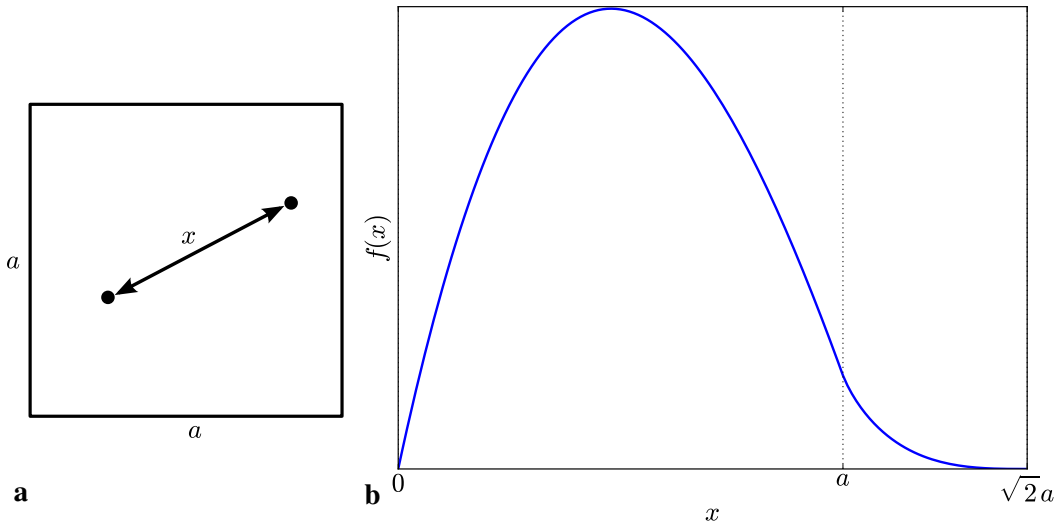

Figure 3.5.: Distance distribution of random points in a square. (a) Square with side length a and two random points, their distance is x. (b) Probability distribution (as given in equation 3.10) of the distance x.

In several places of this thesis, the question arises whether molecules or switching events are randomly distributed in space. Their distances can be measured in STM images. As STM images are usually square, it is helpful to know the distance distribution of random points in a square, for comparison.

For a square with the side length a, the probability distribution of the distances between two random points is given by [60]

$$f(x) = \frac{4x}{a^4} \phi(x) \tag{3.10}$$

with

$$\phi(x) = \begin{cases} a^2\left(\sin^{-1}\left(\frac{a}{x}\right) - \sin^{-1}\left(\sqrt{1-\frac{a^2}{x^2}}\right) - 1\right) - \frac{x^2}{2} + 2a\sqrt{x^2-a^2}, & a \le x \le \sqrt{2}a \\ \frac{\pi a^2}{2} - 2ax + \frac{x^2}{2}, & 0 \le x < a \\ 0, & \text{elsewhere} \end{cases} \tag{3.11}$$

This distribution is plotted in Fig. 3.5 and reveals a maximum at $x = \frac{a}{3}\left(4 - \sqrt{16-3\pi}\right) \approx 0.4786\, a$.

3.6.6. Poisson and Skellam distribution

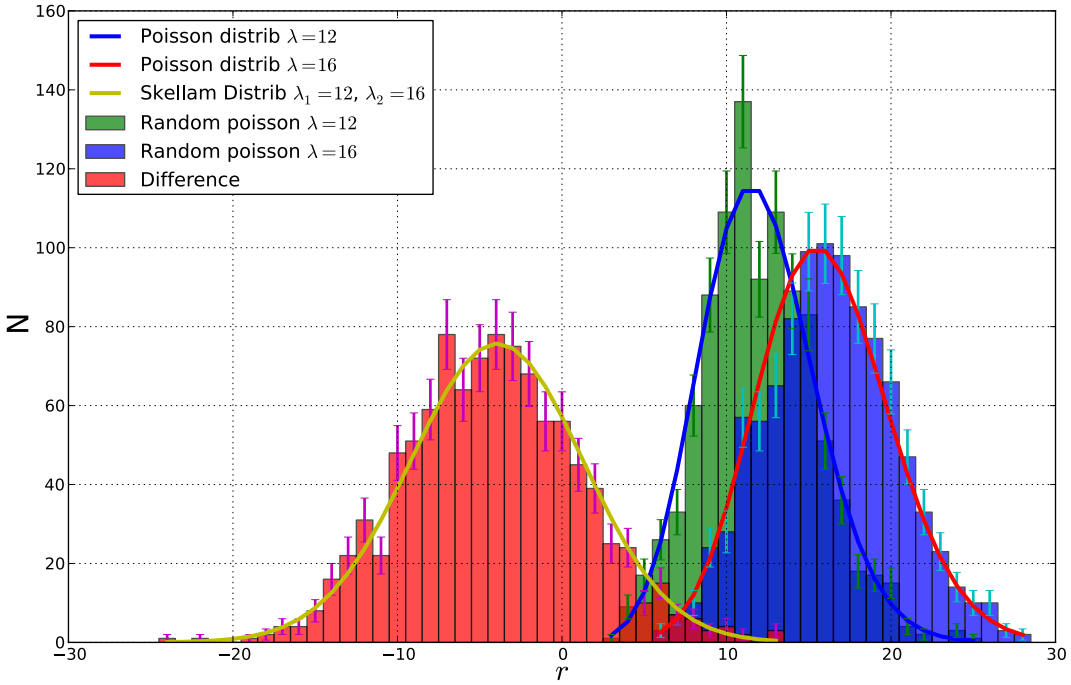

Figure 3.6.: Examples for Poisson and Skellam distributions. The green and blue histograms show the distribution of 1000 Poisson distributed random numbers with the respective rates $\lambda = 12$ and $\lambda = 16$ and the red histogram shows their difference. The error bars are the $\sqrt{N}$ counting errors. Corresponding Poisson and Skellam distributions are shown as colored lines.

The Poisson distribution is the well known distribution for independent events [55], when it is known that the events happen at certain rate λ:

$$P(r;\lambda) = \frac{e^{-\lambda}\lambda^r}{r!} \tag{3.12}$$

It gives the probability for r events happening per time interval. One interesting property of the Poisson distribution is that when two independent Poisson processes with different rates λ_1 and λ_2 are summed up, the resulting distribution is again a Poisson distribution and its rate λ is the sum of the individual rates ($\lambda = \lambda_1 + \lambda_2$) [55].

In chapter 4.5.7 it is looked at the difference of two processes. For comparison it is helpful to know the difference between two Poisson processes, which has first been calculated by Skellam [61], and the resulting difference distribution is now named Skellam distribution:

$$P(r;\lambda_1,\lambda_2) = e^{-(\lambda_1+\lambda_2)} \left(\frac{\lambda_1}{\lambda_2}\right)^{\frac{r}{2}} I_r\left(2\sqrt{\lambda_1\lambda_2}\right) \tag{3.13}$$

Where r is the difference of the events, λ_1 and λ_2 the respective rates of the original Poisson distributions and $I_\alpha(x)$ is the modified Bessel function. Fig. 3.6 shows two examples of Poisson distributed random numbers with different rates and their difference. The corresponding Poisson and Skellam distributions describe the histograms nicely.

3.6.7. The χ^2 distribution and the P value

To quantify the deviation between a measured distribution and a fitting function, the χ^2 value can be calculated [55]:

$$\chi^2 = \sum_i \frac{[f(x_i) - y_i]^2}{\sigma_i^2} \tag{3.14}$$

where x_i and y_i are the measured values, σ_i is the measurement error for y_i and $f(x_i)$ is the value of the fitting function at position x_i.

Considering the case that the data and the distribution agree, the expected deviation of every datum y_i from the distribution $f(x_i)$ is σ_i and therefore every term in the sum gives a contribution of ≈ 1. When N data points were measured, the expected value would be $\chi^2 \approx N$. On the other hand, if $\chi^2 \gg N$, data and distribution probably disagree and if $0 < \chi^2 \ll N$, probably the measurement errors were overestimated.

To quantify this sort of argumentation, the distribution of χ^2 was calculated, assuming that the measurements follow Gaussian distributions [55]:

$$p\left(\chi^2;n\right) = \frac{2^{-\frac{n}{2}}}{\Gamma\left(\frac{n}{2}\right)} \chi^{n-2} e^{-\frac{\chi^2}{2}}. \tag{3.15}$$

$n = N - m$ is the number of the degrees of freedom, where N is the number of measurements and m is the number of fitting parameters.

Now, depending on the number of degrees of freedom, the probability can be calculated to observe a given χ^2 or higher by evaluating the following integral

$$P\left(\chi^2;n\right) = \int_{\chi^2}^{\infty} p\left(\chi'^2;n\right) d\chi'^2. \tag{3.16}$$

This P value also measures the degree of similarity between the data and the distribution, but compared to χ^2 it has the advantage that it has values between 0 and 1, which describe a probability and do not change their magnitude with the number of data points. The higher the value of P, the smaller is the deviation of the data from the distribution.

3.6.8. Principle component analysis

A very powerful technique for statistical data analysis is principle component analysis (PCA) [62]. It aims at identifying variability patterns in high dimensional correlated data and to reduce its complexity by introducing new uncorrelated coordinates.

When looking at N variables $x_1, x_2, \ldots, x_N$, the covariance matrix is defined as [55]

$$V_{ij} = cov(x_i, x_j) = \overline{x_i x_j} - \overline{x_i}\,\overline{x_j}. \tag{3.17}$$

This symmetric matrix has the variances of the variables on its diagonal and the covariances between all variables as off diagonal elements. Identifying the important structures in such a $N \times N$ matrix (just by looking at it) is generally difficult.

The idea of PCA is to apply a principle axis transformation to the covariance matrix, i.e. to introduce new coordinates, with the eigenvectors as base vectors, which are called principle components. The eigenvectors are necessarily linearly independent and in this new coordinate system, the covariance matrix is diagonal. Its elements, the N eigenvalues corresponding to the N principle components, give the variance of every component. If there was a sufficient degree of correlation in the original variables, it can occur that only few (much less than N) eigenvalues have a considerable variance and that the others are close to zero. In this case, most of the variability of the data can be explained only by these components and the others can be safely discarded, which is a strong reduction of complexity. The eigenvectors of the strong components can the be transformed back into the original coordinates for further investigation and interpretation.

If the original data is uncorrelated, i.e. its covariance matrix is already diagonal, no reduction in complexity can be expected from PCA, because there are no variability patterns to be found.

Part II.

Experiments and results

4. *Tetra*-Phenyl-Porphyrin (TPP)

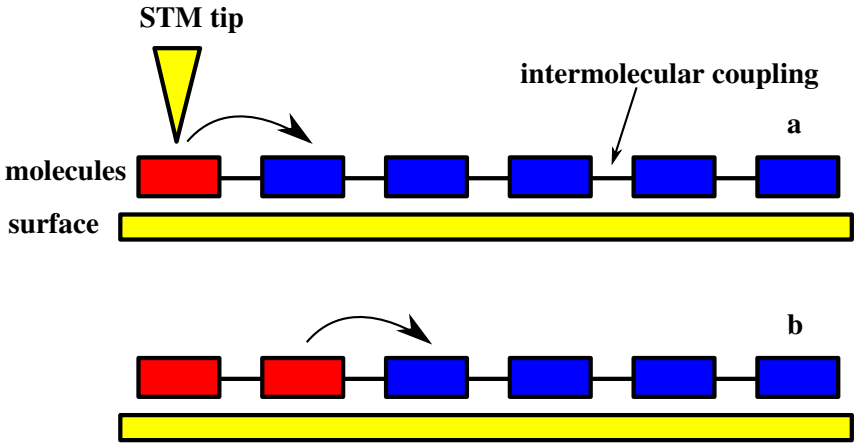

Figure 4.1.: Schematic of coupled molecular switches on a surface. In (a), one of the switching units is switched by an STM tip and in (b) the conformation is propagating along the chain.

During the evolution of life on earth, nature developed various molecules for performing complex tasks inside the bodies of humans, animals and in plants. Two examples of such molecules with a complex functionality, hemoglobin and myosin V, were presented in detail in the introduction of this thesis. They have in common that their functionality stems from cooperative effects between their subunits. Cooperativity as defined in [2] is present, when a structure containing several subunits behaves differently than would be expected from the subunits alone. Understanding the principle mechanisms of cooperative processes in nature is interesting by itself, but this knowledge might also be a big help when synthetic functional molecules shall be designed and their function relies on cooperativity. One potential field of application is molecular electronics, which aims at replacing the components of conventional electronics with single molecules [63], leading to a massive reduction of the structure sizes and consequently to higher operation speed, lower costs and less energy consumption.

In conventional electronics, information is transported by electric currents in metallic wires. Copying this method for the use in molecular electronics is difficult because of several reasons. First, also fully conjugated molecules are relatively poor electric conductors [64, 65] as compared to metals and second, the reliable forming of contacts between molecular wires and metallic electrodes is difficult to achieve in a reproducible manner [66].

With these difficulties in mind it is worth evaluating the possibility of different approaches to information transport on the atomic scale. For example, it has been shown recently, that the information of the magnetization direction of a ferromagnetic island can be transported along an antiferromagnetically coupled chain consisting of iron atoms on a copper substrate [67]. Moreover, in the junction of two such chains, a logic function is formed without any further modification of the structure. Of course, such a system is hardly suitable for a real application in electronic devices as the required temperature of 0.3 K poses a considerable experimental challenge and the atom-by-atom assembly using lateral

tip manipulation is too slow for mass production. Nevertheless, it is interesting to asses different mechanisms of information transport which might eventually one day lead to a working device.

Another approach is followed by the ARTIST research project (**A**lternative **R**outes **T**owards **I**nformation **S**torage and **T**ransport at the Atomic and Molecular Scale) [68] by the European Union that funded the presented PhD thesis. The idea investigated in the following is conformational transport along cooperatively coupled molecular switches (Fig. 4.1). If a group of molecular switches, each having two or more distinct states, was assembled on a supporting surface in a one-dimensional arrangement and the intermolecular coupling was adjusted to yield a cooperative interaction, it might be possible to transport information along this chain by changing the state of the first molecular switch and passing this change of state on to the neighboring molecule via the cooperative interaction, as shown in Fig. 4.1, where the first element is changed with the tip of an STM.

In the present chapter it will be tried to identify a cooperative coupling between neighboring molecular switches and, if present, to characterize the interaction mechanism and coupling strength and their dependence on the type of the intermolecular coupling. The results might lead to a better understanding of the requirements for cooperative coupling and their application in synthetic molecules.

4.1. The choice of porphyrins

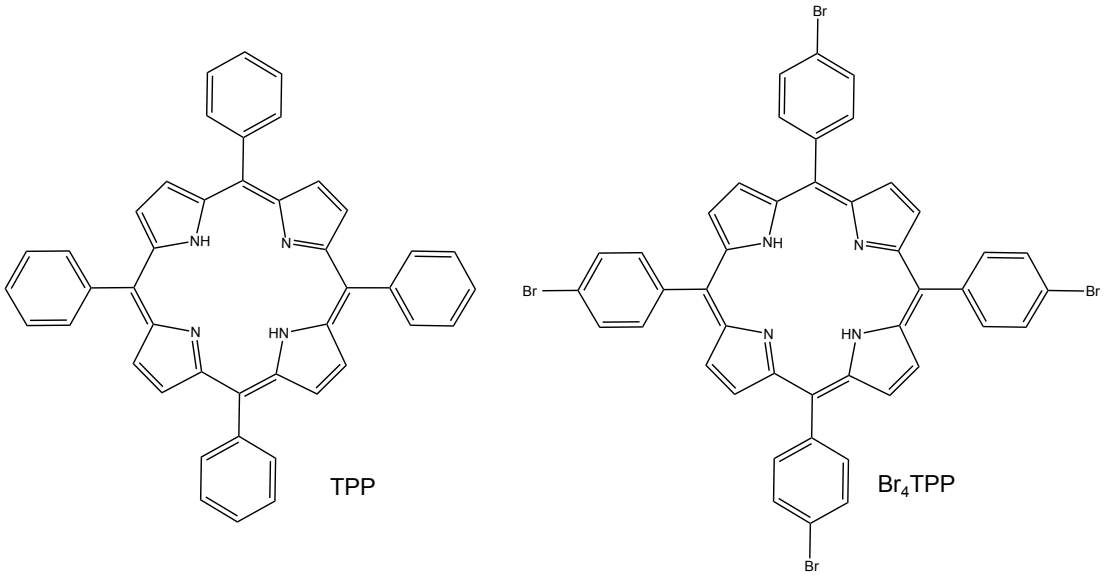

Figure 4.2.: Chemical structures of the two molecules investigated in this chapter, *tetra*-phenyl-porphyrin (TPP) and *tetra*(4-bromophenyl)porphyrin (Br_4TPP)

The molecules that were chosen for the presented project are *tetra*-phenyl-porphyrin (TPP) and *tetra*(4-bromophenyl)porphyrin (Br_4TPP), which are presented in Fig. 4.2. They have several properties which are useful for the desired experiments. First of all, due to the π-conjugation of the central porphyrin core, the molecules are very stable compounds which can be evaporated in vacuum easily without dissociation, leading to very clean preparations. Due to their inherent stability, they are almost flat and generally adsorb on metal surfaces in a flat lying geometry. Furthermore, some porphyrin derivatives are known to be able to switch on surfaces ([8, 9]) between a flat and a buckled adsorption geometry. Another important point is that, depending on the reactivity of the surface, the molecules

have the freedom to diffuse and assemble in close-packed islands or when functionalized with Br atoms, they can even form covalent assemblies [10]. This control over the bonding strength is a very valuable property, when trying to achieve a cooperative coupling between the porphyrin units.

4.2. Porphyrins in nature

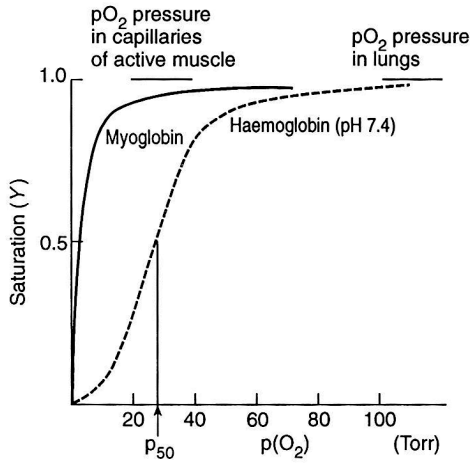

Figure 4.3.: Oxygen saturation curve of hemoglobin and myoglobin as a function of the partial O_2 pressure in the blood. Reprinted with permission from [1]. Copyright 1997, Oxford University Press.

Porphyrin groups play a big role in biochemical molecules ([1] and references therein), serving as a host for metal atoms which are important in the processes of life. The most prominent examples are chlorophyll, the protein responsible for photosynthesis in plants, and hemoglobin, which takes care of the oxygen transport inside the bloodstream.

In chlorophyll, the porphyrin unit is responsible for absorbing photons. A magnesium center adjusts its absorption bands to the desired wavelengths. The photon energy is transfered to an electron, which is passed on over several different proteins and finally reduces water to O_2 and CO_2 to hydrocarbons. But porphyrins also play an important role in the inverse process, namely the oxygen transport from the lungs to the cells through the bloodstream. Hemoglobin contains four porphyrin groups, each with an iron center to which an O_2 molecule can bind. Although hemoglobin is quite a large molecule and the porphyrin units are far apart, they can communicate through the backbone of the hemoglobin, leading to cooperative [2] oxygen uptake. This cooperative effect is an essential part of the hemoglobin function, as the oxygen is released only in the desired body regions and not during the transport in the blood.

Fig. 4.3 shows the implications of this effect. The O_2 saturation curve for hemoglobin is shown as a function of the partial oxygen pressure in the blood. As a comparison the corresponding graph for myoglobin is shown in the same diagram. Myoglobin is responsible for the oxygen storage in the muscle tissue. The difference between these two proteins is that myoglobin only contains one oxygen binding iron porphyrin and therefore cannot show any cooperative oxygen uptake. In the region of the lung oxygen pressure, hemoglobin reaches almost full saturation, whereas in the pressure region of the muscle tissue oxygen is released, the saturation drops to 0.5. At the same pressure, myoglobin still has full saturation and can take over the oxygen delivered by the hemoglobin.

4.3. Porphyrins on surfaces

Porphyrins have attracted a lot of attention in various fields of surface science. For example they were used as a host for magnetic metal centers [9, 69], allowing to study magnetism in molecules.

The incorporation of the metal center into the porphyrin macrocycle can be followed directly on surfaces. First, the free base porphyrins are deposited and the metal atoms are added in a second step. As the atoms are free to diffuse, they will get bound in the porphyrin core when they reach the required position. This process can be followed both, by STM [70, 71, 72] and diffraction methods [73, 74, 75, 76].

In biomolecules, porphyrins with metal centers are often used to reversibly bind gas molecules and it has been tried to simulate this process on surfaces using model systems [77, 78, 79, 80]. Porphyrins have also been used to study switching processes within molecules, whereby different mechanisms can play a role: The possibility to rotate side groups can be exploited [81], the bending of the central macrocycle can be changed [8, 9] and also the tautomerization of the central hydrogen atoms can be used as a switch [82].

Furthermore, there has been intensive research on the assembly of porphyrins, ranging from close-packed arrangements [83, 84, 85, 86, 87], over adatom-mediated bound structures [88, 89, 90] to covalent assemblies [10, 91, 92, 93].

4.4. Low temperature measurements

At first, the TPP molecules are studied on Au(111) by low temperature STM (see chapter 3.1). This instrument offers the best conditions for the controlled investigation of the molecules because of several reasons: Due to the low temperature of about 5 K all thermal processes are significantly slowed down or completely suppressed such that stable conditions are achieved over timescales of months. This includes internal processes as conformational changes or vibrations as well as diffusion of the molecules on the surface. Single molecules can be investigated stably on the surface and, depending on the preparation conditions, close-packed molecular islands can be found, too.

The design of the LT-STM, having the STM head and the surrounding helium cooled radiation shield at the same temperature leads to very small temperature gradients across the system and thereby to very small drift rates of $< 1\ nm/hour$. The high stability of the STM as well as of the adsorbate/substrate system at these low temperatures enables us to perform reliable dI/dV measurements (chapter 2.2) with a good signal to noise ratio (SNR), because at 5 K the experimental linewidths are very small and spectra can be taken repeatedly of the same point of the surface for rather long periods, thus reducing the noise.

The measurements in this chapter are compared with theoretical calculations presented in chapter 4.8.

4.4.1. Molecular appearance

A typical overview image of TPP molecules on Au(111) can be found in Fig. 4.4. About 0.13 monolayers of molecules have been evaporated on the surface at room temperature and were then cooled down to the imaging temperature of 5 K. The well known herringbone reconstruction of the Au(111) surface [52] can be seen unperturbed in the presence of the molecules in the inset of the figure. This is generally regarded as a sign for a rather weak interaction of the molecules with the substrate, because in the case of strong adsorption the reconstruction can be lifted or modified in the presence of molecules [94]. Single TPP molecules can be found on all sites of the reconstruction: the fcc and hcp

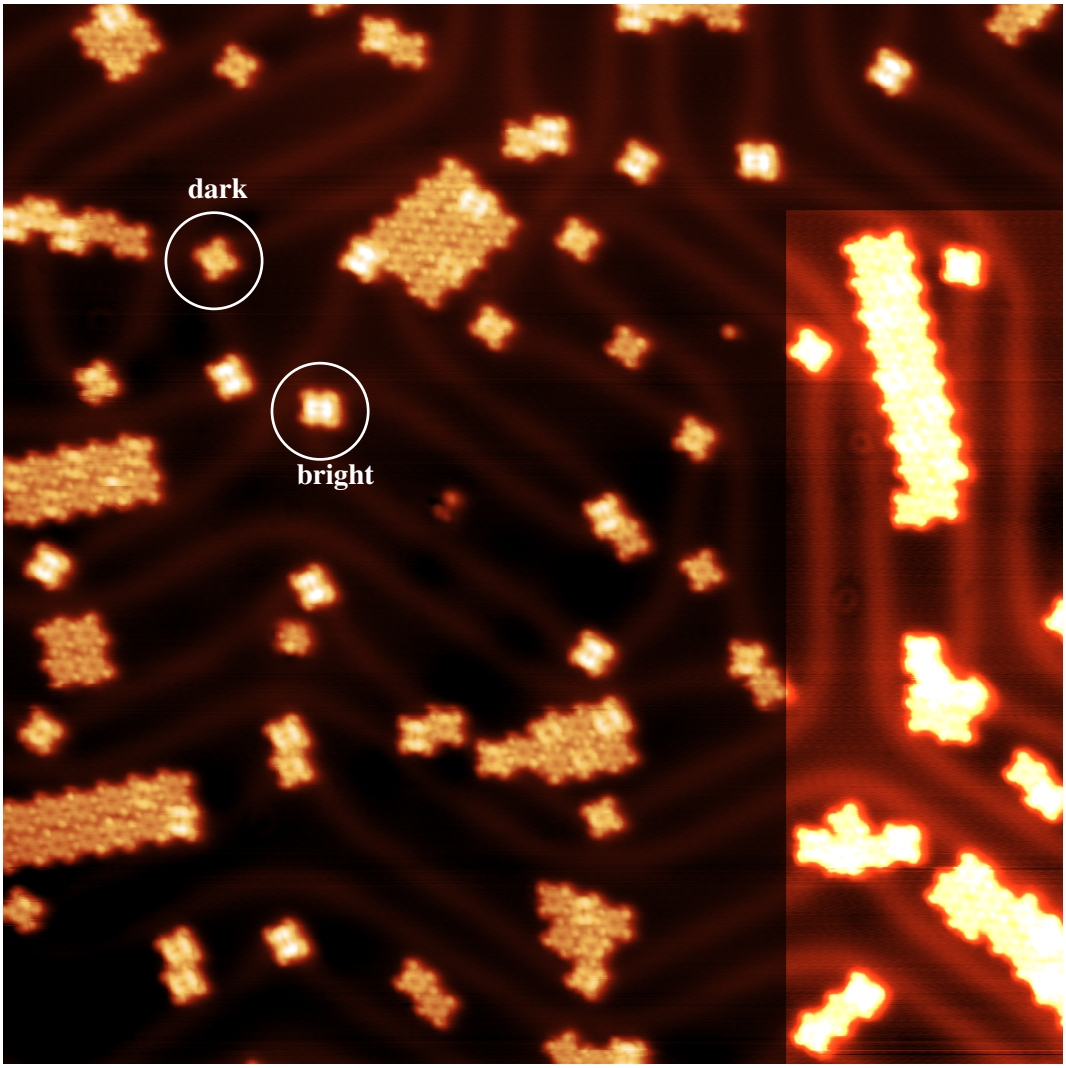

Figure 4.4.: Overview image of TPP on Au(111). In the inset, the image contrast was adopted to clearly show the herringbone reconstruction. ($48 \times 48\ nm^2$, $U_{tip} = -1\ V$, $I = 0.41\ nA$, $T = 5\ K$)

regions, the ridges and the elbows. The molecules also assemble in close-packed islands, the island sizes scale with the total coverage on the surface. The growth of these islands seems to be guided by the reconstruction lines of the herringbone reconstruction (as can be seen in the inset of Fig. 4.4).

Although only one species of molecules has been evaporated on the surface, depending on the tunneling conditions, two types of molecules can be seen in the image, a darker and a brighter form. In order to find out more about the origin of these two molecular appearances, bias dependent images have been recorded, which can be seen in Fig. 4.5. These images show two small close-packed islands, consisting of four molecules each and a single bright molecule in between, being adsorbed on an elbow of the herringbone reconstruction. The best contrast between the different states of the molecules is found in (d), at a tip voltage of $-1\ V$, where it is easy to distinguish between the three bright and the dark molecules. At the other bias voltages, however, this distinction is almost impossible. Close inspection of the island in the lower right corner reveals that there are actually two groups of dark molecules which are hard to distinguish in STM measurements but will be assigned later (chapter 4.8)

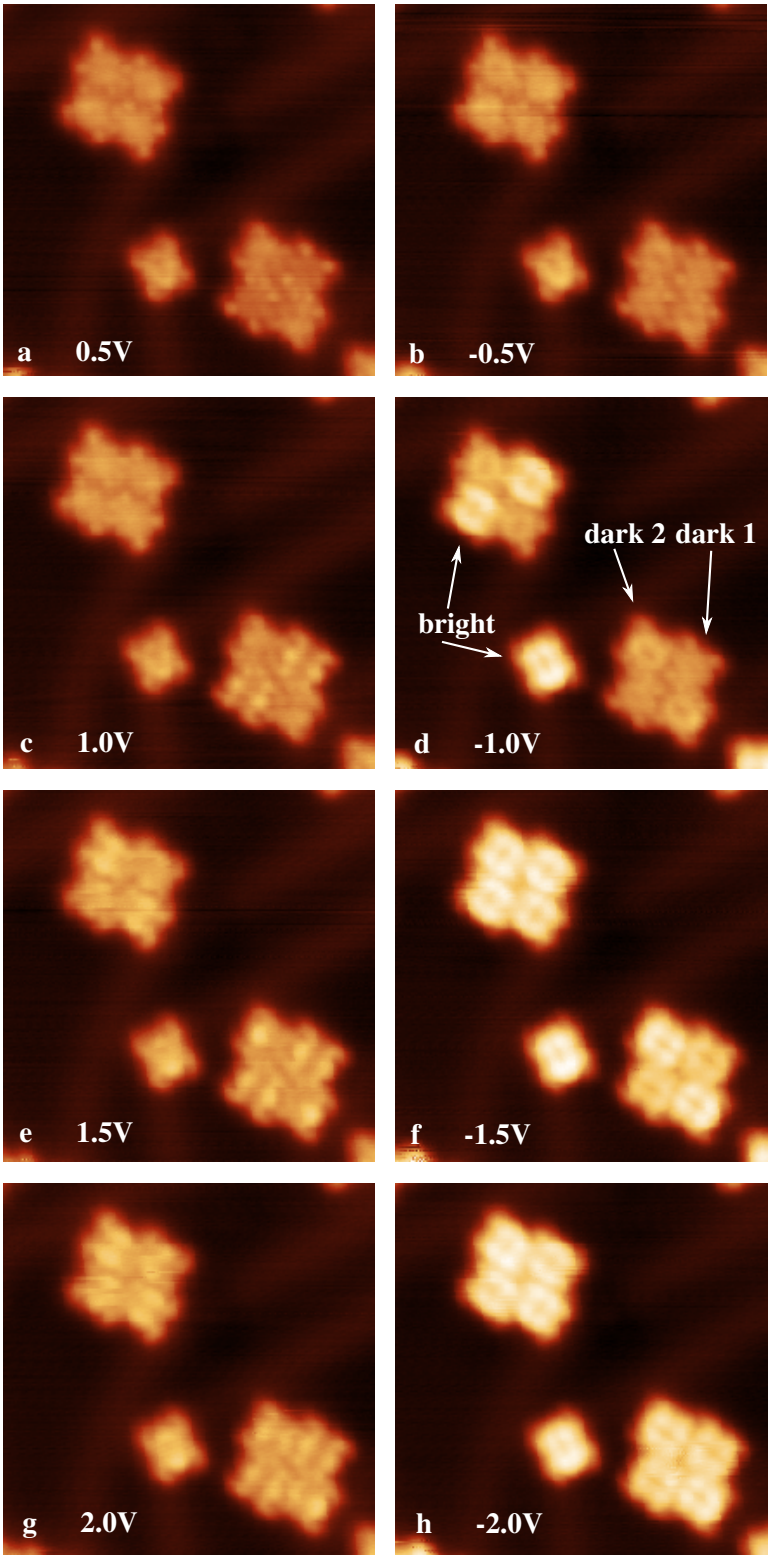

Figure 4.5.: Bias dependence of the TPP STM images at low temperature. The tip voltages are given in the images, the other image parameters are: $11.4 \times 11.4\ nm^2$, $I = 0.44\ nA$, $T = 5\ K$.

to two tautomers of the same molecular state.

A large part of this work is dedicated to the switching of the TPP molecules on Au(111), but as the clear distinction between the two dark states is very difficult to achieve, in the analysis they will be simplified in the following to only one dark state, unless stated otherwise. Variations in the sample

T	Arrangement	Bright TPP molecules
5 *K*	single molecules	none
80 *K*	clusters	few on herringbone elbows
90 *K*	clusters and small ordered islands	at elbows only
130 *K*	large ordered islands	at elbows, in islands

Table 4.1.: Summary of the temperature dependence as presented in Fig. 4.6. The observations from 78 *K* and 80 *K* were summarized under 80 *K*, as they are similar and the differences most probably stem from the slightly different coverages.

temperature during preparation can yield interesting facts about the thermal processes playing a role for this system. In Fig. 4.6, STM images of TPP on Au(111) are shown after preparation at different sample temperatures. (a) shows the surface after depositing the molecules at 5 *K* sample temperature by evaporating them directly into the STM. The molecules are found single on the terrace, they do not even form clusters yet, indicating that at this temperature no diffusion takes place. Furthermore there are no bright molecules on the surface, showing that creating the bright state also requires thermal energy. The same surface has been heated at 80 *K* for 10 *min* and then cooled to 5 *K* before taking (b) and (c). The molecules started to form small disordered molecular clusters, but not enough diffusion has taken place yet to allow them to build ordered islands. The number of bright TPP molecules is still very small, only few could be found.

In (d), the molecules were evaporated into the STM filled with liquid nitrogen, having a temperature of about 78 *K*. At this temperature the molecules cannot form ordered islands yet, but they arrange into elongated clusters, guided by the reconstruction lines. Some bright molecules can be found, but they are exclusively situated on the elbow sites of the reconstruction. The difference between the images (c) and (d) is surprising, as they had been up to almost the same temperature. Two explanations are possible: Either the annealing time of 10 *min* in (b) and (c), which is much shorter then the several hours image (d) stayed at 78 *K*, were too short to completely establish equilibrium conditions, or the slightly different coverages of the two preparations (0.31 monolayers (*ML*) in (a) vs. 0.41 *ML* in (e)) lead to different equilibrium configurations. As the molecular self assembly times are usually much shorter than minutes, the latter possibility appears to be the more likely one.

After heating up the same surface at 90 *K* (e), small ordered islands have formed and the number of bright molecules is growing, still being situated only at the elbow sites. After the next heating step at 130 *K* in (f), the island size significantly increased, the bright molecules are still predominantly on the elbows, but the first ones can also be found inside the islands. The previously described temperature dependence is summed up in table 4.1.

The temperature dependence clearly shows that the dark state is the more stable, i.e. energetically favored, state and that the bright state can only be created by thermal activation on the surface. Furthermore, the diffusion is quenched at 5 *K* (which is in agreement with the capability of taking stable STM images at this temperature) and even the kinetic energy the molecules have when being evaporated into the STM is not sufficient to overcome the diffusion barrier on the surface, before the molecules are cooled down. At around 80 *K*, the molecules are capable of diffusing to a close potential minimum, leading to the formation of disordered clusters. In these clusters, the molecules are bound

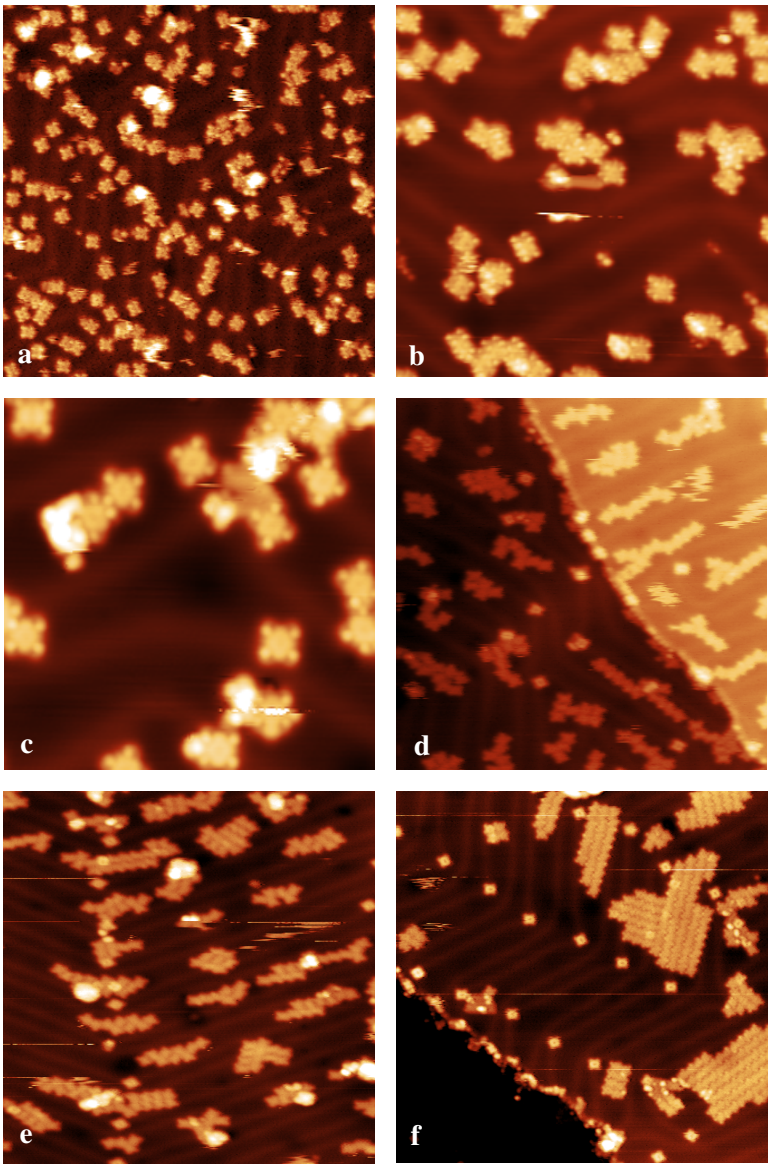

Figure 4.6.: Temperature dependence of the TPP/Au(111) preparation. (a) Surface after deposition at 5 K, (b) and (c) the same surface after annealing at 80 K for 10 min. (d) Surface after deposition at 78 K, (e) and (f) the same surface after annealing at 90 K for 1 h and 130 K for 25 min, respectively. Image parameters: (a) ($42.7 \times 42.7\ nm^2$, $U_{tip} = -1\ V$, $I = 2.0\ pA$, $T = 5\ K$), (b) ($25.1 \times 25.1\ nm^2$, $U_{tip} = -1\ V$, $I = 50\ pA$, $T = 5.2\ K$), (c) ($13.6 \times 13.6\ nm^2$, $U_{tip} = -1\ V$, $I = 0.52\ nA$, $T = 5.7\ K$), (d) ($49.7 \times 49.7\ nm^2$, $U_{tip} = -1\ V$, $I = 2.9\ pA$, $T = 77.8\ K$), (e) ($70.6 \times 70.6\ nm^2$, $U_{tip} = -0.87\ V$, $I = 4.4\ pA$, $T = 78.4\ K$), (f) ($54.7 \times 54.7\ nm^2$, $U_{tip} = -1\ V$, $I = 3.3\ pA$, $T = 82.0\ K$)

by sufficient strength, permitting stable imaging at these temperatures. At 130 K, sufficient energy is present, allowing the molecules to find their energetically favored arrangement in ordered islands.

4.4.2. Molecular assembly

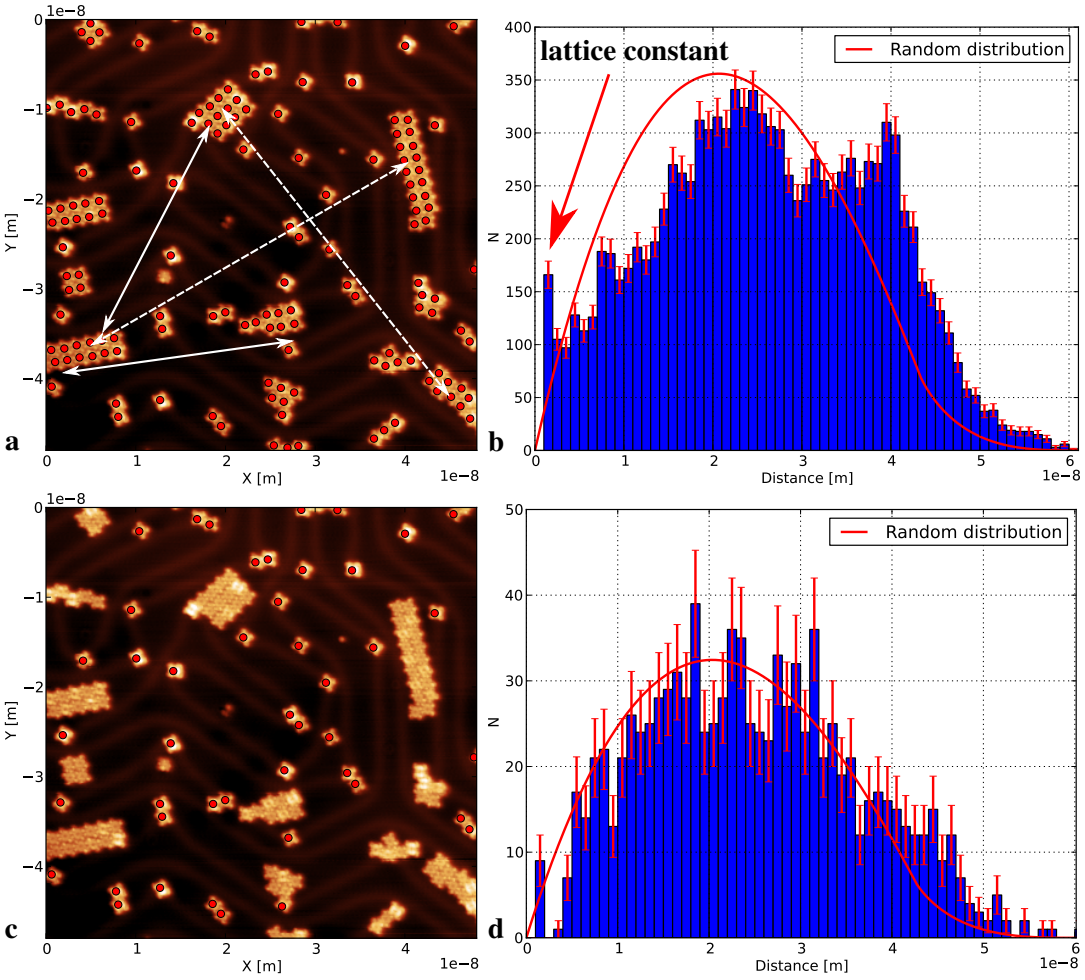

Figure 4.7.: Distances between the molecules in the STM image shown in Fig. 4.4. (a) and (c) show the selected molecules in the STM image, (b) and (d) the respective distance histograms, where the errorbars correspond to the $\sqrt{N}$ counting errors. For comparison, the expected random distribution from [60] (chapter 3.6.5) is plotted as a red line. The solid arrows in (a) have a length of 25 *nm* and the broken ones 40 *nm*.

To understand in detail the assembly of the TPP molecules on the Au(111) surface, it is instructive to look at Fig. 4.7, where the STM image from Fig. 4.4 is used to measure the distances between the molecules. In Fig. 4.7 (a), the centers of all molecules are marked with a red dot, all possible distances between them are measured and shown as a histogram in (b). For comparison, the expected distance distribution for random points in a square (chapter 3.6.5) is plotted as a red curve. There is a pronounced difference between the histogram and the random distribution, which is the result of the existence of the close-packed molecular islands. Several features can be assigned: The strong bin

between 1 *nm* and 2 *nm* corresponds to the lattice constant in the islands and the two other peaks at around 25 *nm* and 40 *nm* have their origin in the distances between the islands. To demonstrate this, there are solid arrows in (a) with a length of 25 *nm* and broken ones with 40 *nm*. Both of these distances can be found several times between the islands which have, due to the high number of molecules within them, a high statistical weight in the distance distribution and therefore dominate the histogram.

If the same analysis is performed excluding the molecules in ordered islands (Fig. 4.7(c) and (d)), the distance histogram and the random distribution agree quite well, which shows that the single molecules are randomly distributed.

Obviously, there is a short range force acting between the molecules (presumably VdW force), which holds them together in the close-packed islands. By this analysis it could be shown that because the molecules outside the islands assemble in a random fashion, there are no long-range forces acting between them, neither attractive nor repulsive, which could potentially point to charge transfer between molecules and sample, leading to electrostatic repulsion.

4.4.3. Spectroscopy

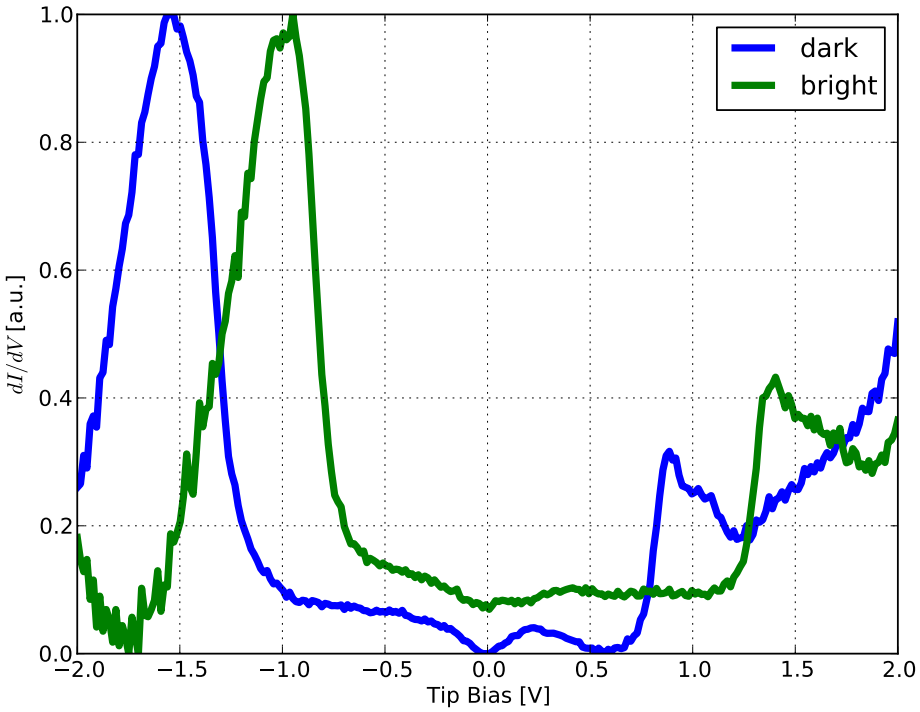

Figure 4.8.: dI/dV spectra of TPP on Au(111) at 5 K, measured at the molecular center. The spectra have been scaled such that the maximum intensities are equal. The modulation frequency is 710 Hz with an amplitude of 20 mV. The bright spectrum was measured over a single molecule, whereas the dark spectrum is an average over several molecules.

By performing dI/dV spectroscopy, the local density of states (LDOS) of the molecule/substrate system can be probed around the Fermi level (chapter 2.2). Typical spectra of bright and dark TPP

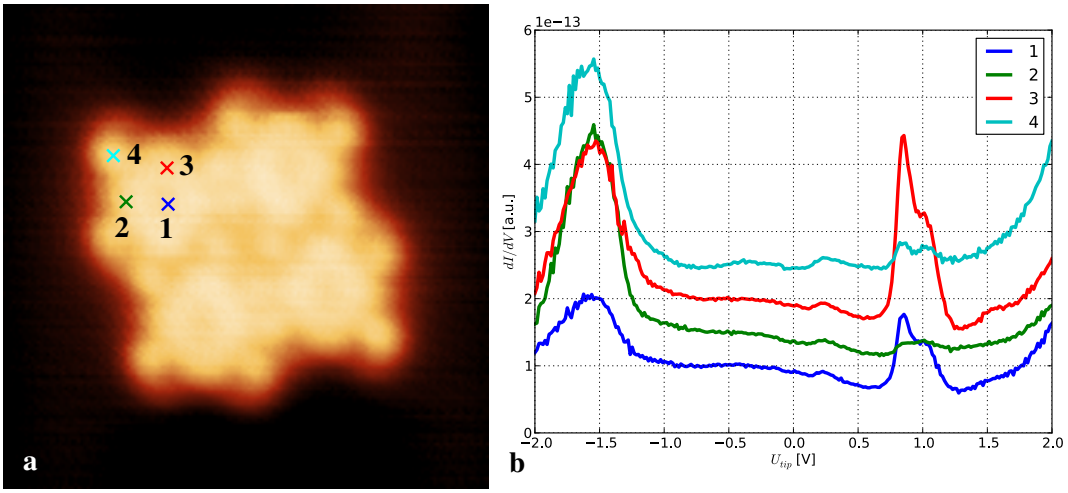

Figure 4.9.: dI/dV spectra of a dark TPP molecule on Au(111) taken over different parts of the molecule. The spectra were recorded with 20 mV modulation amplitude at 710 Hz, at every position five sweeps were averaged to the final spectrum and slightly offset in the plot for clarity. The positions of the spectra in (b) are marked in the image (a). Image parameters in (a): $5.5 \times 5.5\ nm^2$, $U_{tip} = -1\ V$, $I = 0.37\ nA$, $T = 5\ K$.

molecules can be found in Fig. 4.8. As the spectra are plotted as a function of the tip voltage with the sample being on the ground potential, negative voltages correspond to unoccupied, positive voltages to the occupied states.

The spectrum of the dark molecules has the LUMO at $-1.5\ V$ and the HOMO at $0.8\ V$ with respect to the Fermi level. On the other hand, the bright molecules have the LUMO at $-1.0\ V$ and the HOMO at $1.3\ V$. An important observation is that the spectrum of the bright molecules has almost exactly the same shape, but it appears to be shifted entirely by $0.5\ eV$ towards the occupied states. Now it is possible to understand the contrast between dark and bright molecules in bias dependent imaging (Fig. 4.5), where the best contrast between the two is found for a tip voltage of $-1\ V$. At this voltage, the LUMO of the bright molecules is already in the energy range of the tunneling electrons, whereas the LUMO of the dark molecules is not. Outside the voltage region between the two LUMOs, the two states are almost impossible to distinguish.

Fig 4.9 shows dI/dV spectra which were recorded over different parts of a dark molecule. One spectrum was recorded over the center, two over the porphyrin ring and one over the phenyl leg. All spectra show the positions of HOMO and LUMO at the same energies, but they have different intensities depending on their position within the molecule.

The most interesting observation is obviously the rigid shift between the spectra of dark and bright molecules. The easiest explanation for such a behavior would be a charging of the molecules due to charge transfer with the surface as observed in [95, 96]. In the present case, however, charging does not seem to be an explanation because of two reasons: No long-range repulsion could be found in chapter 4.4.2 and second, although HOMO and LUMO are shifted with respect to the Fermi level, they do not cross it, which would be a requirement for charging. As will be shown in chapter 4.8.1, the shift can perfectly be reproduced by density functional theory (DFT) calculations when assuming the presence of a gold adatom underneath the bright molecules.

4.4.4. Heated TPP

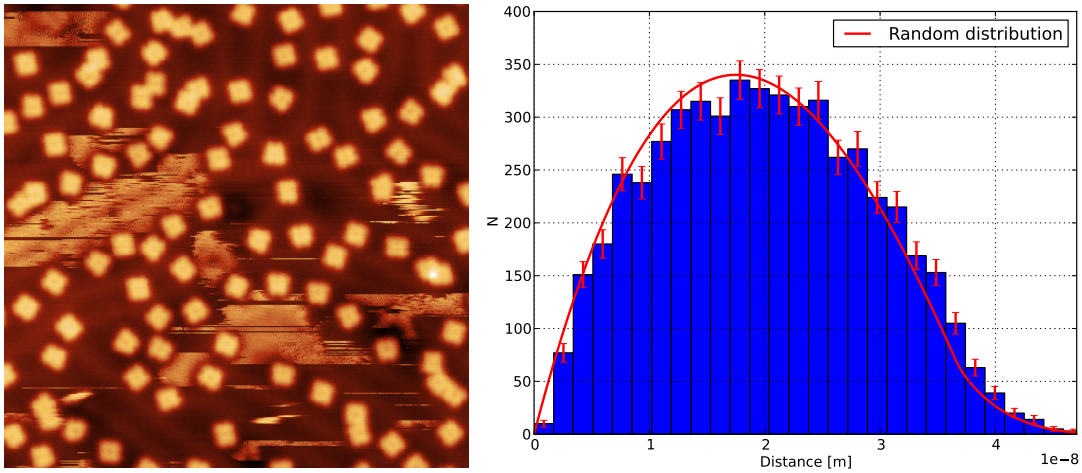

Figure 4.10.: TPP molecules on Au(111) after heating to 360°C for 5min ($36.6 \times 36.6\ nm^2$, $U_{tip} = -1\ V$, $I = 0.4\ nA$, $T = 5\ K$). The histogram shows the distribution of distances between the molecules in the image and the expected distance distribution for a random pattern (red line) as described in chapter 3.6.5. The error bars represent the $\sqrt{N}$ counting errors.

The appearance and behavior of the TPP molecules changes drastically upon annealing of the Au(111) surface to more than 360°C (Fig. 4.10). Bias dependent images of the annealed molecules can be found in Fig. 4.11. Apparently there are no dark and bright molecules any more, all molecules have the same apparent height at all bias voltages. In comparison with the TPP molecules before the annealing (Fig. 4.5) much less internal structure can be seen and the apparent height is almost constant over the covered bias voltage range. Furthermore, the shape of the molecules are not the same any more: Some have a rectangular shape, others are trapezoidal and some appear to be rectangular but with one elongated corner. These forms are marked in Fig. 4.11 (a) with the numbers 1,2 and 3, respectively.

However, the most striking difference to not annealed TPP molecules is that they do not form close-packed islands any more. In order to understand the change in interaction of the molecules better, the distances between all the molecules in Fig. 4.10 were measured and drawn as a histogram. As a comparison, the expected distribution for randomly distributed molecules (chapter 3.6.5) is shown in the same diagram as a red line and there is obviously a good agreement between the two, which means that the molecules are randomly distributed. Attractive short-range van der Waals forces are always present between molecules, which usually lead to the formation of close-packed islands (as in Fig. 4.7 (a) and (b)). As no island formation is observed, there needs to be a short-range repulsive force acting between the molecules. Possibly the molecules are charged and repel each other due to electrostatic interaction, similar to the one dimensional case presented in [95]. A possible explanation for the changed appearance will be given in chapter 4.8.2.

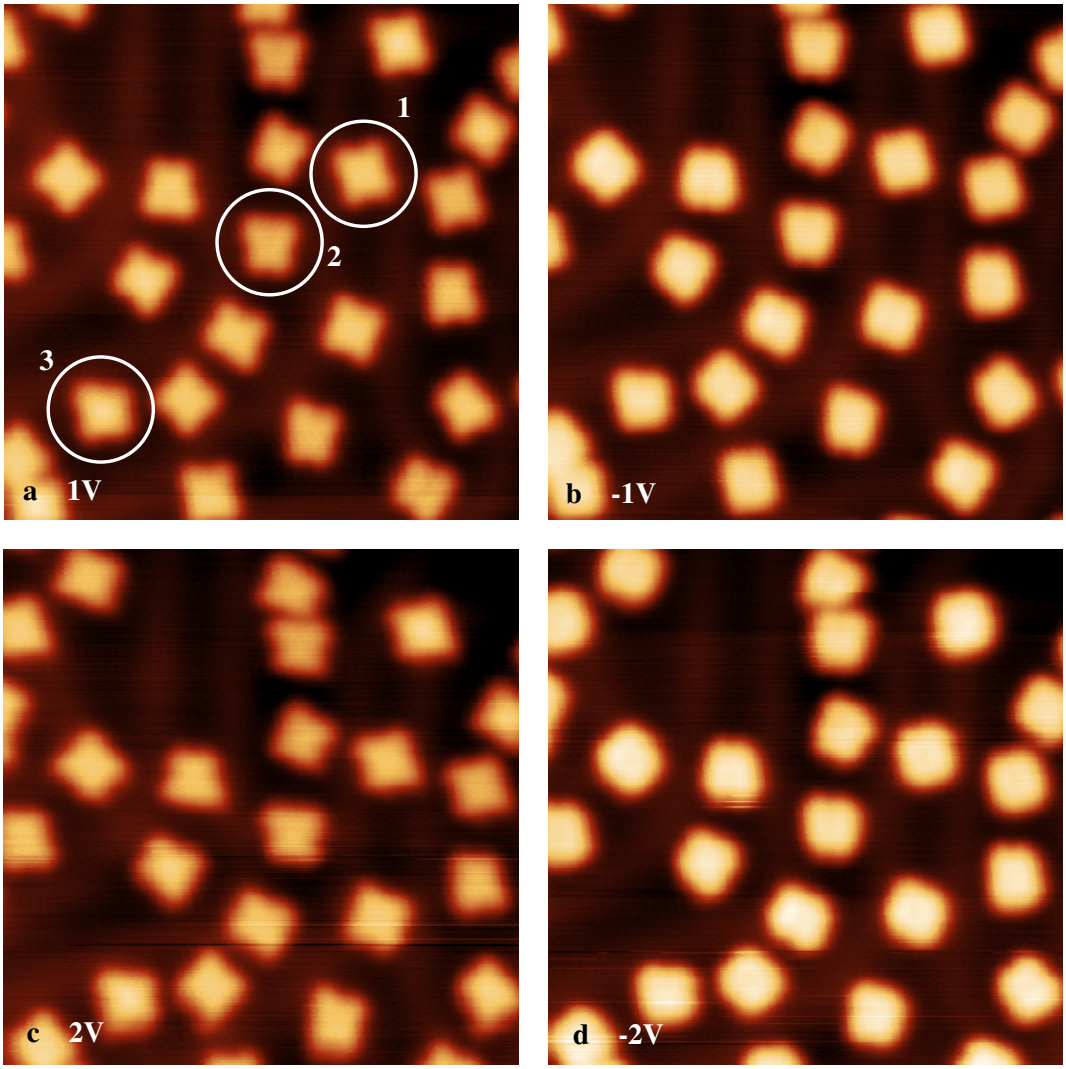

Figure 4.11.: Bias dependent imaging of TPP on Au(111) after heating to 360°C for 5min. In (a) the different possible shapes of molecules are marked with 1: rectangular, 2: trapezoidal and 3: rectangular with one elongated corner. The tip voltages are given in the images, the other imaging parameters are: $17 \times 17\ nm^2$, $I = 0.37\ nA$, $T = 5\ K$

4.5. Room temperature measurements

In chapter 4.4 it was demonstrated that TPP molecules adopt two distinct states on Au(111), which can be distinguished in STM measurements. In this chapter, it will be shown that switching between these two states can be induced thermally and it is tried to understand the switching process. Compared to tip-induced switching, which will be investigated in chapter 4.6, thermal activation addresses all molecules on the surface and therefore leads to a high number of switching events. Hence, it quickly yields significant statistics, which can then be exploited to look for cooperative effects within the molecular layer.

All measurements in this chapter were done with Br_4TPP molecules (Fig. 4.2). The presence of the four bromine atoms does not suppress their ability to switch and they have the additional possibility of forming covalent networks upon heating [10].

4.5.1. Imaging at room temperature

When imaging physisorbed, i.e. weakly bonded, molecules at room temperature, rapid diffusion of the molecules is observed, which can be so fast that the molecules become invisible to STM. Consequently, investigation of single isolated molecules is impossible at room temperature. The most convenient way of preventing the molecules from diffusing without changing their structure is to fill up the whole surface with molecules, i.e. to evaporate exactly one monolayer, which forces the molecules to assemble in large, close-packed islands, leaving no space for diffusion.

In order to learn something about the kinetic properties of the switching process, the temporal evolution of the molecular state needs to be investigated. This can either be achieved by fixing the tip above one molecule and looking at the change of the tunneling current over time, or by recording images of the same surface area over and over again to obtain a movie of the surface development. Both methods have their advantages and disadvantages: While fixing the tip above one molecule, a high time resolution in the *ms* range can be achieved, but the state of the surrounding molecules is unknown. When recording series of images, the opposite is the case: the time resolution is not as good (about 8 *s* per frame at fastest), but the state of all molecules is known, which permits looking for cooperative effects. Due to the desire to study cooperativity and to limitations in the STM electronic, recording series of images has been used exclusively.

It is important to note that the time resolution of these movies must be at least comparable to the time constants of the observed processes because otherwise, no significant results can be obtained. The typical time resolution, achievable with a SPECS Århus STM, is about 8s for an image of $20 \times 20\ nm^2$ with sufficient image quality. This speed is apparently sufficient because, as will be explained in chapter 4.5.3, even on rather slow images (108 *s* per frame), the molecules can be imaged clearly in unperturbed regions. Only in the vicinity of defects where the switching rates is largely enhanced, the molecules appear fuzzy.

4.5.2. Molecular appearance at RT

Bias dependent images of a monolayer of Br_4TPP on Au(111) at room temperature can be found in Fig. 4.12. They look slightly different than TPP (compared with Fig. 4.5 at low temperature): Dark and bright molecules can be clearly distinguished and there are still three states observed, which means that the ability to switch is not lost upon attachment of the four Br atoms. However, in comparison to TPP where two of the states appeared dark, Br_4TPP molecules have two bright and one dark state. Similar to TPP, the best contrast is observed at about $+1\ V$ sample voltage (which corresponds to $U_{tip} = -1\ V$

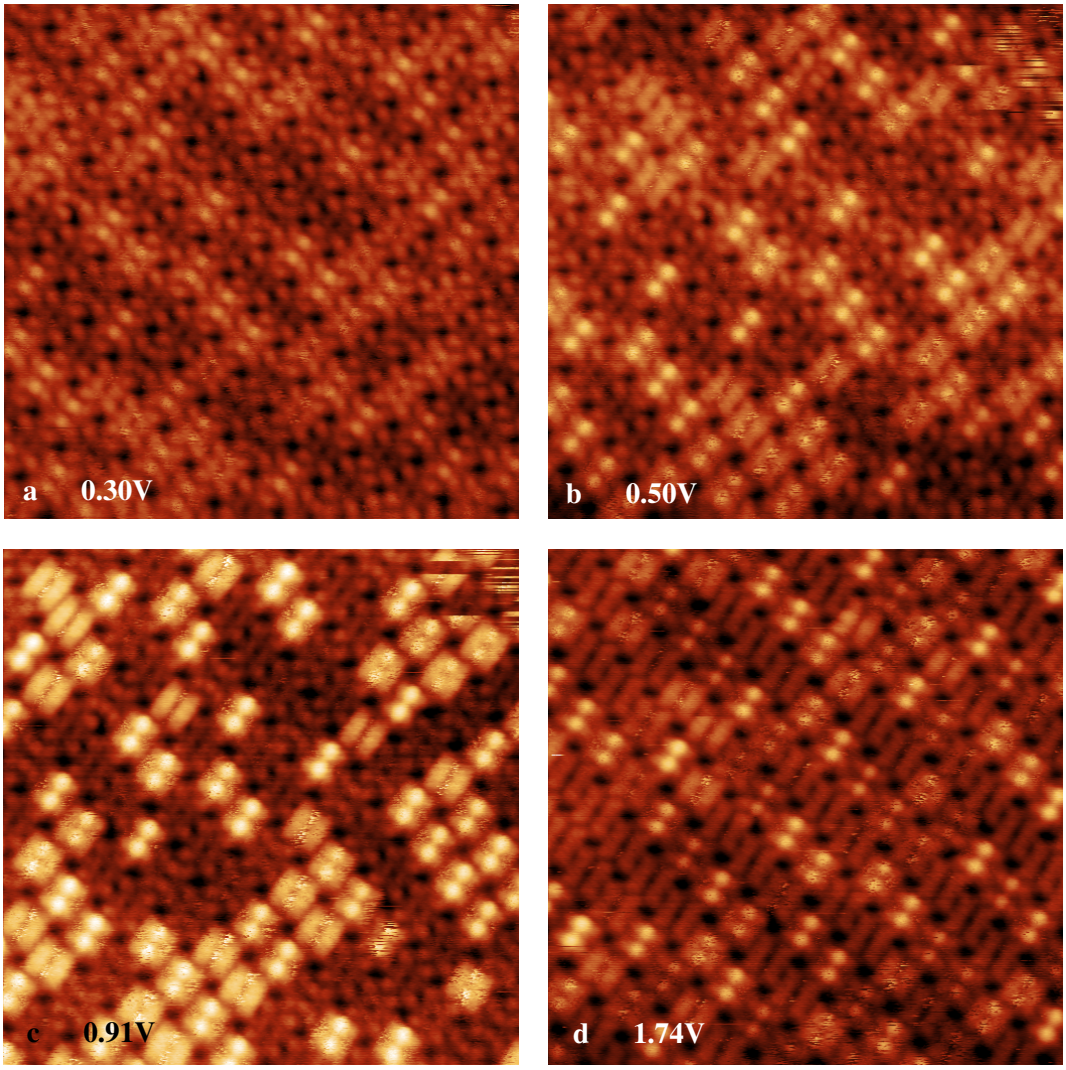

Figure 4.12.: Bias dependent imaging of Br_4TPP on Au(111) at room temperature. Due to thermal drift, the images do not show exactly the same area. The sample voltages are given in the images, the other imaging parameters are: $18.8 \times 18.8\ nm^2$, $I = 0.1\ nA$, $T = 300\ K$

in the low temperature STM). This is another indication that the origin of the dark and bright state is the same as in the case of TPP.

Fig 4.12 (c) clearly shows that there are actually two bright molecular states, which can only be distinguished in a limited voltage range. As it is very difficult to obtain such high image quality in room temperature STM and keep it unchanged over the full duration of a movie (several hours), both bright states are treated as one.

When the same area of the sample is imaged at room temperature over and over again, thermal switching of the molecules can be observed. This evolution of the surface will be studied in the following sections in greater detail.

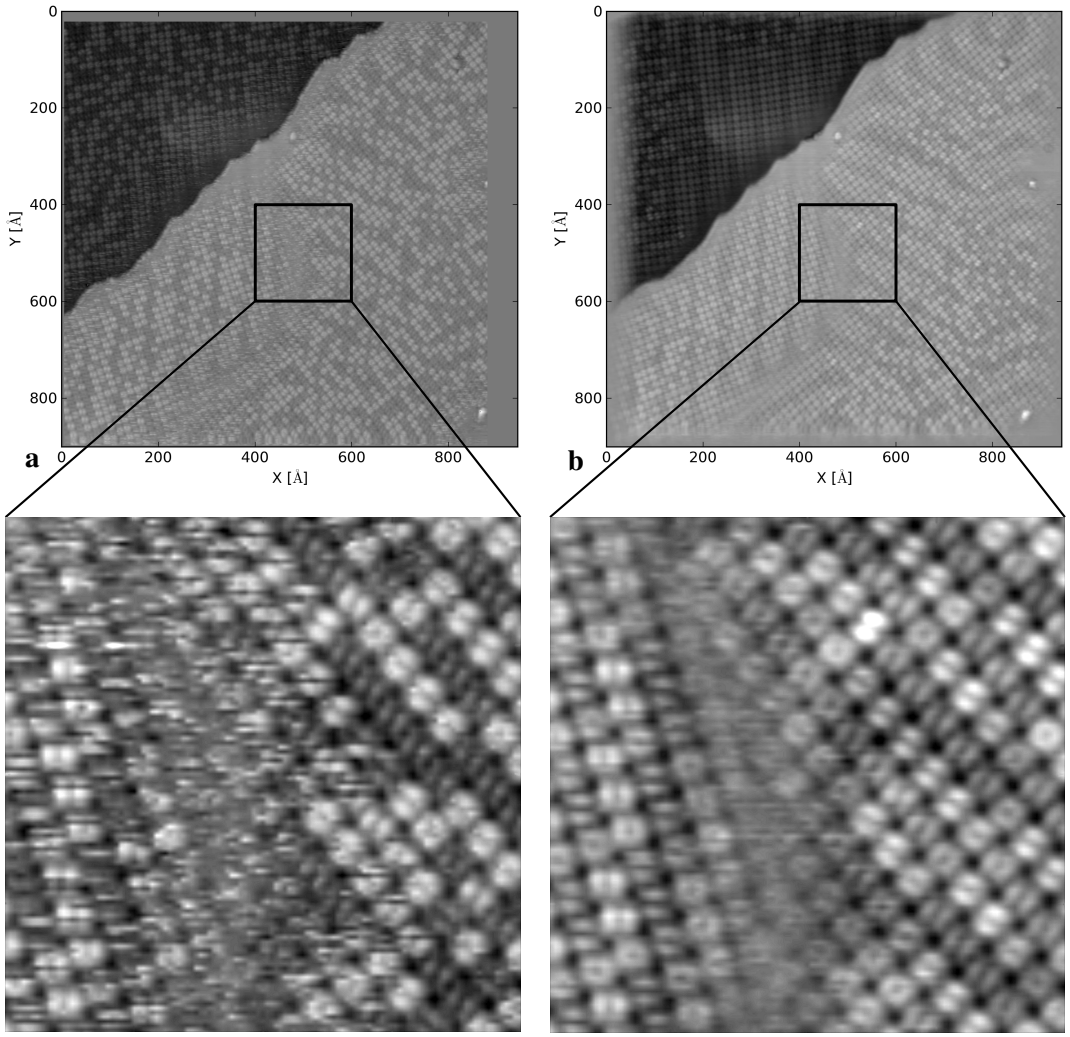

Figure 4.13.: Influence of defects as step edges, domain boundaries and point defects on the switching speed: (a) single frame from a movie with 108 s/frame, rapid switching close to defects can be seen, (b) average of all frames of this movie, clearly showing that diffusion cannot be responsible for the fuzzy appearance. $U_{sample} = 1.25\ V$, $I = 0.13\ nA$, $T = 300\ K$

4.5.3. Influence of defects

When looking at the surface at a larger scale (Fig. 4.13 (a)), where defects like step edges, domain boundaries and point defects perturb the regular arrangement of the molecular lattice, it becomes already clear from a single image that the switching properties of the molecules change drastically in the vicinity of these defects. In these regions the molecules are switching so fast, that they change their state even in the short time the tip is above them and therefore appear fuzzy. However, when inspecting (b) where all the frames of the movie have been averaged together, taking into account the relative thermal drift between the images (as described in section 3.6.2), the molecules can be seen clearly again, especially in the region of the domain boundary, unambiguously showing that this effect cannot be due to rapid molecular diffusion.

Before it is possible to understand the origin of the increased switching rates close to the defects,

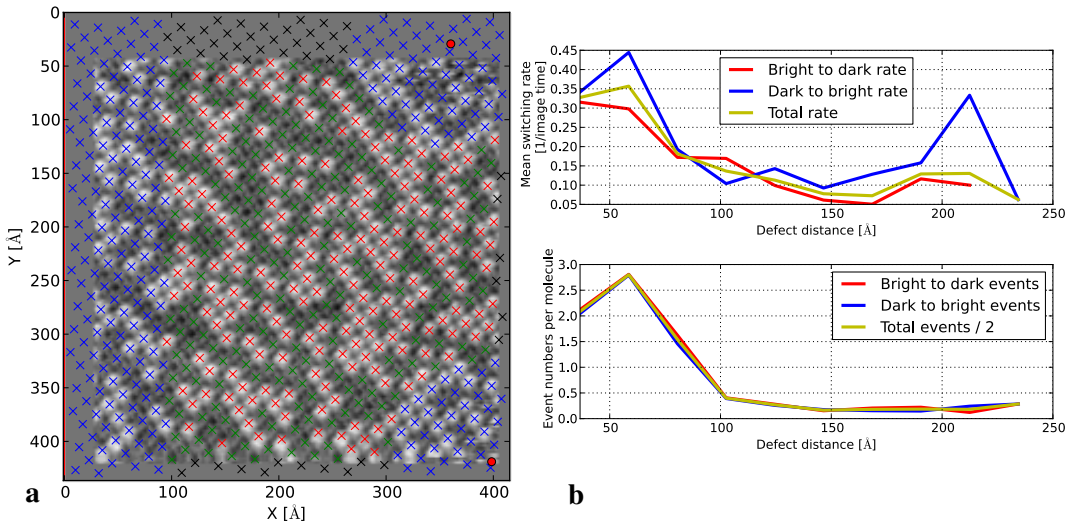

Figure 4.14.: Influence range of defects. (a) One frame of a movie $U_{sample} = 0.884\ V$, $I = 0.14\ nA$, $T = 300\ K$ with crosses indicating the positions of the molecules (green: dark molecules, red: bright molecules, black: molecules outside of the current frame, blue: molecules inside influence range of defects), red dots and lines indicate defect sites. In (b) the averaged switching rates and the number of switching events are shown as a function of the distance to the nearest defect. The influence range of the defect is about 9.5 *nm*, which corresponds in the islands to the distance of six molecules.

it is necessary to understand the normal switching rate in the unperturbed molecular island, which raises the question of how far from a defect the unperturbed surface starts. To answer this question, two quantities were calculated as a function of the distance to the closest defect: The switching rate was calculated by averaging the dwell times (as in equation 3.8 from chapter 3.6.4) and the average number of switching events per molecule in the entire movie was calculated, which is also a measure that correlates with the switching rate. A typical scenario can be found in Fig 4.14. In the upper panel of (b), the distance dependent switching rate is shown and the average event numbers in the lower panel. Especially from the lower panel it becomes clear that the unperturbed island starts at about 9.5 *nm* distance from the defects, which corresponds to six molecules inside the perfectly ordered island.

It is important to keep in mind that the quantities calculated in Fig. 4.14 (b) cannot yield any kinetic data like switching rates because of several reasons:

- As was demonstrated in Fig. 4.13, the time resolution is not sufficient close to the defects: Due to their high switching rate the molecules are only imaged as streaks. Therefore, it is expected that a significant amount of switching events is not captured due to the low time resolution.

- In chapter 3.6.4 it was explained that averaging the dwell times only yields a meaningful switching rate if the dwell times are exponentially distributed, which could not be checked in the vicinity of defects, due to the low number of molecules in the respective distance bins, leading to poor statistics.

- It is demonstrated in chapter 4.5.5 that the time dependence of the unperturbed layer cannot be understood with simple switching rates. Therefore, assuming that switching rates are a meaningful quantity in the vicinity of defects has no justification.

For the reasons given above, Fig. 4.14 (b) should be seen rather as a measure of the defect distance dependent "switching speed" without connection to kinetic parameters, which can nevertheless be used to determine the influence range of defects in the ordered molecular layer.

On average, the unperturbed monolayer starts after 7 ± 2 molecular lattice constants, which is a surprisingly large distance.

Maybe the origin of this effect is a slightly larger distance between the molecules close to the defects compared to the unperturbed island or a broken symmetry due to the presence of the defect. However, a convincing explanation for this behavior could not be found within this thesis, but all the following evaluations were done only on the parts of the surface which were considered unperturbed in the sense explained above.

4.5.4. Ordered patterns

Molecular islands of Br_4TPP molecules on Au(111) at room temperature show a distribution of dark and bright molecules, as in Fig. 4.15 (a). There is no apparent order in this pattern visible in the STM images. To statistically substantiate this observation and to find out whether the state of one molecule has an influence on the state of his neighbors, the two statistical tests described in chapter 3.6.3 were applied to the observed distribution of dark and the bright molecules.

Fig. 4.15 (b) shows the distribution of bright molecules within all possible patches of three by three molecules of image (a) compared to a binomial distribution with the parameter $p = 0.16$. This value is just the ratio of bright molecules in (a), where 16% of the molecules are bright and 84% are dark. The measured and the theoretical distribution agree quite well, the P-value (chapter 3.6.7) is 0.21, signifying that there is no significant deviation from the random distribution.

The SRO parameter α, calculated for both cases, once with the reference molecule dark and once bright, can be found in Fig. 4.15 for lattice vectors up to $(\pm 2, \pm 2)$. As a correlation would manifest itself as a deviation from zero (chapter 3.6.3) and the only clear difference from zero is found at the $(0,0)$ position, there seems to be no correlation between the state of one molecule and the state of its neighbors.

Of course, for every movie under consideration, these results look slightly different. Nevertheless, no significant correlation could be found. Apparently there is no influence of the state of one molecule on the state of its neighbors.

4.5.5. Time dependence of the switching

The thermal evolution of a system over time is described by its rate constants [97]. Estimation of the rate constants involved in the switching process of the porphyrin molecules is attempted in this chapter.

As was already explained in chapter 3.6.4, the time constants are estimated from the histogram of the dwell times. Fig. 4.16 (a) and (c) show such histograms together with a fitted exponential function shown as a green curve. Another exponential function has been fitted to the same data but excluding the first three bins and is displayed as a red curve. The respective fitting parameters can be found in the legends.

Obviously the red and green curves disagree quite substantially both, in their k values and their amplitudes. This observation clearly shows that a single exponential is not sufficient to explain the observed dwell time distribution and that apparently several different processes (possibly one tip-induced and one thermal process) lead to a change between the dark and bright molecular state, each having its distinct time constant. The dwell time histograms can usually by fitted by a sum of two exponentials. However, fitting with even more exponential functions leads to ever better agreement

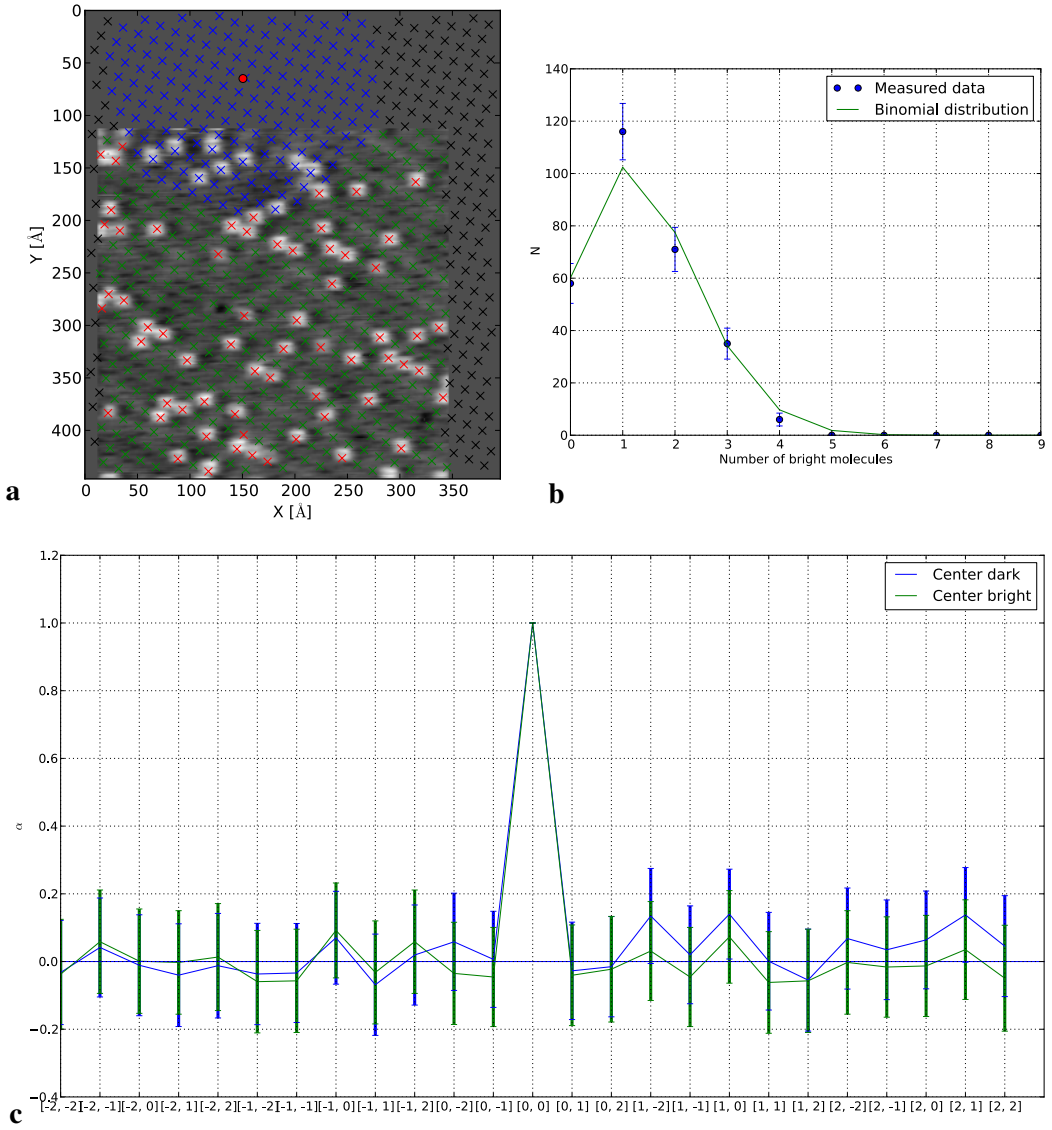

Figure 4.15.: Patterns of dark and bright molecules: (a) single frame from a movie with 13.2 s/frame, $U_{sample} = 1.3\ V$, $I = 40\ pA$, $T = 300\ K$. Red crosses are bright, green crosses dark molecules and molecules with blue crosses are excluded from the analysis because of their proximity to a defect. The dark border in the right and the upper part of the image are not imaged in this frame but due to the thermal drift in other frames of the movie. (b) shows the distribution of bright molecules in all three by three molecule patches in (a) compared to the binomial distribution with the parameter $p = 0.16$. (c) short range order parameter for lattice positions up to $(\pm 2, \pm 2)$.

between the data and the model due to the increasing number of free parameters, but the significance of the thereby estimated parameters is questionable.

To separate these processes in an assumption free way, i.e. without manually choosing the number of exponentials or other assumptions, the method developed by Zhou et al. [59] (chapter 3.6.4) was applied to the measured data. The distributions of k values $\rho(k)$ can be found in Fig. 4.16 (b) and (d).

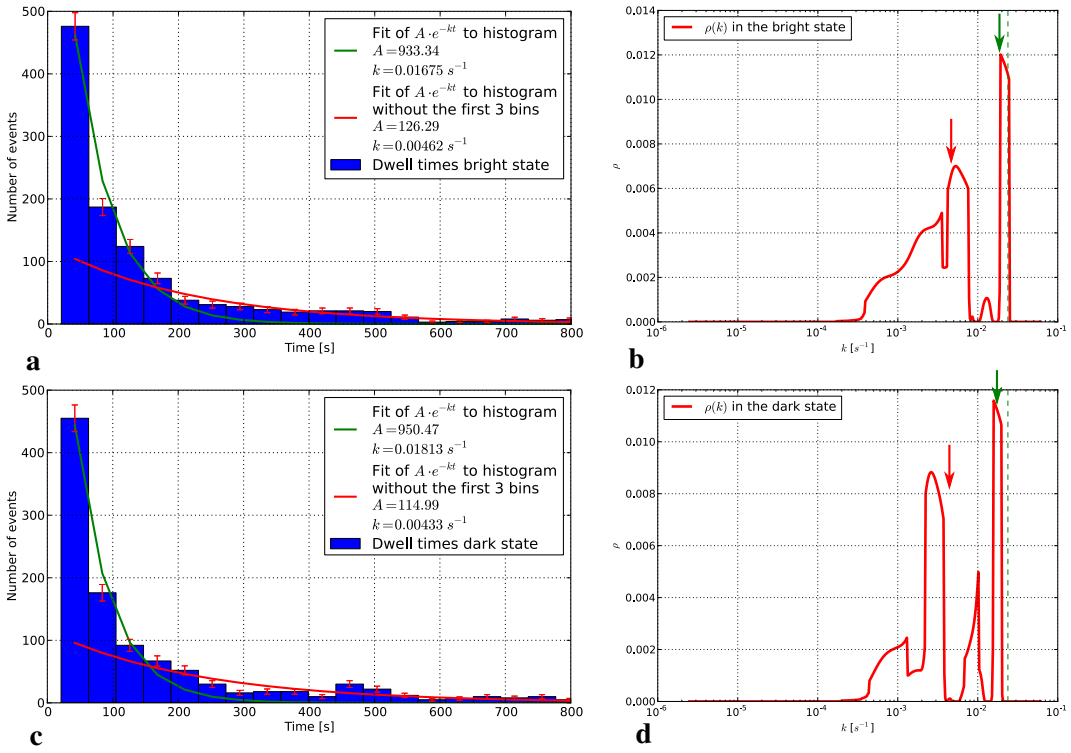

Figure 4.16.: Estimating the switching rates of Br_4TPP on Au(111). (a) and (c) show dwell time histograms from a movie with the following parameters: 42 s/frame, $U_{sample} = 302\ mV$, $I = 0.11\ nA$, $T = 300\ K$, the errorbars are the $\sqrt{N}$ counting errors. Each histogram has been fitted with an exponential function (green curves). A second exponential has been fitted to the same histogram excluding the first three bins (red curves). (b) and (d) show the respective reconstructions of the rate constant probabilities as described in chapter 3.6.4. The vertical green lines are at the position of the inverse frame duration and the positions of the k values obtained by fitting in (a) and (c) are marked with arrows in (b) and (d), respectively.

They obviously consist of several components, with the first strong ones corresponding to the k values obtained by fitting in (a) and (c) and are marked in the figure with colored arrows.

This method was applied to all movies with sufficient quality and the position and width as well as the total statistical weight of all the observed peaks were recorded. A likely explanation for the existence of several processes could be that there is thermal switching on one hand (maybe with different rate constants for different sites) and one or several tip induced process on the other hand. By plotting the observed k values as a function of the bias voltage or the tunneling current it should be possible to confirm such an idea, because the thermal process should have a constant rate, but the tip induced process should change its rate depending on the tunneling conditions. The complementary method of keeping the tunneling parameters fixed and changing the sample temperature could not be realized within this thesis due to experimental limitations of the used microscopes which is quite unfortunate because also the size of the switching barrier could not be estimated from an Arrhenius plot, which would require plotting the k values as a function of the inverse temperature [97].

Fig. 4.17 shows the dependence of the k values on the tunneling conditions for both switching directions. The k values are distributed over two orders of magnitude, but the data points scatter too

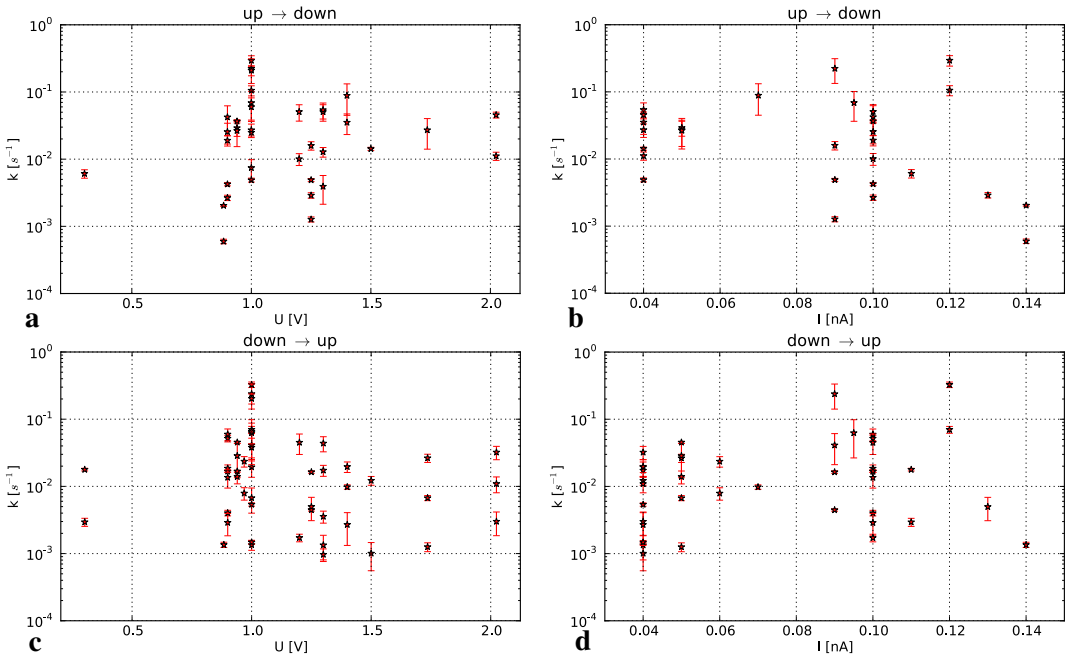

Figure 4.17.: k values estimated from all recorded movies with sufficient length and quality for both switching directions, plotted as a function of the tunneling voltage and current. The k values were estimated from the dwell time histograms using the method described in [59] (chapter 3.6.4).

much for drawing any clear conclusions about their dependence on the tunneling parameters.[1]

This result can potentially be understood by correlation effects in the molecular layer. As will be explained in the following chapter 4.5.6, if one molecule switches, another molecule in its vicinity might switch in the opposite direction with a high probability. Furthermore, in many movies it has been observed that over several frames, almost no switching activity can be observed (like in Fig. 4.19 (c)) and suddenly, a larger number of molecules switches between two frames (Fig. 4.19 (d)), to be followed by several more frames with very low activity. The existence of these cascade events, which will be analyzed in more detail in chapter 4.5.7, shows that the switching events cannot be regarded as independent.

Another interesting observation is that many molecules never change their state during a whole movie, whereas others change their state several times. In Fig. 4.18 an average image of a movie can be found, in which all non-switching molecules are marked with a red cross. In this particular case, 72 % of the molecules do not switch. However, when estimating an average switching constant using equation 3.8 and evolving the observed pattern of bright and dark molecules in the first frame using a random number generator with the estimated average switching constants, only 4 % of the molecules would be expected not to switch during the course of this movie. Apparently, the molecules also cannot be treated as equal.

When analyzing the spatial distribution of the non-switching molecules, no apparent reason for their static behavior can be found. There is no periodicity, which might point to a Moiré effect with respect to the underlying gold lattice (as in [39]), and it does not seem to depend on the herringbone

[1] It was also tried to fit the dwell time histograms with the sum of two exponentials, but the resulting k values also show no clear dependence on the tunneling parameters, just as in Fig. 4.17.

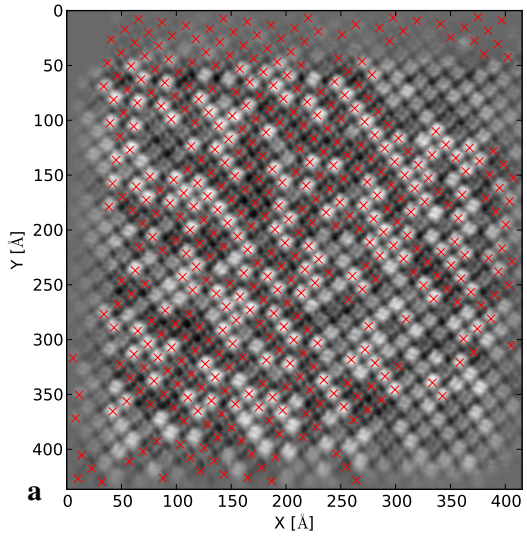

Figure 4.18.: Molecules which did not change during the entire movie (81 s/frame, $U_{sample} = 884\ mV$, $I = 0.14\ nA$, $T = 300\ K$) are marked with a red cross. In the presented case, 72 % of the molecules did not change their state but only 4 % would be expected, assuming that all molecules are equal and switch with the same average switching rate as the active ones.

reconstruction of the Au(111) surface either. Consequently, the reason for the observed changes in activity is unknown.

Now, after pointing out two effects of correlation between the molecules and showing that the molecules are apparently not equal, it appears unlikely that a simple time constant approach, which assumes uncorrelated behavior of all molecules could yield any sensible results.

4.5.6. Distribution of switching events

Although chapter 4.5.5 shows that not all molecules are equal, it was demonstrated in chapter 4.5.4 that there is no order in the pattern of dark and bright molecules. Independently, it is interesting to look at the spatial distribution of switching events, where correlated processes still might be found.

To make the switching events more visible to the human eye, difference movies were calculated as demonstrated in Fig. 4.19. From every frame of the movie, the preceding frame was subtracted, yielding values close to zero for unchanged molecules, a positive value for molecules switching from dark to bright (red in the colorscale of the figure) and a negative value for molecules switching from bright to dark (blue). When looking at these movies, there is obviously a lot of activity close to all the defects (as identified in Fig. 4.14), but in the unperturbed regions a completely different picture emerges: Most of the switching events are not isolated but very often an event from dark to bright and one in the opposite direction happen in close vicinity (blue and red areas next to each other).

To quantify this observation, the distances between switching events of opposite directions were measured (Fig. 4.20 (b)) and compared to the corresponding random distribution (chapter 3.6.5). Obviously, the measured and the random distribution disagree. There is a strong preference for close switching events of opposite direction, which reflects the observation made by eye on the difference movies (Fig. 4.19). The molecules behave as if the state of one molecule could be transfered to a neighboring one, which is an interesting observation. This kind of hopping is compatible with the presence and the motion of gold adatoms underneath the molecular layer which, when underneath the

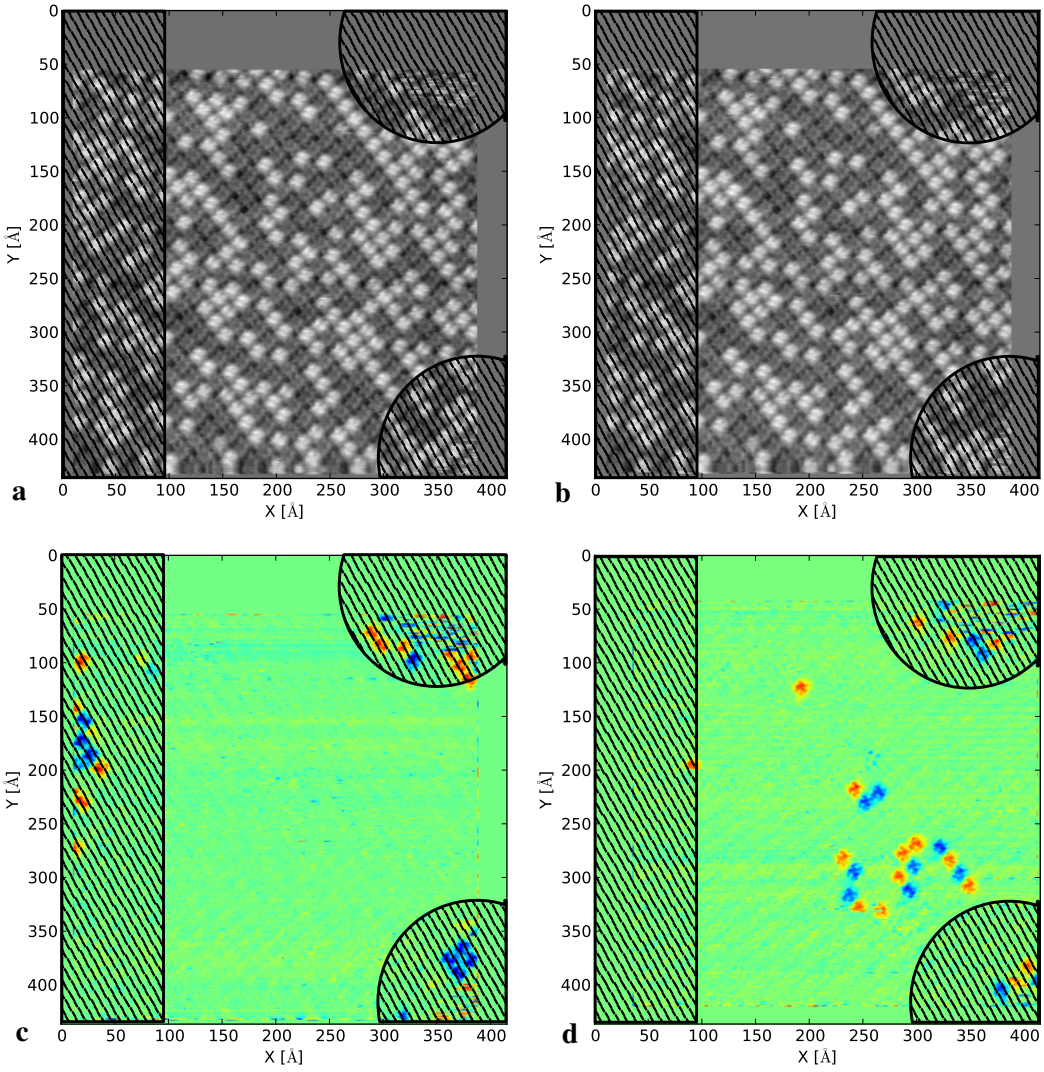

Figure 4.19.: Creating difference movies: (a) and (b) are two subsequent STM images taken from a movie with 81 s/frame, $U_{sample} = 884\ mV$, $I = 0.14\ nA$, $T = 300\ K$. (c) is the difference (b) - (a). In this colorscale red means switching from dark to bright and blue switching from bright to dark. (d) another difference frame between other subsequent frames of the same movie but with a higher switching activity. The hatched areas are excluded from the analysis because of their proximity to defects.

molecule, make it appear bright (chapters 4.6 and 4.8).

As will be explained in chapter 4.5.7, cascade events are observed. This means that over several frames, a very low switching activity is measured (like in Fig. 4.19 (c)) but rarely, between two subsequent frames, many molecules switch next to each other (Fig. 4.19 (c)), which is called a cascade event. They can also be captured with a similar statistic (Fig. 4.20 (c) and (d)). In these graphs, the distances between switching events of the same direction are measured and compared to the same random distribution. Also in this case a preference for close events can be observed, which can be understood by the nature of a cascade, where many events happen in a certain sample region, whereas in others no events can be observed. Therefore, the switching events are not randomly distributed.

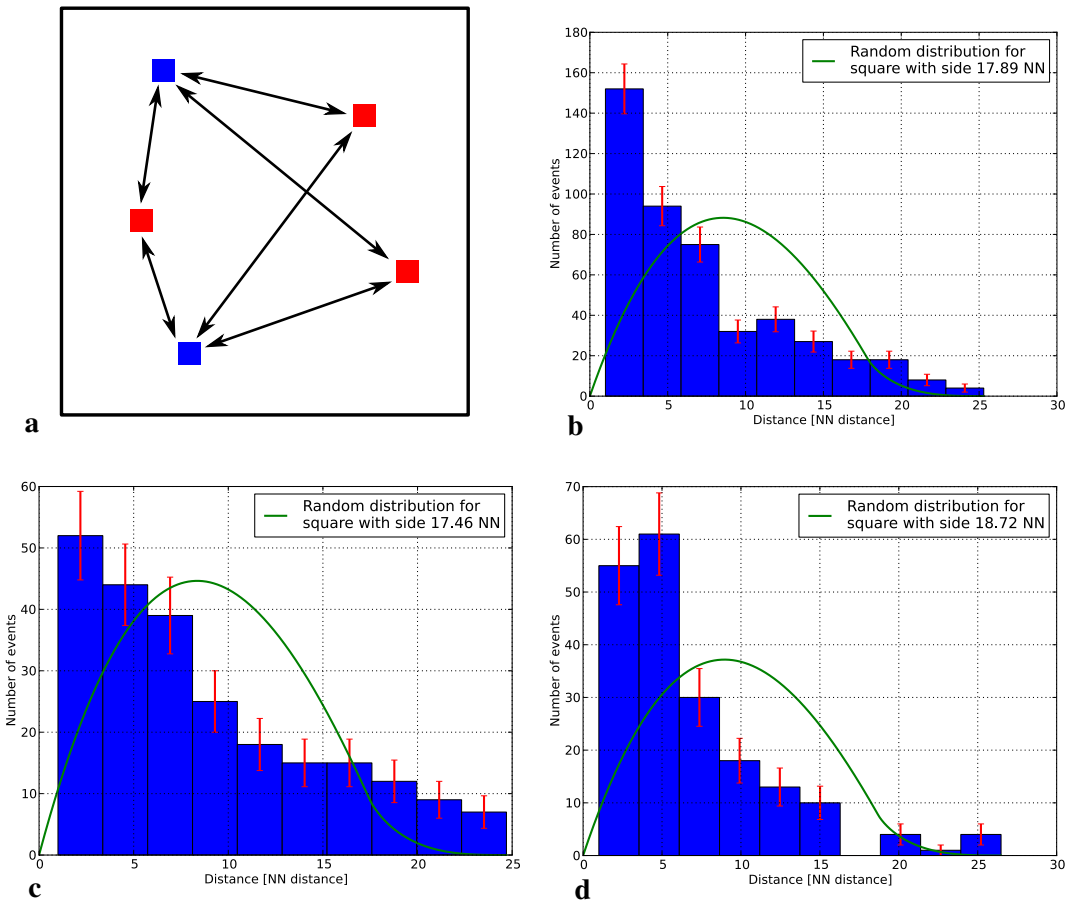

Figure 4.20.: Distance distribution between switching events for the movie of Fig. 4.19. (a) Schematical drawing of a difference movie with the typical colorscale where red indicates switching from dark to bright and blue the other direction. The arrows indicate the distances measured for (b). (b) distance distribution between switching events of opposite direction compared to the random distribution. (c) and (d) show the distance distribution between down switching events and up switching events, respectively. The random distribution is explained in chapter 3.6.5 and [60]. In this figure, the errorbars indicate the $\sqrt{N}$ counting errors and the distances are measured in units of the nearest neighbor distances (NN) of the molecular lattice.

Furthermore it was tried to find variability patterns in the switching molecules by performing a principle component analysis (chapter 3.6.8) in smaller portions of the data. Typically four by four or six by six patches of molecules were extracted from a movie and analyzed. Although in many cases, there were few eigenvalues explaining a larger portion of the observed variance, no statistically significant conclusions could be found. In particular, when performing the analysis only on half of the movie, it was not possible to obtain any valid predictions for the second half. This means that probably the amount of data is not sufficient to draw significant conclusions about correlation patterns in the molecular layer.

As a conclusion it was found that switching events can in principle happen in random locations on the surface (besides at inactive molecules as described in chapter 4.5.5), but the events of opposite

switching direction are coupled together, presumably due to adatom motion underneath the molecular layer, which makes these events happen in close vicinity. Additionally, cascade events can occur, where in a certain area, many switching events can be registered, followed by a longer period of time without any switching events.

4.5.7. Number of up and down switching molecules

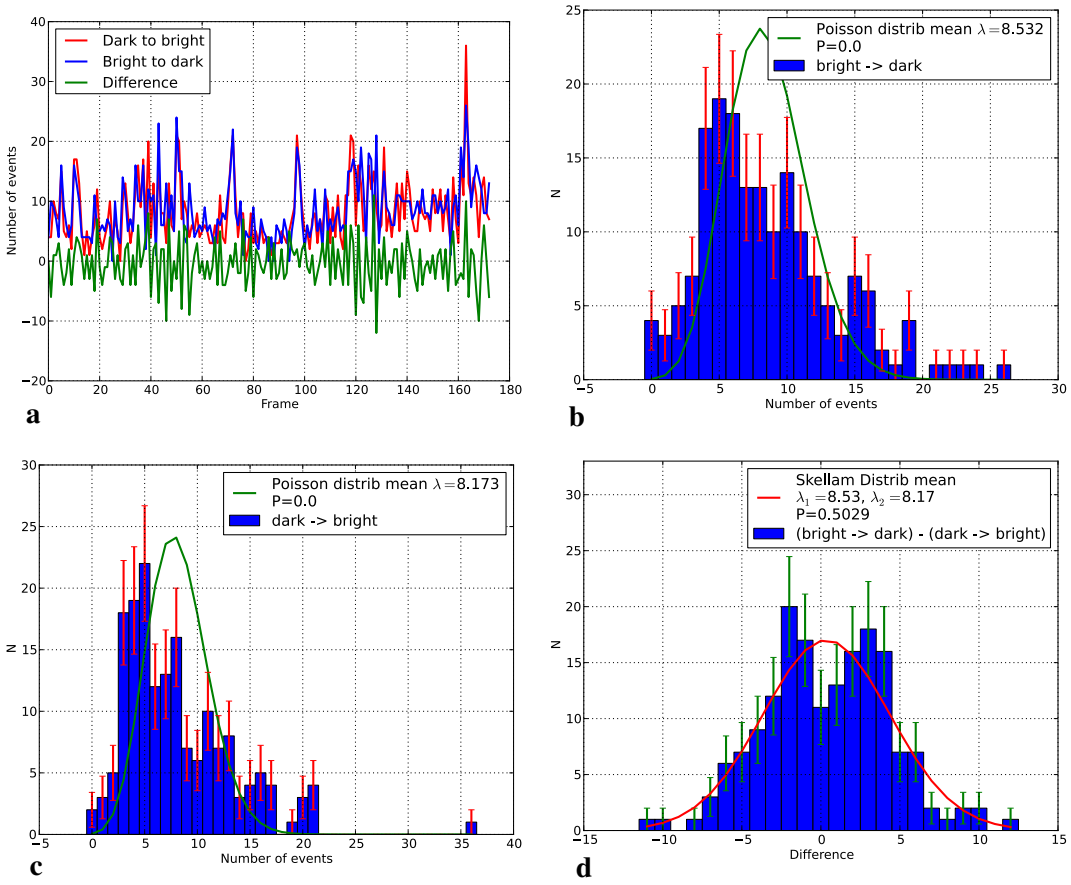

Figure 4.21.: Distribution of up and down switching events for a movie with the image parameters 42 s/frame, $U_{sample} = 302\ mV$, $I = 0.11\ nA$, $T = 300\ K$. (a): number of switching events in both directions and their difference as a function of the frame number. (b) and (c) show the histograms of the event numbers for both directions together with the Poisson distribution with the parameter λ, obtained by simply averaging all data points. (d) shows a similar histogram for the difference, this time compared to a Skellam distribution. All errors are the $\sqrt{N}$ counting errors and P values can be found in the respective legends.

If the switching events were occurring at random times, one would expect that the number of molecules switching from dark to bright as well as the number of molecules switching in the opposite direction between every pair of subsequent frames are Poisson distributed. To verify whether this situation is met in the measured data, the number of switching events in both directions were counted for every movie and plotted as histograms together with a Poisson distribution with λ obtained from simply averaging the event numbers. An example can be found in Fig. 4.21. In (b) and (c), the

measured distribution and the theoretical Poisson distribution disagree, which is also reflected in a very low P value (chapter 3.6.7). Obviously this mismatch cannot be fixed by a better choice of the scale parameter λ, because a smaller λ would be needed to match the distribution maxima, but a larger λ would be needed to match the broader measured distribution. Consequently, the number of up and down switching molecules are not Poisson distributed.

Interestingly, for the majority of the movies, when calculating the difference between the number of up and down switching events and plotting it as a histogram, the Skellam distribution, which is the difference distribution of two Poisson processes (chapter 3.6.6), with the two respective means from the original data fits the histogram quite nicely, producing a considerably high P value of $P \approx 0.5$ in Fig. 4.21 (d). Apparently, the numbers of switching events (Fig. 4.21 (b) and (c)) are not randomly distributed, but their difference is (Fig. 4.21 (b)).

This can be understood as follows: There is always thermal random switching, with a rather low activity and on top of this, between few frames, many molecules switch in one direction and about the same number of molecules switches in the opposite direction (cascade events). These cascade events lead to a deviation from the Poisson distribution when considering the histogram for switching in either direction. However, as in the cascade events the number of up and down switching events are almost equal, they cancel out when calculating the difference distribution. What stays behind and is not canceled out is the contribution from the thermal random switching, which is convincingly explained by the Skellam distribution.

It is important to note that as this analysis is based on the number of switching events only, there is no unambiguous way of exploiting it to clearly separate between cascade and random switching events.

Fig. 4.21 (a) reminds of the hopping activity observed in [98] where the diffusion of H atoms on FeO is studied. The authors of this paper plot the number of hopping events as a function of the frame number of their movie and observe, similarly to the here analyzed switching events, that over many frames almost nothing happens, but between some frames a high activity is observed. This also leads to a clear deviation from a Poisson distribution, which would be expected for thermally activated hopping. It is then demonstrated that the diffusion is actually triggered by the presence of water molecules which, when present, activate the motion of the hydrogen without being visible to the STM. Another example of hopping triggered by an additional particle was described in [99, 100], where the motion of indium atoms, embedded into the surface layer of Cu(001) is studied. The authors find that the motion is actually triggered by diffusing vacancies within the surface layer, which move so fast that they cannot be imaged in STM. They observe that nearby indium atoms are likely to move in between the same frame, i.e. when a vacancy passes by, which would not be expected when the atoms were independently hopping by thermal activation.

Based on the similarity with the two systems described above, it is actually interesting to investigate whether also in the case of the porphyrins, the switching process can be induced by another particle diffusing across the surface and passing the scanned area at random times. As explained above, water was observed to trigger the diffusion in [98] and as water is always present in the rest gas of the UHV chamber it might play a role for the cascade events. To check whether this is true, water was dosed into the chamber: 10^{-7} *mbar* for 60 *s*, corresponding to a dosage of 4.5 *L* [101]. The rest gas spectra before and while dosing can be found in Fig. 4.22 (a) and their difference in (b). Before the dosing, the chamber has a typical UHV rest gas spectrum with some contributions from H, H_2, OH, H_2O and N_2. While dosing, there is a large increase in H_2O and all related fragments like H, H_2, OH and O_2, which shows that the dosed water vapor was very clean. The total dose was 4.5 *L*. Assuming a sticking coefficient of 1, a coverage of 4.5 *ML* would be expected. Of course this sticking coefficient is not met in the real experiment and is presumably much lower, but nevertheless every porphyrin molecule encounters a water molecule several times during the exposure.

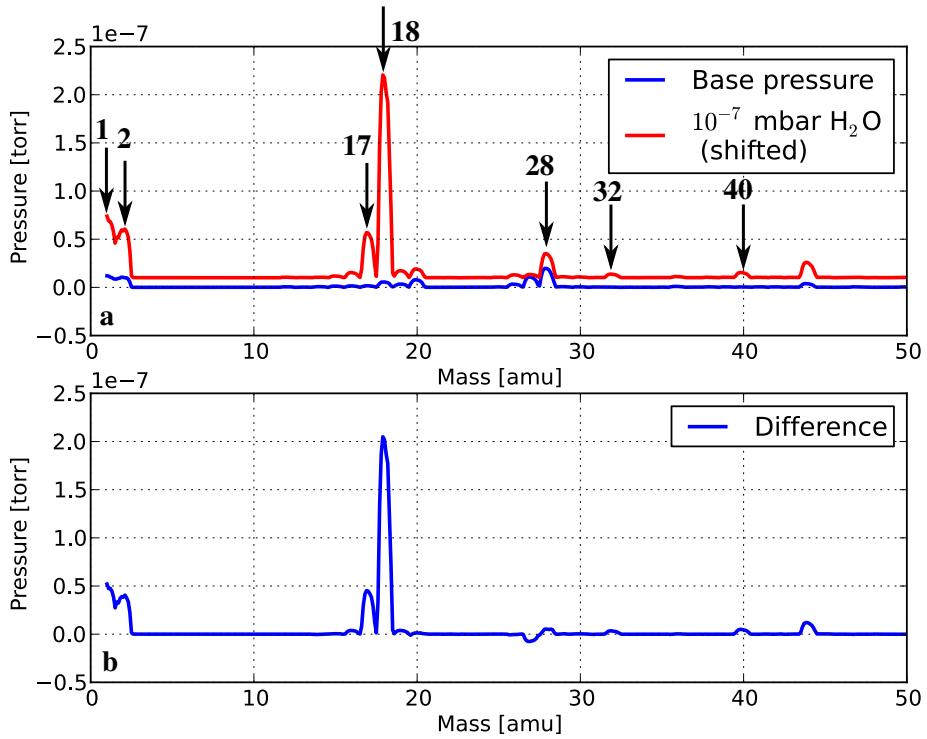

Figure 4.22.: Mass spectra before and while dosing 10^{-7} *mbar* H_2O on the Br_4TPP covered Au(111) surface (a), the red curve is slightly shifted up for clarity. (b) shows the difference between both curves. The molecules at the indicated masses are: 1: H, 2: H_2, 17: OH, 18: H_2O, 28: N_2, 32: O_2, 40: Ar.

The behavior of the switching porphyrin molecules was compared before and after the dosing. The only apparent change was that the amount of bright porphyrins had changed from $(13 \pm 1)\%$ to $(19 \pm 3)\%$ indicating that the water had some effect on the molecules. However, no increase in the number of switching events could be detected ($3.84 \cdot 10^{-4}$ events per molecule and *s* before, compared to $3.59 \cdot 10^{-4}$ events per molecule and *s* after the dosing). This can mean two things: either H_2O does not increase the switching rate and has only an influence on the amount of bright molecules or it did not stay on the surface in sufficient amounts after termination of the exposure.

4.5.8. Br_4TPP on Ag(111)

As described in the previous chapters, the behavior of Br_4TPP on Au(111) is quite complex. This is due to the nature of the molecule itself, but certainly also the particular structure of the Au(111) surface plays a role in this context as the molecules have the possibility to adsorb in a multitude of different regions of the herringbone reconstruction: The fcc and hcp regions, the ridges and the elbows. As can be seen in Fig. 4.13 there is a different distribution of dark and bright molecules between the fcc and hcp regions. Ideally one would have to do the statistical evaluation separately for each of these regions in order to obtain unbiased results of general validity, but this approach has not proven successful because the statistical significance would be lowered so much that no clear conclusions can be obtained. Therefore it was tried to reduce the complexity of the system by changing to a simpler surface, namely Ag(111), which shows no reconstruction but is more reactive than Au(111)[50]. Previous studies of

Bonding type	center-center distance
C – C	1.646 *nm*
C – Ag – C	1.906 *nm*
C – Br – Ag – C	2.135 *nm*
C – Br – Ag – Br – C	2.367 *nm*

Table 4.2.: Center - center distance of two TPP units bound together with different possible atom configurations in the gas phase. The calculations have been performed using the Hyperchem 7 package and the MM+ force field.

TPP on Ag(111) ([70, 76, 72]) did not find any evidence for dark and bright states and consequently also not for switching, but the brominated version was never investigated on this surface before.

The molecules were evaporated on the clean Ag(111) surface, held at room temperature, exactly as in the case of Au(111). Images of the surface for increasing coverages can be found in Fig. 4.23. In (a) the coverage is quite low, the terraces are essentially free of molecules and just some molecules can be found at the step edges, but the molecules assemble differently than in the close packed islands observed on Au(111). Here the molecules apparently bind together via their phenyl legs, which reminds very much of the covalent linking of TPP molecules investigated in [10] and the dimers from chapter 4.7. The fact that close-packed islands cannot be found can have two causes: either all the Br_4TPP molecules are locked up in this bound state or they still exist on the terrace but at a low coverage, where they are diffusing at room temperature or being dragged around by the STM tip and therefore are invisible to the STM. In (b), more molecules were dosed on the surface, leading to an increased coverage of molecules in this bonded structure. As the silver terraces on this image appear to be higher than the pores inside the bonded structure, obviously there is a two dimensional molecular gas [102]. By further increasing the dosage of molecules in (c), no qualitative change of the surface can be found. Only in (d) where even more molecules had been dosed, close-packed islands can be found besides the bound structures.

Bias-dependent imaging of the Br_4TPP molecules in the close-packed structures (Fig. 4.24) shows that on Ag(111), the molecules display only one state and that its appearance does not depend on the bias voltage (unlike on Au(111), Fig. 4.12). Therefore no switching occurs on a flat, unreconstructed surface.

A very similar system has been investigated in [82] at low temperatures, where a tautomerization can be observed upon stimulation with the STM tip. Probably the tautomerization barrier is so small, that rapid tautomerization is taking place at room temperature, making it impossible to distinguish the two tautomers in our measurements.

The bonding of the molecules at room temperature without additional heating is interesting. In principle the interaction could be covalent linking as in [10] or a metal coordination bond involving an adatom as in [103]. As no such bonding has been observed in the case of TPP on Ag(111) ([70, 76, 72, 82]), the Br atoms have to play a role in this context. One way of judging which type of bonding is present on the surface is to compare the measured bond length (Fig. 4.25) with gas phase calculations of the different possible types of bonding between two TPP units (Tab. 4.2). The average bond length of the smaller structures in Fig. 4.25 (a) of (1.89 ± 0.07) *nm* matches very closely the gas phase bond length of two TPP units coupled with a C – Ag – C bond of 1.906 *nm* and clearly deviates from the C – C bond length of 1.646 *nm*.

Obviously, the Br_4TPP molecules are behaving differently on Ag(111) than on Au(111). The catalytic activity of the silver surface lowers the dissociation barrier for Br atoms so much [51] that they

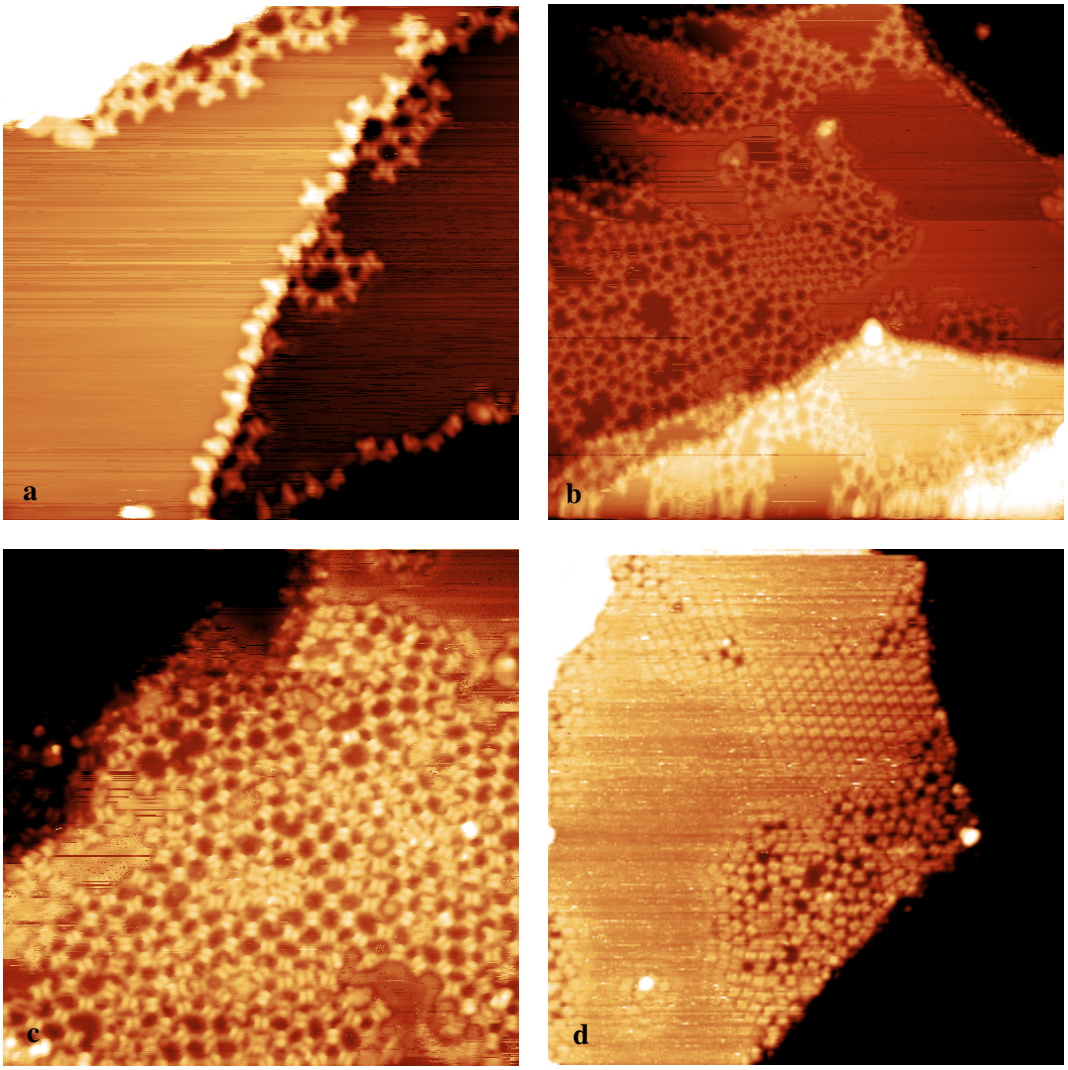

Figure 4.23.: Overview images of Br_4TPP on Ag(111) at room temperature for different coverages. (a): Ag(111) surface with $1.1Hz$ of molecules ($37.5 \times 37.5\ nm^2$, $U_{sample} = 0.88\ V$, $I = 0.13\ nA$, $T = 300\ K$). (b): The same surface but with an increased amount of molecules of $1.78\ Hz$ ($62.5 \times 62.5\ nm^2$, $U_{sample} = 0.83\ V$, $I = 0.12\ nA$, $T = 300\ K$). (c): Further increased coverage of $2.3\ Hz$ ($37.5 \times 37.5\ nm^2$, $U_{sample} = 0.83\ V$, $I = 0.14\ nA$, $T = 300\ K$). (d): Higher dosage of molecules, for the first time close packed islands are visible ($62.5 \times 62.5\ nm^2$, $U_{sample} = 0.83\ V$, $I = 0.21\ nA$, $T = 300\ K$).

get split off already at room temperature, leaving behind an activated site. At this site, a silver adatom can be bound, which is present on the surface at room temperature. The presence of the activated site is crucial for the described structure as no metal coordination networks were found when using the TPP molecules on the same surface [70, 76, 72, 82]. It would be an interesting experiment to anneal the surface after deposition in order to find out whether direct C – C bonds are obtained at higher temperatures.

In Fig. 4.25 (b), a more complicated structure can be found, consisting of horizontally aligned

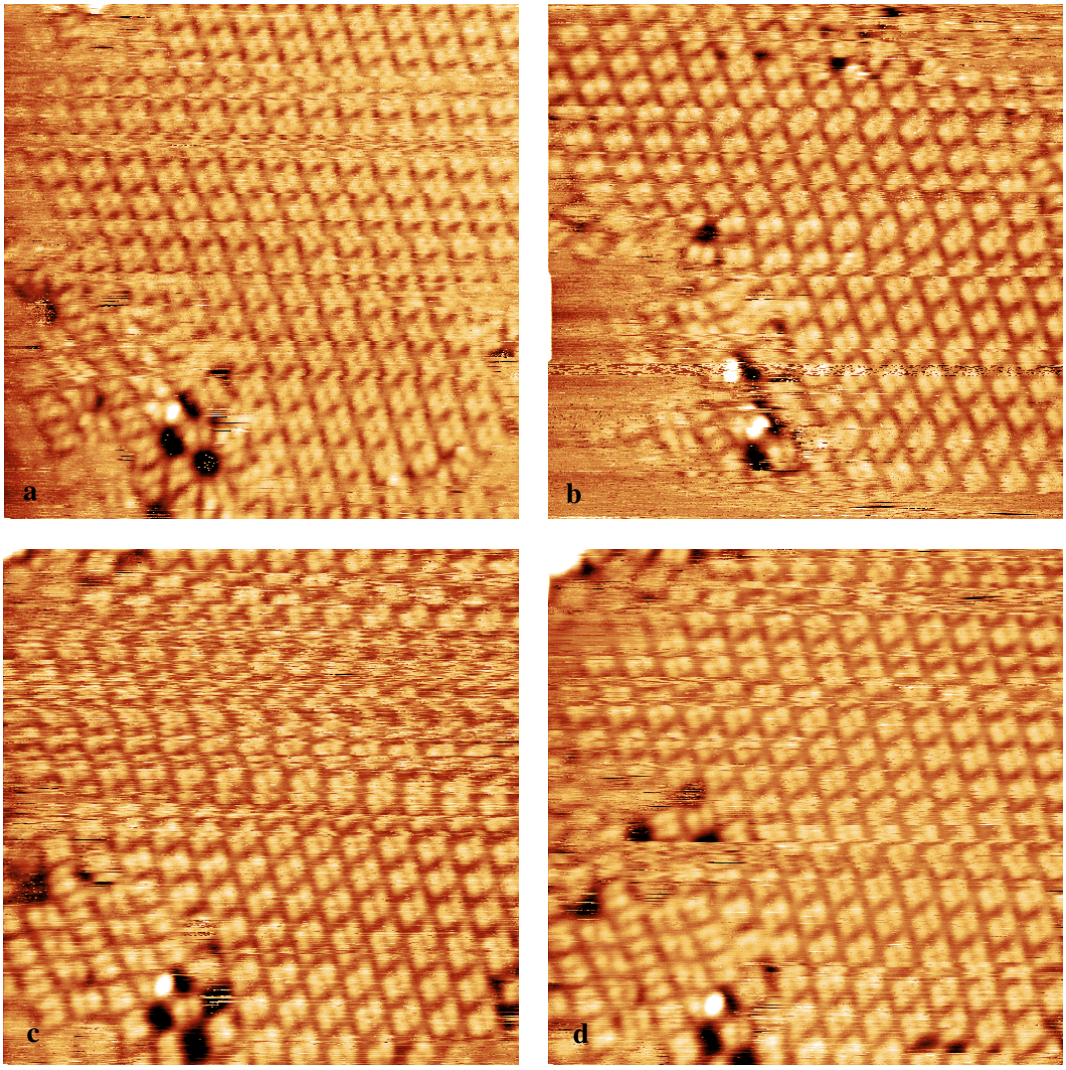

Figure 4.24.: Bias dependence of Br_4TPP in a close packed structure on Ag(111). (a): $U_{sample} = 0.37\,V$, (b): $U_{sample} = 0.86\,V$, (c): $U_{sample} = 1.32\,V$, (d): $U_{sample} = 1.58\,V$. The other image parameters are $25 \times 25\,nm^2$, $I = 0.14\,nA$, $T = 300\,K$. The strong thermal z-drift of the instrument was corrected in these images by subtracting its median value from each scan line.

molecular chains. These chains have a porphyrin - porphyrin distance of $(1.98 \pm 0.05)\,nm$, which is slightly larger than in (a) but still lies sufficiently close to the expected bond length for C – Ag – C. The distance which is indicated by the broken arrow in the figure has a value of $(2.6 \pm 0.1)\,nm$. As this cannot be identified as one of the distances from Tab. 4.2, the presented structure must be a close packed stacking of metal coordination bonded TPP chains.

In chapter 4.7, covalently bound TPP structures are investigated on Au(111). Their center to center distance of $(1.74 \pm 0.08)\,nm$ corresponds to the calculated value of the C – C bond in Tab. 4.2 and is clearly different from the values measured here, which is a further hint that something different is happening on this surface.

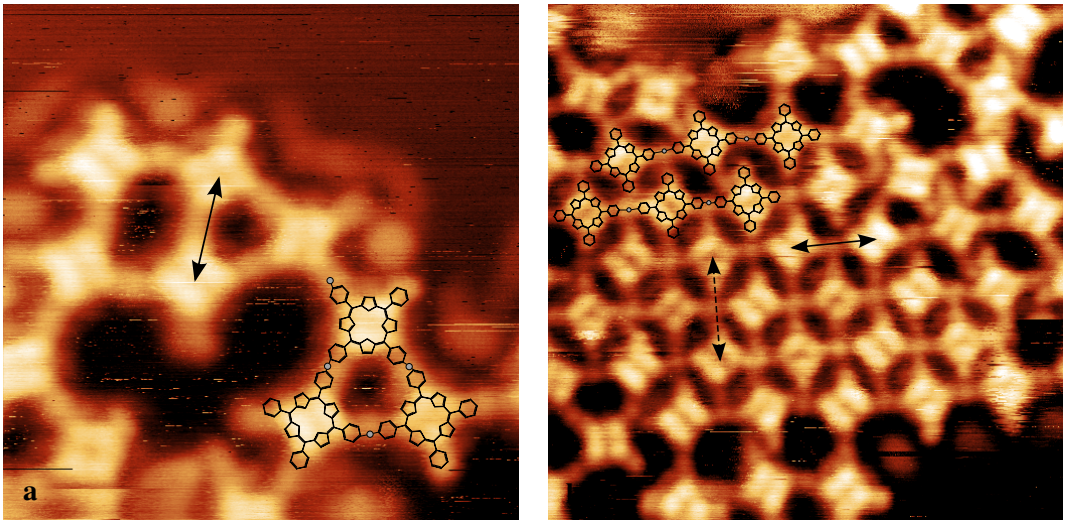

Figure 4.25.: Bonding distances of Br_4TPP on Ag(111) at room temperature. Molecular structures can be found in both images, gray circles symbolize the silver atoms. (a): The average center to center distance between two porphyrin units is (1.89 ± 0.07) *nm* (image parameters: 8.75×8.75 nm^2, $U_{sample} = 0.83$ V, $I = 0.11$ nA, $T = 300$ K). (b): Molecules in a network structure with two types of lengths. The average of the bond marked with the solid arrow is (1.98 ± 0.05) *nm* and of the broken arrow (2.6 ± 0.1) *nm* (image parameters: 12.5×12.5 nm^2, $U_{sample} = 0.83$ V, $I = 0.12$ nA, $T = 300$ K).

A further argument for the metal coordination bond can be found in Fig. 4.26, where two images of the same area are presented. They have been recorded with a time difference of 2h 30min. In the mean time, many other images have been recorded, covering a large range of bias voltages. It is apparent that during that time, some of the molecules have been changing their bonding arrangement from close packed chains as in Fig 4.25 (b) to higher coordinated coordination networks, maybe due to thermal motion, maybe due to the presence of the STM tip and that new bonds between the molecules have formed. As such a behavior is not expected to occur in the case of covalent bonding, this finding strongly supports the theory of a metal coordination bond. However, the formation of the networks is not terminated yet, not all molecules are coordinated to four others but this might be observed after an even longer waiting time. Apparently the formation of these network happens at room temperature on a timescale which can easily be followed by STM and could be an interesting object for future investigations.

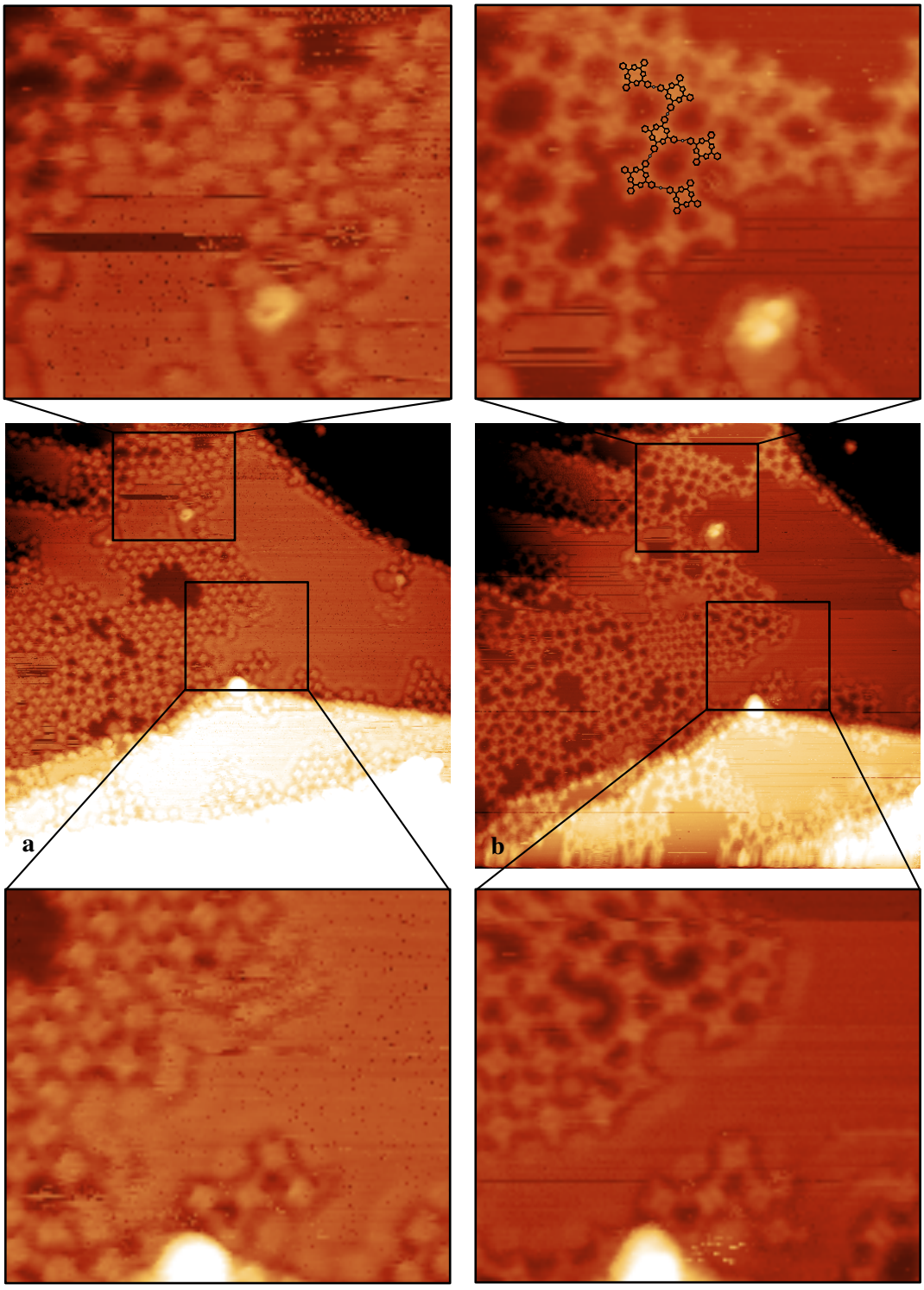

Figure 4.26.: Time dependence of bonded structures of Br_4TPP on Ag(111) at room temperature. Image (a) ($62.5 \times 62.5\ nm^2$, $U_{sample} = 0.88\ V$, $I = 0.14\ nA$, $T = 300\ K$) has been taken 2h 30min before image (b) ($62.5 \times 62.5\ nm^2$, $U_{sample} = 0.83\ V$, $I = 0.12\ nA$, $T = 300\ K$). In between, 25 images with voltages of $-1.58\ V \leq V_{sample} \leq 1.54\ V$ have been recorded.

4.6. Manipulation

It was shown in chapter 4.4 that the TPP molecules on Au(111) can be found in a dark and in a bright state and in chapter 4.5 they were shown to reversibly switch at room temperature. From the analysis of the distance between switching events of opposite direction (chapter 4.5.6) and from the theory results, which are presented in chapter 4.8, there is some evidence that the origin of the bright state involves a gold adatom siting underneath the molecule and is not caused by a transition between a flat and a saddle shape conformation of the TPP molecules [8, 9]. To collect further evidence for either possibility, low temperature switching experiments of the molecules have been performed which are presented in this chapter.

It is demonstrated that switching TPP molecules between their dark and bright state can also be induced with the STM tip by applying voltage pulses (Fig. 4.27). Switching from bright to dark occurs with high efficiency while the opposite direction can also be induced in the same voltage range but happens only so rarely that no meaningful statistics about its occurrence could be made. This observation favors the adatom theory, because when switching from bright to dark, a present adatom has to leave the molecule in some way, which should be easily achievable, but when switching from dark to bright, an adatom needs to be available nearby, which is not expected at low temperatures of 5 K.

4.6.1. Switching voltage threshold

At first, the voltage threshold for the switching process from bright to dark is determined. Therefore, the STM tip is positioned above a bright molecule and the bias voltage is ramped up until the molecule is switched to dark, the voltage at which the switching event occurred is recorded and added as a new value for the histogram presented in Fig. 4.27 (d). As is apparent from the histogram, the switching happens at voltages above around $\pm 2\ V$. However, when inspecting the appearance of the molecules at $\pm 2\ V$ in Fig. 4.5, it is impossible to distinguish the different states at these voltages. Therefore, it is necessary to apply a series of bias pulses with increasing voltage to the molecule and to return to $-1\ V$ in between to test whether a change has occurred or not. This experiment is shown in 4.27 (e), where an abrupt change in the tip height after applying a $-2.15\ V$ pulse clearly indicates that a change occurred in the molecule. The switching process is reversible but happens only so rarely from dark to bright (chapter 4.6), that practically the switching needs to be treated as irreversible and the statistics for the bright to dark direction have to be done with a new molecule for every switching attempt. An equivalent threshold histogram for the switching from dark to bright could not be obtained because of the rare occurrence of these events described above.

When comparing the onset of the switching in Fig. 4.27 (d) with the position of the molecular orbitals of the bright TPP molecules in Fig. 4.8, they apparently disagree. Consequently, the switching process cannot be a resonant tunneling into a molecular orbital [104]. Also the symmetry of the switching threshold with respect to the applied tip bias points to this conclusion, as the molecular orbitals are not symmetrically aligned with respect to the Fermi energy.

The origin of the switching mechanism could not be revealed by these measurements, only resonant tunneling into the molecular orbitals could be excluded and further measurement would be needed in order to gain a better insight. It would be interesting to investigate how many electrons are needed to trigger a switching event as in [40]. If more than one electron is needed, this could point to an excitation of molecular vibrations, which then induce the switching. Alternatively, if no electrons are needed, the switching could be induced by the electric field between tip and sample as observed in [8, 38].

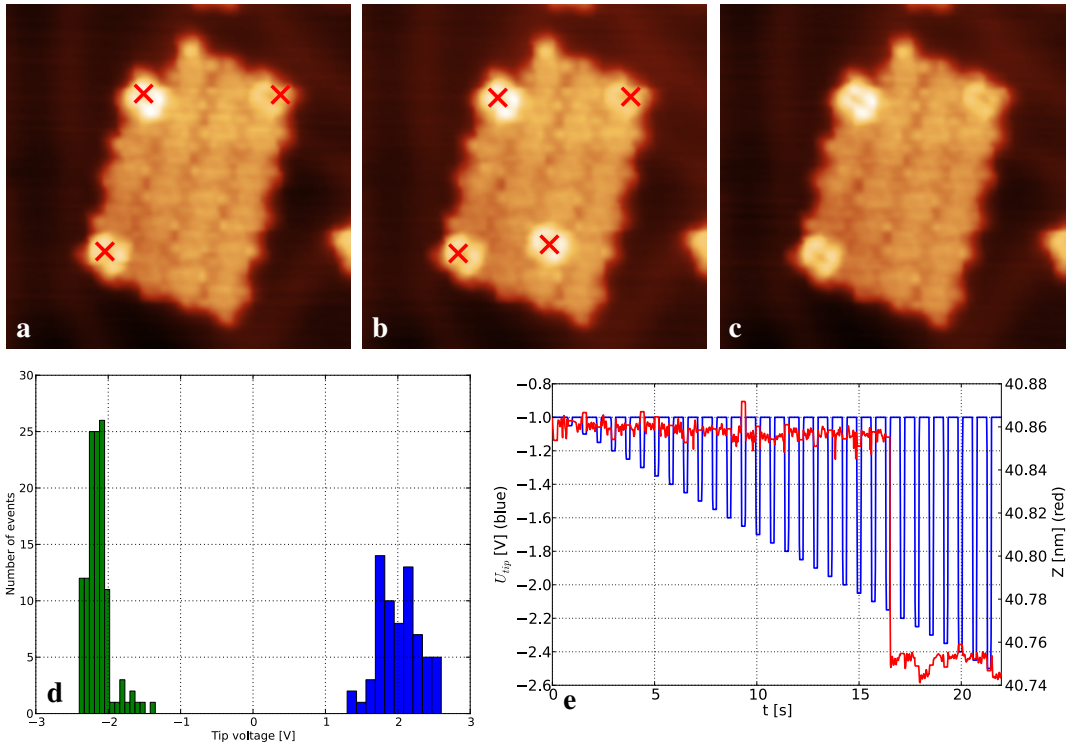

Figure 4.27.: Images (a) - (c): reversible switching of TPP on Au(111) induced by the STM tip: $12.5 \times 12.5\ nm^2$, $U_{tip} = -1\ V$, $I = 0.31\ nA$, $T = 5.6\ K$. Voltage pulses were applied at the positions marked with a red cross with the following parameters: (a) $0\ V$ to $-1.7\ V$, (b) $0\ V$ to $-1.8\ V$. (d) Threshold voltage for tip induced switching from the bright to the dark state. (e) determining the switching threshold voltage from bright to dark with a series of bias pulses at a current of $0.26\ nA$.

4.6.2. Creating adatoms

It is known from literature, that adatoms can be created on Ag(111) by dipping the tip of the STM into the surface [105] and that Au adatoms are stable on Au(111) at low temperatures [106]. It was tried whether direct creation of gold adatoms in the vicinity of TPP molecules on the surface can be used to switch them from dark to bright easily.

Creating adatoms on Au(111) by crashing the STM tip was found to be relatively easy to do. Good results were obtained using a tip voltage of $3\ V$ and an indentation of $3\ nm$ from the normal tunneling conditions. However, it was found that the amount of adatoms depends on the indentation speed of the tip. The highest numbers of adatoms were obtained when the indentation is done as fast as the STM electronics allows. Nevertheless, the number of created adatoms is not predictable and, using the same parameters, varies drastically from attempt to attempt.

Fig. 4.28 shows a typical example of such tip crashes. The STM images (a) - (c) show the unperturbed surface, where (b) and (c) are detailed zoom-ins into (a). (d) - (f) show the same areas, respectively, after two tip crashes at the positions marked with a red cross. In (d) can be seen, that many adatoms have been created (they have an apparent height of $\approx 100\ pm$ above the gold surface) which are now situated on the terrace and apparently, several TPP molecules in ordered islands have switched from

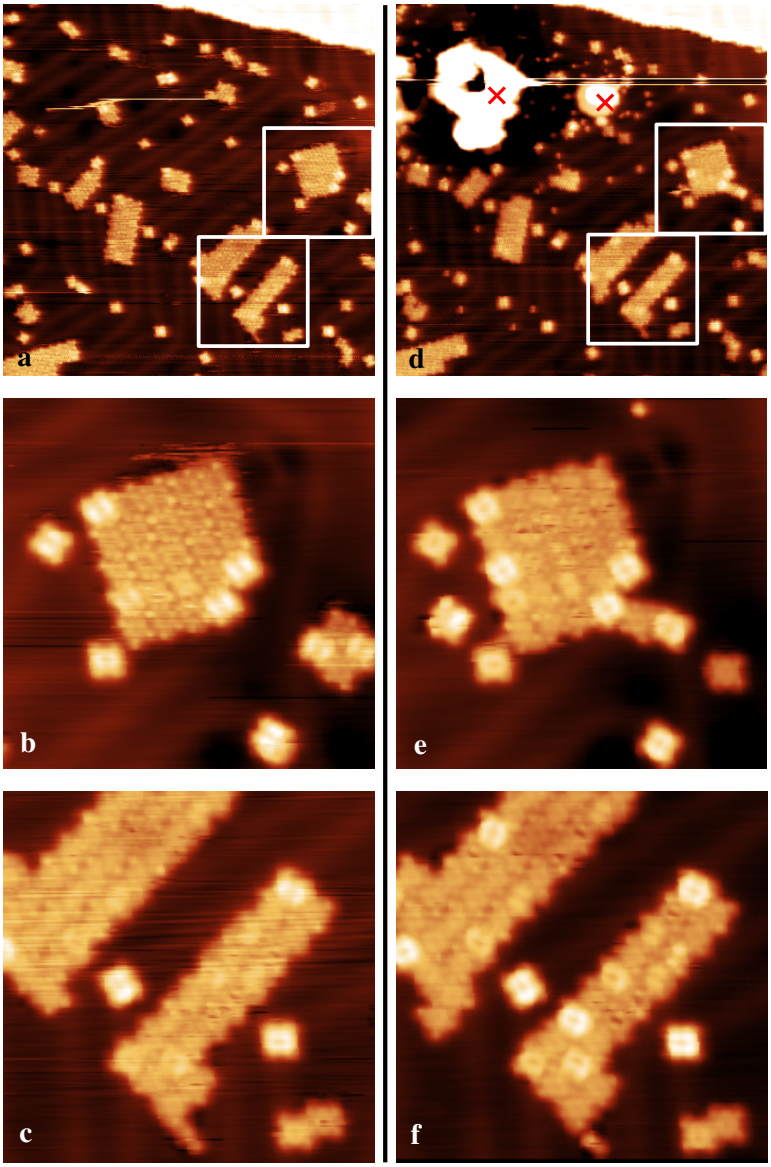

Figure 4.28.: Switching TPP molecules from dark to bright by creating adatoms in their vicinity using tip crashes. (a) - (c) Surface area before the tip crash, (d) - (f) after two tip crashes ($U_{tip} = 3\ V$, $3\ nm$ indentation from tunneling conditions) at the indicated positions. Bright molecules were created. The white rectangles in (a) and (d) indicate the positions of (b), (c), (e) and (f). Image parameters: (a) and (d) $58.9 \times 58.9\ nm^2$, the others images $17.5 \times 17.5\ nm^2$, all other parameters: $U_{tip} = -1\ V$, $I = 0.18\ nA$, $T = 5.7\ K$

dark to bright (e,f). They look exactly like the bright molecules which have been on the surface before. It was mentioned in chapter 4.6 that switching dark molecules to bright by applying a voltage pulse only happens very rarely, probably due to a lack of available adatoms. In the present example, several molecules were switched to bright in a distance of more than 30 *nm* from the point of indentation which would not be expected to happen when applying only a voltage pulse of 3 *V* at the same position

without touching the surface. This experiment shows that the availability of adatoms from the tip crash facilitates switching from dark to bright, which is a strong indication that adatoms play a role in the switching process and for the existence of the bright molecular state.

4.6.3. Manipulation of TPP on and off adatoms

In order to obtain a direct proof that an adatom is present underneath the bright TPP molecules, lateral manipulation experiments were performed in which it was tried to separate bright TPP molecules from the potential adatom underneath or, the inverse experiment, pushing a dark molecule on an artificially created adatom to make it switch to the bright state.

The first experiment was to switch bright molecules to the dark state by a voltage pulse (just as shown in Fig. 4.27). If there is an adatom underneath the bright molecules but not underneath the dark ones, it would be expected that this adatom leaves the molecule when switching it to the dark state. It was tried intensively to find this adatom after switching molecules from bright to dark, but no adatoms were ever found by this method. Besides the switched molecule, the STM images before and after inducing the switching look identical. Therefore the tip apex cannot have changed while applying the voltage pulse and consequently, no potential adatom is transfered to the tip. It still has to be present on the surface. However, as it is not found on the gold surface surrounding the molecule, it can only be still underneath the molecule, possibly in a different position, or not existing.

Subsequently, the molecule was moved away from its original position by lateral manipulation, but also here, no adatoms were found afterwards. Consequently, if the adatom theory is true, the adatom is probably still underneath the molecule and moving with it during lateral manipulation, but not in the position where it leads to the bright appearance of the molecule. Pushing dark TPP molecules onto artificially created adatoms on the terrace was not successful and can thus not be used to proof the adatom theory.

It was found out that if bright molecules are situated above the elbow of the herringbone reconstruction (which is frequently the case), it is possible to manipulate the molecule away, an adatom being stabilized on the elbow site [107] stays behind and very often, the molecule switches to the dark state. Such a situation can be found in Fig. 4.29, where the bright molecule is manipulated away from the elbow in (a), leaving behind an adatom and switching to dark. The adatom has an apparent height of 72 *pm* which fits to the adatom height of 100 *pm* observed in chapter 4.6.2. After being pushed back onto the adatom in (b), the molecule is found in an unresolvable state (c). Taking a dI/dV spectrum over the molecule, reveals that it is switching after the first sweep to the bright state again, which is also confirmed by STM imaging in (d). It seems as for revealing the presence of an adatom, it has to be anchored on the surface, as in this case on the elbow of the herringbone reconstruction, otherwise it moves together with the molecule.

However, when pushing the molecule away again it turned dark and a pointlike structure is staying behind (e) which has an apparent height of 10 *pm* only, and therefore clearly deviates from the adatom height. Another occurrence of the observation is presented in Fig. 4.30 where a bright molecule is being pushed away from an elbow site, a pointlike structure with a height of 17 *pm* is staying behind exactly at the former molecular center, but the molecule stays in the bright state. Due to their similar height, these two structures probably have the same origin. Presumably, they are just the apex of the dislocation at the elbows of the herringbone reconstruction [108], which would mean that a potential adatom is not bound as strongly at the elbow site.

It is known from previous studies [94, 109], that a removal of atoms from the surface, regardless whether it is done by the STM tip or the interaction with adsorbates, leads to a restructuring of the surface reconstruction, resulting in a different distribution of the herringbone ridges. As in the presented

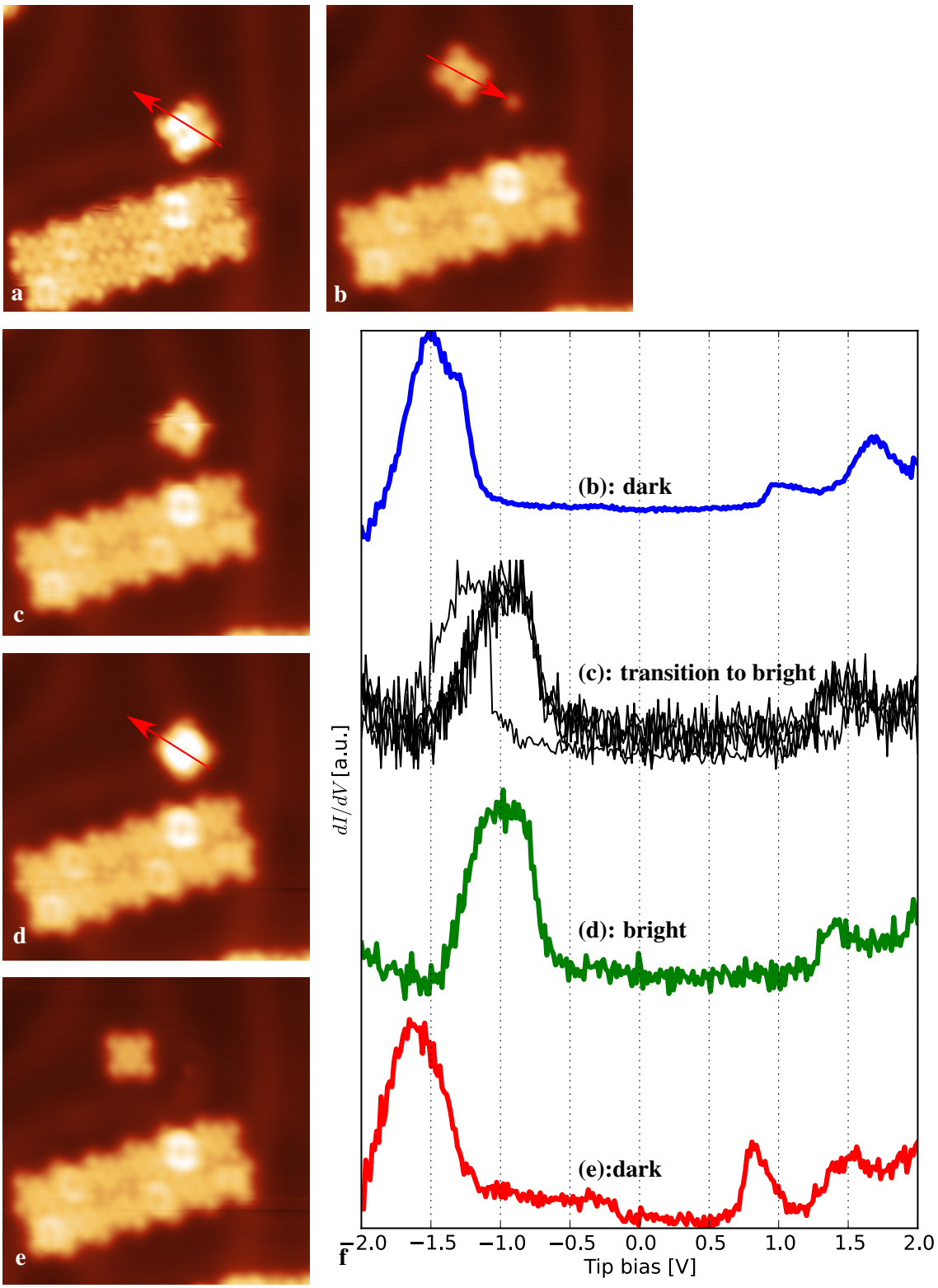

Figure 4.29.: (a) - (e) Lateral manipulation sequence of a bright TPP molecule adsorbed on an elbow site. Red arrows indicate the manipulation path, manipulation parameters: $U_{tip} = 10\ mV$, $I = 50\ nA$. Image parameters: $11.1 \times 11.1\ nm^2$, $U_{tip} = -1\ V$, $I = 86\ pA$, $T = 5.8\ K$. (f) shows dI/dV spectra taken above the molecule in the indicated image.

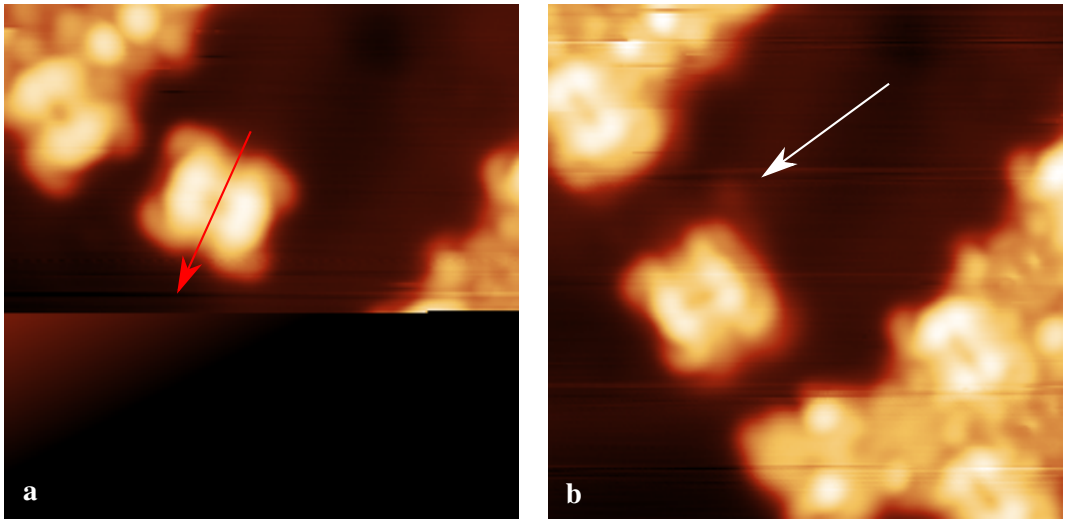

Figure 4.30.: Lateral manipulation of a bright TPP molecule situated on an elbow site of the herringbone reconstruction. The red arrow in (a) shows the manipulation path ($U_{tip} = -30\ mV$, $I = 50\ nA$). The lower part of this image was not scanned. In (b), the molecule has moved and a pointlike structure with a height of 17 *pm* stays behind exactly at the former center position of the molecule (white arrow), but the molecule stays in the bright state. Both image parameters: $7.3 \times 7.3\ nm^2$, $U_{tip} = -1\ V$, $I = 0.1\ nA$, $T = 5.7\ K$.

experiments, the reconstruction lines appear to stay unperturbed in the presence of the molecules, the adatoms underneath the molecules cannot be pulled out of the first surface layer, but rather must have been mobile adatoms coming from the surrounding step edges.

The experiments of this chapter clearly confirm the presence of an adatom underneath the bright TPP molecules. As shown in Fig. 4.29, a bright molecule can be displaced laterally and switches to the dark state. During the manipulation, a bias voltage of $U_{tip} = 10\ mV$ was applied, which would not lead to a switching of the molecule when applying a voltage pulse (Fig. 4.27 (d)) and indicates that a different process is happening. At the former center of the molecule, an adatom is staying behind which is identified by its typical height. Furthermore, when pushing the molecule back onto the adatom and taking a spectrum, the molecule is switched back to the bright state, which could almost never be observed when applying voltage pulses (chapter 4.6) on dark molecules and confirms that an adatom needs to be present for facilitating switching in this direction. However, it seems that this process is only possible when the adatom is trapped on the surface, as in this case at the elbow of the herringbone reconstruction, otherwise it just moves with the molecule. But also at the elbow sites, the trapping is rather weak and does not always succeed in keeping the adatom at its position (Fig. 4.30).

4.7. Covalent assemblies

Until now, the TPP molecules have only been investigated in close-packed islands or, as in chapter 4.5.8, in presumably metal coordinated bonding arrangements on Ag(111). However, bromine functionalized TPP molecules can be covalently assembled into dimers, chains or two dimensional networks, depending on the number and position of the bromine substituents [10]. As will be seen, switching in covalently bound arrangements is still possible on Au(111) and it is interesting to look on the differences of the switching process between close-packed and covalent arrangements of TPP molecules.

4.7.1. Creation of dimers

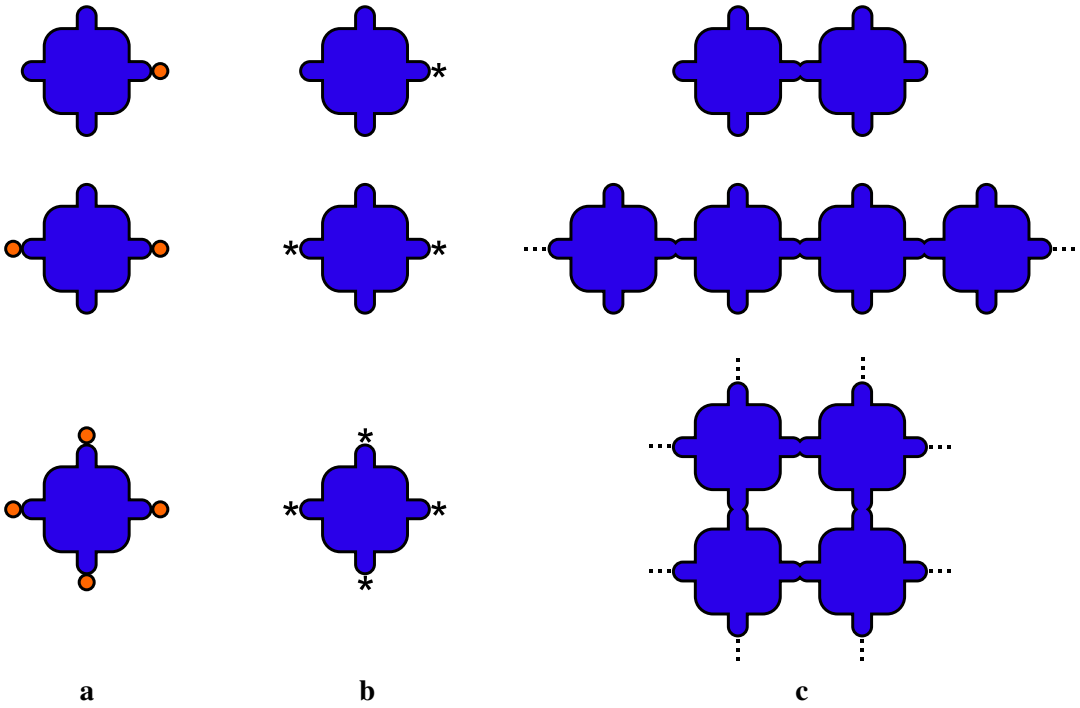

Figure 4.31.: Schematic representation of the on-surface synthesis method [10]. In (a), three types of TPP molecules are presented, each functionalized with bromine atoms drawn in orange. Upon annealing of these molecules, typically at about 250°C, the bromine is split off (b), leaving the TPP molecules behind with unpaired electrons in the former position of the bromine atoms. As these activated molecules continue to diffuse on the surface, covalent bonds between molecules can be formed when sites with unpaired electrons meet (c). Depending on the initial number and position of the bromine atoms, different structures can be obtained, dimers in the first, chains in the second and two dimensional networks in the third row.

The simplest covalent structure are dimers of TPP molecules. They can be created on the surface by the method of on-surface synthesis [10, 93, 110]. TPP molecules functionalized with one bromine atom are evaporated onto a clean Au(111) surface at room temperature. As the carbon – bromine bond

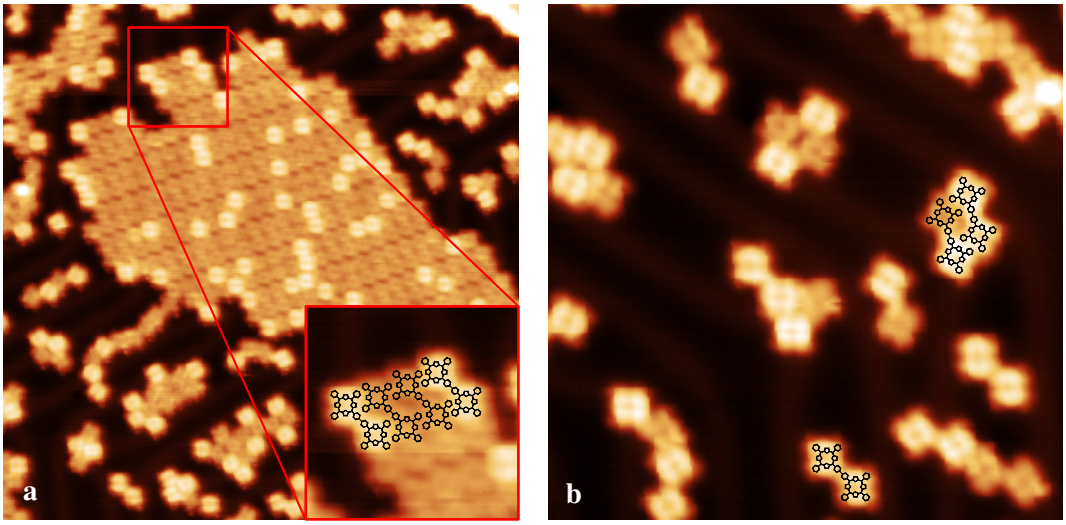

Figure 4.32.: Typical STM images of TPP dimers on Au(111). In the large scale image (a) a large dimer island can be found as well as many smaller islands in the surroundings ($49.2 \times 49.2\ nm^2$, $U_{tip} = -1.3\ V$, $I = 0.61\ nA$, $T = 5\ K$). (b) shows single dimers and clusters of dimers. Each side of the dimers can still adopt the dark and bright state ($22.0 \times 22.0\ nm^2$, $U_{tip} = -1.3\ V$, $I = 0.61\ nA$, $T = 5\ K$).

is the weakest bond in the molecule, heating the surface to the dissociation temperature (about 250°C) selectively removes the bromine atom and leaves the molecule behind with an activated site. As the molecules continue to diffuse, two activated sites can meet and form a covalent bond between the molecules (Fig. 4.31).

Typical low temperature images of the surface after the formation of dimers can be found in Fig. 4.32. The dimers form large islands (a), but also single molecules and small clusters can be found (b) and rarely, even unconnected monomers. As these images clearly show, each side of the dimers is still capable of adopting the dark and bright state, which was also observed for the single molecules (chapter 4.4). In chapter 4.7.4 it is demonstrated that at room temperature, the distribution of dark and bright dimer sides is completely random.

Bias dependent images have also been recorded (Fig. 4.33), which look very similar to the ones of the monomers (Fig. 4.5) and also show a strong dependence of the STM image contrast on the applied bias voltage. As for the monomers, the contrast difference between the dark and bright dimer sides is also strongest at $U_{tip} = -1\ V$. Due to these similarities, the dark and bright state has probably the same origin both, for dimers and monomers.

The center to center distance between the two porphyrin units is $(1.74 \pm 0.08)\ nm$ as measured from STM images. By comparison with the values given in table 4.2, it can be concluded that, as expected, a covalent bond was formed between the two TPP monomers.

4.7.2. Switching of single dimers

As the two sides of the dimers are still able to adopt the dark and bright state, it was also tried to switch them by applying voltage pulses with the tip of the STM. It was found that the dimers behave very similar to the monomers, they also switch easily, in about 95% of the attempts, from bright to dark

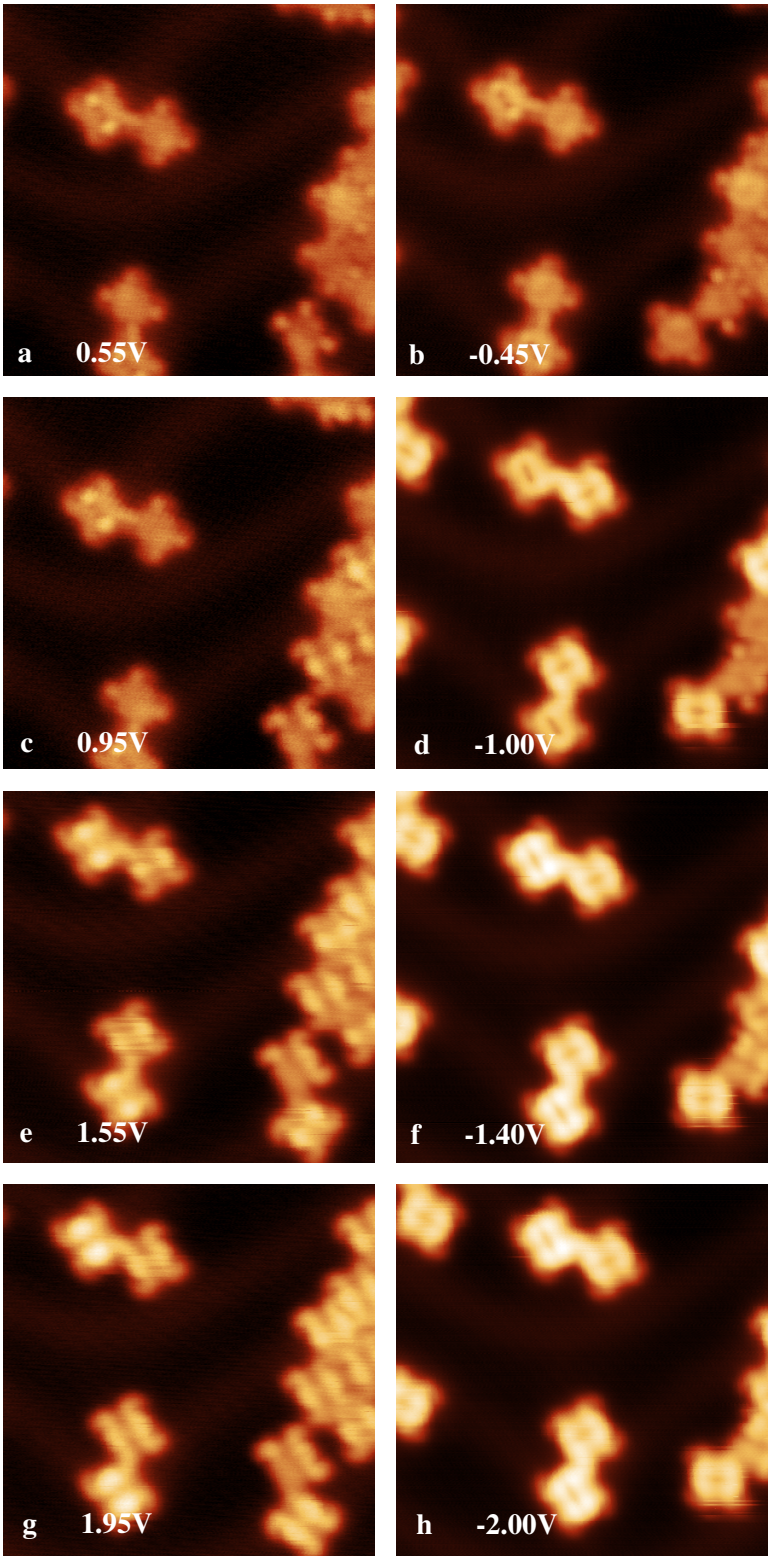

Figure 4.33.: Bias dependent imaging of TPP dimers. The tip voltages are given in the images, the other imaging parameters were: $10.7 \times 10.7\ nm^2$, $I = 0.35\ nA$, $T = 5\ K$.

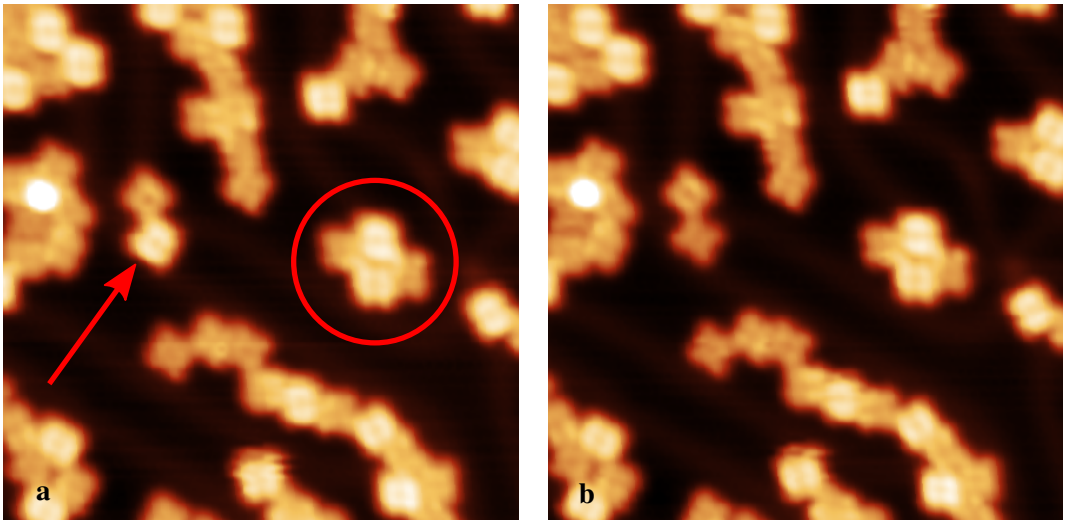

Figure 4.34.: Switching TPP dimers on Au(111). Between the two images, a voltage pulse from 0 V to -2.3 V was applied over the bright molecule marked in (a) with the red arrow. In the subsequent image (b), this molecule has changed to the dark state. Two-dimer islands are studied in chapter 4.7.3. One of them is marked in (a) with a red circle. The imaging parameters of both images are: 20.7×20.7 nm^2, $U_{tip} = -1.3$ V, $I = 0.61$ nA, $T = 5$ K.

when a voltage ramp from 0 V to ± 2.3 V was applied (Fig. 4.34), but switching in the other direction happens so rarely, that no meaningful statistic could be obtained.

In order to find out whether a correlation exists between the states of the two switching units in a dimer, the experiment presented in Fig. 4.35 was performed. Voltage pulses, which almost certainly (with 95% probability) switch the porphyrin unit underneath the STM tip from bright to dark were applied over one side (B) of the dimer, indicated by a red cross in the figure. It is important to note that the other side in the dimer (A) always was in the bright state. Now the probability was determined with which A was switched to dark. All possible combinations and their respective probabilities are shown in the figure and it turns out that the state of B does not have any influence on the switching probability of A because, within the margin of error, the switching probabilities are equal.

Another way of testing for a potential correlation is the experiment shown in Fig. 4.36. It is very similar to the one described above: The probability of switching A is determined in dependence of the state of B, but this time, the pulse is not applied over the molecules but over the bare metal surface in the same distance from A as before. Again, the switching probabilities of A are within the error bars identical, regardless whether B is bright or dark.

Hence, no communication between the two sides of the dimer could be found when inducing the switching with a voltage pulse. As the bright states requires the presence of a gold adatom underneath the molecule (chapters 4.6.3 and 4.8.1), it could be expected that the adatom hops to the other side of the dimer when applying the voltage pulse and thereby switching it to the bright state. However, this does not seem to be the case. But as was demonstrated in chapter 4.6.1, also in the case of the monomer switching, the adatom is never found in the surroundings after the voltage pulse, which probably means that it is still underneath the molecule. This could also be the case for the dimers, the adatom simply stays underneath the dimer side which was bright before the pulse and is not moving to the other side.

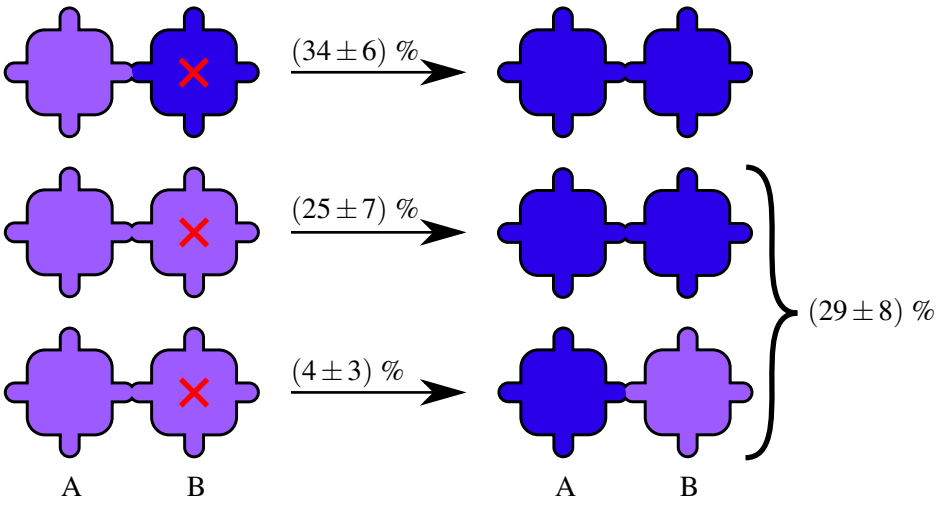

Figure 4.35.: Switching statistics for single TPP dimers on Au(111). Voltage pulses from 0 to ±2.3 *V* were applied on the positions marked with the red cross. TPP units in violet symbolize the bright molecular state, dark blue the dark state.

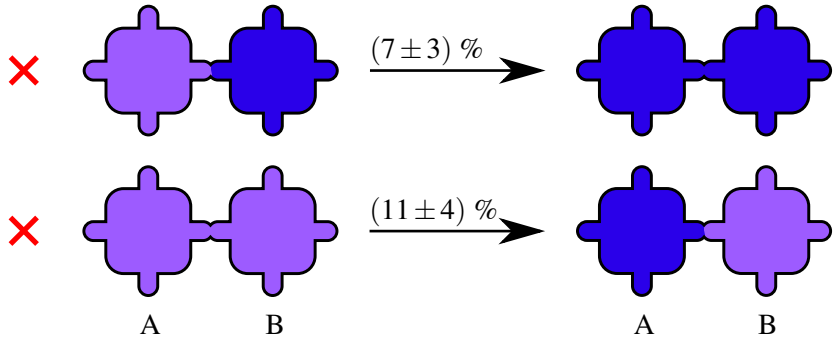

Figure 4.36.: Switching statistics of an experiment similar to the one in Fig. 4.35. The only difference is that the pulse supposed to switch A was applied over the metal surface, at the indicated position, in the same distance from A as the distance between A and B. The colors are identical to those in Fig. 4.35.

4.7.3. Switching of dimers in two-dimer-islands

The red circle in Fig. 4.34 marks a two dimer island formed by two close-packed dimers. This sort of molecular arrangement can be found quite frequently on the surface and is interesting to study in terms of switching because it contains four switchable porphyrin units in similar distances. Every TPP unit has one covalently bound neighbor and one or two close-packed neighbors which are slightly closer than the covalently bound ones (the exact dimensions can be found in Fig 4.37). This particular arrangement can be exploited to find out whether a the different type of bonding has an effect on the switching probabilities of the switching units.

The experiment which was performed on these two dimer islands is shown in Fig. 4.37. Only islands with both outer TPP units dark and the inner ones bright were used. Over one of the outer units, a

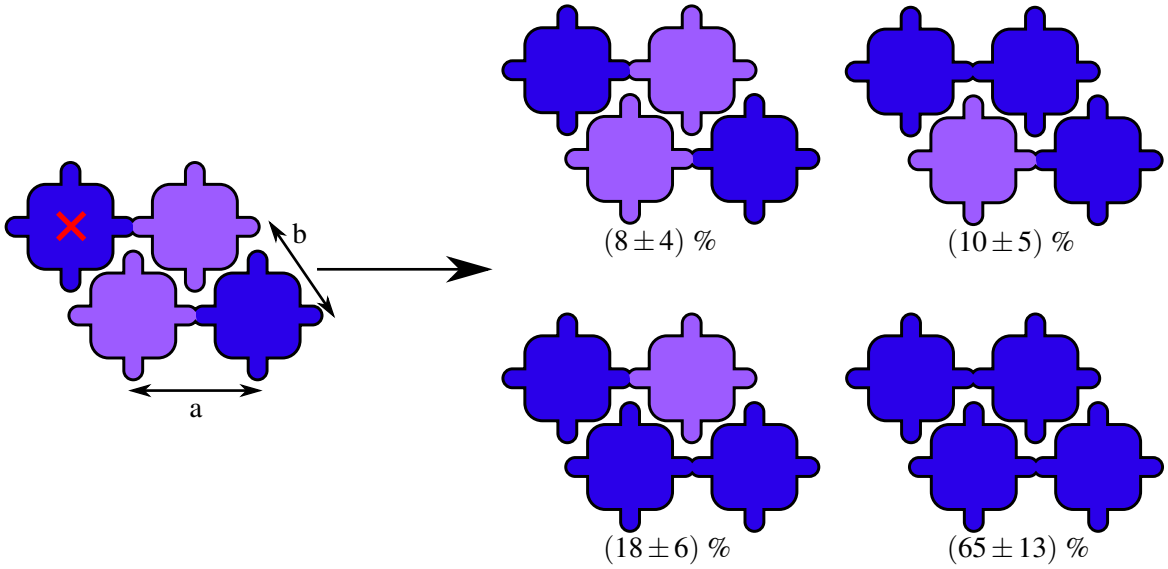

Figure 4.37.: Switching statistics of two dimer islands. The indicated dimensions are a: (1.72 ± 0.1) *nm* and (b): (1.42 ± 0.06) *nm*. The colors and pulse parameters are the same as in Fig. 4.35.

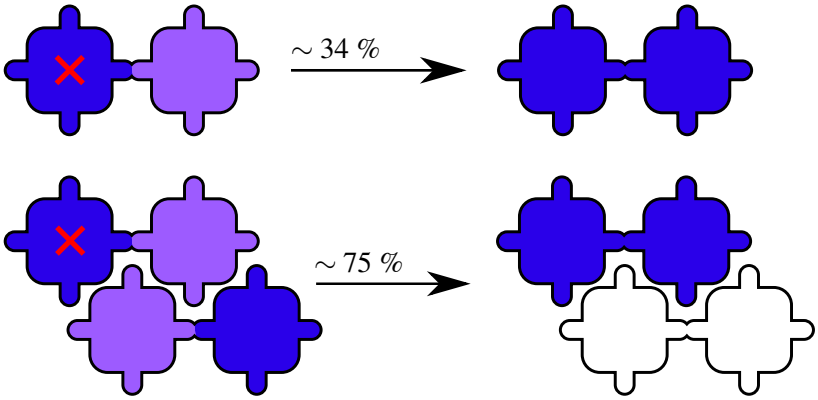

Figure 4.38.: Summary of Fig. 4.35 and Fig. 4.37. The lower row shows the probability of switching the molecule underneath the tip, independently whether the other dimer in the island switches or not.

voltage pulse was applied in the same way as for the single dimer experiments. The probabilities for the different outcomes were derived and can be found in the figure. It turns out that switching only the covalently bound (10 ± 5) % or the close-packed neighbor (18 ± 6) % has, within the error bars, the same probability, but the most likely event to happen is that the complete two dimer island is switched to dark (65 ± 13) %.

These results indicate that also different bonding mechanisms (covalent vs. close-packing) do not lead to communication between the switching units. As explained already in chapter 4.7.2, the voltage pulse probably does not remove the adatom from underneath the porphyrin unit, which is probably the reason why there is no communication between the two sides. It is however instructive

to compare the results obtained for the single dimer case with the one from the two dimer islands (Fig. 4.38). Applying a pulse over the dark side of a single dark – bright dimer switches it to dark – dark with a probability of about ~ 34 %. The presence of a second dimer next to it, regardles of its state, increases this probability to ~ 75 %. This effect could not be explained so far and would require additional investigation. However, it shows that the switching process is influenced by the atomic-scale environment of the molecule.

4.7.4. Room temperature switching of dimers

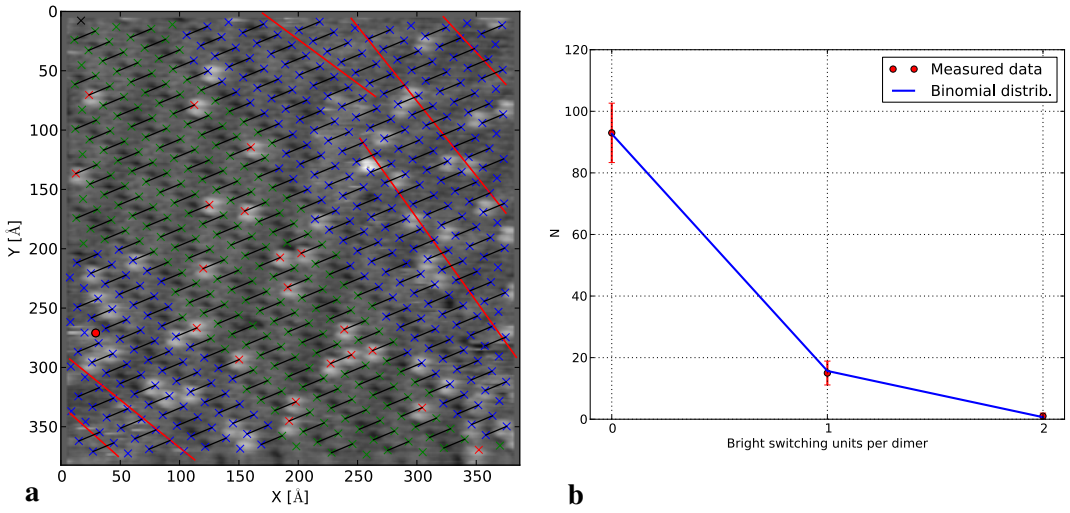

Figure 4.39.: TPP Dimers at room temperature. (a) shows a single frame out of a movie of TPP dimers on Au(111) (33 s/frame, $U_{sample} = 884\ mV$, $I = 0.03\ nA$, $T = 300\ K$). The dimers are marked with black lines, the other colors are the same as in Fig. 4.14. In (b), the occupation distribution of the dimers in (a) can be found together with the corresponding binomial distribution. The errorbars are the $\sqrt{N}$ counting errors.

The thermal switching of the dimers was also investigated at room temperature, which required a special sample preparation. As described in chapter 4.7.1, the dimers are formed by evaporating Br functionalized TPP monomers onto the surface, followed by a thermal activation. For room temperature measurements, a complete monolayer of molecules is required to prevent them from rapid surface diffusion. Such a monolayer is not easily achievable. Even when dosing several layers of monomers on the surface, after the thermal activation at 250°C, only a submonolayer of dimers stays on the surface, because at elevated temperatures, the desorption rate of the molecules is increased as well. Due to its rapid diffusion, the submonolayer cannot be imaged by STM. This problem could be solved by evaporating monomers after the thermal activation step again until the monolayer was completed. Both the dimers and the monomers segregate on the surface into single species domains, which can be investigated separately and therefore facilitate the experiment.

A typical image of TPP dimers on Au(111) can be found in Fig. 4.39 (a), where additionally to the normal colorcode, the dimers are marked by a black line. The size of the molecular island is not as big as in the case of single TPP, which is probably a result of the preparation parameters. Similar to the single TPP molecules (chapter 4.5.3), a high switching activity can be observed close to domain boundaries, step edges and point defects and therefore also in the case of the dimers, a large portion

of the molecules has to be excluded from the analysis (blue crosses in the image), in order to study only the unperturbed island. Additionally, the switching rate is lower than in the case of single TPP, and therefore the total number of observed switching events is much lower, leading to less significant statistics.

To find out whether the dark and bright states are distributed randomly in the dimers, the number of bright switching units per dimer was counted and compared to a binomial distribution (equation 3.4). The result can be found in Fig. 4.39 (b). Just as described in chapter 3.6.3, only a single frame can be used for this analysis because the change between the frames is very small. Obviously, the measured and the theoretical distribution agree perfectly and therefore, there cannot be any influence of the state of one side on the state of the other side within one dimer.

Otherwise, the dimers behave exactly as the single TPP molecules. The switching rate increases in the vicinity of defects, the dwell time histograms cannot be explained by a single exponential function and many molecules do not change their state over the entire movie.

After describing the TPP dimer experiments both at low temperature (chapters 4.7.2 and 4.7.3) and at room temperature in the present chapter, it is found as a conclusion that the different type of bonding (covalent vs. close-packing) does not affect the switching mechanism. Both sides of the dimers appear to be independent of each other and behave just like the monomers in close-packed structures. The presence of adatoms underneath the bright TPP units (chapters 4.6.3 and 4.8.1) could not further be confirmed in the dimer experiments, but also no contradictory results were obtained.

4.8. Theory

Conformer	Total energy (meV)
saddle A	0
saddle B	-61
saddle *cis*	271
planar	472
planar *cis*	808
saddle/planar mix	204
adatom A	0
adatom B	278
adatom C	222

Table 4.3.: Relative total energies of the different stable conformers of the TPP molecules on Au(111), resulting from the DFT calculations. The two groups with and without the adatoms are not comparable in terms of total energy and therefore are offset by a different amount. By courtesy of Felix Hanke and Mats Persson (University of Liverpool).

In order to understand the origin of the dark and bright molecular state (chapter 4.4.1), but also of the heated form of TPP molecules (chapter 4.4.4), density functional theory (DFT) calculations have been performed by Felix Hanke from the group of Mats Persson in the University of Liverpool. Their results are presented here in comparison with the experimental findings presented before.

The calculations were done with the VASP code [111], using vdwDF [112] in the implementation from [113] and the PBE exchange functional [114]. From the DFT results, STM images were calculated with the Tersoff-Hamann method [22] using the implementation described in [24].

4.8.1. The dark and bright state of TPP on Au(111)

The principle goal of this combined experimental and theoretical study was to understand the origin of TPPs dark and bright state on Au(111), then investigate the switching mechanism and eventually to find a way of how to couple the molecules together, such that a cooperative switching between them can be observed. Already the first step, namely identifying the molecular configuration for the dark and bright states, is very difficult.

The first guess was a switching between a saddle shape and a planar porphyrin core as in the case of [9], and they could indeed be identified as stable conformations in the DFT calculations. The results for the saddle shape can be found in Fig. 4.40. In this configuration, two opposing pyrole rings in the porphyrin macro cycle are bent up, the other two are bent down, which reduces the symmetry of the molecular core from four-fold to two-fold. Due to this symmetry breaking, the two H atoms in the center can be found in two different opposite configurations (saddle A and saddle B), but also in the saddle *cis* configuration, where the H atoms occupy neighboring N atoms. From a comparison between the calculated STM images in the same figure and the measured ones from Fig. 4.5, it becomes clear that saddle A and saddle B correspond to the dark molecules of the four molecule island in the lower right corner.

The calculations for the flat conformer can be found in Fig. 4.42. As the flat porphyrin core has the full four-fold symmetry, the H atoms only have the choice of either being in opposite positions (planar conformation) or adjacent positions (planar *cis*). Also a hypothetical saddle/planar mix was calculated.

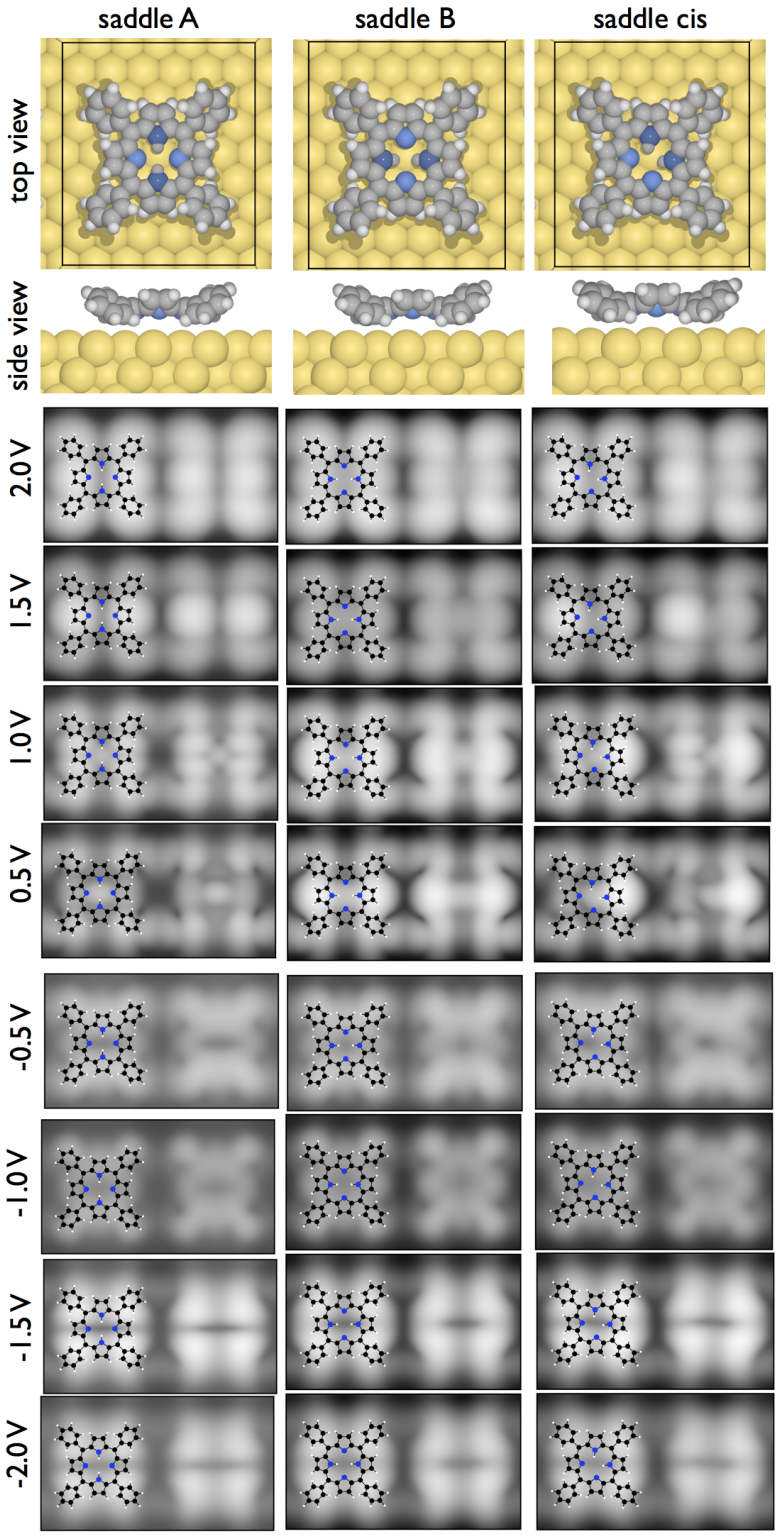

Figure 4.40.: DFT + vdW calculations and calculated STM images of TPP in saddle conformation on Au(111). The three configurations only differ in the position of the central H atoms. By courtesy of Felix Hanke and Mats Persson (University of Liverpool).

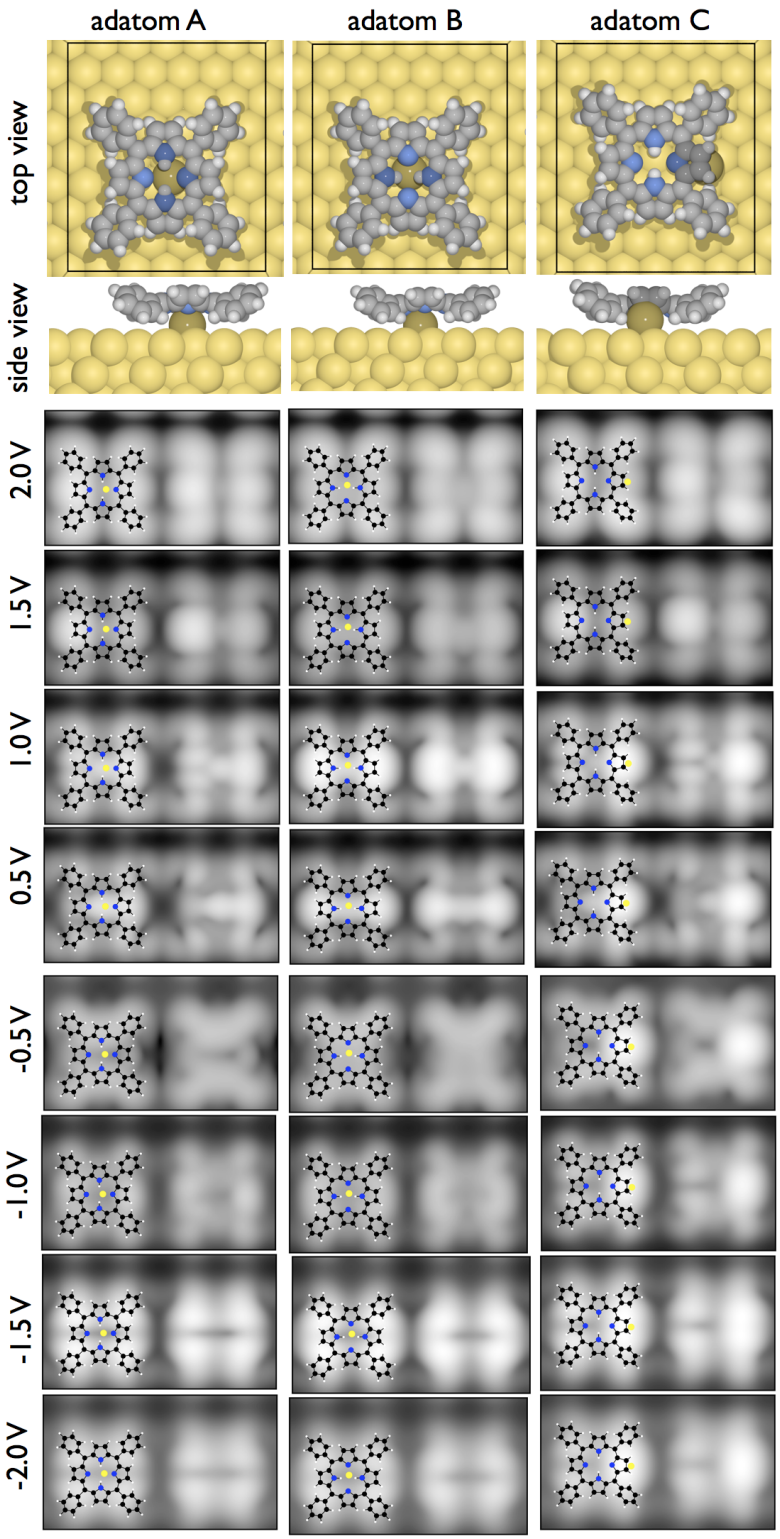

Figure 4.41.: DFT + vdW calculations and calculated STM images of TPP on Au(111) with a Au adatom underneath in three different positions. By courtesy of Felix Hanke and Mats Persson (University of Liverpool).

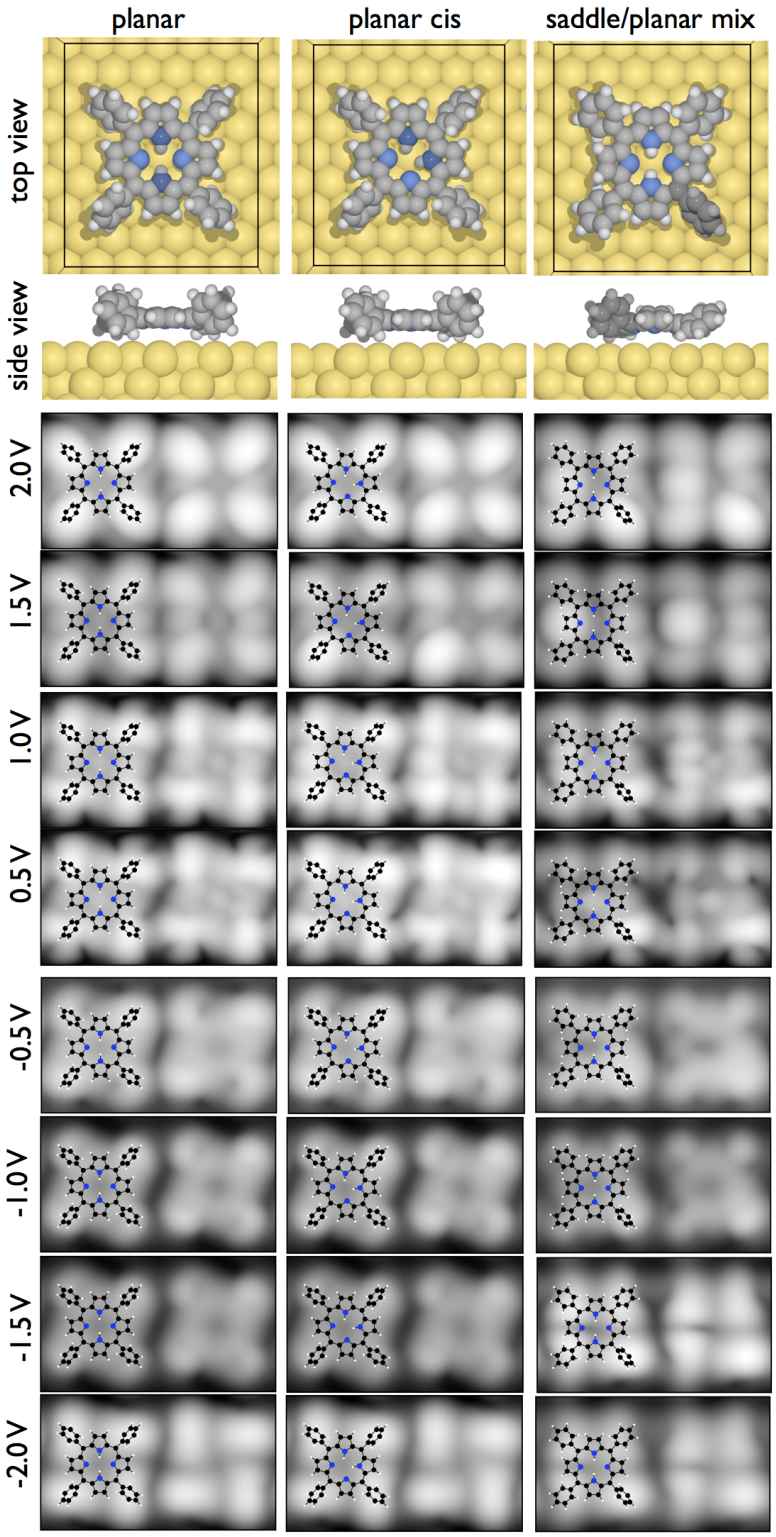

Figure 4.42.: DFT + vdW calculations and calculated STM images of TPP in two different planar configurations and one saddle/planar mix on Au(111). By courtesy of Felix Hanke and Mats Persson (University of Liverpool).

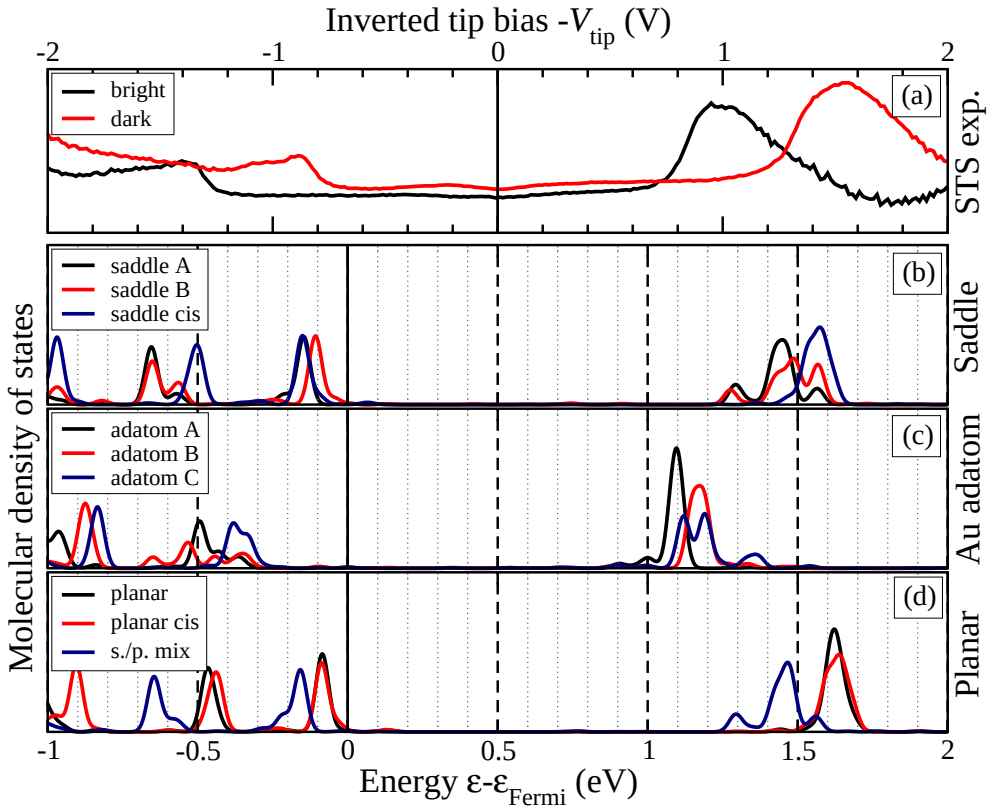

Figure 4.43.: Experimental and theoretical spectra of TPP on Au(111). (a) shows the measured dI/dV spectra of the dark and bright state. In (b), (c) and (d) calculated spectra corresponding to the conformations presented in Fig. 4.40, Fig. 4.41 and Fig. 4.42 can be found, respectively. The voltage scale in (a) has been inverted to allow for a better comparison with the calculated spectra. By courtesy of Felix Hanke and Mats Persson (University of Liverpool).

None of the calculated STM images show a sufficient agreement with the bright state in the measured images (Fig. 4.5).

Table 4.3 shows the calculated total energies of the different conformers, with respect to the conformer with the lowest energy. Obviously, saddle A and saddle B have the lowest energy, with only a minor energy difference, and are therefore expected to be seen at low temperatures on the surface in any case. All the other conformers, including the *cis* and especially the flat conformer, are so high in energy that even at room temperature ($k_BT = 25\ meV$) they would not be expected to be observed.

Furthermore, a valid solution would be expected to explain the rigid shift in the molecular density of states (DOS), which was observed in the measured dI/dV spectra (chapter 4.4.3). Fig. 4.43 (b) and (d) show the calculated spectra of the conformers discussed above, but none of them shows the expected rigid shift, the spectra only differ in the relative intensities of the orbitals involved. The easiest explanation for such a shift would be a charging/decharging of the molecule on the surface as observed in [35, 96]. Calculated ionizations potentials and electron affinities in the gas phase (Tab. 4.4) show that saddle and planar conformations in the gas phase could reduce their energy by about 2 eV when accepting an additional electron. Nevertheless, on the surface, DFT calculations do not show charging

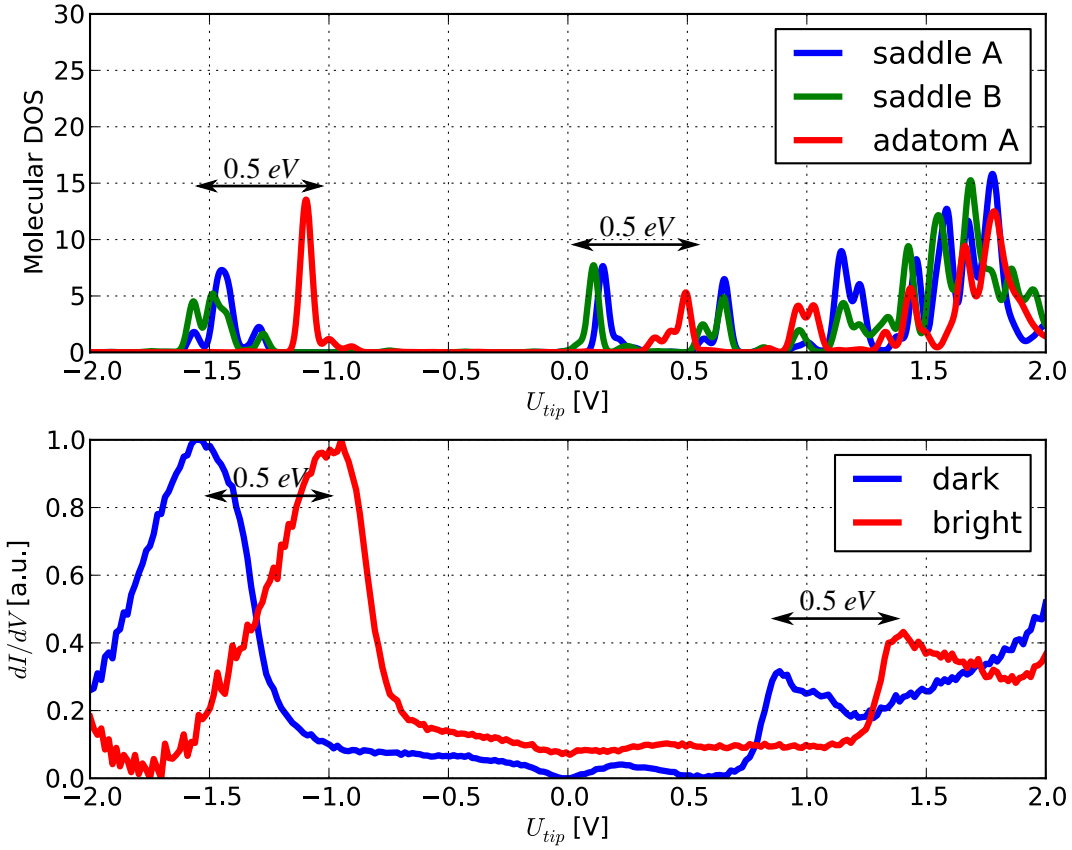

Figure 4.44.: Detailed comparison between the calculated spectra (upper panel) from Fig. 4.43 and the measured ones (lower panel) from Fig. 4.8. The experimental spectra of dark and bright molecules are shifted by 0.5 eV with respect to the Fermi level. A shift of almost the same amount was found in the calculated spectra when assuming an adatom underneath the TPP molecule. Calculated spectra by courtesy of Felix Hanke and Mats Persson (University of Liverpool).

for any of the conformations considered so far. This finding actually agrees with the measured spectra, as the LUMO of the bright molecules is shifted towards the Fermi energy but is not crossing it, which would lead to a population of this orbital with electrons and consequently, due to the charging of the molecules, an electrostatic repulsion between them would be expected [95] which was not observed experimentally (chapter 4.4.2).

Another possibility is that a gold adatom is involved in the bright molecular state. At first it was tried if the TPP molecules can pull an adatom out of the top surface layer and partially incorporate it in the porphyrin core, similar to what was described in [75] for Br_4TPP on Cu(111), but in the calculations no such configuration could be found, the gold atom always relaxes back into the surface. Consequently, if an adatom plays a role, it must be an additional free adatom on the surface. Fig. 4.41 shows three possible configurations of a buckled TPP molecule with an additional adatom underneath. The relative energies of these configurations (Tab. 4.4), show that the configuration adatom A is clearly energetically preferred, and its calculated STM images agree with the measured ones (Fig. 4.5) reasonably well. Moreover, although the exact shape of the spectra could not be reproduced by the calculations, the

charge	saddle	planar
$+e$	6.23 eV	6.42 eV
0	0 eV	-0.04 eV
$-e$	-2.02 eV	-2.01 eV
$-2e$	-1.66 eV	-1.62 eV

Table 4.4.: Calculated total energies for TPP molecules in the gas phase depending on their charge. By courtesy of Felix Hanke and Mats Persson (University of Liverpool).

shift in the spectra of half an eV is reproduced for this configuration in the calculated spectra (Fig. 4.44) perfectly. Due to this good agreement between theory and experiment, the bright state of TPP on Au(111) could be identified as adatom A.

As a summary, the experimentally observed dark states could be identified as saddle A and saddle B, a saddle shape deformation of the central porphyrin macrocycle with the H atoms in the two opposing configurations. The bright state, could be identified as adatom A, also a TPP molecule in a saddle shape deformation but having a gold adatom underneath its center, which is a very surprising result that to my knowledge has not been observed before.

4.8.2. Annealed TPP

After having understood the origin of the dark and bright TPP molecules, it would be interesting to also understand the annealed form, which was presented in chapter 4.4.4. Knowing that an adatom is involved in the bright state of the TPP molecules on Au(111), the first guess was that during the annealing the central H atoms leave the porphyrin and the Au adatom gets fully integrated as a metal center as in [75, 70, 76, 72]. Calculated STM images of such a metalated porphyrin (First two columns in Fig. 4.45) and the STM images of TPP with a gold center presented in [115, 108], however, do not agree with the annealed TPP molecules.

Another possibility would be that the two central H atoms leave the molecule. Calculated STM images of this configuration can be found in the last two columns of Fig. 4.45, which also do not agree with the measured STM images. However, if the change in contrast upon annealing was due to a change in the porphyrin center, it would be expected to see only one type of molecules after the annealing, but this is not the case, the appearance in the STM images seems to vary from molecule to molecule (Fig. 4.11).

A possible explanation taking into account different appearances of the molecules could be a chemical modification of the phenyl rings, which could form a second covalent bond to the porphyrin core, just like observed in [116, 117]. Every phenyl ring would have the option of binding on the right or on the left side of his first bond, which could in principle lead to 16 different structures. As an example, one of these structures has been calculated by DFT (Fig. 4.46). Obviously, the additional bonds force the molecule in a flat configuration, a saddle deformation can therefore not be stable. The calculated STM images show much more internal structure than the measured ones, which might be due to the state at the Fermi level in the calculations, contributing to the image contrast at every bias voltage. A state at the Fermi energy could be an indication for a charged molecule, explaining the experimentally observed repulsion between the molecules and their inability of forming islands. However, the STM images do not show this internal structure.

Even though the origin of the molecular state after annealing could not unambiguously be determined, the cyclodehydrogenated state seems to be the most likely option and could be tested experimentally

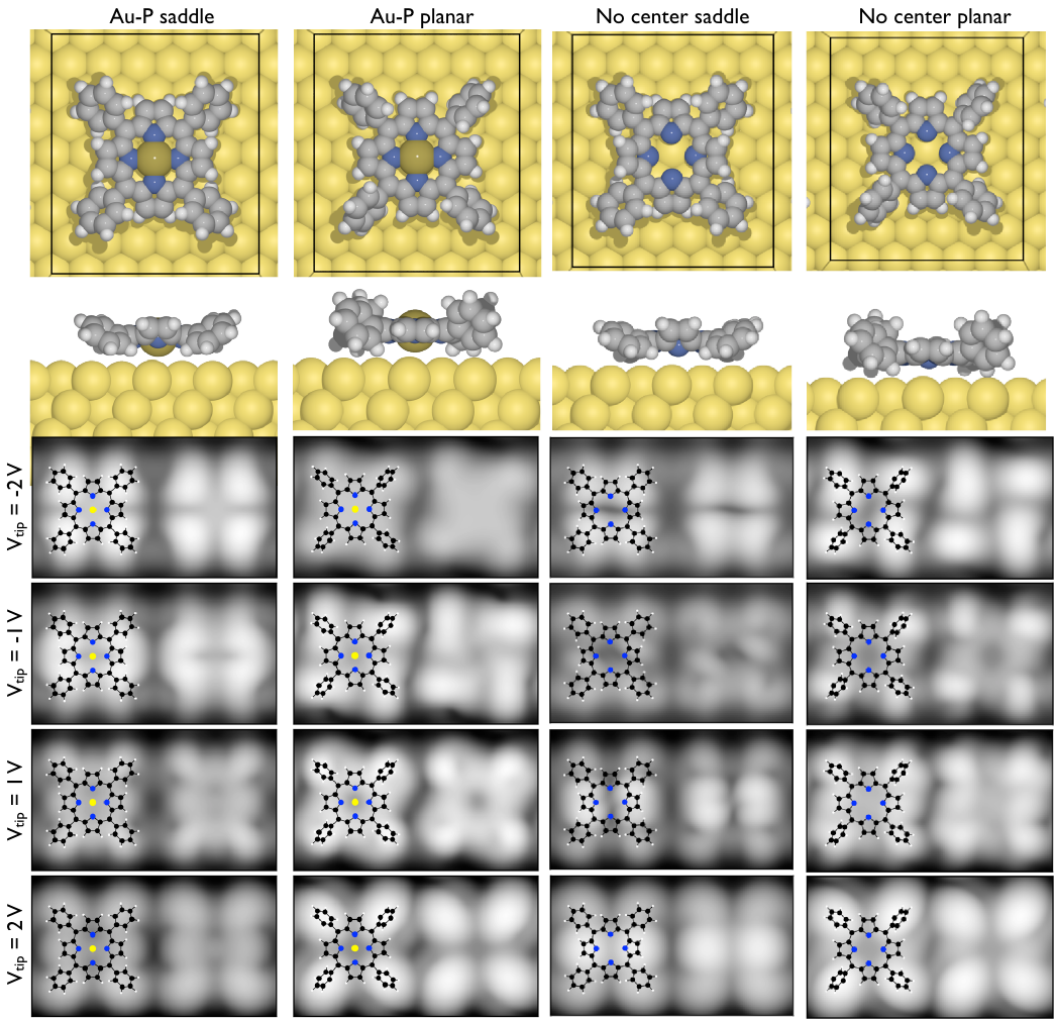

Figure 4.45.: Optimized structures and STM images calculated by DFT of saddle and planar Au-TPP molecules in the first two columns and of saddle and planar dehydrogenated TPP in the last two columns. By courtesy of Felix Hanke and Mats Persson (University of Liverpool).

by synthesizing such a molecule, evaporating it on Au(111) and comparing its appearance with the one of heated TPP (Fig. 4.11).

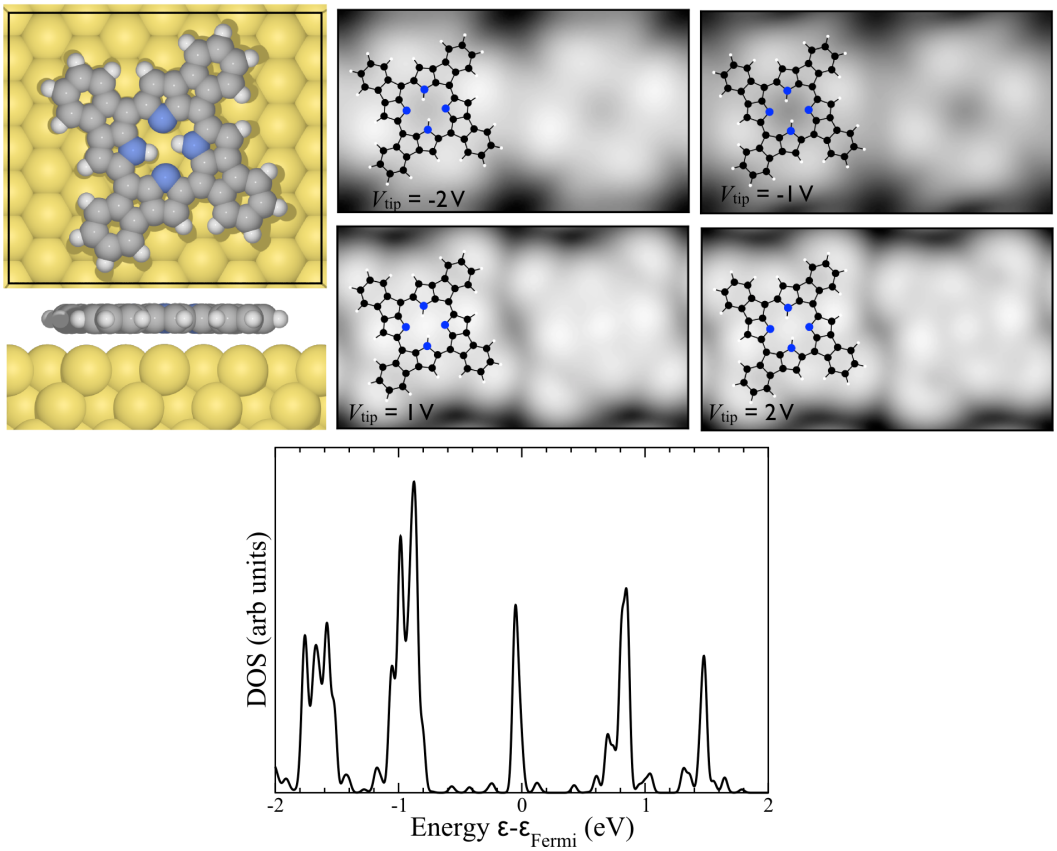

Figure 4.46.: Calculated structure, STM images and dI/dV spectrum of a cyclodehydrogenated TPP molecules. By courtesy of Felix Hanke and Mats Persson (University of Liverpool).

4.9. Conclusion

Tetra-phenyl-porphyrin (TPP) molecules as well as Br_4TPP molecules have been investigated mainly on Au(111), but also on Ag(111). On Au(111), they show two distinct states, which can be distinguished in STM images by their characteristic bright and dark appearances (chapter 4.4.1). This is because the dI/dV spectra of the dark and bright molecules have the same shape but the bright spectrum is shifted by half an electron volt towards the occupied states (chapter 4.4.3). Reversible switching is possible between these two states and can be triggered by voltage pulses, which are applied with the STM tip (chapter 4.6), or by thermal activation at room temperature (chapter 4.5). The origin of the dark and bright states is investigated and the molecules are tested for cooperative effects between neighboring molecules, in dependence on their respective bonding mechanism.

When a full monolayer is investigated at room temperature (chapter 4.5), the temporal evolution of the dark–bright pattern of the molecules can be studied by scanning the same sample area repeatedly. Due to the dense packing of the molecules, a high number of them (typically several hundred) is imaged in one frame and the thermally activated switching leads to a high number of switching events. By analyzing the distribution of dark and bright molecules, it could be shown that there is no influence of the state of one molecule on the state of its neighbors (chapter 4.5.4). The switching process, however, is not random. When one of the molecules switches from bright to dark between two frames there is a high probability that in its vicinity a dark molecule changes to the bright state (chapter 4.5.6). In other words, it seems as the bright state can be transferred to a surrounding molecule.

The origin of the dark and bright state could be understood in collaboration with Felix Hanke and Mats Persson from the University of Liverpool, who performed DFT calculations of the molecules adsorbed on Au(111) (chapter 4.8.1). They were able to identify the dark state as a saddle shape conformation of the porphyrin macrocycle on the surface and the bright state as a similar saddle shape conformation but this time having an additional gold adatom underneath. The calculated STM images agree well with the measured ones and even the experimentally observed rigid shift in the dI/dV spectra by half an electron volt were reproduced in the calculations.

The presence of adatoms underneath the bright molecules is in agreement with the observed hopping of the bright state at room temperature. Also STM experiments at low temperature confirm the presence of the adatoms. It is shown that molecules can be switched from dark to bright when artificial adatoms are created on the surface by crashing the STM tip into it (chapter 4.6.2). Furthermore, when a bright molecule is situated above an elbow of the Au(111) herringbone reconstruction, it is possible to laterally manipulate the molecule away which turns dark, leaving an adatom behind which is trapped at the elbow site (chapter 4.6.3). When pushing the same molecule back on the adatom, it can return to the bright state again. The switching of a molecule due to the presence of an adatom is an interesting phenomenon which, to my knowledge, has not been observed before.

Even after understanding the origin of the dark and bright state, the temporal evolution of the molecule covered surface at room temperature remains unexplained (chapter 4.5.5). It was noticed that a high number of molecules remains inactive and does not show a single switching event during the duration of a movie ($> 1\ h$). Furthermore, the switching events are correlated in time. It was observed that over longer periods, no switching is detected, but suddenly, between two frames, many molecules change their state, to be followed again by a longer period of low switching activity (chapter 4.5.7). The mechanism behind this correlation could not be clarified. A model of the adatom migration between the surface and the molecular layer would be of great interest for identifying the relevant processes and remains as a challenge for future theoretical investigations.

To investigate the influence of the bonding mechanism on the switching process, the molecules where covalently linked into dimers (chapter 4.7). Inside the dimers, every porphyrin group can switch

between dark and bright. By applying voltage pulses at low temperature, it was tested if there is some influence of the state of one side to the switching probability of the other side, but no such correlation could be found. The dimers were also investigated at room temperature where they also display thermal switching. Here it was found that the distribution of dark and bright states in the dimers is random and that they behave very similar to the monomers.

At this point, after describing all the experiments done with the porphyrin molecules, it is necessary to ask the question whether cooperativity has been found between the molecules or not, i.e. whether the molecular ensemble behaves differently than single TPP molecules. The answer is: Maybe yes, because as was demonstrated in chapter 4.5.7, during the cascade events, many molecules switch at the same time and there obviously needs to be some sort of communication between them. However, the mechanism of this process could not be resolved yet and therefore nothing can be said about whether this is a cooperative effect or not. An example for a process that looks like cooperative at first glance is the hopping of the bright state from one molecule to neighboring ones at room temperature (chapter 4.5.6). When looking at it phenomenologically, this hopping reminds very much of the hypothetical conformational transport process described in Fig. 4.1. However, after understanding that the bright state is created by the presence of a gold adatom underneath the molecule, this transfer of the bright state can simply be understood as a hopping of the adatom from one molecule to the next, which is not a cooperative process. As can be seen from this example, the appearance of correlated processes does not necessarily mean that they are cooperative. Further experiments or theoretical investigations would be needed to investigate the origin of the cascade events in order to decide whether this process is cooperative or not.

5. Nanocars

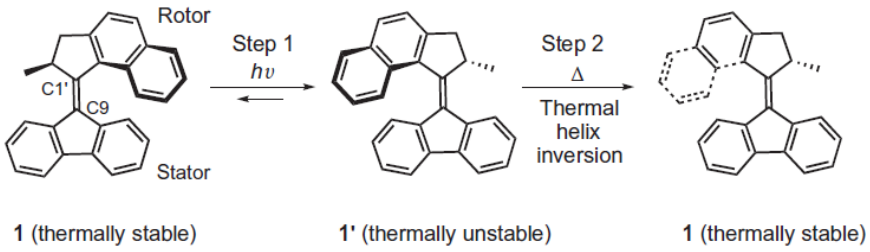

Figure 5.1.: Working principle of the molecular motor based on overcrowded alkenes, developed in the group of Ben Feringa. In the first step, the central double bond is excited by light and the motor turns by almost 180°. This step is followed by a thermal helix inversion. Repeating these steps another time leads to a full 360° unidirectional rotation of the motor. Reprinted by permission from Macmillan Publishers Ltd: Nature Chemistry [118], copyright 2012.

Molecular diffusion usually happens in three dimensions and is important in biological processes [119]. If macroscopic concentration gradients are present, the diffusion will make them vanish over time until the thermal equilibrium is reached. When molecules are adsorbed on a surface, the diffusion motion is restricted to two or, depending on the substrate symmetry, even to one dimension [120]. Even in the one dimensional case, the adsorbates still have the possibility of diffusing forward and backward.

Molecular machines capable of doing work, sufficient energy input provided, can drive a system out of its thermal equilibrium. For example, nature uses the protein myosin V to transport cargo inside living cells. Propelled by adenosine-5'-triphosphate (ATP), it is "walking" along actin filaments [4, 5] with a strong direction preference. To mimic this function, i.e. to transport cargo by directed motion at the atomic level, using synthetic molecules is a severe design challenge. One approach which has been followed actively in the last years is to synthesize a so called nanocar with several wheels, restricting the motion on a flat surface to one dimension only, and a molecular motor that drives it forward.

Several attempts have been taken to realize such a nanocar, most intensively this goal was pursued in the group of James Tour at Rice university. They were the first to come up with a nanocar design having a chassis and fullerene wheels but no motor, yet. This car was placed on a Au(111) surface and motion could be induced thermally and with the STM tip [121]. Although there were signs of directionality, it did not become clear whether the wheels are actually rolling on the surface, or if the normal hopping prevails which means that the wheels are moving to the next adsorption site without changing their orientation. However, due to their spherical shape it is very difficult to proof rolling of molecular wheels in general, the only successful example so far is [34] (vide infra). Moreover, as fullerene groups, which serve as wheels in this car, are normally insoluble, ten long $C_{10}H_{21}$ side chains had to be attached to the molecule to make it soluble. The role of these chains on the surface is unknown, but due to their length and their high number, they probably cannot be neglected.

In parallel, the group of Ben Feringa at the University of Groningen developed a light- and thermally

activated class of unidirectional molecular motors [122, 123, 124, 125, 126, 118]. These motors consist of two helical, overcrowded alkene units, connected by a carbon - carbon double bond (Fig. 5.1). Due to the design of the molecule, steric hindrance is present between the two sides which prevents the molecule from free rotation. Upon illumination with light of the correct wavelength, the central double bond can undergo a *trans - cis* isomerization, followed by a thermally induced helix inversion of the overcrowded alkenes, leading to a 180° rotation. Repeating this process yields a full 360° unidirectional rotation of the two halfs of the molecule.

Obviously these kinds of motors are promising candidates for propelling nanocars. For a first time in contact with a solid, these motors were reported working on the surface of gold nano particles [127], and were soon after incorporated into the fullerene wheeled nanocars. They were supposed to drive the car by the rotating paddle of the motor. However, the presence of the fullerene wheels seemed to quench the function of the motor [128]. As an alternative, p-carborane wheels where employed, which also have the advantage over fullerene, that the molecule stays soluble even without the side chains that become unnecessary in the molecular design. The rotation speed of the motor in this car was very low, only 1.8 rotations per hour were measured at 65°C in solution, which is not sufficient for low temperature STM surface studies (in addition to the role of the surface).

It was tried to prove the rolling of the cars by fluorescence spectroscopy [129, 130, 131], too, but rolling of the wheels could not be proven unambiguously. The only molecule so far which was shown to roll on a surface consists of two triptycene molecules connected by an axle [34]. With its three spikes, triptycene can be turned by STM because one spike is always pointing up and and that is where the STM tip applies the force during lateral manipulation. It also leads to a characteristic manipulation signal, which proves that the wheel is rotating. However, molecules with a more spherical shape like fullerenes, p-carboranes and adamantanes have presumably a lower rotation barrier and were therefore used in the nanocars.

In the meanwhile, many different types of cars where synthesized by the Tour group, including a nano dragster [132] having two fullerene and two p-carborane wheels, a nano truck [133] containing a porphyrin unit, that could potentially take up metal atoms, similar to what has been reported by lateral STM manipulation [134], and deliver them somewhere, and nano trains [103], molecular wagons with two p-carborrane wheels each, which are assembled on the surface to long chains via metal coordination bonds.

To overcome the problem of the low rotation speed in the motorized nanocar, a new version was synthesized [11] using a different motor with less steric hindrance, capable of a much higher rotation speed in the MHz range [124]. Investigating this molecule by STM on surfaces and trying to activate the motor by illuminating it with light was done within the presented PhD thesis.

At the same time, Feringas group also synthesized a nanocar with a completely different design [12]. Instead of the wheels they put four motors in the molecule and were able to show that they could induce rotation and directed motion on a Cu(111) surface by activating the motor with tunneling electrons from the STM tip.

5.1. Carborane cars

In this chapter, the experiments of the p-carborane car with the fast motor (Fig. 5.2) are described. The goal of this study was to deposit the molecules intact on the surface, image them and - if possible - make the motor rotate either by tunneling electrons from the STM tip or with light (the used lasers are described in chapter 3.5). Different surfaces were tried.

Already the deposition of the nanocars is a significant challenge because the molecules are rather

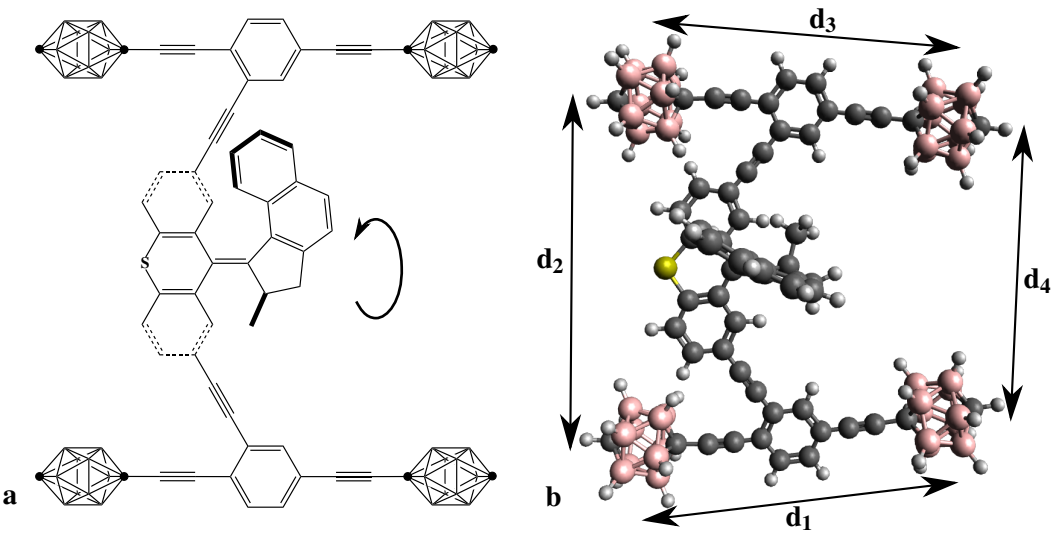

Figure 5.2.: Chemical structure of the carborane car (a) where in the wheels every intersection corresponds to BH and only the black dots to C or CH and its gas phase structure calculated with Hyperchem 7 (b). The calculated dimensions are d_1: 1.38 *nm*, d_2: 1.42 *nm*, d_3: 1.38 *nm*, d_4: 1.51 *nm*, the mass of one molecule is 1241 *u*, it dissolves in non-polar solvents like hexane or dichloromethane and can be excited in solution with a wavelength of 355 *nm*.

large and therefore the sublimation temperature can exceed the dissociation temperature, leading to fragmentation during evaporation and thereby to dirty samples. Furthermore, the molecules are not stable in air, and were therefore delivered in a protecting atmosphere. Regardless of the surface, many attempt of evaporation were undertaken until a sufficient coverage of car molecules was reached. Clearly, sample preparation was the most time-consuming step in the nanocar experiments.

5.1.1. Au(111)

The first surface to be tried was Au(111) because it is the most commonly used surface for molecular adsorption, providing an inert support for the molecules. Overview images can be found in Fig. 5.3. After thermal evaporation on the surface held at room temperature, some nanocar molecules are present on the surface, consisting of five lobes, most probably corresponding to the four wheels and the motor group. However, as the preparation was not very clean and actually most of the adsorbed material are unidentified fragments, the molecules are never found isolated on a terrace, they are always surrounded by fragments and are generally found close to a step edge. This happens probably because of the low diffusion barrier on gold, which permits that molecules and fragments assemble in clusters. Separating the molecules from the contamination using tip manipulation was not successful because the amount of fragments was too high.

It was tried to illuminate the sample with light of 248 *nm*, which is not exactly the wavelength needed in solution ($\approx$ 360 *nm* [124]), but molecular levels usually get broadened on the surface and different excitation mechanism are possible on surfaces, too. An example is the azobenzene derivative TBA, which is switched in solution by exciting the HOMO – LUMO transition directly with light of the appropriate wavelength, but on Au(111) the light creates a hole in the metal d-bands, which migrates to the molecular HOMO and triggers the switching [135, 136]. This process happens with all photon energies above a certain threshold. In the case of the nanocar, a similar *trans-cis* isomerization

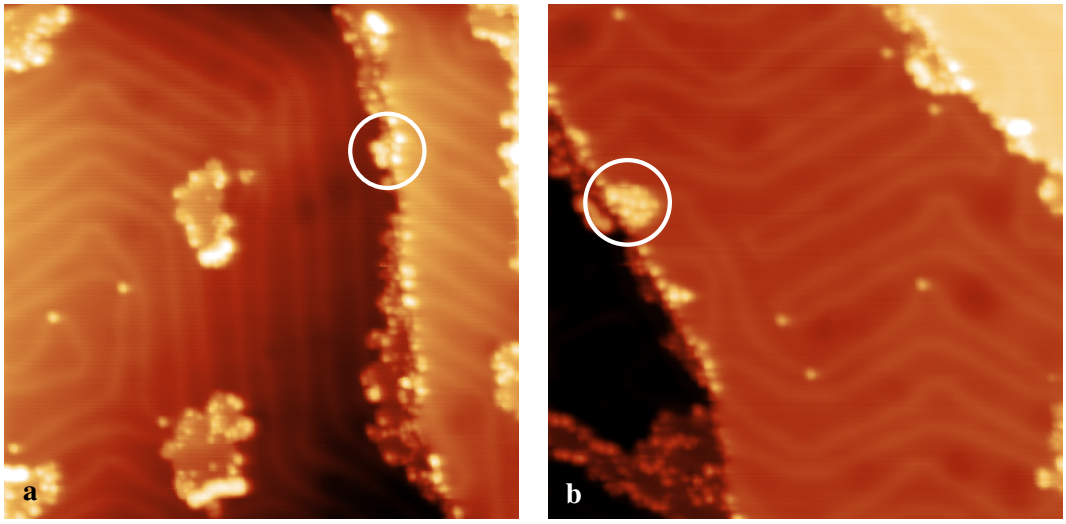

Figure 5.3.: Overview images of p-caborane nanocar molecules on Au(111), two cars are marked with white circles. Image parameters: (a) $55.6 \times 55.6\ nm^2$, $U_{tip} = 1\ V$, $I = 0.1\ nA$, $T = 5.7\ K$, (b) $49.8 \times 49.8\ nm^2$, $U_{tip} = 1\ V$, $I = 0.1\ nA$, $T = 5.6\ K$.

needs to be activated for the rotation of the motor and because the used photon energy is higher than the necessary energy in solution, a similar mechanism as in the case of TBA might be possible.

Images before and after the illumination can be found in Fig. 5.4. Apparently, there was no change in the intact nanocar molecules but after the illumination there were slightly more fragments on the terrace than before, probably because the light activated their diffusion, which shows that the light must have arrived to the spot of the sample under investigation.

In conclusion, Au(111) turned out not to be the right surface for the carborane nanocars. Apparently the cars and other fragments are too mobile at room temperature, such that the cars can never be found alone on a terrace, which is an important prerequisite for manipulation experiments. Because of this unknown atomic-scale environment, an analysis of the illumination experiments is difficult. To overcome the mobility problem a different, more reactive surface was chosen as a substrate: Cu(110).

5.1.2. Cu(110)

Due to the problems on the Au(111) surface described in the previous chapter, it was tried to deposit the molecules on the more reactive Cu(110) surface. This surface is harder to prepare as the (111) coinage metal surfaces because in the presence of even minute quantities of oxygen, an added row reconstruction is formed [137]. Due to a leak in the manipulator, this reconstruction was always present on the surface, but also sufficiently clean metal areas could be found. As the molecules were exclusively found on the bare metal, the existence of the oxygen reconstruction is not a problem for the planned experiments.

After evaporation of the nanocars at room temperature onto the Cu(110) surface, the sample is clean (Fig. 5.5) and many intact cars can be found. Every car consists of five lobes (Fig. 5.5 (b)). By comparison of the measured dimensions on the surface and the calculated dimensions in the gas phase (Fig. 5.2), the four outer lobes can be assigned to the carborane wheels and the inner one to the motor. The cars are exclusively found adsorbed on step edges and at the border of the oxygen reconstruction, indicating that they are mobile at room temperature, because they had the freedom to diffuse to their

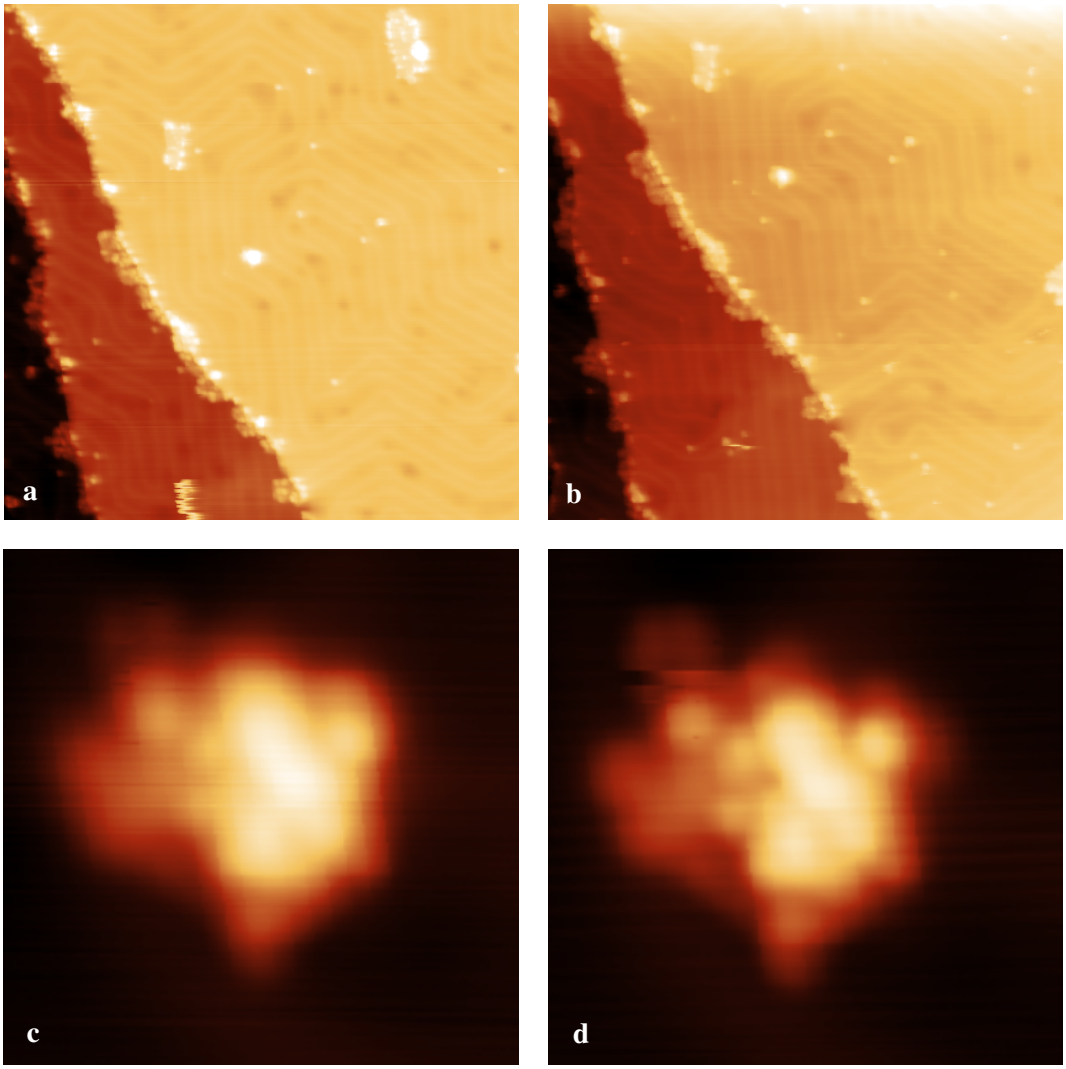

Figure 5.4.: Carborane nanocars on Au(111) before and after illuminating the sample with light. Illumination parameters: $\lambda = 248\ nm$, repetition rate: $10\ Hz$, duration: $20\ min$, $T_{STM} = 6.1\ K$ (the laser system is described in detail in chapter 3.5). Image parameters: (a) and (b) $102.3 \times 102.3\ nm^2$, $U_{tip} = 1\ V$, $I = 0.1\ nA$, $T = 5.6\ K$, (c) and (d) $6 \times 6\ nm^2$, $U_{tip} = 1\ V$, $I = 0.1\ nA$, $T = 5.6\ K$.

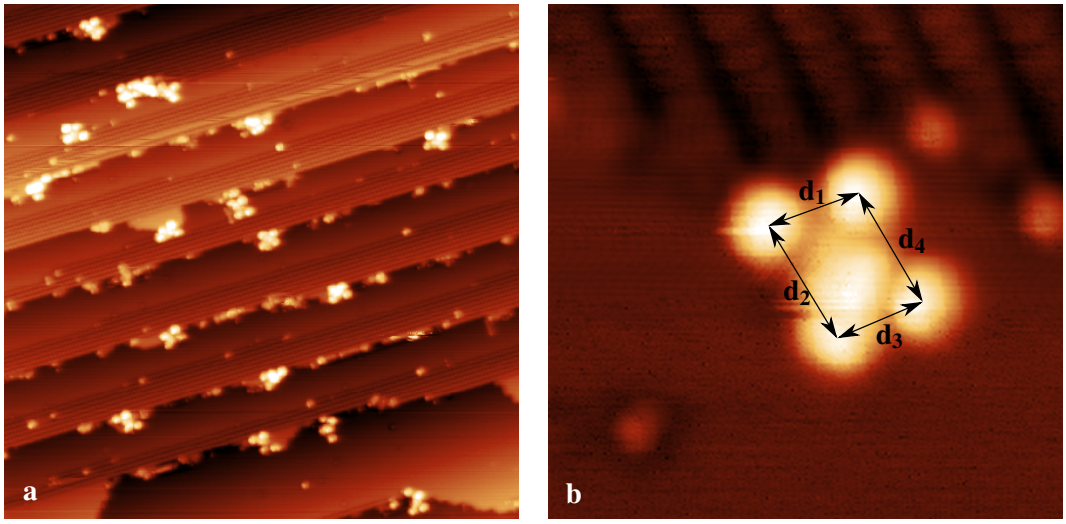

Figure 5.5.: Carborane nanocars on Cu(110). Flat terraces correspond to the clean copper surface, the rough areas are the oxygen added row reconstruction [137]. The dimensions of the nanocar in (b) are d_1: 1.38 *nm*, d_2: 1.83 *nm*, d_3: 1.30 *nm*, d_4: 1.74 *nm*. Image parameters: (a) 63.5×63.5 nm^2, $U_{tip} = 1$ V, $I = 0.1$ nA, $T = 5.5$ K, (b) 7.3×7.3 nm^2, $U_{tip} = 1$ V, $I = 0.1$ nA, $T = 5.6$ K.

preferred adsorption site. However, the nanocars could not be moved by lateral manipulation (with manipulation resistances down to 10^5 Ω), which points to a strong adsorption of the molecules. This shows that the molecules are weakly bound on the terrace, where they are mobile at room temperature, but strongly bound at step edges and the border of the reconstruction.

As in the case of the gold surface, it was also tried to trigger motion of the motor by illuminating it with light at a wavelength of $\lambda = 248$ *nm* and a repetition rate of 10 Hz (chapter 3.5), but no changes in the molecular appearance could be detected after three repetitions of the experiment (once for 10 *min*, twice for 45 *min*). Using rather strong voltage pulses of more than ± 3.5 V it is possible to change the appearance of the car (Fig. 5.6). However, it is not only possible to change the apparent height of the motor but also the height of the wheels. As the changes in appearance were not periodic nor reversible and the required voltages are quite high, this is probably not an effect of a turning motor but rather a dissociation of the molecule.

5.1.3. Ag(111)

After the experience from the Au(111) surface, where the molecules were so weakly bound that they were always surrounded by fragments and the Cu(110) surface, where they were bound so strongly that even lateral manipulation was not possible, making any motorized motion very unlikely, a different substrate with an intermediate reactivity was chosen for the further experiments: Ag(111). It shows no reconstruction and is just a flat truncation of the bulk crystal.

When evaporated on a Ag(111) surface at room temperature, molecules can be found exclusively on the stepped regions of the surface (Fig. 5.7), never on larger terraces. As can be seen in the same figure, lateral manipulation is possible (at a manipulation resistance of $6 \cdot 10^7$ Ω), but the nanocars strongly bind to the step edges, and behave as if they were on rails. As shown in (b) and (c), they can easily be displaced parallel to the step edge, but when manipulation is attempted in the perpendicular direction

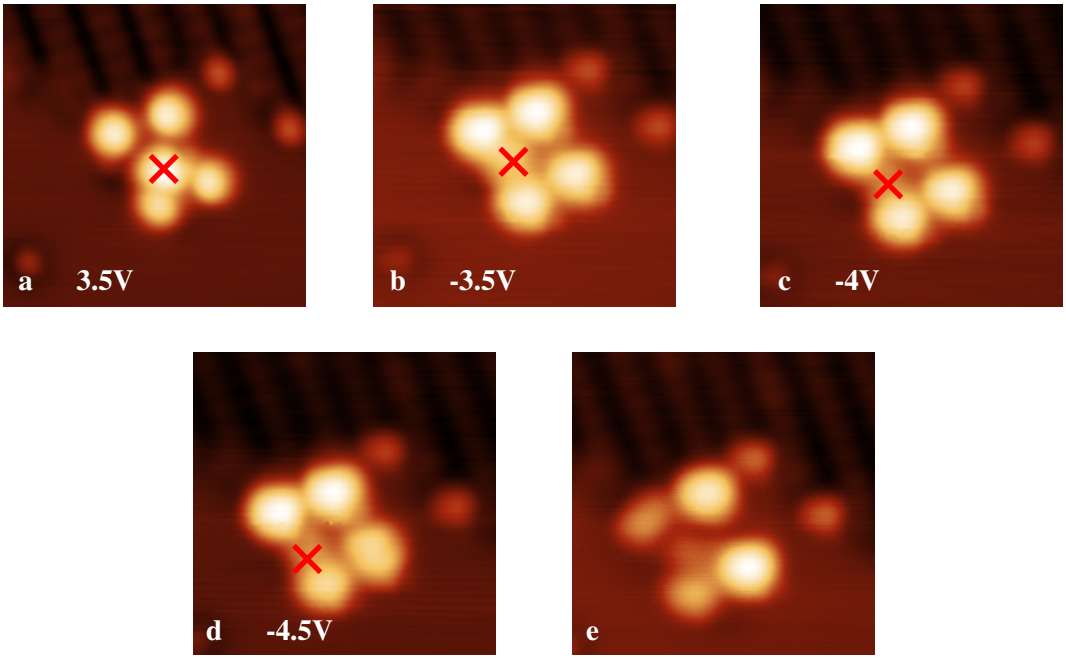

Figure 5.6.: Applying voltage pulses to the carborane nanocars on Cu(110) over the indicated position, ramping the voltage from 0 V to the indicated voltage. Image parameters for all images: $6.8 \times 6.8\ nm^2$, $U_{tip} = 1\ V$, $I = 0.1\ nA$, $T = 5.5\ K$.

((d) to (g)), it is difficult to separate the wheels from the steps and they easily snap back already during scanning. Having the molecules single on the terrace would be interesting also with the illumination experiments in mind, but could not be achieved because high coverages saturating all steps cannot be done with this molecule and deposition at low temperature was not possible experimentally.

However, the same illumination experiment as in the case of the previous substrates with light of $\lambda = 248\ nm$ was tried also on the Ag(111) surface in several attempts, but again without inducing any change in the molecular appearance.

5.1.4. Cu(111)

Another metal substrate used to study the carborane nanocars was Cu(111). It was hoped to obtain rather clean preparations with single molecules on terraces and just the right binding strength for the molecules to facilitate motion upon illumination, because too strongly bonded wheels might quench the motion, but there needs to be at least some friction between the surface and the potentially rotating motor to convert the rotation into directed motion on the surface. Furthermore, Cu(111) shows no reconstruction and the only working motorized nanocar so far [12] has been studied on Cu(111), which makes this particular surface a good candidate.

In the first evaporation attempts, very clean surfaces with many intact molecules at the step edges could be obtained (Fig. 5.8 (a)). Unfortunately, only in few exceptional cases single molecules were found on the terraces. It was tried to force the molecules onto the terraces by increasing the coverage and thereby saturating the preferred adsorption sites at the step edges (Fig. 5.8 (b)). However, at the same time, the number of molecular fragments on the surface also increased up to a considerable coverage, but it was still possible to find single molecules on the terraces (Fig. 5.9). Hence, the

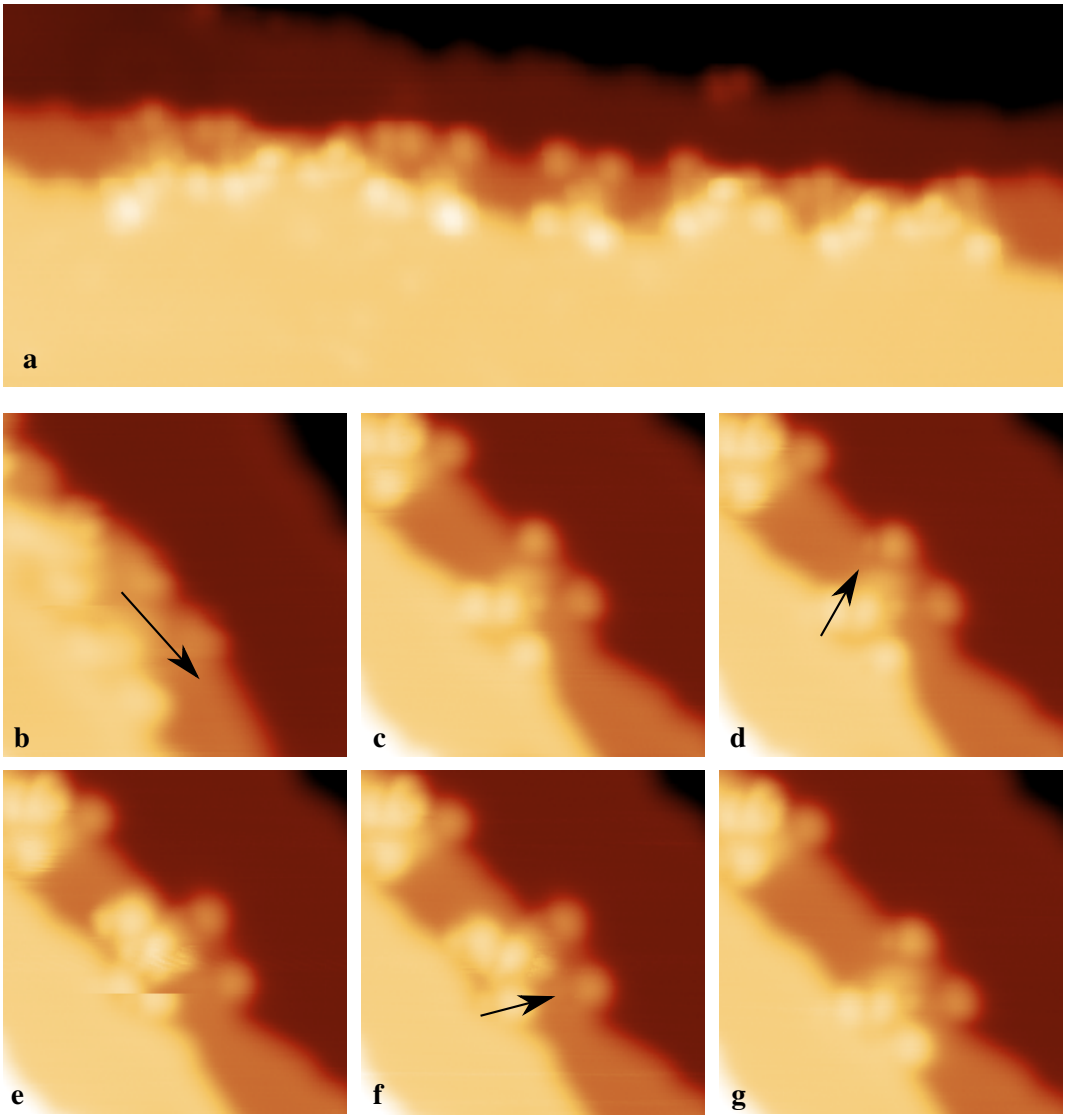

Figure 5.7.: Carborane nanocars on Ag(111). (a) typical adsorption geometry at step edges, (b) - (g) lateral manipulation sequence, the arrows indicate the path of the tip during the manipulation. Image parameters: (a) $28.2 \times 10.2\ nm^2$, (b) - (g) $7.2 \times 7.2\ nm^2$, all other parameters: $U_{tip} = 1\ V$, $I = 0.1\ nA$, $T = 5.7\ K$. Manipulation parameters: $U_{tip} = 60\ mV$, $I = 1\ nA$.

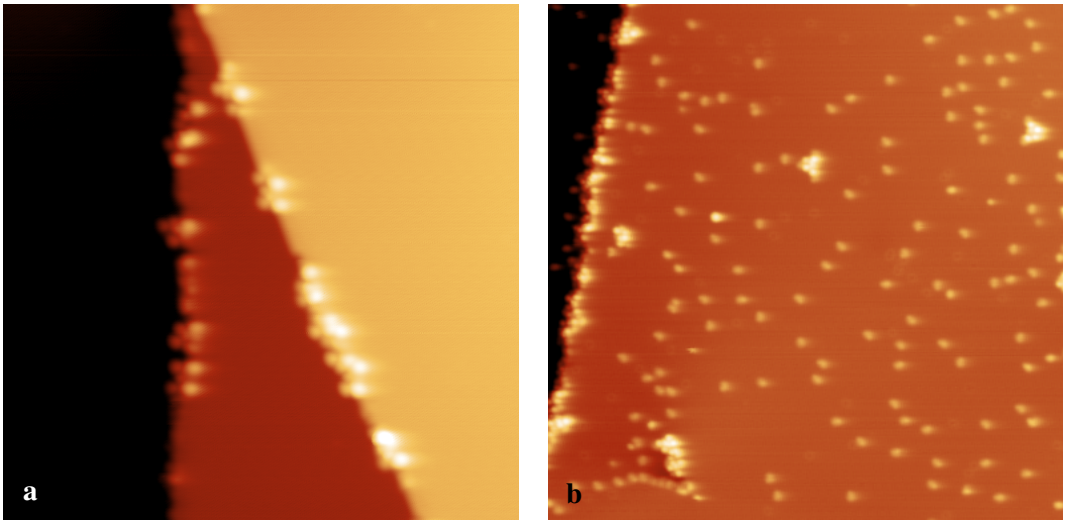

Figure 5.8.: Coverage dependent adsorption of carborane nanocars on Cu(111). In (a) ($39 \times 39\ nm^2$) a low coverage of nanocars was deposited on the surface. Only few fragments can be found and almost all cars are adsorbed at the step edges. In (b) ($77.5 \times 77.5\ nm^2$), the coverage was increased until the step edges are saturated and the cars are forced to adsorb on the terrace. However, also the amount of fragments increased. All other image parameters are: $U_{tip} = -1\ V$, $I = 0.1\ nA$, $T = 5.6\ K$

objective of isolated molecules was achieved by saturating the step edges.

The origin of the small fragments, which are marked with the white box in Fig. 5.9 (a), is unknown. But as they are found all over the surface in large numbers, they might be wheels which have been detached from the nanocars. The fragments forming the islands in the same image cannot be identified due to their irregular structure.

Due to the design of the nanocar, containing several single bonds in its chassis, the axes are free to rotate around them and the car can be found either with the axes parallel or crossed. Both of these possibilities are also realized on the Cu(111) surface as shown in Fig. 5.9 [11]. In these figures, the dimensions on the surface are compared with gas phase calculation performed with the HyperChem 7 software. The agreement is particularly good for the length of the axes, whereas the other lengths are slightly off, due to the internal flexibility of the molecule and its adoption to the surface, which was not considered in the calculations. Also on Cu(111), attempts of lateral manipulation (with manipulation resistances down to $2 \cdot 10^5\ \Omega$) and illumination with light of $\lambda = 248\ nm$ did not lead to any changes in the molecules and propelled motion was also not observed.

5.1.5. NaCl

During the experiments on various metal surfaces (Au(111), Ag(111), Cu(111), Cu(110)) the carborane cars did not show any response to illumination with light of the wavelength $\lambda = 248\ nm$. It is known from surface studies of azobenzene molecules that isomerization of molecular switches which also rely on the *trans* - *cis* isomerization of a double bond can be quenched on metal surfaces [138, 139] and also that a decoupling of the functional group from the surface by attachment of sidegroups can re-enable the switching process [38]. Another way to achieve decoupling is the deposition of the molecules on a thin film of NaCl on top of a metal surface [140, 64, 141].

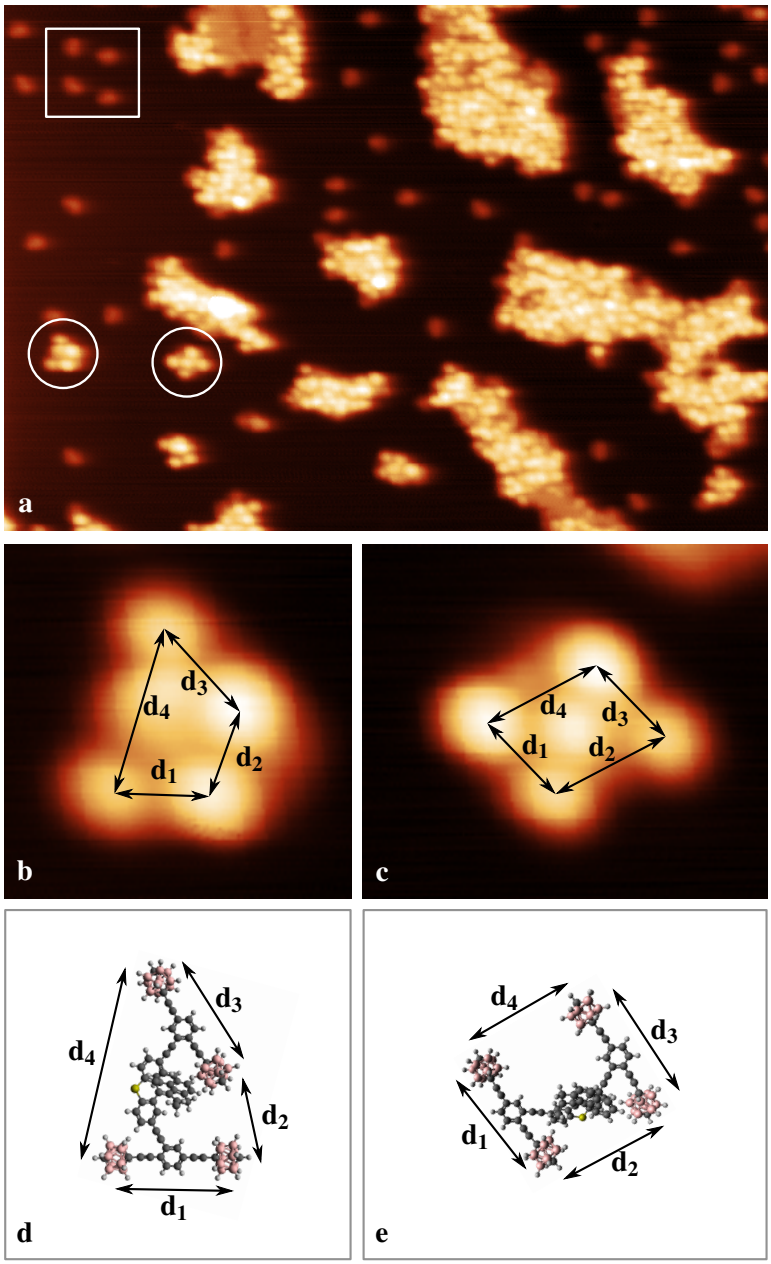

Figure 5.9.: Carborane nanocars on Cu(111) with their axes parallel or crossed in comparison to their gas phase structures. (a) is an overview image ($64 \times 44\ nm^2$) showing several intact molecules and many unidentified fragments. The regions marked with white circles are shown in detail in (b) ($4.5 \times 4.6\ nm^2$) and (c) ($5.7 \times 5.0\ nm^2$). All other image parameters: $U_{tip} = -1\ V$, $I = 0.1\ nA$, $T = 5.7\ K$. Corresponding gas phase structures calculated with HyperChem 7 are shown in (d) and (e). The molecules with crossed axes in (b) and (d) have the dimensions $d_1 = 1.33\ nm$ in the STM image and 1.38 *nm* in the calculation. $d_2 = 1.10\ nm$, 1.07 *nm*, $d_3 = 1.39\ nm$, 1.38 *nm* and $d_4 = 2.15\ nm$, 2.29 *nm*. The molecules with parallel axes in (c) and (e) have the dimensions $d_1 = 1.38\ nm$ in the STM image and 1.38 *nm* in the calculation. $d_2 = 1.65\ nm$, 1.42 *nm*, $d_3 = 1.37\ nm$, 1.38 *nm* and $d_4 = 1.70\ nm$, 1.51 *nm*.

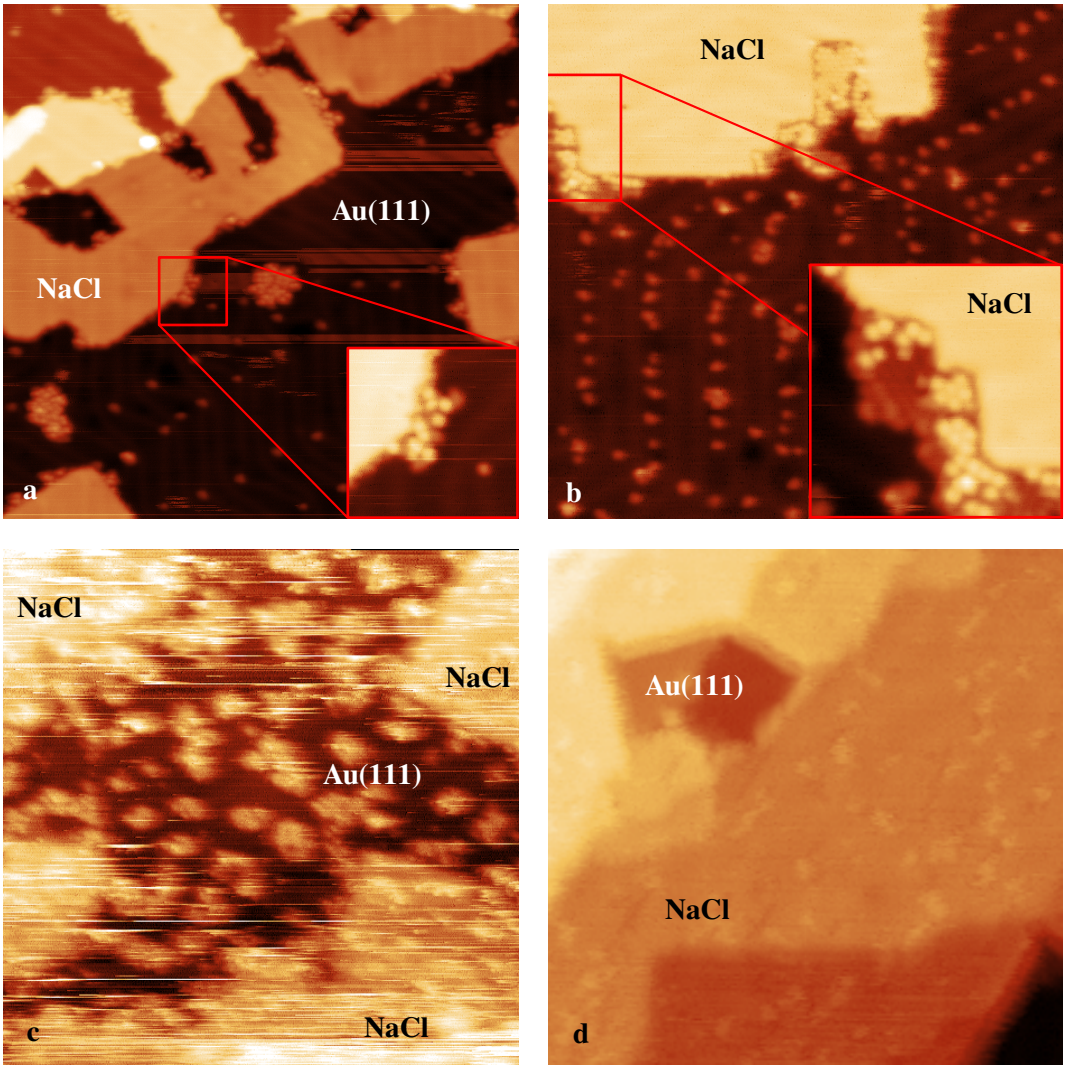

Figure 5.10.: Attempted depositions of carborane nanocars on NaCl/Au(111). In (a) the nanocars were evaporated on NaCl/Au(111) at 0°C (Image parameters: $84,3 \times 84,3\ nm^2$, $U_{tip} = -1\ V$, $I = 7.8\ pA$ (inset: $I = 3.1\ pA$), $T = 5.8\ K$). In (b) the nanocars were evaporated on NaCl/Au(111) at 154 K ($51.8 \times 51.8\ nm^2$, $U_{tip} = -1\ V$, $I = 2\ pA$, $T = 5.8\ K$). In (c) the nanocars were evaporated on NaCl/Au(111) at $\approx 10\ K$ on the manipulator ($77.4 \times 77.4\ nm^2$, $U_{tip} = -1\ V$, $I = 1\ pA$, $T = 5.8\ K$). In (d) the nanocars were evaporated on NaCl/Au(111) at 5.5 K directly into the STM ($34.4 \times 34.4\ nm^2$, $U_{tip} = 551\ mV$, $I = 1.2\ pA$, $T = 6.1\ K$).

A general problem of this approach is that the molecules generally adsorb so weakly that they are highly mobile, which makes deposition at room temperature impossible because the molecules would diffuse to free metal areas and also acquiring STM images can be challenging because the tip easily moves the molecules and consequently very low tunneling currents have to be employed in order to avoid this problem.

It was tried to deposit the p-carborane nanocar on a NaCl layer on Au(111). NaCl can be evaporated onto a clean metal surface from a quartz crucible held at slightly above 500°C. The coverage was chosen such that half of the surface was covered with a NaCl double layer and the other half was uncovered metal, which is convenient for cleaning the STM tip. When the metal substrate is held at room temperature, large NaCl islands are formed, which are so large that finding the transition between NaCl and the uncovered surface can be very time-consuming. However, if the surface is only slightly cooled for deposition, to around 0°C, the NaCl islands are becoming much smaller and are better suited for STM imaging [44].

Several approaches were tried to deposit the nanocar molecules on the so prepared NaCl film:

- Evaporating the nanocars onto the NaCl film at 278 K in the preparation chamber and subsequent transfer in the STM resulted in clean NaCl and the molecules adsorbed on the free gold areas next to it only (Fig. 5.10 (a)). Apparently, the molecules are too mobile on the NaCl at this temperature. Reducing the surface temperature to 154 K during preparation increased the number of adsorbed fragments on the gold, but still the molecules did not adsorb on the NaCl (Fig. 5.10 (b)), which means that the temperature during deposition was still not low enough.

- To make the molecules stick on the NaCl, the temperature needs to be reduced further. When reducing it to 10 K on the manipulator in the preparation chamber, after the evaporation, the salt is covered with molecular fragments or other unknown adsorbates which make scanning very difficult and no intact molecules could be found (Fig. 5.10 (c)). On the manipulator, the sample is not protected against the rest gas of the UHV chamber which can also adsorb on the sample at these low temperatures, leading to even more unwanted adsorbates.

- To reduce the amount of contamination from the background pressure, it was tried also to evaporate the nanocars directly into the STM at 5.5 K, where the sample is protected against the rest gas of the chamber by the radiation shields surrounding the STM head, which adsorb the rest gas on their cold surface. The evaporation is done through a small hole in the shields. On a bare Cu(111) surface, intact nanocars could be deposited successfully but as always, accompanied by a high number of molecular fragments. When trying the same evaporation on NaCl/Au(111), the same large amount of fragments is adsorbed on the surface as well (Fig. 5.10 (d)). In contrast to the case on Cu(111), these fragments are highly mobile on the NaCl and get easily dragged around by the tip during scanning, even at very low tunneling currents of about 1 pA, which makes it very difficult to obtain STM images of sufficient quality. Although this method was tried intensively, no carborane nanocars could be found on the NaCl film.

Due to the experimental problems described above, imaging and manipulation as well as illumination experiments could not be done.

5.2. Adamantane cars

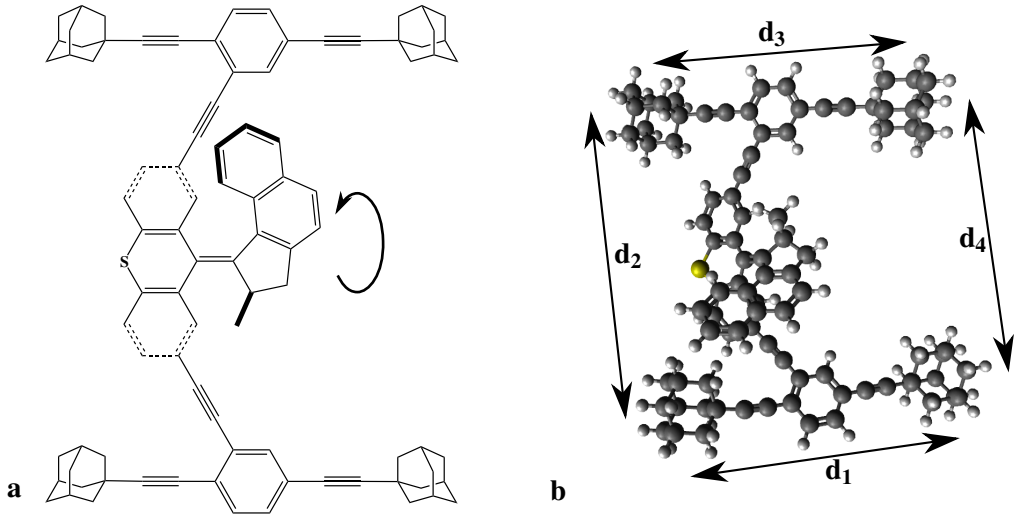

Figure 5.11.: Chemical structure of the adamantane-wheeled nanocar (a) and its gas phase structure calculated with HyperChem 7 (b). The indicated dimensions which are measured between the center of the wheels are: $d_1 = 1.32\ nm$, $d_2 = 1.61\ nm$, $d_3 = 1.32\ nm$ and $d_4 = 1.48\ nm$ and the total mass of one molecule is 1210 u.

In chapter 5.1, it was described extensively that motorized nanocars equipped with p-carborane wheels show no change upon illumination on metal substrates. When copper was chosen as a substrate it was not even possible to move the cars using lateral manipulation by the tip of the STM. One idea of how to improve the structure of the nanocar to make it work is to change the wheels. As already explained in the introduction, in former works, fullerene wheels had been employed because of their spherical shape [121]. However, these wheels have strong drawbacks. From the synthetic point of view, fullerene wheels make the plain nanocar insoluble. To make it soluble, several side chains ($C_{10}H_{21}$) have to be attached to the molecule. In STM images, only the four wheels could be seen. Consequently, the behavior of these chains on the surface could not be investigated, but due to their length and their high number in every molecule, it is very likely that they play a role for the adsorption of the molecules on the surface. Furthermore, already in solution, the molecular motor in the car becomes inoperative when the car is equipped with fullerene wheels [128]. Both of these problems were conveniently solved by the use of p-carborane wheels (chapter 5.1).

Another almost spherical molecule which can be used as a wheel is adamantane ($C_{10}H_{16}$), which is in fact a small diamondoid [142]. As diamond is very inert, it was hoped that adamantane wheels would reduce the interaction between the molecule and the metal substrates [131] compared to the carborane case. A motorized adamantane nanocar (Fig. 5.11) was synthesized by Pinn-Tsong Chiang from the group of James Tour. It has exactly the same structure as the carborane nanocar (Fig. 5.2), besides the wheels which have been changed to adamantane. The adamantane wheels have the same advantages as the carborane ones, the molecules stay soluble without side chains in non polar solvents like hexane and dichloromethane, the molecular motor is operative in solution and the sublimation temperature in vacuum is the same as in the case of the carborane car (chapter 3.4). In the following, the experiments with these molecules on Au(111) and Cu(111) are described.

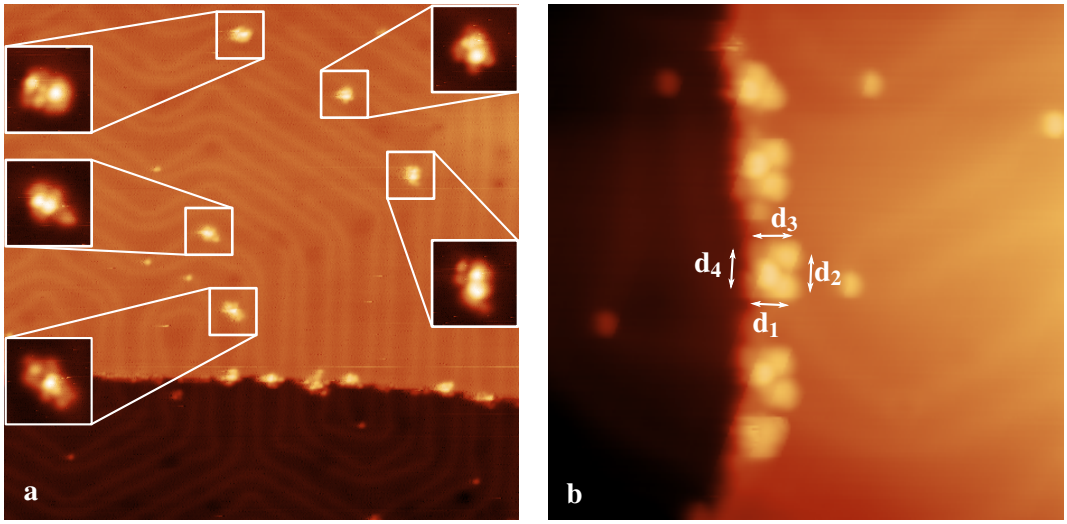

Figure 5.12.: Adamantane nanocars on Au(111). (a) shows an overview image of the surface, in (b) three nanocars can be found on a step edge. The measured dimensions are: $d_1 = 1.3\ nm$, $d_2 = 1.5\ nm$, $d_3 = 1.4\ nm$, $d_4 = 1.5\ nm$. Image parameters: (a): $80.7 \times 80.7\ nm^2$ (insets: $5 \times 5\ nm^2$), $U_{tip} = 551\ mV$, $I = 2\ pA$, $T = 5.8\ K$, (b): $23.3 \times 23.3\ nm^2$, $U_{tip} = -551\ mV$, $I = 0.59\ nA$, $T = 5.8\ K$.

Laser configuration	Average power	Average displacement	T_{STM}
355 *nm* at 10 *kHz*	40 *mW*	$(3.3 \pm 0.2)\ nm$	8.9 *K*
266 *nm* at 10 *kHz*	8 *mW*	$(2.1 \pm 0.5)\ nm$	6.5 *K*
355 *nm* at 3 *kHz*	9 *mW*	$(1.9 \pm 0.3)\ nm$	6.56 *K*

Table 5.1.: Average displacement of the molecular fragments from the adamantane nanocars on Au(111) after 15 *min* illumination with various laser configurations (chapter 3.5). These measurements were performed on the same sample preparation, i.e. the coverages are identical for all three measurements. The time averaged power was measured behind the first Al mirror.

5.2.1. Au(111)

At first, the adamantane nanocars were evaporated onto Au(111). Typical images of a clean preparation can be seen in Fig. 5.12. In (b), three nanocars can be identified on the upper terrace close to a step edge by their typical five lobe appearance, which was already observed for the carborane nanocars, and their dimensions, which are in good agreement with the gas phase dimensions given in Fig. 5.11 (b). The overview image (a) shows the typical distribution of the molecules on the surface, some cars can be found on the steps, but almost no cars can be found on the terrace. The adsorbates in the insets are no cars, because they do not have the typical five-lobe appearance and they are also larger than the cars in (b).

In order to find out more about the bonding strength of the molecules on the steps and the terraces, lateral manipulation experiments have been performed (Fig. 5.13). It was tried to separate a molecule from a step edge and to move it on the terrace. After several attempts with a resistance of $3.3 \cdot 10^6\ \Omega$ ((a), (c), (d)) without success, the resistance was lowered to $2.5 \cdot 10^6\ \Omega$ ((e), (g)) leading to a successful separation. However, the molecule did not stay on the terrace because in (h) it is found at the next step

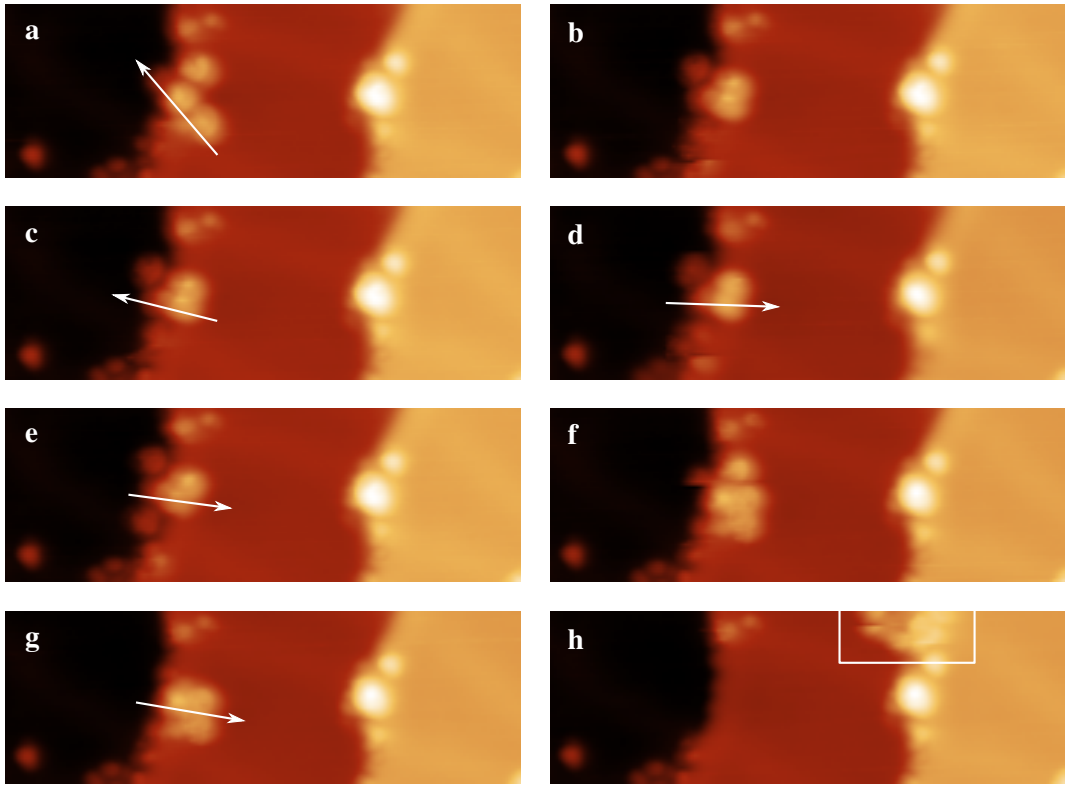

Figure 5.13.: Lateral manipulation sequence of an adamantane nanocar on Au(111). The manipulation paths are indicated with white arrows, in (h) the molecular position is shown by a white rectangle. Manipulation parameters: $U_{tip} = 10\ mV$, (a), (c), (d): $I = 3\ nA$, (e), (g): $I = 4\ nA$. Image parameters: $17.5 \times 5.8\ nm^2$, $U_{tip} = -0.5\ V$, $I = 0.52\ nA$, $T = 5.7\ K$.

edge, far away from the end point of the manipulation path in the previous image (g). This shows how different the bonding strength at the step is from the diffusion barrier on the terrace and it is no surprise that after preparing the molecules at room temperature, they can be found almost exclusively at the steps.

In order to obtain isolated molecules on the terrace, it was tried to evaporate them on the more reactive Cu(111) surface (see chapter 5.2.2), but also there, the molecules are exclusively found on the steps. Another possibility is to evaporate the molecules on a cooled sample, to reduce their mobility, which generally has the disadvantage that even more molecular fragments, which are created during the evaporation, stick to the surface. The surface was cooled on the manipulator to 10 K and the molecules were evaporated as usual. Images of the resulting surface can be found in Fig. 5.14. There are a lot of fragments and scanning is therefore difficult. Due to the low sample temperature during evaporation, the adsorbates did not have the chance to move to an the thermodynamic equilibrium position and are easily moved by the tip. However, now it is possible to find single cars on the terrace as expected (b).

It was also tried to activate the molecular motor in the nanocars by illuminating it with light of $\lambda = 266\ nm$ and $\lambda = 355\ nm$ (the laser systems are described in chapter 3.5), both after deposition at room temperature and at low temperature, but no change could ever be observed in the nanocars after illumination (Fig. 5.14). Nevertheless, the fragments moved a lot, probably due to the heating during illumination. This effect was strongest when the 355 nm laser was used at the full repetition

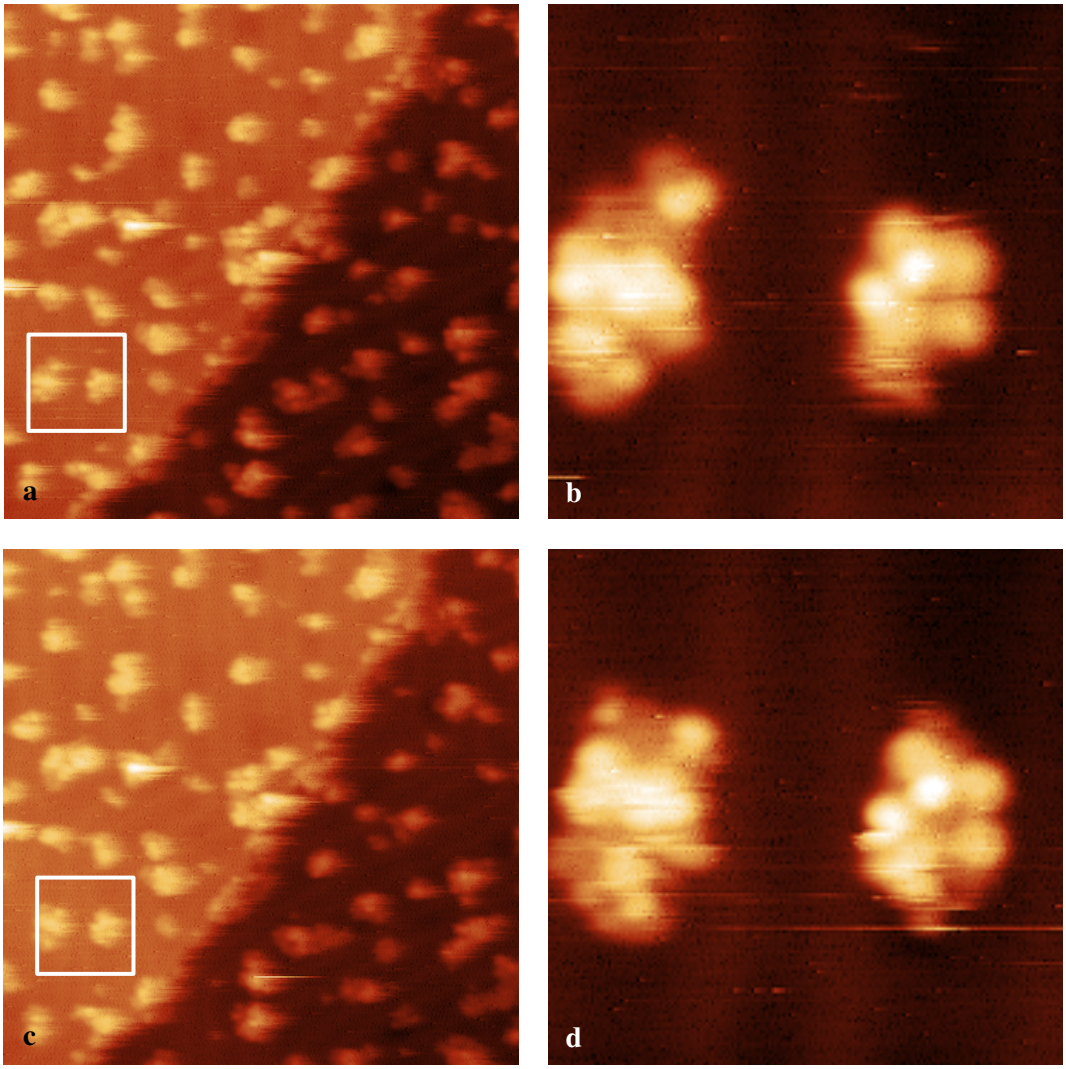

Figure 5.14.: Adamantane nanocars after evaporation on the Au(111) surface held at 10 K. (a) is an overview image, the white rectangle is the position of (b), where a single car can be found on a terrace. (c) and (d) show the same areas after 15 min illumination with 266 nm at 10 kHz, during which the temperature rose to 6.56 K. The nanocar did not change its position nor its appearance during the illumination. Image parameters: (a) and (c): $57.2 \times 57.2\ nm^2$, (b) and (d): $10.5 \times 10.5\ nm^2$, the others are in all images: $U_{tip} = -551\ mV$, $I = 2\ pA$, $T = 5.7\ K$.

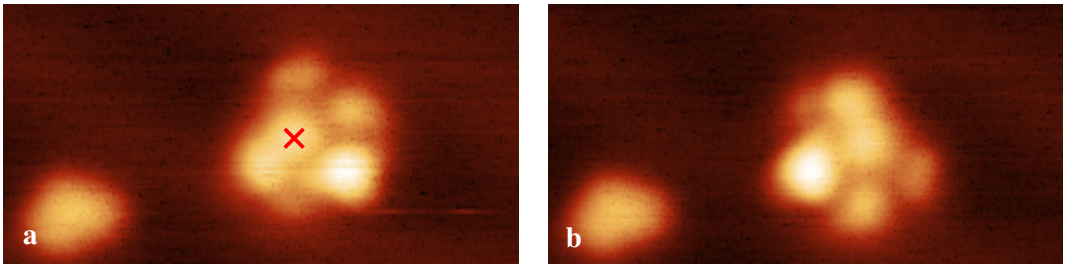

Figure 5.15.: Rotation of an adamantane nanocar on Au(111) upon applying a voltage ramp from 0 to $-2\ V$ at the position indicated in (a). Image parameters: $7.0 \times 3.5\ nm^2$, $U_{tip} = 551\ mV$, $I = 1.7\ pA$, $T = 5.7\ K$

rate of 10 kHz (with a time averaged power of 40 mW after the first Al mirror), where the measured temperature of the helium cooled STM was rising from 5.7 K to 8.9 K. The temperature directly at the surface must have been much higher than that because the temperature is measured more than 1 cm away from the sample and outside of the laser spot. By reducing the repetition rate to 3 kHz, which reduces the time averaged power of the laser (9 mW after the first mirror) to the one of the 266 nm laser at 10 kHz (8 mW after the first mirror), the temperature rose in both cases only to 6.5 K and also the amount of displacement of the fragments was then comparable in magnitude (Tab. 5.1). As the displacement apparently only depends on the laser power and thereby on the surface temperature but not on the wavelength of the light, the most probable origin of this displacements is thermally induced diffusion of the fragments on the surface.

It was also tried to apply voltage pulses with the tip of the STM in the hope to make the molecular motor turn, similar to what was observed in [12]. In this paper, the car started to move when a voltage of about 500 mV was exceeded, but at this voltage range no effect could be observed for the adamantane cars. At a tip voltage of about $\pm 2\ V$, it can be observed sometimes that the car rotates as a whole in a random fashion without changing its appearance or lateral position (Fig. 5.15). At about 4 V the molecule is dissociated.

5.2.2. Cu(111)

As already in the case of the carborane cars, the preparations on copper were generally much cleaner than on gold, which is an unexpected behavior, because the copper surfaces are more reactive [50] and should therefore bind molecular fragments, originating from the evaporation, more efficiently than gold. Also on Cu(111), the molecules appear as five lobes in the STM images (Fig. 5.16), four corresponding to the wheels and one to the motor, which can either be found with the axes parallel (c) and (e) as well as with the axes crossed (b) and (d). The measured dimensions agree fairly well with the dimensions in the gas phase which are given in the figure caption and were calculated using the HyperChem 7 software.

It can be seen in the overview image of Fig. 5.16 that, as in the case of Au(111), almost all molecules are found at step edges, signifying that they have to be mobile at room temperature, where the evaporation has taken place. However, it was not possible to remove the molecules from the step edge using lateral manipulation with manipulation resistances down to 33.3 $k\Omega$ at low temperature. Also illuminating the sample with the wavelength $\lambda = 266\ nm$ and $\lambda = 355\ nm$ for 15 min did not lead to any changes on the surface. Furthermore it was tried to apply voltage pulses with the STM tip in order to activate the rotation of the motor, but no periodic nor repeatable change could be observed. At

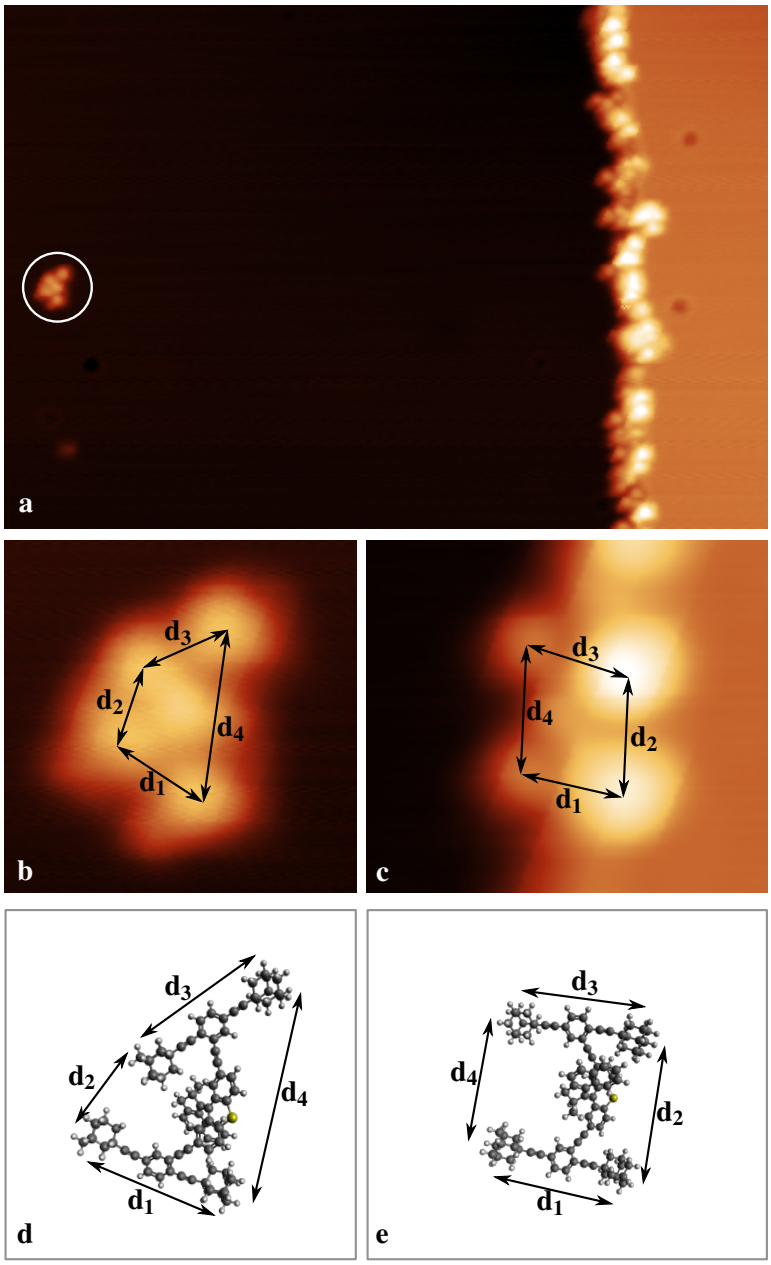

Figure 5.16.: Adamantane nanocars on Cu(111) both in the crossed and parallel axle configuration. (a) is an overview image of the surface ($63.6 \times 43.6\ nm^2$) with a crossed axle nanocar in the white circle, which is shown in detail in (b) ($4.6 \times 4.6\ nm^2$). (c) shows an adamantane nanocar in the parallel axis configuration ($5.3 \times 4.6\ nm^2$) adsorbed on a step edge. The other image parameters are $U_{tip} = -0.5\ V$, $T = 5.7\ K$ and $I = 0.49\ nA$ in (a) and (b), $I = 1.0\ nA$ in (c). (d) and (e) show the corresponding gas phase structures calculated with HyperChem 7. For (b) and (d) the dimensions are $d_1 = 1.28\ nm$ in the STM image and 1.33 *nm* in the calculation. $d_2 = 0.95\ nm$, 0.95 *nm*, $d_3 = 1.17\ nm$, 1.34 *nm* and $d_4 = 2.32\ nm$, 2.13 *nm*. The molecules with parallel axes in (c) (e) have the dimensions $d_1 = 1.32\ nm$ in the STM image and 1.32 *nm* in the calculation. $d_2 = 1.64\ nm$, 1.61 *nm*, $d_3 = 1.30\ nm$, 1.32 *nm* and $d_4 = 1.70\ nm$, 1.48 *nm*.

voltages of about $\pm 3.5\ V$, the molecules are dissociated.

5.3. Conclusions

In this chapter, the low temperature STM experiments with p-carborane (Fig. 5.2) and adamantane nanocars (Fig. 5.11) were described. Despite their high mass of over 1200 *u*, it is still possible to evaporate both of them thermally from a Knudsen cell, but at the evaporation temperature the respective dissociation rates are high which generally leads to dirty samples, where the molecules are adsorbed together with many fragments, and severely limits the number of evaporations possible from one crucible filling. Interestingly, the adamantane cars, which have slightly less weight (1210 *u*) than the p-carborane ones (1241 *u*) and should therefore be more stable during evaporation, are more difficult to evaporate and lead to more contamination.

It was tried to activate the rotation of the molecular motor by illuminating it with light. For the p-carborane molecules 248 *nm* on the surfaces Au(111), Ag(111), Cu(111), Cu(110) and for the adamantane cars 355 *nm* and 266 *nm* on Au(111) and Cu(111) were used, but no change in the molecular appearance, nor directed motion could be observed after the illumination, regardless of the surface and the employed molecule. Furthermore it was tried to deposit the carborane cars on a NaCl bilayer, but the desired preparation could not be achieved. The molecular fragments, however, did move upon illumination, probably due to a heating of the surface. Voltage pulses were applied to the nanocars with increasing voltage until the molecule was dissociated, but no repeating contrast change of the motor, which could be an indication for a rotation, could be found. Sometimes, the whole molecules is rotated when applying a voltage pulse.

The reason why the molecules show no response to excitation with light or tunneling electrons could not be found within this thesis. Possible reasons could be that the molecules bind so strongly to the surface (possibly via the wheels) that the strength of the motor is not sufficient to overcome the rotation barriers. Another possibility would be that the *trans-cis* isomerization, which is the first step in the rotation of the motor, is quenched on metal surfaces due to overlap of the molecular states with the states of the substrate. Maybe DFT calculations could be helpful to determine the precise adsorption geometry and electronic structure on the surface and then to find out what hinders the rotation of the molecular motor.

Summary

Within this thesis, two types of molecules were investigated which can be seen as prototypes of functional molecules, similar to molecules found in biological systems.

The first molecule, *tetra*-phenyl-porphyrin (TPP), was studied on the Au(111) surface (chapter 4), where it exhibits two distinct states. In STM images, one of the states appears brighter than the other and therefore is called the bright state, the other state is consequently called the dark state. The dI/dV spectra of the molecules, which reflect the electronic density of states, have the same overall structure, but are rigidly shifted in energy by half an electron volt with respect to the Fermi level. Reversible switching between these two states is possible, either by thermal activation at room temperature, or with voltage pulses from the STM tip at low temperatures of about 5 K.

It was investigated whether cooperative effects can be found between neighboring TPP molecules, depending on the bonding mechanism between them. The quickest way of observing a high number of switching events, leading to significant statistics, is to scan a full monolayer of molecules at room temperature where the switching is induced thermally. Scanning the same sample area repeatedly, yields a movie of the evolving pattern of dark and bright molecules. By analyzing the distribution of dark and bright molecules on the surface, no influence of the state of one molecule on the state of its neighbors could be found. However, when looking at the switching process, there is a correlation between neighboring molecules: When a molecule switches from bright to dark, there is a high probability that in its vicinity another molecule switches from dark to bright, which means that the bright state is transferred to the neighboring molecules.

The nature of the dark and bright state could be understood with DFT calculations performed by Felix Hanke and Mats Persson from the University of Liverpool. Switching of porphyrin molecules between a flat and a buckled conformation have been reported in the literature. It turned out that for this particular system, the central porphyrin macrocycle is always in a saddle shape conformation but underneath the bright molecules a gold adatom is situated, which leads to the observed change in the molecular appearance. From the DFT results, STM images were simulated, which agree well with the measured ones and also the spectral shift of half an electron volt could be reproduced in the calculations.

With these results, the observed hopping of the bright state at room temperature can simply be explained by the motion of the adatoms underneath the molecular layer. After understanding the mechanism behind this observed transfer of the bright state, it is clear that this is not a cooperative effect. From this example can be learned that a correlated process is not necessarily a cooperative one.

The presence of the adatoms underneath the bright molecules could also be confirmed experimentally. When the switching is induced by applying voltage pulses at low temperatures, switching from bright to dark is easily achievable by applying a pulse of $\approx \pm 2\ V$, the switching in the opposite direction happens in the same voltage range but can only be observed extremely rarely. When switching from bright to dark, a present adatom only needs to leave its former position, which is easily achievable. When switching in the other direction, an adatom needs to be present for facilitating the transition to the bright state, which is not expected at low temperatures. It was found that switching to the bright state can be achieved easier, when adatoms are created artificially by crashing the STM tip into the surface in the vicinity of the molecules and thereby supplying the necessary adatoms for the switching

process. Furthermore, at the elbow sites of the herringbone reconstruction, the adatoms can be trapped and when a bright molecule is situated at such a site, it can be moved away by lateral tip manipulation, whereby it turns dark and an adatom is left behind at the former position of the molecule. Manipulating the molecule back onto the atom returns it to the former bright state.

However, even after understanding the origin of the dark and the bright state, the temporal evolution of the dark–bright pattern remains unexplained. The dwell times in the two states cannot be explained by a single exponential function and apparently there is a high degree of correlation in the switching of the molecules. Cascade events can be observed, which means that over several frames almost no switching activity can be observed but between two frames many molecules change their state, which is then followed by a longer period of low switching activity. Apparently there is some sort of communication between the molecules, but the origin of this communication could not be revealed within this thesis. Consequently there is still the possibility that this is a cooperative process, but it could also be mediated by a different kind of interaction.

It was tried whether the switching process changes when two TPP molecules are covalently linked together. After the linking, the two sides of the dimers are still capable of adopting the two states and at room temperature, the distribution of the dark and bright state in one dimer is completely random. By applying voltage pulses at low temperature, it could be shown that the state of one porphyrin unit in the dimer does not influence the switching probability of the other.

The second type of molecules investigated in this thesis are so-called nanocars (chapter 5), which are prototypes of molecular machines, capable of converting external energy into action. These nanocars have four wheels, which could potentially roll across the surface, restricting its motion to one dimension on the surface. Furthermore, they contain a molecular motor, which can convert light and thermal energy into unidirectional rotation and could drive the nanocar forward. With a mass of more than 1200 u, these nanocars are so heavy that their evaporation temperature is close to their vacuum dissociation temperature. Therefore, one of the main experimental challenges during the nanocar experiments is to evaporate them on the surface in an intact and clean way, i.e. without having too many molecular fragments on the surface, to allow for a clear identification of the intact molecules and stable imaging conditions.

One version of the nanocars had p-carborane wheels and was evaporated on various metal surfaces: Au(111), Ag(111), Cu(111), Cu(110). On all these surfaces, the cars have a typical appearance of five lobes. By comparing the dimensions on the surface with the dimensions from gas-phase calculations, four of the lobes could be identified as the wheels, the fifth lobe consequently stems from the molecular motor. On these surfaces it was tried to activate the molecular motor by illuminating it with light of the wavelength $\lambda = 248\ nm$, but no directed motion, nor a change in the appearance of the motor could be observed afterwards. To decouple the molecules further from the metal surface, it was tried to evaporate them onto a NaCl bilayer on Au(111), but due to the high fragmentation of the molecules during thermal evaporation, large amounts of fragments were always present on the NaCl, making scanning difficult and no nanocars could be found.

It was suspected that the nanocars bind too strongly to the metal surfaces, possibly via the wheels. Therefore a second version was synthesized, this time with adamantane wheels, in the hope that different wheels would change the coupling of the molecule to the surface and thereby might enable the motion of the nanocar. The adamantane-wheeled nanocars were evaporated on Au(111) and Cu(111). Interestingly, although the adamantane version of the cars has slightly less weight than the carborane version, they were more difficult to evaporate, leading to even more fragments. However, illuminating the cars with light of the wavelength $\lambda = 266\ nm$ and $\lambda = 355\ nm$ did not lead to observable changes in the molecular appearance and directed motion was also not observed. However, the molecular fragments moved upon illumination. Sometimes, a rotation of the whole molecule could be induced by

applying voltage pulses with the STM tip.

The experiments performed in this thesis show how difficult it is to predict the behavior of functional molecules on surfaces in general. Often the functionality of the molecules is quenched completely, as in the case of the nanocars, and in others examples processes are encountered, which were not anticipated when designing the experiment. An example for such an unexpected process is the involvement of a gold adatom in the bright molecular state of the TPP molecule. Such an adatom mediated switching of a molecule has, to my knowledge, not been observed before.

It would be an interesting future project to further investigate the motion of adatoms between the metal surface and a molecular adsorbate layer. However, it turned out that for the study of cooperative switching, TPP molecules are actually not well suited, because although they display distinct states, the bright state is created by the presence of an adatom and therefore, TPP is no molecular switch. Investigations similar to the ones presented in this thesis could be done with molecules capable of isomerizing on a surface and maybe there, cooperative switching is observed.

For achieving progress with the nanocar molecules, it seems necessary to reduce their weight in order to make them evaporate at lower temperatures and thereby reduce the fragmentation rate. With a lower amount of fragments, it should be possible to successfully deposit them on NaCl, which largely decouples them from the underlying metal substrate and might thereby enable the motor function. However, a substantial weight reduction can probably only be achieved by a completely changed design. Another possibility would be to change the molecular motor. The group of Ben Feringa has shown that slight changes in the structure of the rotor and stator part of the motor drastically influence its rotation kinetics in solution. Maybe, a different motor design can be found, which is better suited for the adsorption on metal surfaces.

Part III.

Appendix

A. CD Contents

The thermal switching of Br_4TPP and TPP dimers is discussed in the chapters 4.5 and 4.7.4, respectively. The evolution of the molecule covered surface is studied by imaging the same surface area repeatedly with the STM and the resulting movies are evaluated.

As movies are hard to present in a printed thesis, some of them are added in form of a CD together with the difference movies resulting from subtracting successive frames (as explained in Fig. 4.19). Furthermore, the self-written source code of the evaluation software is added.

The following movies are contained:

- 280509-movie1: Br_4TPP on Au(111). $U_{sample} = 1.25\ V$, $I = 0.13\ nA$, $T = 300\ K$, 108 s/frame. This movie is used in Fig. 4.13.
- 280509-movie3: Br_4TPP on Au(111). $U_{sample} = 0.884\ V$, $I = 0.14\ nA$, $T = 300\ K$, 81 s/frame. This movie is used in Fig. 4.14, Fig. 4.18 and Fig. 4.19.
- 101210-movie5: TPP dimers on Au(111). $U_{sample} = 884\ mV$, $I = 0.03\ nA$, $T = 300\ K$, 33 s/frame. This movie is used in Fig. 4.39.

The evaluation software is written in Python 2.7 and requires the libraries numpy, scipy and matplotlib. It consists of three classes:

- The class “movie” reads in the movie from the hard disk and performs the drift compensation as described in chapter 3.6.1. Every frame of the movie needs to be stored in a two-dimensional numpy array file (.npy), containing the topographic height. Preferentially, all frames should be plane corrected before loading them to allow for a more reliable drift compensation.
- The class “molecules” takes an instance of a “movie” object as an input and provides methods for defining the molecular grid, determination of the molecular state (as described in chapter 3.6.2) and all the data evaluation functions relevant for the monomers.
- The class “dimers” takes two “molecules” objects as an input. Each of them needs to have the same number of positions defined corresponding to the first and the second side of the dimers. It provides methods for the statistical evaluation of the dimer movies.

Additionally, there is a file called “poisson.py”, which contains some functions for plotting Poisson and Skellam distributions.

B. Publication list

Publications related to this thesis:

- Chiang, P.-T.; Mielke, J.; Godoy, J.; Guerrero, J. M.; Alemany, L. B.; Villagómez, C. J.; Saywell, A.; Grill, L. & Tour, J. M.
  Toward a Light-Driven Motorized Nanocar: Synthesis and Initial Imaging of Single Molecules
  ACS Nano, 2012, 6, 592 – 597

Publications unrelated to this thesis:

- Bombis, C.; Ample, F.; Mielke, J.; Mannsberger, M.; Villagómez, C. J.; Roth, C.; Joachim, C. & Grill, L.
  Mechanical Behavior of Nanocrystalline NaCl Islands on Cu(111)
  Phys. Rev. Lett., American Physical Society, 2010, 104, 185502

- Mielke, J.; Leyssner, F.; Koch, M.; Meyer, S.; Luo, Y.; Selvanathan, S.; Haag, R.; Tegeder, P. & Grill, L.
  Imine Derivatives on Au(111): Evidence for "Inverted" Thermal Isomerization
  ACS Nano, 2011, 5, 2090 – 2097

- Mielke, J.; Selvanathan, S.; Peters, M.; Schwarz, J.; Hecht, S. & Grill, L.
  Molecules with multiple switching units on a Au(111) surface: self-organization and single-molecule manipulation
  Journal of Physics: Condensed Matter, 2012, 24, 394013

- Gahl, C.; Brete, D.; Leyssner, F.; Koch, M.; McNellis, E. R.; Mielke, J.; Carley, R.; Grill, L.; Reuter, K.; Tegeder, P. & Weinelt, M.
  Coverage- and Temperature-Controlled Isomerization of an Imine Derivative on Au(111)
  Journal of the American Chemical Society, 2013, 135, 4273 – 4281

C. Acknowledgments

An dieser Stelle möchte ich mich bei all denen bedanken, die mich im Verlauf meiner Doktorarbeit unterstützt und mir geholfen haben.

Bei Leonhard Grill möchte ich mich dafür bedanken, dass ich dieses spannende Forschungsprojekt in seiner Gruppe durchführen konnte, sowie für seine exzellente Betreuung, die guten Ideen und das geduldige Korrekturlesen dieser Arbeit. Allen Mitgliedern seiner Gruppe danke ich für die spontane Hilfsbereitschaft bei allen kleinen (und großen) Laborproblemen.

Mats Persson and Felix Hanke from Liverpool University I wish to thank for their DFT calculations of the porphyrin molecules, as well as for the good and intensive collaboration.

Karsten Horn danke ich für die Möglichkeit, sein Århus VT STM für viele Monate zu benutzen sowie Jesús Martínez Blanco für die umfangreiche und geduldige Unterstützung während dieser Messungen.

Stefan Hecht und seiner Gruppe an der Humboldt-Universität zu Berlin danke ich für die Synthese der Porphyrin Moleküle.

I wish to thank James Tour and Pinn-Tsong Chiang from Rice University, Texas for providing me with the nanocar molecules and the interesting discussions about their future structures.

For trying his inverse Ising model on my data, and the helpful discussion about data analysis I want to thank Gašper Tkačik from the IST, Austria.

Bei dem europäischen Forschungsprojekt ARTIST und der Max-Planck-Gesellschaft bedanke ich mich für die Finanzierung dieser Arbeit.

Ein besonderer Dank gilt meiner Familie, die immer für mich da ist und an Jana für ihre moralische Unterstützung im Verlauf dieser Arbeit.

Bibliography

[1] L.R. Milgrom. *The Colours of Life: An Introduction to the Chemistry of Porphyrins and Related Compounds*. Oxford University Press, USA, 1997. ISBN 9780198559627. LCCN 96027452.

[2] Christopher A. Hunter and Harry L. Anderson. What is cooperativity? *Angewandte Chemie International Edition*, 48(41):7488–7499, 2009.

[3] Kazushi Kinbara and Takuzo Aida. Toward intelligent molecular machines: Directed motions of biological and artificial molecules and assemblies. *Chemical Reviews*, 105(4):1377–1400, 2005. PMID: 15826015.

[4] Noriyuki Kodera, Daisuke Yamamoto, Ryoki Ishikawa, and Toshio Ando. Video imaging of walking myosin V by high-speed atomic force microscopy. *Nature*, 468(7320):72–76, November 2010.

[5] R. Dean Astumian. Microscopic reversibility as the organizing principle of molecular machines. *Nat Nano*, 7(11):684–688, November 2012.

[6] Wesley R. Browne and Ben L. Feringa. Making molecular machines work. *Nat Nano*, 1(1): 25–35, October 2006.

[7] James R. Heath and Mark A. Ratner. Molecular electronics. *Physics Today*, 56(5):43–49, 2003.

[8] X. H. Qiu, G. V. Nazin, and W. Ho. Mechanisms of reversible conformational transitions in a single molecule. *Phys. Rev. Lett.*, 93:196806, Nov 2004.

[9] Violeta Iancu, Aparna Deshpande, and Saw-Wai Hla. Manipulating kondo temperature via single molecule switching. *Nano Letters*, 6(4):820–823, 2006.

[10] Leonhard Grill, Matthew Dyer, Leif Lafferentz, Mats Persson, Maike V. Peters, and Stefan Hecht. Nano-architectures by covalent assembly of molecular building blocks. *Nat Nano*, 2(11): 687–691, November 2007.

[11] Pinn-Tsong Chiang, Johannes Mielke, Jazmin Godoy, Jason M. Guerrero, Lawrence B. Alemany, Carlos J. Villagómez, Alex Saywell, Leonhard Grill, and James M. Tour. Toward a light-driven motorized nanocar: Synthesis and initial imaging of single molecules. *ACS Nano*, 6(1):592 – 597, 2012.

[12] Tibor Kudernac, Nopporn Ruangsupapichat, Manfred Parschau, Beatriz Macia, Nathalie Katsonis, Syuzanna R. Harutyunyan, Karl-Heinz Ernst, and Ben L. Feringa. Electrically driven directional motion of a four-wheeled molecule on a metal surface. *Nature*, 479(7372):208–211, November 2011.

[13] B. Bleaney. Microwave spectroscopy in oxford: The first decade part i: Microwave gas spectroscopy. *Contemporary Physics*, 25(4):315–329, 1984.

[14] G. Binnig, H. Rohrer, Ch. Gerber, and E. Weibel. Surface studies by scanning tunneling microscopy. *Phys. Rev. Lett.*, 49:57–61, Jul 1982.

[15] C. Cohen-Tannoudji, B. Diu, and F. Laloë. *Quantenmechanik: Teil 1: 2. Durchgesehene und verbesserte Auflage*. Quantenmechanik. De Gruyter, 1999. ISBN 9783110164589.

[16] G. Binnig, H. Rohrer, Ch. Gerber, and E. Weibel. Tunneling through a controllable vacuum gap. *Applied Physics Letters*, 40(2):178 –180, jan 1982.

[17] James Nicol, Sidney Shapiro, and Paul H. Smith. Direct measurement of the superconducting energy gap. *Phys. Rev. Lett.*, 5:461–464, Nov 1960.

[18] Ivar Giaever. Electron tunneling between two superconductors. *Phys. Rev. Lett.*, 5:464–466, Nov 1960.

[19] J. Bardeen. Tunnelling from a many-particle point of view. *Phys. Rev. Lett.*, 6:57–59, Jan 1961.

[20] R. Wiesendanger. *Scanning Probe Microscopy and Spectroscopy: Methods and Applications*. Scanning Probe Microscopy and Spectroscopy: Methods and Applications. Cambridge University Press, 1994. ISBN 9780521428477. LCCN gb94094616.

[21] Alex D Gottlieb and Lisa Wesoloski. Bardeen's tunnelling theory as applied to scanning tunnelling microscopy: a technical guide to the traditional interpretation. *Nanotechnology*, 17 (8):R57, 2006.

[22] J. Tersoff and D. R. Hamann. Theory and application for the scanning tunneling microscope. *Phys. Rev. Lett.*, 50:1998–2001, Jun 1983.

[23] J. Tersoff and D. R. Hamann. Theory of the scanning tunneling microscope. *Phys. Rev. B*, 31: 805–813, Jan 1985.

[24] Nicolas Lorente and Mats Persson. Theoretical aspects of tunneling-current-induced bond excitation and breaking at surfaces. *Faraday Discuss.*, 117:277–290, 2000.

[25] Leo Gross, Nikolaj Moll, Fabian Mohn, Alessandro Curioni, Gerhard Meyer, Felix Hanke, and Mats Persson. High-Resolution Molecular Orbital Imaging Using a *p*-Wave STM Tip. *Phys. Rev. Lett.*, 107:086101, Aug 2011.

[26] L. Bartels, G. Meyer, and K.-H. Rieder. Controlled vertical manipulation of single CO molecules with the scanning tunneling microscope: A route to chemical contrast. *Applied Physics Letters*, 71(2):213–215, 1997.

[27] R. J. Hamers. Atomic-resolution surface spectroscopy with the scanning tunneling microscope. *Annual Review of Physical Chemistry*, 40:531–559, 1989.

[28] William Shockley. On the surface states associated with a periodic potential. *Phys. Rev.*, 56: 317–323, Aug 1939.

[29] M. F. Crommie, C. P. Lutz, and D. M. Eigler. Imaging standing waves in a two-dimensional electron gas. *Nature*, 363(6429):524–527, June 1993.

[30] L. Bartels, G. Meyer, and K.-H. Rieder. Basic steps of lateral manipulation of single atoms and diatomic clusters with a scanning tunneling microscope tip. *Phys. Rev. Lett.*, 79:697–700, Jul 1997.

[31] Saw-Wai Hla, Kai-Felix Braun, and Karl-Heinz Rieder. Single-atom manipulation mechanisms during a quantum corral construction. *Phys. Rev. B*, 67:201402, May 2003.

[32] R. S. Becker, J. A. Golovchenko, and B. S. Swartzentruber. Atomic-scale surface modifications using a tunnelling microscope. *Nature*, 325(6103):419–421, January 1987.

[33] D. M. Eigler and E. K. Schweizer. Positioning single atoms with a scanning tunnelling microscope. *Nature*, 344(6266):524–526, April 1990.

[34] Grill L., Rieder K.-H., Moresco F., Rapenne G., Stojkovic S., Bouju X., and Joachim C. Rolling a single molecular wheel at the atomic scale. *Nat Nano*, 2(2):95–98, February 2007.

[35] Jascha Repp, Gerhard Meyer, Fredrik E. Olsson, and Mats Persson. Controlling the charge state of individual gold adatoms. *Science*, 305(5683):493–495, 2004.

[36] Jörg Henzl, Thomas Bredow, and Karina Morgenstern. Irreversible isomerization of the azobenzene derivate Methyl Orange on Au(111). *Chemical Physics Letters*, 435(4-6):278 – 282, 2007.

[37] Byoung-Young Choi, Se-Jong Kahng, Seungchul Kim, Hajin Kim, Hyo Won Kim, Young Jae Song, Jisoon Ihm, and Young Kuk. Conformational molecular switch of the azobenzene molecule: A scanning tunneling microscopy study. *Phys. Rev. Lett.*, 96:156106, Apr 2006.

[38] Micol Alemani, Maike V. Peters, Stefan Hecht, Karl-Heinz Rieder, Francesca Moresco, and Leonhard Grill. Electric Field-Induced Isomerization of Azobenzene by STM. *Journal of the American Chemical Society*, 128(45):14446–14447, 2006.

[39] Carlo Dri, Maike V. Peters, Jutta Schwarz, Stefan Hecht, and Leonhard Grill. Spatial periodicity in molecular switching. *Nat Nano*, 3(11):649–653, November 2008.

[40] B. C. Stipe, M. A. Rezaei, W. Ho, S. Gao, M. Persson, and B. I. Lundqvist. Single-molecule dissociation by tunneling electrons. *Phys. Rev. Lett.*, 78:4410–4413, Jun 1997.

[41] Saw-Wai Hla, Ludwig Bartels, Gerhard Meyer, and Karl-Heinz Rieder. Inducing all steps of a chemical reaction with the scanning tunneling microscope tip: Towards single molecule engineering. *Phys. Rev. Lett.*, 85:2777–2780, Sep 2000.

[42] Gerhard Meyer. Bauen mit einzelnen Atomen. *Physik in unserer Zeit*, 31(1):8, 2000.

[43] Francesca Moresco, Gerhard Meyer, Karl-Heinz Rieder, Hao Tang, Andre Gourdon, and Christian Joachim. Low temperature manipulation of big molecules in constant height mode. *Applied Physics Letters*, 78(3):306–308, 2001.

[44] Ch. Bombis, F. Ample, J. Mielke, M. Mannsberger, C. J. Villagómez, Ch. Roth, C. Joachim, and L. Grill. Mechanical Behavior of Nanocrystalline NaCl Islands on Cu(111). *Phys. Rev. Lett.*, 104:185502, May 2010.

[45] D. M. Eigler, C. P. Lutz, and W. E. Rudge. An atomic switch realized with the scanning tunnelling microscope. *Nature*, 352(6336):600–603, August 1991.

[46] L. Bartels, G. Meyer, K.-H. Rieder, D. Velic, E. Knoesel, A. Hotzel, M. Wolf, and G. Ertl. Dynamics of Electron-Induced Manipulation of Individual CO Molecules on Cu(111). *Phys. Rev. Lett.*, 80:2004–2007, Mar 1998.

[47] Shiwu Gao, M. Persson, and B. I. Lundqvist. Theory of atom transfer with a scanning tunneling microscope. *Phys. Rev. B*, 55:4825–4836, Feb 1997.

[48] Saw-Wai Hla and Karl-Heinz Rieder. STM CONTROL OF CHEMICAL REACTIONS: Single-Molecule Synthesis. *Annual Review of Physical Chemistry*, 54(1):307–330, 2003.

[49] Hans Lüth. *Solid Surfaces, Interfaces and Thin Films*. Springer Berlin Heidelberg, 2010.

[50] B. Hammer and J. K. Nørskov. Why gold is the noblest of all the metals. *Nature*, 376(6537): 238–240, July 1995.

[51] Jonas Björk, Felix Hanke, and Sven Stafström. Mechanisms of halogen-based covalent self-assembly on metal surfaces. *Journal of the American Chemical Society*, 135(15):5768–5775, 2013.

[52] J. V. Barth, H. Brune, G. Ertl, and R. J. Behm. Scanning tunneling microscopy observations on the reconstructed Au(111) surface: Atomic structure, long-range superstructure, rotational domains, and surface defects. *Phys. Rev. B*, 42:9307–9318, Nov 1990.

[53] Thomas Michely, Karl H. Besocke, and George Comsa. Observation of sputtering damage on Au(111) . *Surface Science*, 230(1 - 3):L135 – L139, 1990.

[54] David Nečas and Petr Klapetek. Gwyddion: an open-source software for SPM data analysis. *Central European Journal of Physics*, 10:181–188, 2012.

[55] R.J. Barlow. *Statistics: A Guide to the Use of Statistical Methods in the Physical Sciences*. Manchester Physics Series. John Wiley & Sons, 1989. ISBN 9780471922940. LCCN 88033908.

[56] B. Sadigh, M. Asta, V. Ozoliņš, A. K. Schmid, N. C. Bartelt, A. A. Quong, and R. Q. Hwang. Short-range order and phase stability of surface alloys: PdAu on Ru(0001). *Phys. Rev. Lett.*, 83: 1379–1382, Aug 1999.

[57] H. E. Hoster, E. Filonenko, B. Richter, and R. J. Behm. Formation and short-range order of two-dimensional Cu_xPd_{1-x} monolayer surface alloys on Ru(0001). *Phys. Rev. B*, 73:165413, Apr 2006.

[58] H. E. Hoster, A. Bergbreiter, P. M. Erne, T. Hager, H. Rauscher, and R. J. Behm. Pt_xRu_{1-x}/Ru(0001) surface alloys-formation and atom distribution. *Phys. Chem. Chem. Phys.*, 10:3812–3823, 2008.

[59] Yajun Zhou and Xiaowei Zhuang. Robust reconstruction of the rate constant distribution using the phase function method. *Biophysical Journal*, 91(11):4045 – 4053, 2006.

[60] A. Mathai, P. Moschopoulos, and G. Pederzoli. Random points associated with rectangles. *Rendiconti del Circolo Matematico di Palermo*, 48:163–190, 1999. 10.1007/BF02844387.

[61] J. G. Skellam. The frequency distribution of the difference between two poisson variates belonging to different populations. *Journal of the Royal Statistical Society*, 109(3):296, 1946.

[62] I.T. Jolliffe. *Principal Component Analysis*. Springer Series in Statistics. Springer, 2002. ISBN 9780387954424. LCCN 02019560.

[63] Arieh Aviram and Mark A. Ratner. Molecular rectifiers. *Chemical Physics Letters*, 29(2):277 – 283, 1974.

[64] Christian Bombis, Francisco Ample, Leif Lafferentz, Hao Yu, Stefan Hecht, Christian Joachim, and Leonhard Grill. Single molecular wires connecting metallic and insulating surface areas. *Angewandte Chemie International Edition*, 48(52):9966–9970, 2009.

[65] Leif Lafferentz, Francisco Ample, Hao Yu, Stefan Hecht, Christian Joachim, and Leonhard Grill. Conductance of a single conjugated polymer as a continuous function of its length. *Science*, 323 (5918):1193–1197, 2009.

[66] Mark Ratner. A brief history of molecular electronics. *Nat Nano*, 8(6):378–381, June 2013.

[67] Alexander Ako Khajetoorians, Jens Wiebe, Bruno Chilian, and Roland Wiesendanger. Realizing all-spin-based logic operations atom by atom. *Science*, 332(6033):1062–1064, 2011.

[68] **A**lternative **R**outes **T**owards **I**nformation **S**torage and **T**ransport at the Atomic and Molecular Scale (ARTIST). http://www.artist.cemes.fr/.

[69] H. Wende, M. Bernien, J. Luo, C. Sorg, N. Ponpandian, J. Kurde, J. Miguel, M. Piantek, X. Xu, Ph. Eckhold, W. Kuch, K. Baberschke, P. M. Panchmatia, B. Sanyal, P. M. Oppeneer, and O. Eriksson. Substrate-induced magnetic ordering and switching of iron porphyrin molecules. *Nat Mater*, 6(7):516–520, July 2007.

[70] Florian Buchner, Veronika Schwald, Karmen Comanici, Hans-Peter Steinrück, and Hubertus Marbach. Microscopic evidence of the metalation of a free-base porphyrin monolayer with iron. *ChemPhysChem*, 8(2):241–243, 2007.

[71] Willi Auwärter, Alexander Weber-Bargioni, Susan Brink, Andreas Riemann, Agustin Schiffrin, Mario Ruben, and Johannes V. Barth. Controlled metalation of self-assembled porphyrin nanoarrays in two dimensions. *ChemPhysChem*, 8(2):250–254, 2007.

[72] Florian Buchner, Ken Flechtner, Yun Bai, Elisabeth Zillner, Ina Kellner, Hans-Peter Steinrück, Hubertus Marbach, and J. Michael Gottfried. Coordination of iron atoms by tetraphenylporphyrin monolayers and multilayers on Ag(111) and formation of iron-tetraphenylporphyrin. *The Journal of Physical Chemistry C*, 112(39):15458–15465, 2008.

[73] J. Michael Gottfried, Ken Flechtner, Andreas Kretschmann, Thomas Lukasczyk, and Hans-Peter Steinrück. Direct synthesis of a metalloporphyrin complex on a surface. *Journal of the American Chemical Society*, 128(17):5644–5645, 2006.

[74] Andreas Kretschmann, Marie-Madeleine Walz, Ken Flechtner, Hans-Peter Steinrück, and J. Michael Gottfried. Tetraphenylporphyrin picks up zinc atoms from a silver surface. *Chem. Commun.*, pages 568–570, 2007.

[75] Catherine M. Doyle, Sergey A. Krasnikov, Natalia N. Sergeeva, Alexei B. Preobrajenski, Nikolay A. Vinogradov, Yulia N. Sergeeva, Mathias O. Senge, and Attilio A. Cafolla. Evidence for the formation of an intermediate complex in the direct metalation of tetra(4-bromophenyl)-porphyrin on the Cu(111) surface. *Chem. Commun.*, 47:12134–12136, 2011.

[76] Tatyana E. Shubina, Hubertus Marbach, Ken Flechtner, Andreas Kretschmann, Norbert Jux, Florian Buchner, Hans-Peter Steinrück, Timothy Clark, and J. Michael Gottfried. Principle and mechanism of direct porphyrin metalation: Joint experimental and theoretical investigation. *Journal of the American Chemical Society*, 129(30):9476–9483, 2007. PMID: 17625856.

[77] Ken Flechtner, Andreas Kretschmann, Hans-Peter Steinrück, and J. Michael Gottfried. No-induced reversible switching of the electronic interaction between a porphyrin-coordinated cobalt ion and a silver surface. *Journal of the American Chemical Society*, 129(40):12110–12111, 2007.

[78] Knud Seufert, Marie-Laure Bocquet, Willi Auwärter, Alexander Weber-Bargioni, Joachim Reichert, Nicolás Lorente, and Johannes V. Barth. Cis-dicarbonyl binding at cobalt and iron porphyrins with saddle-shape conformation. *Nat Chem*, 3(2):114–119, February 2011.

[79] Benjamin A. Friesen, Ashish Bhattarai, Ursula Mazur, and K. W. Hipps. Single molecule imaging of oxygenation of cobalt octaethylporphyrin at the solution/solid interface: Thermodynamics from microscopy. *Journal of the American Chemical Society*, 134(36):14897 – 14904, 2012.

[80] Shiri R. Burema, Knud Seufert, Willi Auwärter, Johannes V. Barth, and Marie-Laure Bocquet. Probing nitrosyl ligation of surface-confined metalloporphyrins by inelastic electron tunneling spectroscopy. *ACS Nano*, 2013.

[81] Francesca Moresco, Gerhard Meyer, Karl-Heinz Rieder, Hao Tang, André Gourdon, and Christian Joachim. Conformational changes of single molecules induced by scanning tunneling microscopy manipulation: A route to molecular switching. *Phys. Rev. Lett.*, 86:672–675, Jan 2001.

[82] Willi Auwärter, Knud Seufert, Felix Bischoff, David Ecija, Saranyan Vijayaraghavan, Sushobhan Joshi, Florian Klappenberger, Niveditha Samudrala, and Johannes V. Barth. A surface-anchored molecular four-level conductance switch based on single proton transfer. *Nat Nano*, 7:41 – 46, December 2012.

[83] Takashi Yokoyama, Shiyoshi Yokoyama, Toshiya Kamikado, and Shinro Mashiko. Nonplanar adsorption and orientational ordering of porphyrin molecules on Au(111). *The Journal of Chemical Physics*, 115(8):3814–3818, 2001.

[84] S. B. Lei, C. Wang, S. X. Yin, H. N. Wang, F. Xi, H. W. Liu, B. Xu, L. J. Wan, and C. L. Bai. Surface stabilized porphyrin and phthalocyanine two-dimensional network connected by hydrogen bonds. *The Journal of Physical Chemistry B*, 105(44):10838–10841, 2001.

[85] Jens Brede, Mathieu Linares, Stefan Kuck, Jörg Schwöbel, Alessandro Scarfato, Shih-Hsin Chang, Germar Hoffmann, Roland Wiesendanger, Roy Lensen, Paul H J Kouwer, Johan Hoogboom, Alan E Rowan, Martin Bröring, Markus Funk, Sven Stafström, Francesco Zerbetto, and Roberto Lazzaroni. Dynamics of molecular self-ordering in tetraphenyl porphyrin monolayers on metallic substrates. *Nanotechnology*, 20(27):275602, 2009.

[86] Soichiro Yoshimoto. Effects of protonation of pyridine moieties on the 2D assembly of porphyrin layers on Au(111) at electrochemical interfaces. *Chem. Commun.*, 48:4612–4614, 2012.

[87] Thilo Glatzel, Lars Zimmerli, Shigeki Kawai, Ernst Meyer, Leslie-Anne Fendt, and Francois Diederich. Oriented growth of porphyrin-based molecular wires on ionic crystals analysed by nc-AFM. *Beilstein J. Nanotechnol.*, 2:34 – 39, 2011.

[88] Sam Haq, Felix Hanke, Matthew S. Dyer, Mats Persson, Patrizia Iavicoli, David B. Amabilino, and Rasmita Raval. Clean coupling of unfunctionalized porphyrins at surfaces to give highly oriented organometallic oligomers. *Journal of the American Chemical Society*, 133(31):12031–12039, 2011.

[89] Yang Li and Nian Lin. Combined scanning tunneling microscopy and kinetic Monte Carlo study on kinetics of Cu-coordinated pyridyl-porphyrin supramolecular self-assembly on a Au(111) surface. *Phys. Rev. B*, 84:125418, Sep 2011.

[90] Yang Li, Jie Xiao, Tatyana E. Shubina, Min Chen, Ziliang Shi, Martin Schmid, Hans-Peter Steinrück, J. Michael Gottfried, and Nian Lin. Coordination and Metalation Bifunctionality of Cu with 5,10,15,20-Tetra(4-pyridyl)porphyrin: Toward a Mixed-Valence Two-Dimensional Coordination Network. *Journal of the American Chemical Society*, 134(14):6401 – 6408, 2012.

[91] Mendel In't Veld, Patrizia Iavicoli, Sam Haq, David B. Amabilino, and Rasmita Raval. Unique intermolecular reaction of simple porphyrins at a metal surface gives covalent nanostructures. *Chem. Commun.*, pages 1536–1538, 2008.

[92] Sergey Krasnikov, Catherine Doyle, Natalia Sergeeva, Alexei Preobrajenski, Nikolay Vinogradov, Yulia Sergeeva, Alexei Zakharov, Mathias Senge, and Attilio Cafolla. Formation of extended covalently bonded Ni porphyrin networks on the Au(111) surface. *Nano Research*, 4:376–384, 2011. 10.1007/s12274-010-0092-7.

[93] Lafferentz L., Eberhardt V., Dri C., Africh C., Comelli G., Esch F., Hecht S., and Grill L. Controlling on-surface polymerization by hierarchical and substrate-directed growth. *Nat Chem*, 4:215 – 220, January 2012.

[94] Peter Maksymovych, Dan C. Sorescu, and John T. Yates. Gold-Adatom-Mediated Bonding in Self-Assembled Short-Chain Alkanethiolate Species on the Au(111) Surface. *Phys. Rev. Lett.*, 97:146103, Oct 2006.

[95] I. Fernandez-Torrente, S. Monturet, K. J. Franke, J. Fraxedas, N. Lorente, and J. I. Pascual. Long-range repulsive interaction between molecules on a metal surface induced by charge transfer. *Phys. Rev. Lett.*, 99:176103, Oct 2007.

[96] Daniel Wegner, Ryan Yamachika, Yayu Wang, Victor W. Brar, Bart M. Bartlett, Jeffrey R. Long, and Michael F. Crommie. Single-molecule charge transfer and bonding at an organic/inorganic interface: Tetracyanoethylene on noble metals. *Nano Letters*, 8(1):131–135, 2008. PMID: 18069869.

[97] P. Atkins and J. de Paula. *Atkins' Physical Chemistry*. OUP Oxford, 2009. ISBN 9780199543373. LCCN 2010286938.

[98] Lindsay R. Merte, Guowen Peng, Ralf Bechstein, Felix Rieboldt, Carrie A. Farberow, Lars C. Grabow, Wilhelmine Kudernatsch, Stefan Wendt, Erik Lægsgaard, Manos Mavrikakis, and Flemming Besenbacher. Water-mediated proton hopping on an iron oxide surface. *Science*, 336 (6083):889–893, 2012.

[99] R. van Gastel, E. Somfai, W. van Saarloos, and J.W.M. Frenken. A giant atomic slide-puzzle. *Nature*, 408(6813):665–665, December 2000.

[100] R. van Gastel, E. Somfai, S. B. van Albada, W. van Saarloos, and J. W. M. Frenken. Nothing moves a surface: Vacancy mediated surface diffusion. *Phys. Rev. Lett.*, 86:1562–1565, Feb 2001.

[101] A. Zangwill. *Physics at Surfaces*. Cambridge University Press, 1988. ISBN 9780521347525. LCCN gb87034212.

[102] S Berner, M Brunner, L Ramoino, H Suzuki, H.-J Güntherodt, and T.A Jung. Time evolution analysis of a 2D solid-gas equilibrium: a model system for molecular adsorption and diffusion. *Chemical Physics Letters*, 348(3-4):175 – 181, 2001.

[103] Carlos J. Villagómez, Takashi Sasaki, James M. Tour, and Leonhard Grill. Bottom-up assembly of molecular wagons on a surface. *Journal of the American Chemical Society*, 132(47):16848–16854, 2010.

[104] Micol Alemani, Sofia Selvanathan, Francisco Ample, Maike V. Peters, Karl-Heinz Rieder, Francesca Moresco, Christian Joachim, Stefan Hecht, and Leonhard Grill. Adsorption and switching properties of azobenzene derivatives on different noble metal surfaces: Au(111), Cu(111), and Au(100). *The Journal of Physical Chemistry C*, 112(28):10509–10514, 2008.

[105] Saw-Wai Hla, Kai-Felix Braun, Violeta Iancu, and Aparna Deshpande. Single-atom extraction by scanning tunneling microscope tip crash and nanoscale surface engineering. *Nano Letters*, 4 (10):1997–2001, 2004.

[106] We-Hyo Soe, Carlos Manzano, Nicolas Renaud, Paula de Mendoza, Abir De Sarkar, Francisco Ample, Mohamed Hliwa, Antonio M. Echavarren, Natarajan Chandrasekhar, and Christian Joachim. Manipulating Molecular Quantum States with Classical Metal Atom Inputs: Demonstration of a Single Molecule NOR Logic Gate. *ACS Nano*, 5(2):1436–1440, 2011.

[107] L. Gao, Q. Liu, Y. Y. Zhang, N. Jiang, H. G. Zhang, Z. H. Cheng, W. F. Qiu, S. X. Du, Y. Q. Liu, W. A. Hofer, and H.-J. Gao. Constructing an array of anchored single-molecule rotors on gold surfaces. *Phys. Rev. Lett.*, 101:197209, Nov 2008.

[108] S. Müllegger, M. Rashidi, T. Lengauer, E. Rauls, W. G. Schmidt, G. Knör, W. Schöfberger, and R. Koch. Asymmetric saddling of single porphyrin molecules on Au(111). *Phys. Rev. B*, 83: 165416, Apr 2011.

[109] Y. Hasegawa and Ph. Avouris. Manipulation of the Reconstruction of the Au(111) Surface with the STM. *Science*, 258(5089):1763–1765, 1992.

[110] Jinming Cai, Pascal Ruffieux, Rached Jaafar, Marco Bieri, Thomas Braun, Stephan Blankenburg, Matthias Muoth, Ari P. Seitsonen, Moussa Saleh, Xinliang Feng, Klaus Mullen, and Roman Fasel. Atomically precise bottom-up fabrication of graphene nanoribbons. *Nature*, 466(7305): 470–473, July 2010.

[111] G. Kresse and J. Furthmüller. Efficient iterative schemes for *ab initio* total-energy calculations using a plane-wave basis set. *Phys. Rev. B*, 54:11169–11186, Oct 1996.

[112] M. Dion, H. Rydberg, E. Schröder, D. C. Langreth, and B. I. Lundqvist. Van der Waals Density Functional for General Geometries. *Phys. Rev. Lett.*, 92:246401, Jun 2004.

[113] Jiři Klimeš, David R. Bowler, and Angelos Michaelides. Van der Waals density functionals applied to solids. *Phys. Rev. B*, 83:195131, May 2011.

[114] John P. Perdew, Kieron Burke, and Matthias Ernzerhof. Generalized gradient approximation made simple. *Phys. Rev. Lett.*, 77:3865–3868, Oct 1996.

[115] Stefan Müllegger, Wolfgang Schöfberger, Mohammad Rashidi, Lorenz M. Reith, and Reinhold Koch. Spectroscopic STM Studies of Single Gold(III) Porphyrin Molecules. *Journal of the American Chemical Society*, 131(49):17740–17741, 2009. PMID: 19995071.

[116] Giovanni Di Santo, Stephan Blankenburg, Carla Castellarin-Cudia, Mattia Fanetti, Patrizia Borghetti, Luigi Sangaletti, Luca Floreano, Alberto Verdini, Elena Magnano, Federica Bondino, Carlo A. Pignedoli, Manh-Thuong Nguyen, Roberto Gaspari, Daniele Passerone, and Andrea Goldoni. Supramolecular Engineering through Temperature-Induced Chemical Modification of 2H-Tetraphenylporphyrin on Ag(111): Flat Phenyl Conformation and Possible Dehydrogenation Reactions. *Chemistry – A European Journal*, 17(51):14354 – 14359, 2011.

[117] Tomoya Ishizuka, Yuta Saegusa, Yoshihito Shiota, Kazuhisa Ohtake, Kazunari Yoshizawa, and Takahiko Kojima. Multiply-fused porphyrins-effects of extended π-conjugation on the optical and electrochemical properties. *Chem. Commun.*, 49:5939–5941, 2013.

[118] Jamie Conyard, Kiri Addison, Ismael A. Heisler, Arjen Cnossen, Wesley R. Browne, Ben L. Feringa, and Stephen R. Meech. Ultrafast dynamics in the power stroke of a molecular rotary motor. *Nat Chem*, 4(7):547–551, July 2012.

[119] S W de Laat, P T van der Saag, E L Elson, and J Schlessinger. Lateral diffusion of membrane lipids and proteins during the cell cycle of neuroblastoma cells. *Proceedings of the National Academy of Sciences*, 77(3):1526–1528, 1980.

[120] T. R. Linderoth, S. Horch, E. Lægsgaard, I. Stensgaard, and F. Besenbacher. Surface Diffusion of Pt on Pt(110): Arrhenius Behavior of Long Jumps. *Phys. Rev. Lett.*, 78:4978–4981, Jun 1997.

[121] Yasuhiro Shirai, Andrew J. Osgood, Yuming Zhao, Kevin F. Kelly, and James M. Tour. Directional control in thermally driven single-molecule nanocars. *Nano Letters*, 5(11):2330–2334, 2005.

[122] Nagatoshi Koumura, Robert W. J. Zijlstra, Richard A. van Delden, Nobuyuki Harada, and Ben L. Feringa. Light-driven monodirectional molecular rotor. *Nature*, 401(6749):152–155, September 1999.

[123] Rienk Eelkema, Michael M. Pollard, Javier Vicario, Nathalie Katsonis, Blanca Serrano Ramon, Cees W. M. Bastiaansen, Dirk J. Broer, and Ben L. Feringa. Molecular machines: Nanomotor rotates microscale objects. *Nature*, 440(7081):163–163, March 2006.

[124] Martin Klok, Nicola Boyle, Mary T. Pryce, Auke Meetsma, Wesley R. Browne, and Ben L. Feringa. MHz Unidirectional Rotation of Molecular Rotary Motors. *Journal of the American Chemical Society*, 130(32):10484–10485, 2008.

[125] Andranik Kazaryan, Jos C. M. Kistemaker, Lars V. Schäfer, Wesley R. Browne, Ben L. Feringa, and Michael Filatov. Understanding the dynamics behind the photoisomerization of a light-driven fluorene molecular rotary motor. *The Journal of Physical Chemistry A*, 114(15):5058–5067, 2010. PMID: 20349978.

[126] Artem A. Kulago, Emile M. Mes, Martin Klok, Auke Meetsma, Albert M. Brouwer, and Ben L. Feringa. Ultrafast light-driven nanomotors based on an acridane stator. *The Journal of Organic Chemistry*, 75(3):666–679, 2010. PMID: 20030300.

[127] Richard A. van Delden, Matthijs K. J. ter Wiel, Michael M. Pollard, Javier Vicario, Nagatoshi Koumura, and Ben L. Feringa. Unidirectional molecular motor on a gold surface. *Nature*, 437 (7063):1337–1340, October 2005.

[128] Jean-François Morin, Yasuhiro Shirai, and James M. Tour. En route to a motorized nanocar. *Organic Letters*, 8(8):1713–1716, 2006.

[129] Saumyakanti Khatua, Jason M. Guerrero, Kevin Claytor, Guillaume Vives, Anatoly B. Kolomeisky, James M. Tour, and Stephan Link. Micrometer-scale translation and monitoring of individual nanocars on glass. *ACS Nano*, 3(2):351–356, 2009. PMID: 19236071.

[130] Saumyakanti Khatua, Jazmin Godoy, James M. Tour, and Stephan Link. Influence of the substrate on the mobility of individual nanocars. *The Journal of Physical Chemistry Letters*, 1 (22):3288–3291, 2010.

[131] Pin-Lei E. Chu, Lin-Yung Wang, Saumyakanti Khatua, Anatoly B. Kolomeisky, Stephan Link, and James M. Tour. Synthesis and single-molecule imaging of highly mobile adamantane-wheeled nanocars. *ACS Nano*, 7(1):35 – 41, 2013.

[132] Guillaume Vives, JungHo Kang, Kevin F. Kelly, and James M. Tour. Molecular machinery: Synthesis of a "nanodragster". *Organic Letters*, 11(24):5602–5605, 2009. PMID: 20000442.

[133] Takashi Sasaki, Jean-François Morin, Meng Lu, and James M. Tour. Synthesis of a single-molecule nanotruck. *Tetrahedron Letters*, 48(33):5817 – 5820, 2007.

[134] Leo Gross, Karl-Heinz Rieder, Francesca Moresco, Sladjana M. Stojkovic, Andre Gourdon, and Christian Joachim. Trapping and moving metal atoms with a six-leg molecule. *Nat Mater*, 4 (12):892–895, December 2005.

[135] Sebastian Hagen, Peter Kate, Felix Leyssner, Dhananjay Nandi, Martin Wolf, and Petra Tegeder. Excitation mechanism in the photoisomerization of a surface-bound azobenzene derivative: Role of the metallic substrate. *The Journal of Chemical Physics*, 129(16):164102, 2008.

[136] Martin Wolf and Petra Tegeder. Reversible molecular switching at a metal surface: A case study of tetra-tert-butyl-azobenzene on Au(111) . *Surface Science*, 603(10 - 12):1506 – 1517, 2009. Special Issue of Surface Science dedicated to Prof. Dr. Dr. h.c. mult. Gerhard Ertl, Nobel-Laureate in Chemistry 2007.

[137] D. J. Coulman, J. Wintterlin, R. J. Behm, and G. Ertl. Novel mechanism for the formation of chemisorption phases: The (2×1)O-Cu(110) “added row” reconstruction. *Phys. Rev. Lett.*, 64: 1761–1764, Apr 1990.

[138] Matthew J. Comstock, Niv Levy, Armen Kirakosian, Jongweon Cho, Frank Lauterwasser, Jessica H. Harvey, David A. Strubbe, Jean M. J. Fréchet, Dirk Trauner, Steven G. Louie, and Michael F. Crommie. Reversible photomechanical switching of individual engineered molecules at a metallic surface. *Phys. Rev. Lett.*, 99:038301, Jul 2007.

[139] Johannes Mielke, Sofia Selvanathan, Maike Peters, Jutta Schwarz, Stefan Hecht, and Leonhard Grill. Molecules with multiple switching units on a Au(111) surface: self-organization and single-molecule manipulation. *Journal of Physics: Condensed Matter*, 24(39):394013, 2012.

[140] Peter Liljeroth, Jascha Repp, and Gerhard Meyer. Current-induced hydrogen tautomerization and conductance switching of naphthalocyanine molecules. *Science*, 317(5842):1203–1206, 2007.

[141] Ali Safiei, Jörg Henzl, and Karina Morgenstern. Isomerization of an azobenzene derivative on a thin insulating layer by inelastically tunneling electrons. *Phys. Rev. Lett.*, 104:216102, May 2010.

[142] Hartmut Schwertfeger, Andrey A. Fokin, and Peter R. Schreiner. Diamonds are a chemist's best friend: Diamondoid chemistry beyond adamantane. *Angewandte Chemie International Edition*, 47(6):1022–1036, 2008.

Erklärung

Ich versichere, dass ich diese Arbeit selbständig verfasst und keine anderen als die angegebenen Quellen und Hilfsmittel benutzt habe.

Berlin, den 12. Juni 2013